FABRICATION AND PLASTIC DEFORMATION OF COPPER AT SMALL SCALES

By

XINXIN ZHAO

A thesis submitted to the University of Birmingham

for the degree of

DOCTOR OF PHILOSOPHY

School of Metallurgy and Materials

University of Birmingham

July 2014

ABSTRACT

In the current study, copper nanowires are fabricated by filling the nanochannels of anodic aluminium oxide (AAO) templates using electrodeposition. The nanowires with different growth orientations as well as twin boundaries in some cases are obtained. Cu micropillars are machined from bulk materials using focused ion beam (FIB) milling. The micropillars oriented in the [235] and [156] directions, with and without a twin boundary, with a cylindrical or square shape and with different sizes are prepared. These pillars are then compressed by a nanoindenter equipped with a flat tip, and the stress-strain curves are obtained. The morphologies of the pillars are observed using scanning electron microscopy (SEM). Thin foils of the pillars are prepared by FIB and examined using transmission electron microscopy (TEM) and scanning TEM (STEM). Finally, the dislocation structures are analysed to shed light on the investigation of the deformation mechanisms.

An atypical two-stage hardening has been found in the deformation of the single crystal micropillars. Stage I, characterised by a high hardening rate, is controlled by the gradual exhaustion and activation of single-armed dislocation sources. Stage II with a relatively low hardening value is dominated by dislocation-escape mediated forest hardening. Dislocations are not retained in pillars smaller than 1 µm while dislocation networks and even cell structures have been observed in the larger samples. Due to the limited number of dislocation sources in the micropillars, single slip occurs in some of the multiple-slip oriented [156] cylinders. The [235] square pillars exhibit lower hardening rates than the [156] ones, as separate long primary screw dislocation arrays prevail in the former while intensive dislocation interactions are found in the latter. In general, the [156]/[516] twinned pillars exhibit higher hardening rates than the [156] single crystals, for both cylinders and square prisms. Dislocations can cut through the twin boundary in the early stage of deformation, but as the dislocation density increases, the twin boundary starts to block the dislocation movement and to strengthen the pillar. Both single crystal and twinned square pillars display higher hardening rates

than their cylindrical counterparts. In the square pillars, stress inhomogeneities are caused by the side edges. The dislocation distribution on the various slip systems is different from that in the cylindrical ones. The fact that the cross-sectional area of the square pillars is smaller than that of the cylinders may also contribute to the higher strengths of the former.

PREFACE

The work described in this thesis was carried out by the author in the Department of Metallurgy and Materials, at The University of Birmingham, from October 2009 to July 2014, under the supervision of Dr. Y.L. Chiu and Prof. I.P. Jones.

The material presented here is original and no part of this work has been submitted for a degree at this or any other university. Where the work of others has been drawn upon, it is acknowledged in the text.

Part of the present work has been presented at the Electron Microscopy and Analysis Group Conference 2011 (EMAG 2011) and published as:

Zhao X, Chiu YL and Jones IP, Electron microscopy of electrochemically deposited copper nanowires. Electron Microscopy and Analysis Group Conference 2011 (Emag 2011), 2012. 371.

Papers based on micropillars are in preparation.

ACKNOWLEDGEMENTS

To my mother.

Contents

4

Chapter 1 Introduction

Over the past decade, focused ion beam (FIB) has been used as a powerful tool for preparing small-scale samples [1]. Pillars ranging from several tens of micrometres to a few hundreds of nanometres can be readily extracted from the bulks [2-7]. These small samples can then be compressed using a nanoindenter equipped with a flat punch, which provides accurate load and displacement measurements.

Deformation behavior of metals has consequently been investigated extensively in the micron and sub-micron regimes. A "smaller is stronger" trend has consistently been observed for samples below 10 μm; the flow stresses exhibit a power-law dependence on the sample sizes; the power exponents were found to range from -0.4 to -1.0 for various materials [4, 8-10]. In addition, intermittent deformation of microsamples is manifested by pronounced strain bursts [11-13] and stochastic scattering in the deformation curves is commonly observed, especially in smaller samples [3, 6, 14].

Nevertheless, the plasticity in micro-scale is still not fully understood. Several models have been proposed to explain the significantly higher flow stresses found in the microsamples. These include i) dislocation starvation: dislocations escape through free surfaces, leaving the sample in a dislocation-starved state and new dislocation sources need to be nucleated for further deformation [15]. ii) Source exhaustion: only a limited number of dislocation sources exist in the confined sample volume and the progressive operation of harder dislocation sources strengthens the microsamples [16]. iii) Source truncation: the dislocation sources are truncated by the free surfaces, hence smaller samples contains smaller sources, which require

a higher applied stress to activate [17, 18].

Most of the studies concentrate on single crystals [4, 8-10]; only a few investigations involve samples with internal interfaces [19-21]. Also, none of the studies has attempted to compare the mechanical response of samples oriented for single or multiple slip. Furthermore, besides the in-situ TEM investigations, which target sample sizes below several hundred nanometres [16, 17, 22], only a limited number of studies have examined dislocation microstructures in samples with diameters above 1 μm [5, 23].

This thesis focuses on the study of small-scale Cu samples. Firstly, the fabrication of Cu nanowires has been attempted, which paved the way for the future investigation of their deformation behaviour. No deformation testing was done due to the lack of available equipment, as the initial plan of building up a homemade in-situ TEM tensile block turned out to be extremely challenging. Hence we started to work on the second part of Cu micropillars. Compression tests on Cu micropillars oriented in [235] or [156] directions, with or without a twin boundary, in a cylindrical or square shape and with different sizes have been conducted. Finally, direct observations of the dislocation structures in these deformed microcrystals have been used to shed light on the possible explanations for their different plastic response.

Scope of the present work:

Chapter 2 will begin with an introduction to the anodic aluminium oxide (AAO) based fabrication of nanowires. The next section will highlight the deformation mechanisms in bulk FCC crystals, followed by an overview of the literature on micro-compression testing. Lastly, reactions of slip dislocations with twin boundaries will be introduced.

Chapter 3 will summarize the fabrication method used for the Cu nanowires and the experimental procedure for the compression of Cu micropillars.

Chapter 4 will present the microstructure of the Cu nanowires as well as of the AAO template.

Chapter 5 will describe the mechanical response of the Cu micropillars, followed by their surface morphology.

Chapter 6 will concentrate on the TEM observations of the deformed micropillars.

Chapter 7 will discuss the deformation behaviour of the micropillars in the light of the dislocation analysis.

Chapter 2 Literature review

2.1 Fabrication of nanowires/nanopillars

In recent years, due to the discovery of ordered-pore AAO, many efforts have been made to synthesize nanowires via the nanopores in AAO using electrochemical deposition. The AAO template has significant advantages such as uniform and well-aligned pores, high temperature resistance and a large range of pore diameters. Compared to other methods, the AAO-based fabrication of nanowires is of relatively low cost and simple in operation [24].

2.1.1 Growth mechanism of the AAO template

During the anodisation of aluminium, two types of oxide films can grow depending on the electrolyte's dissolution ability. Barrier-type films, which are dense and flat, are obtained in nearly neutral electrolytes in which the dissolution is very slow, while porous-type films (AAO), which contain not only pores passing normal to the metal surface but also a thin barrier layer at the pore bottoms, are formed in acid solutions in which the dissolution is fast [25].

The reaction equations of the anodisation process of AAO are listed below：

$$\text{Cathode：} \quad 2H^{+}+2e=H_2 \tag{2.1}$$

$$\text{Anode：} \quad 2Al-6e=2Al^{3+} \tag{2.2}$$

$$4OH^{-}=2H_2O+O_2+4e \tag{2.3}$$

(O_2 may exist in the form of O^{2-} when OH^- loses more electrons)

$$2 \, Al^{3+}+6OH^- =Al_2O_3+3H_2O \tag{2.4}$$

$$2 \, Al^{3+}+3O^{2-}= Al_2O_3 \tag{2.5}$$

Dissolution at the oxide/electrolyte interface:

$$Al_2O_3+6 \, H^+=2 \, Al^{3+}+3H_2O \tag{2.6}$$

The formation process of AAO can be divided into four steps. First, the electrochemical reaction results in a dense oxide layer on the highly pure aluminium surface which significantly decreases the conductivity and thus the anodic current decreases rapidly. In the second step, dissolution becomes competitive and the pores nucleate randomly on the oxidation membrane due to the roughness of the metal surface. In the third step, the pores grow gradually and the pore position modulates spontaneously. The final step is a steady state process of pore growth. In this process, there is an equilibrium between field-enhanced oxide dissolution at the oxide/electrolyte interface and oxide growth at the metal/oxide interface. Thus the thickness of the barrier layer at the pore bottom remains constant and the pores grow continuously upwards. The resulting structure of AAO is shown in Figure 2-1 [26].

Although AAO with hexagonal pores was first reported more than 50 years ago [27, 28], it took a long time to obtain a hexagonally ordered pore structure, because only certain sets of parameters can secure it. In 1995, Masuda et al. [29] produced AAO as a periodic array using fabrication conditions which are now widely used in this field. They found that anodisation conducted in oxalic acid at 40V for 160 hours, produced an almost ideally arranged honeycomb structure. They suggested that the long anodising duration improved the

5

regularity of the nanoholes by rearranging the structure. However, in recent years, instead of anodising for such a long period to fabricate ordered pore arrays, people have been using aluminium with pretextured patterns as the starting material [30] or a two-step anodisation process which will be described in detail in the next chapter, to shorten the duration of the experiment [31].

The applied voltage has a major effect on the interpore distance of AAO regardless of the other anodising conditions (e.g. temperature, pH value, electrolyte type and concentration). The general rule is

$$D_{int} = kU \tag{2.7},$$

where D_{int} is the interpore distance, U is the applied voltage and k is a constant with an approximate value of 2.5 nm/V. The thickness of the barrier layer, which is almost half the interpore distance under optimum conditions, is also determined by the voltage [32]. The diameter of the pores is controlled by the specific electrolyte and subsequent etching process.

In an acid solution, the dissolution rate of the oxide is uneven due to impurities, dislocations, grain boundaries, nonmetallic inclusions, roughness, etc. [32]. This dissolution leads to the formation of pits acting as the initial step for the pore growth.

There are several possible explanations for the oxide dissolution and pore growth:

1. Field-assisted dissolution: the electric field which is concentrated at the bottom of the pores increases the dissolution rate.

2. Local electrolyte heating: the current increase due to the concentrated electric field induces

overheating, which speeds up the dissolution rate, causing the pores to grow. [33]

3. Direct ion transfer: the oxygen-containing ions move from the electrolyte through the oxide layer at the pore bottom to form new oxide at the metal/oxide interface, while some Al^{3+} ions moving through the oxide layer are ejected into the electrolyte at the oxide/electrolyte interface, as shown in Figure 2-2.

4. The precipitation of gel-like aluminium hydroxide: Al^{3+} ejected at the interface can form hydrated ions in the solution and thus the growth of oxide at the oxide/electrolyte interface, which forms the pore wall, can be realized by precipitation from initially colloidal hydrous alumina [34].

Notwithstanding the above, it is commonly accepted that there is an equilibrium between oxide dissolution at the oxide/electrolyte interface and oxide growth at the metal/oxide interface during steady-state anodisation. This balance ensures the constant thickness of the barrier layer and the continuous growth of the porous layer.

The self-organized formation mechanism for AAO still remains an open question although great achievements have been made in recent years. Mechanical stress serving as the driving force for the self-organization process is the most popular model. According to Jessensky et al. [35], the volume expansion during oxide formation causes mechanical stress at the metal/oxide interface, and this stress is considered as the origin of the repulsive forces between neighbouring pores, which can facilitate the self-organisation. The authors believe that a moderate volume expansion will result in ordered nanopore arrays while the large volume expansion associated with a higher anodising voltage and thus a larger growth rate can induce structural defects and also shorten the time for the self-organisation process.

Therefore, ordered nanopore arrays can only occur at certain voltages in different electrolyte solutions to ensure moderate volume expansion. The model was further supported by Li et al. [36], who estimated that the stress in the self-organization process was of the order of 4.0×10^3 MPa or less which mainly depended on volume expansion via the following equations:

$$E_p = E_{alo}(1 - p)^2 \tag{2.8}$$

$$\varepsilon = \sqrt[3]{V_R} - 1 \tag{2.9}$$

where E_p is the Young's modulus of porous alumina, p is the porosity of the alumina, E_{alo} corresponds to bulk alumina, ε is the linear elastic strain at the metal/oxide interface and V_R is the volume expansion factor for AAO.

There is another interesting mechanism involved in the equifield model proposed by Su et al. [37]. They reported that the self-organization was governed by electric field enhanced electrochemical reactions. The electric field applied to the oxide layer can be written as $E = U/d$, where E is the electric field, U is the voltage and d is the thickness of the oxide. According to them, a critical value of electric field strength E_c always exists, below which the anions cannot be driven through the barrier layer by the weak field strength. When the oxide is thick, dissolution will dominate the process and reduce the thickness. When the oxide is thin, the ion migration rate enhanced by the electric field tends to increase the oxidation rate, and thus the thickness would also be increased. Under a balanced field E_b, the anodisation will continue and the thickness of the barrier layer will remain constant. The scalloped shape at the oxide/metal interface is the only morphology for a uniform thickness and equifield strength in the whole area. Also the equifield model contains a 2-D interpore distance

adjustment process to generate the hcp structure.

2.1.2 Nanowires fabricated by electrochemical deposition

Deposition into the pores of AAO membrane is an efficient method to fabricate nanowires at low cost. Metal nanowires such as Ag [38], Co [39], Ni [40], Bi [24]and Cu [41] have been synthesized via the AAO-based method. It is well known that deposition parameters can strongly affect the microstructure of the resulting products.

A higher deposition potential which increases the crystal nucleation rate and enlarges the nucleation sites is likely to form polycrystalline nanowires. Gao et al. [41] successfully obtained single crystal copper nanowires using a quite low deposition voltage. Furthermore, the side reaction of hydrogen generation is aggravated as the applied voltage increases: the resulting small hydrogen gas bubbles are likely to block the migrating path of metal ions in the pores, which tends to hinder the deposition of metal into the nanopores. Tian et al. [42] also reported that the texture of nanowires transformed from polycrystalline to bamboolike structures and then to single crystals as the applied potential decreased. A two dimensional nucleation/growth mechanism was proposed by them to explain the formation of the single crystal nanowires. The critical dimension N_c for a 2D-like nucleus can be expressed as

$$N_c = bs\varepsilon^2/(Ze\eta)^2 \tag{2.10}$$

where s is the area occupied by one atom on the surface of the nucleus, ε is the edge energy, Z is the effective electron number, η is the overpotential and b is a constant [43]. During electrodeposition, if the size of the initial cluster exceeds the critical value N_c, new grains will grow and thus a polycrystalline structure will form. According to the above equation, a lower

9

over potential secures a larger N_c and the chance of obtaining single crystals. Furthermore, Huang et al. [39] found that Co nanowires would transform from HCP to FCC, because the electrodeposition of atomic hydrogen increased and thus a metastable Co hydride with an FCC structure formed.

Current density plays an important role in deciding the growth orientation of nanowires. Different crystalline planes have different broken-bond numbers and surface energies; thus ions with different kinetic energies under different current densities will selectively deposit onto planes of lowest energy and form different growth orientations [39].

There are contradictory points of view in the literature about the effects of deposition temperature on the structure of nanowires. Toimil-Molares et al. [44] reported that fine-grained polycrystalline nanowires were obtained at room temperature, larger grain polycrystalline nanowires were created at 40°C and single crystalline nanowires were formed at 60°C. They suggested that the increased temperature caused a decrease of the cathode polarization, which resulted in a more efficient transport of ions towards the electrode and an increase in surface diffusion. The growth of pre-existing nuclei was preferred in such a situation and single crystals appeared. However, Wang et al. [38] claimed that polycrystalline nanowires were produced at higher temperature. The reason, according to their explanation, was that the thermal energy agitated the growth and distorted the competition between adjacent grains.

The pH value of the electrolyte is also considered to have an effect on the growth orientation of nanowires. Huang et al. [39] mentioned that for FCC Co nanowires, a growth direction of <220> was preferred when the pH=2 while <111> was favoured when the pH=4. They

explained that there were more hydrogen ions in the electrolyte with a lower pH value and thus the adsorption of these ions onto the cathode was much easier, stabilising the (110) plane of the nanowires. Moreover, lower quality nanowires composed of oxide or hydroxide are likely to be obtained in a higher pH solution.

Wang et al. [16] investigated the size effect on the growth orientation of Ni nanowires. They found that a small diameter can result in [110] growth, the growth may then turn to [111] with increasing diameter. To explain this phenomenon, they considered the energy minimum principle and proposed an equation $\frac{S_1}{S_2} = \frac{4\Delta h}{D}$ to show the ratio of the area of the circumference side to the area of the top side of the nanowires, where S_1 is the circumferential side area, S_2 is the top side area in a single pore cell of AAO and h and D are the corresponding height and diameter. This ratio represents the contribution of the Ni/Al$_2$O$_3$ and Ni/electrolyte interface energies. When D is small, S_1, which represents the pore wall, is predominant in deciding the growth orientation based on the AAO/Ni interface energy. With increasing diameter, the leading effect in determining the growth orientation is shifted to S_2 by the Ni/electrolyte interface energy.

2.2 The plastic deformation of (bulk) face-centred cubic (fcc) crystals

2.2.1 Stress-strain curves and deformation microstructure of pure fcc crystals

A typical stress-strain curve of a pure fcc metal crystal is shown in Figure 2-3. It consists of

three distinct regions that are defined by different work hardening rates θ, although one or more of these may disappear depending on testing conditions. The extent of each region is affected by the metal, crystal orientation, crystal size and shape, purity, temperature of test and surface condition [45]. Steeds et al. [46] performed detailed observation of the microstructure in copper crystals deformed into different stages using TEM, as further elaborated below.

2.2.1.1 Stage I hardening

Stage I, known as the easy glide region, has low constant hardening rate, typically $\theta_I \sim 10^{-4} G$, where G is the shear modulus. This is a stage where only one glide system operates, thus the dislocations are moving relatively large distances on planes with the highest resolved shear stress without meeting other obstacles. Very few secondary dislocations are formed in this stage therefore no secondary slip systems interact with dislocations on the primary glide system. Thus the flow stress is governed by the ease with which sources start to operate.

As can be seen in Figure 2-4(a), isolated bundles containing many short edge dipoles were observed in stage I. These bundles elongated normal to the primary Burgers vector, in other words, along the primary edge direction. They are formed by the elastic interactions of parallel edge dislocations of opposite sign. Screw dislocations were remarkably absent from the foils due to cross-slip and annihilation.

2.2.1.2 Stage II hardening

Stage II is characterized by a high constant work hardening rate, $\theta_{II}/G \sim 1/300$ for all fcc metals and $\sim 1/150$ for orientations at the corners of the unit triangle [47]. This begins when

the applied stress, together with internal stress from primary dislocations, is sufficient to reach the critical resolved shear stress on the second system. The secondary slip results in strong obstacles and pile-ups of primary dislocations, leading to a high hardening rate [48].

At the beginning of stage II, secondary sources near the dipole bundles are activated, causing local interactions between primary and secondary dislocations and forming dislocation barriers. As presented in Figure 2-5, notably large numbers of secondary dislocations were found in the bundles. The figure clearly reveals that dipoles and edge dislocations from the primary slip system help build the dislocation walls. Previous work [49] also indicates that the density of secondary dislocations is highest in those regions where the primaries accumulated. As shown in Figure 2-4(b), continuous dense bundles were present, and a considerable number of secondary dislocations appeared in the general background. Secondary slip partially relieves the internal stresses around dislocation pile-ups, which become regions of high dislocation density containing secondary dislocation networks and dipoles as the strain rises. These regions obstruct dislocation motion, and lead to further secondary slip, facilitating the formation of new obstacles. Therefore a two-dimensional dislocation cell structure is formed in stage II, as shown in Figure 2-4(c). The cell structure decreases in size as the stress increases.

2.2.1.3 Stage III hardening

The stress-strain curve in stage III is parabolic, showing a decreasing rate of hardening. This stage begins when dislocations in stage II are moved by the higher applied stress. In this process, in addition to the climb of edge dislocations at high temperatures, cross slip of screw dislocations occurs and thus screws can bypass the obstacles in their glide plane by double

cross-slip without interacting with them directly. Therefore, a decreased work hardening rate is expected because strong dislocation interactions are avoided. The dislocation density is also reduced by the attraction and annihilation of screws of opposite sign which also reduces the internal stress. Moreover, low-angle boundaries are formed at this stage by the rearrangement of the edge dislocations.

TEM observations of a plane inclined to the slip plane show the formation of alternately misoriented bands, as shown in Figure 2-4(d). These bands are mainly composed of boundaries approximately parallel to the primary slip plane. As explained previously, the boundaries result from the double cross slip of screw dislocations.

2.2.2 Taylor hardening

Taylor proposed that internal stress caused by the trapped dislocations hinders the movement of other mobile dislocations. Consequently, work hardening occurs when dislocations become difficult to move under increased strain. The flow stress is then the stress needed for a dislocation to overcome the stress field caused by the surrounding dislocations. Taylor gave the following expression:

$$\tau = \frac{\alpha \mu b}{l} \tag{2.11}$$

where μ is the shear modulus, b is the Burgers vector, l is the mean distance between the dislocations, and $\alpha = 1/8\pi(1-\upsilon)$, where υ is Poisson's ratio. As the line density ρ of a network of dislocations of spacing l is $\rho = l^{-2}$, the equation can be rewritten as

$$\tau = \alpha \mu b \sqrt{\rho} \tag{2.12}$$

14

2.2.3 Crystal orientation

2.2.3.1 Schmid Factor

The Schmid Factor relates the applied stress in the loading direction to the shear stress along the slip direction. Slip occurs when the shear stress on the slip plane reaches some critical value, known as the critical resolved shear stress τ_C. τ_C is a constant for a given material with specified dislocation density and purity.

$$\tau_R = \frac{\text{resolved force on slip plane}}{\text{area of slip plane}} = \frac{F \cos\lambda}{A/\cos\phi} = \frac{F}{A}\cos\phi\cos\lambda = \sigma\cos\phi\cos\lambda = \sigma m$$

(2.13)

The quantity $m = \cos\phi\cos\lambda$ is known as the Schmid Factor, where ϕ is the angle between the slip plane normal and load F and λ is the angle between the slip direction and F.

The Schmid Factor predicts the operative slip systems in deformed single crystals with different orientations. The number of expected operative slip systems is summarized in Figure 2-6. For crystals with a loading orientation within the stereographic triangle, deformation starts on one slip system, while for crystals with orientations lying on the boundaries, deformation commences on more than one slip plane.

2.2.3.2 Influence of crystal orientation

Both stage I and stage II deformation are quite sensitive to crystal orientation. As can be seen from Figure 2-7, there are hard orientations and soft orientations in each unit triangle. Soft orientations are remote from the boundaries of the triangle, while hard orientations lie close to or on the sides of the triangle. This is easy to understand as two or more slip systems operate

in the latter case. Stress-strain curves of copper crystals with different orientations are presented in Figure 2-8. In the hardest orientations, stage I hardening is entirely eliminated and the curves mainly display stage II hardening. However, on the other hand, the softest region shows stage I hardening up to 15% shear strain. The hardening rates in both stage I and II are orientation dependent and follow the same trend, with maximum values near <001> and <111> (where 8 and 6 slip systems respectively operate) and minimum values towards <011>.

2.3 Micro-compression

Mechanical tests of miniature samples at the micron and submicron scale are utilized to improve knowledge of plastic deformation when the sample size shrinks to the fundamental length scales for dislocation-based plastic flow. Uniaxial deformation such as tension and compression is easier to understand and therefore is preferred due to the absence of a strain gradient. Micro-compression tests have frequently been used to investigate micro-mechanical properties since the methodology was first developed by Uchic et al. a decade ago [1]. Micro-samples ranging from single crystals to polycrystals, intermetallics and metallic glasses are fabricated using FIB. Fibbed micro-samples are integrally attached to the bulk substrate, allowing the sample to be placed easily within the testing equipment. Nanoindenters with a flat tip punch are used to perform the compression tests. The applied force at the micro-Newton scale and measured displacement at the nanometre scale make the instrument an ideal system to characterize the mechanical behaviour of the micropillars.

Size dependent strengthening, intermittent and stochastic flows have all commonly been observed.

2.3.1 Dislocation-free micro-samples

In the 1950's Brenner [50] performed tensile tests on whiskers of Fe, Cu and Ag with diameters ranging from 1.2 to 15 μm. He reported that the yield strength of these micro-samples is typically 80 to 1200 times larger than that of bulk specimens and that the average strength is inversely proportional to the sample diameter. The smallest crystal exhibiting the highest strength shows a shear stress approaching the theoretical value ~G/30, where G is the shear modulus. The extremely high yield strength is caused by the necessity of nucleation of dislocations in these nearly dislocation-free whiskers. A typical stress-strain curve is shown in Figure 2-9. The curve is composed of an immensely high yield point followed by remarkable strain softening and an easy glide region with very small flow stress; finally a work hardening region. The low flow stress is attributed to a high density of mobile dislocations after yielding [51].

Recently Bei et al. [52] also investigated the mechanical properties of dislocation-free micro-pillars. A composite material, consisting of single crystal Mo alloy fibres embedded in a NiAl matrix was chemically etched to leave freestanding square fibres as the matrix was removed. The side edge ranged from ~360 nm to 1000 nm. The Critical Resolved Shear Stress of these pillars in compression tests has a value of G/26, which is within the range of expected theoretical strengths, independent of sample size.

2.3.2 Size dependent strength

Initial studies on the deformation of samples at the micron and submicron scale focused on the size effect. Compression tests performed on micropillars with different sample diameters

suggest that flow strength increases dramatically with decreasing sample dimensions.

The empirical size dependence of the compression strength is described by a power law relationship: $\sigma_y = \sigma_0 + Ad^m$, where σ_0 is a scale-independent yield stress, d is the pillar diameter, and A and m are empirical constants, magnitude of m is different for different materials.

After considering the corresponding shear modulus μ and Burgers vector b of various materials, the formula was further modified to $\frac{\sigma_{rss}}{\mu} = A(\frac{d}{b})^m$ by Dou et al. [53], in which σ_{rss} is the resolved yield stress, obtained by multiplying the measured stress by the corresponding Schmid factor. The authors concluded that for most face-centred cubic (fcc) metals A = 0.71 and m= -0.66 after comparing the experimental data from Ni, Au, and Al. However, the data for Cu is separate from the fitted curve with a relatively larger exponent, which is reported to be –0.4 in Kiener's study [54].

Different theories have been proposed to explain this phenomenon, as discussed below.

2.3.2.1 Dislocation starvation

Greer et al. [15] performed uniaxial compression tests on gold pillars with diameters ranging from 400 to 7450 nm, in which a very strong size effect on the flow stresses was found. They compared their results with those from the previously mentioned dislocation-free copper whiskers, as the small samples here also exhibit very high strengths. They found that in the stress-strain curves of their gold pillars, the flow stress does not drop as dramatically as that in the whiskers after yielding. So they suggested that strain burst events caused a dislocation-starved situation in the pillars thus maintaining the high flow stress.

In conventional plasticity, dislocation multiplication and interaction lead to increased dislocation density and strain hardening. However, as Gilman [55]wrote, the distance a dislocation must travel before multiplication occurs is normally on the micrometre scale. For crystals with dimensions smaller than this length scale, dislocation multiplication may be inhibited. Because of this the dislocations annihilate at the free surfaces directly without multiplication, leaving the crystal in a dislocation-starved state. Further deformation in this situation requires dislocation nucleation, requiring a high stress to be applied.

Subsequently Greer et al. [2] analyzed dislocations in a deformed gold pillar using TEM. Only those with Burgers vector perpendicular to the loading axes were left in the pillar. This result supports the dislocation starvation theory by showing that all the mobile dislocations escaped from the crystal during deformation, and only immobile dislocations were left due to their lack of resolved shear stress. Note that the accurate pillar diameter for this dislocation analysis is not given in the publication, but it must have a diameter between 200 nm and several micrometres.

Another direct experimental support for dislocation starvation is given by Shan et al. [16]. They conducted *in situ* compression tests of Ni pillars between 150 and 400 nm in diameter inside a TEM. A complete dislocation-free pillar after deformation was obtained from a pillar with a diameter of 150 nm. During deformation, they observed the escape of pre-existing dislocations as well as the generation of new dislocations. Both the pre-existing and newly generated dislocations traversed the pillar, leaving a dislocation-free state, which they termed 'mechanical annealing'. They suggested that the applied stress activates dislocation nucleation and the image force assists the movement of dislocation towards the free surfaces.

Furthermore, they conducted a compression test on this dislocation-free pillar. A yield stress similar to the value from the first compression test was achieved, despite the remarkable difference in starting dislocation density, i.e., zero versus $10^{15} \, m^{-2}$. This again suggests that dislocation nucleation governs the deformation of the pillar. However, the authors also reported that pillar diameter influenced the extent of mechanical annealing because the image force decreases with increasing sample diameter. Thus in larger pillars the image force would not be able to remove all the dislocations.

2.3.2.2 Source truncation

Another model that explains the size effect is the source truncation model. Finite sample dimensions in the micro-compression tests limit the effective dislocation source length in the crystals, thus affecting strength.

Parthasarathy et al. [18] proposed that at the micrometre scale, the dislocation source length is a function of sample size. They suggested that for micropillars, one double-ended Frank-Read source becomes two truncated sources with single arms. This is due to the influence of the image forces from the free surfaces, as illustrated in Figure 2-10. Direct experimental observation of these single-armed sources was obtained from an in situ TEM straining study on single Al crystals [22]. The stress required to activate these truncated sources is determined by the shortest distance λ from the pinning point to the free surface. For microcrystals which contain several single armed sources, the critical stress to initiate plastic deformation depends on the arm with the longest length λ_{max}. The critical resolved shear strength (CRSS) of a micropillar is given by

$$CRSS = \frac{\alpha Gb}{\lambda_{max}} + \tau_0 + 0.5Gb\sqrt{\rho_{tot}} \qquad (2.14)$$

where α is a geometrical constant, G is the shear modulus, b is the Burgers vector, τ_0 is the friction stress and ρ_{tot} is the total dislocation density. This first term in this expression is similar to that for a full Frank-Read source, while a suitable geometrical constant still needs to be identified. They obtained the mean and standard deviation of the source lengths for different pillar diameters using a numerical simulation based on a single slip model, where a fixed number of pins were randomly placed on an oblique slip plane. By then predicting the corresponding CRSS using the simulation and comparing with experimental data, it was found that the size effect in microcrystals could be rationalized sufficiently by considering the variation of dislocation source lengths, as shown in Figure 2-11.

The model based on these single ended sources was further discussed for multiple slip systems by Ng and Ngan [8]. They performed Monte Carlo simulations, in which the interaction of dislocations lying on different slip systems was considered. As shown in Figure 2-12, dislocations lying on slip plane A would constitute pinning points for the other non-parallel slip planes B, C and D. This also results in the formation of single armed half-Frank-Read sources. Each of them consists of a pinning point at one end and a free moving tail emerging on the surface at the other end. This explains the size dependence of the yield strength, because the weakest source normally possesses a large length λ close to the pillar radius. The stress required to operate each source is calculated using the following equation:

$$\sigma_c = \alpha \left(\frac{Gb}{\lambda \cos \phi \cos \theta} + \frac{Gb}{l_{mean} \cos \theta} \right) + \frac{\tau_0}{\cos \phi \cos \theta}, \qquad (2.15)$$

where ϕ and θ are the angles between the load axis and the slip direction and l_{mean} is the

average distance between pinning points. This equation has a similar form to the previous one proposed by Parthasarathy et al. [18] As this is for multiple slip, a term $\cos\emptyset\cos\theta$ representing the Schmid factor is incorporated.

In addition to explaining the size effect using this source truncation model, the authors also investigated the validity of Schmid's law for the microcrystals based on the simulation. A statistical analysis of the yield probability in each slip system was carried out. They first calculated the compressive yield strength σ_y for a particular slip plane, which equals the minimum value of σ_c for all the sources on that plane. Then they compared σ_y for all the slip systems: the plane with the minimum value is considered to yield first. They performed the simulation for Al pillars with different diameters oriented in the $[3\bar{1}5]$direction, d=6.3, 2.6 and 0.8 μm. Schmid's law was found to break down for small samples. The yield probability of the 12 slip systems is plotted in Figure 2-13. The Schmid factors corresponding to each slip system are shown above the bars. It is clear from the chart that the yield probability of the slip system with the highest Schmid factor drops with decreasing sample size, while the yield probability for the system with the second-highest Schmid factor as well as the tertiary system increase. When the pillar size shrinks to 0.8 μm, the yield probability of both the primary and the secondary systems becomes 0.3 and the tertiary system has a significant probability of yielding first as well. To verify these findings, the authors reexamined the SEM images of deformed Al micropillars from a previous study. After analyzing the slip traces from the images, they obtained a trend for the yield probability for different slip planes similar to the simulated one. They proposed an explanation for this breakdown of Schmid's law, that is, the weakest source may not lie on the highest Schmid factor system because of the limited dislocation sources in a small pillar. Thus the Schmid factor is no longer solely sufficient for

this case.

Kiener et al. [56] also attributed the observed size effect in micro-tension experiments on Cu single crystals to the source lengths. They suggested that the minimum source length which scales to the sample diameter determines the flow stress. In this study, samples with a square cross section and having a side length between 0.5 μm and 8 μm were investigated. Knowing the measured stresses applied on the samples, they calculated the source size for these samples using the following equation:

$$\tau_{source} = \frac{Gb}{2\pi} \cdot \frac{1}{S} \cdot \ln\left(\frac{\alpha \cdot S}{b}\right), \tag{2.16}$$

where S is the source length and τ_{source} is obtained by converting the flow stresses at 1% strain to shear stresses. This equation works for both a Frank-Read source with size S and a single-ended source with size $S/2$. They found that the source size for a single-ended source increased from ~ 300 nm to ~ 2 μm for samples having side lengths from 0.5 μm to 8 μm. The result is shown in Figure 2-14.

2.3.3 Effects of grain boundaries

Most of the micron and submicron compression tests focus on single crystals [16, 23, 52, 54]; some concentrate on amorphous metallic systems [7, 57]. Only a few investigations involve materials with internal interfaces such as grain boundaries [19, 20, 58-62].

Ng et al. [20] introduced a high-angle grain boundary into 6-μm-diameter Al micropillars and compared the deformation of these bicrystal pillars with the single crystal ones. They found a smoother deformation for the bicrystal pillars as well as a higher work hardening rate and

flow stress. The post-mortem TEM observations show high dislocation storage in these pillars, whereas previous studies on single crystal specimens reveal a relatively low dislocation density. Hence they suggested that the grain boundary blocks the dislocations from being removed from the pillars and results in dislocation accumulation. Thus much smaller and fewer strain bursts, a higher work hardening rate and a larger flow stress appear.

On the contrary, Kunz et al. [19] observed the opposite effect of a grain boundary inside smaller Al bicrystals: these bicrystal pillars displayed larger strain bursts and a lower hardening rate compared with their single crystal counterparts. TEM examination shows that the grain boundary region is relatively dislocation-free. Thus the authors suggested that the boundary here serves as a dislocation sink rather than a barrier. They discussed the reasons behind these contradictory phenomena in the two studies. Here the pillar diameters span from 400 nm to 2 μm, which is almost an order of magnitude smaller than those in Ng's study. Also, the characteristics of the boundaries are different. Here the boundary is vertically oriented along the pillar axis, while in the other study the boundary was inclined at a large angle to the pillar axis. The crystallographic orientations and boundary misorientations are completely different as well. It is worth noting that, in this study, a similar power law "smaller is stronger" size effect was observed for these bicrystal pillars.

Aitken et al. [60] carried out a similar investigation on 900-nm-diameter Al bicrystals. This time the grain boundary normal was at 24º to the loading axis, yielding results different from both previous studies. The stress-strain curves were continuous; no strain bursts appeared in the data. In one compression test, the stress reached a peak at the elastic limit and then displayed significant softening over 2% strain, after which the plastic flow gradually

decreased until unloading. The most striking distinction is the morphology of the deformed bicrystals, which shows that the top crystal slides downwards along the grain boundary, leaving an exposed surface with wavy features. Further TEM analysis revealed that the grain boundary region is free of obvious dislocation debris. This frictional grain-boundary sliding normally exists at high temperatures for bulk material. However, here it carries almost all the plastic deformation for the bicrystal at room temperature. The authors concluded that this grain boundary sliding mechanism dominates the deformation in nano bicrystals when the boundary plane experiences shear stress, i.e. when the boundary forms a certain angle to the loading axis instead of being vertically oriented along the pillar.

2.3.4 FIB-induced defects

It is generally accepted that implanted ions and dislocations are common defects introduced by FIB machining. The effect of their presence on the mechanical properties of small samples has been explored in many studies.

Following on from their work on uniaxial compression, Uchic et al. discussed the effect of Ga^+ implantation damage on the mechanical behaviour of the pillars [3]. It is generally accepted that the penetration depth of 30 kV Ga^+ ions is tens of nanometre thick, and this damage layer gradually constitutes a higher percentage of the total pillar volume as the sample size shrinks. However, the authors suggested that the "smaller is stronger" size effect is not simply explained by the presence of this surface damage layer. They pointed out that different material systems display a size effect over various length scales and that the absolute magnitude characterizing the size effect differs notably as well. In addition, morphological observation of the deformed pillars shows that slip steps are distributed along the whole gauge

length, which would not occur if the Ga^+ damage region serves as a hardening layer.

A quantitative analysis of Ga^+ damage on FIB-milled pillars was performed by Kiener et al. [54]. The authors first estimated the penetration depth of Ga^+ ions using SRIM (Stopping Range of Ions in Matter code). For copper receiving Ga^+ milling at 30 keV, the simulation gives a penetration depth of about 30 nm for perpendicular and 18 nm for grazing incidence ions. The Ga^+ content was then measured in the damaged zone at the surface of the samples, which had been exposed to Ga^+ bombardment at 30 keV for 1000s under currents of 0.5 nA, 1 nA and 10 nA, respectively. The examination was conducted using Auger Electron Spectroscopy (AES). Table 2-1 lists the surface concentration of Ga^+ for different milling currents. It is quite evident that smaller milling currents lead to a smaller ion concentration. The authors also plotted a depth profile of the Ga^+ concentration for the case of 10 nA milling, as shown in Figure 2-15. A high concentration of 20 at% was measured at 3 nm beneath the sample surface. The penetration of the ions continued to a maximum depth of about 35 nm, where the concentration was measured as less than 1 at%. Therefore, the authors suggested that for very small samples (100 nm and below), this damage layer may play an important role in the deformation. However, it is worth noting that people normally adopt smaller ion currents for the final polishing step to clean the micropillars.

The contribution of the Ga^+ implantation to the size effect was then further investigated by Greer et al. [15]. They compared the mechanical behaviour of FIB machined Au pillars and electroplated ones: the latter were obviously Ga^+ free. A similar size effect was observed in the electroplated pillars. Thus they concluded that the strengthening of smaller samples was not due to the Ga^+ implantation.

Another comparison between the compressive response of fibbed and non-fibbed pillars was conducted by Bei et al. [63]. Different from Greer's group, who used electroplated pillars as the non-fibbed samples, they used directionally solidified Mo-alloy micropillars as the comparison group mentioned in the previous section 2.2.1. The unique characteristic of these pillars is that they are essentially dislocation-free. Therefore, the pillars yielded at a high stress of 9.21 ± 0.73 GPa, approaching the theoretical value, similar to Brenner's pristine whiskers. No size effect was observed. In addition, these pillars underwent catastrophic plastic collapse after yielding and hence flow stresses were not available. In stark contrast, a significantly lower 0.2% offset yield strength of 0.85 ± 0.16 GPa was found for the fibbed pillars, which also displayed stable strain hardening after yielding. The stress-strain curves of these 670-nm-diameter fibbed pillars were also compared with 550-nm-diameter non-fibbed pillars prestrained before compression in a previous study [64]. It was found that the yield strengths of the fibbed pillars were comparable with that of the 11% prestrained pillars, although the former exhibited larger scatter. The authors did not propose a clear explanation for the different mechanical response of the fibbed and the directionally solidified pillars, as multiple defect types exist in the former pillars. However, it is the author's opinion that FIB-induced dislocations lead to this different behaviour, in view of the similarities between the non-fibbed and prestrained pillars.

The initial dislocation distribution of fibbed nanopillars was shown in Shan's work when they performed in-situ compression tests on Ni crystals of between 150 and 400 nm in diameter [16]. As seen in Figure 2-16, small dislocation loops caused by ion beam irradiation and pre-existing long dislocation lines extending across the pillars formed a high initial dislocation density of $\sim 10^{15}$ m^{-2} in total. This work presents a direct observation of fib damage on small

pillars.

2.4 Dislocations and twin boundaries

Twinned crystals are produced during growth or deformation. The twins we used in this project are coherent annealing twins, which were produced during crystal growth from the solid state. Annealing twins are often seen in copper or α-brass polycrystals which are recrystallized by heat treatment at a temperature where self-diffusion can occur after cold working. In this process, new strain-free grains nucleate among the deformed grains and grow until all the original grains have been entirely consumed. Annealing twins, which are straight-sided lamellae, are likely to be seen in many of these new grains due to atomic readjustment. [65]

In contrast to the high angle grain boundaries that were introduced into the bicrystal pillars in the previous studies [19, 20, 60], coherent twin boundaries (TBs) do not create crystallographic disregistry between adjacent regions of the boundaries. Hence dislocations can glide along the TB planes because of their coherent structure.

2.4.1 Slip-twin interaction mechanisms

Apart from acting as barriers to perfect glide dislocations [66], TBs can also react with them, allowing the dislocations fully or partially to penetrate the TBs or even be absorbed by the TBs [67]. In addition, TBs can serve as dislocation sources [68].

2.4.1.1 Slip transmission and absorption

Using TEM observation, Remy forty years ago investigated the interaction of slip dislocations

with annealing twins inside a polycrystalline FCC cobalt alloy [69]. He reviewed the geometrical analysis of the twin-slip interaction in FCC structure in the beginning. Considering the incorporation of a slip dislocation into twins, the general hypotheses are formed by two aspects: firstly, shear remains the same across the TB, that is, no discontinuity-like crack appears at the TB. Hence, the net Burgers vector is unchanged; additionally, all the resulting dislocations must slip away. Secondly, the intersection line of the incident slip plane and the coherent twin boundary must lie on the relaxation plane (i.e. the outgoing slip plane) in the twin [70]. As both the slip and twinning planes are {111} planes in the FCC structure, the intersection axis is a <110> direction line. Consequently, the only possible relaxation plane in the twin is the $\{111\}_T$ mirror plane of the incident slip plane in the matrix. Remy then discussed the case for an obstacle twin with a (111) twin boundary plane and a ($\bar{1}11$) incident slip plane. The Burgers vectors of perfect dislocations on this incident slip plane are $\pm\frac{1}{2}[01\bar{1}]$, $\pm\frac{1}{2}[110]$ and $\pm\frac{1}{2}[101]$. The first of these is screw type and can easily glide into the twin by cross-slip as it is parallel to the intersection line of the incident slip plane and the relaxation plane. The other two perfect dislocations can only be incorporated in the twin by dislocation dissociation. Two possible reactions exist for each dissociation, both resulting in one perfect dislocation in the twin grain and one or two partial dislocations at the interface. Taking the $\pm\frac{1}{2}[110]$ dislocation as an example, the possible reactions are:

$$\pm\frac{1}{2}[110] \rightarrow \pm\frac{1}{2}[110]_T + 2 \times \frac{1}{6}[11\bar{2}] \tag{2.17}$$

$$\pm\frac{1}{2}[110] \rightarrow \pm\frac{1}{2}[101]_T + \frac{1}{6}[2\bar{1}\bar{1}] \tag{2.18}$$

TEM analysis suggested that the reaction in the experiment was the latter one. Although both

29

of the above reactions are energetically unfavourable due to an increased self-energy (i.e. line energy), reaction (2.18) requires much less of an increase than (2.17): 33% versus 133%. Therefore, this experiment demonstrates that the incorporation interaction actually favours the minimization of self-energy.

Later Jin et al. [71] studied the interaction of screw dislocations with coherent twin boundaries in different FCC metals by means of molecular dynamics simulations. The screw dislocations are those $\pm\frac{1}{2}[01\bar{1}]$ type dislocations which are parallel to the twin boundary planes mentioned in the last paragraph. Different from Remy's simple assumption that they just enter the relaxation plane in the twin grain by cross slip, here the authors proposed that the screw dislocations dissociate and glide within the boundary plane. This is easy to understand, as the boundary plane is also another {111} cross slip plane that the screw dislocations can glide on. In addition, the mirror symmetry of the coherent TB requires that the leading and trailing Shockley partials exchange their order, so they cannot just simply pass through the boundary into the twin crystal without stopping. The simulation also suggested that the material dependent energy barrier to the nucleation of Shockley partials is likely to determine the operating mode. Figure 2-17 depicts the two different interaction mechanisms for a screw dislocation approaching a coherent TB. As the Shockley partials approach the TB, the leading one stops at the boundary and the trailing one catches up. They then constrict again into a perfect screw dislocation at the TB. After this, they start to renucleate Shockley partials either on the boundary plane or on the relaxation plane in the twin. The top right sketch describes the interaction mode applied to Al. The Shockley partials are separate in the boundary and move along the boundary plane in opposite directions. The bottom right sketch shows the interaction mode found in Cu and Ni only. The screw dislocation propagates into

the twin by cutting through the TB, resulting in a dissociated screw dislocation in the twin. It is also worth noting that the repulsive force due to the TB may also repel the incoming dislocations, therefore sufficiently high shear stresses should be applied to force a dislocation to impinge onto the TB.

Jin et al. [72] then completed their investigation by considering non-screw dislocations (in another publication). Several possible reactions may occur at the TB. A 60º perfect dislocation in Cu may be transferred directly into the neighboring twin crystal and leave an additional partial dislocation along the TB. It may also partly penetrate the TB and form sessile twin boundary dislocations pinned at the boundary. Additional reactions were observed for other materials such as Al and Ni, where the TB can either absorb or trap dislocations, i.e. both glissile and sessile dislocations may be created on the boundary plane. All the possible reactions are listed below, using Thompson's notation as shown in Figure 2-18.

$$DA = A'D' + C\delta \tag{2.19}$$

$$AD = \delta'A' + \text{Hirth lock (i} - \text{lock)} \tag{2.20}$$

$$DA = D\delta(\text{Frank Sessile}) + \delta A, \tag{2.21}$$

$$AD = A\delta + \delta C + CD/BA \tag{2.22}$$

$$DA = B\delta + \gamma'D' + v - \text{lock,} \tag{2.23}$$

where a Hirth lock is a sessile dislocation with a Burgers vector of $\frac{1}{3}[001]$ and a mismatch of $\frac{1}{9}[111]$. A v-lock is a twin lock with a Burgers vector of $\frac{1}{6}[001] + \frac{1}{18}[111]$.

Ni et al. [67] considered the effect of dislocation density on the interactions between dislocations and TBs in nanocrystalline materials. They found that the interactions discussed above only appear in a twinned grain with a low dislocation density. For one with a high dislocation density, dislocations tangled with each other and are held at the TBs without penetration. The accumulated dislocations then boost the local strain energy and activate deformation twins from the other side of the TB. This result demonstrates that the slip-twin interactions are not only affected by material-dependent properties like stacking fault energy, the energy barriers for dislocation reactions and the twin thickness, but are also affected by other factors including applied stress and dislocation density.

2.4.1.2 Dislocation emission

Reactions 2.19 and 2.21 were then utilized in Wang et al.'s [68] research to explain dislocation emission from TBs. They carried out *in situ* tensile straining on electroplated Cu with a high density of nanoscale lamellar growth twins inside a TEM. TBs were found to act as dislocation sources under strain and to emit successive dislocations. This emission process consists of three stages. Atomic steps were formed at coherent TBs in the first stage. As described in reaction 2.11, the resulting Shockley partial slipped along the TB plane while the Frank partial was pinned at the TB. Then the sessile Frank partial pinned glissile Shockley partials from the boundary and formed nanometre-sized steps. This incoherent TB with steps served as a dislocation source in the second stage. Many perfect dislocations were emitted from the TB at these steps where stress concentration triggered the emission. With increasing deformation in the third stage, the blocked dislocations in front of the TB led to very high stress concentration and induced reaction 2.19, in which the de-twinning dislocation $C\delta$ increased the step height further and this led to TB migration. The emission process is

illustrated in Figure 2-19, in which dislocations in the form of half-loops were emitted from a TB into the surrounding crystal.

In summary, the above studies indicate that the interactions between slip dislocations and coherent TBs in FCC materials may result in glissile/sessile dislocations or locks at the TBs and outgoing dislocations in the neighbouring crystal. The incident dislocations may be blocked at the TB, absorbed at the TB or transmitted/partly transmitted to the neighbouring crystal.

2.4.2 Mechanical response of samples with TBs

Lu et al. [73] synthesized ultrafine-grained Cu foils containing coherent nanoscale TBs using pulsed electrodeposition. They compared their mechanical properties with those of nanocrystalline Cu samples with the same characteristic structure feature size, i.e., the spacing between two adjoining twin boundaries in the twinned material and the grain size in the nanocrystalline material are similar. The results show that Cu with coherent nanotwins displays comparable yield strength but significantly improved ductility and work hardening compared to the other material. This implies that the coherent TBs not only act as strong barriers to dislocation motion, like grain boundaries, but also have the capacity to nucleate and accommodate dislocations, as suggested in the previous section.

More recently, the deformation behaviour of Cu nanopillars having a very high density of periodic twin boundaries but no grain boundaries were investigated by Jang et al. [74]. They suggested that the dislocations nucleated at the twin boundary-surface intersections. Two impressive findings were obtained here. First, different TB orientations in 50-nm-diameter

nanopillars led to distinct deformation mechanisms. Deformation of pillars having TBs oriented perpendicular to the loading axis was highly localized in the neck periphery. Traces of dislocations across the twin lamellae appeared in TEM images, indicating inter-twin-boundary dislocation activity. In pillars with TBs inclined at 18º to the loading axis, however, detwinning dominated the deformation and the twin lamellae thickness was 14 times larger than that in undeformed pillars. Differently from orthogonal TBs, the slanted TB planes here experienced a resolved shear stress, which enabled the glide of Shockley partials on the boundary plane, facilitating the detwinning process. Secondly, the twin boundary spacing can also affect the mechanical response. In 100-nm-diameter pillars with orthogonal TBs, deformation changed from brittle to ductile when the spacing dropped below a critical value. The authors ascribed the brittle fracture to the intrinsic brittleness of TBs, as revealed by their atomistic simulations. When the TBs are close enough to each other, twinning dislocations will nucleate and propagate on TBs due to the high stresses at the crack tip, leading to ductile failure.
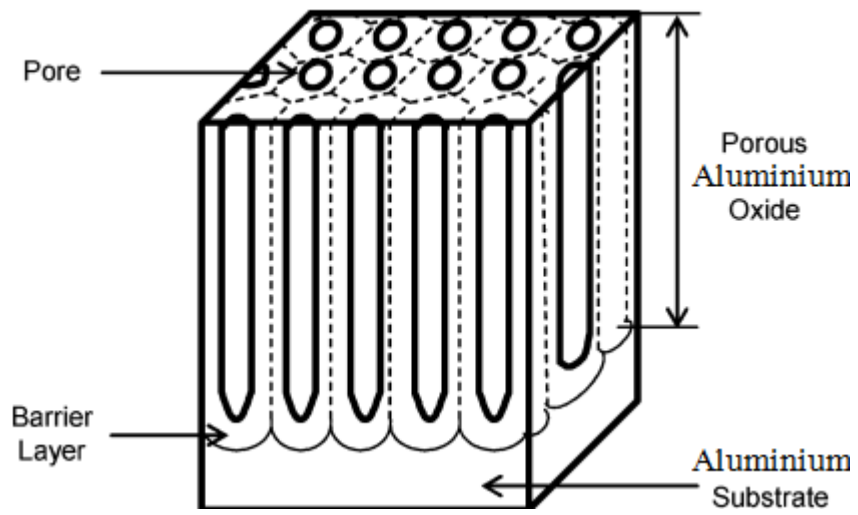
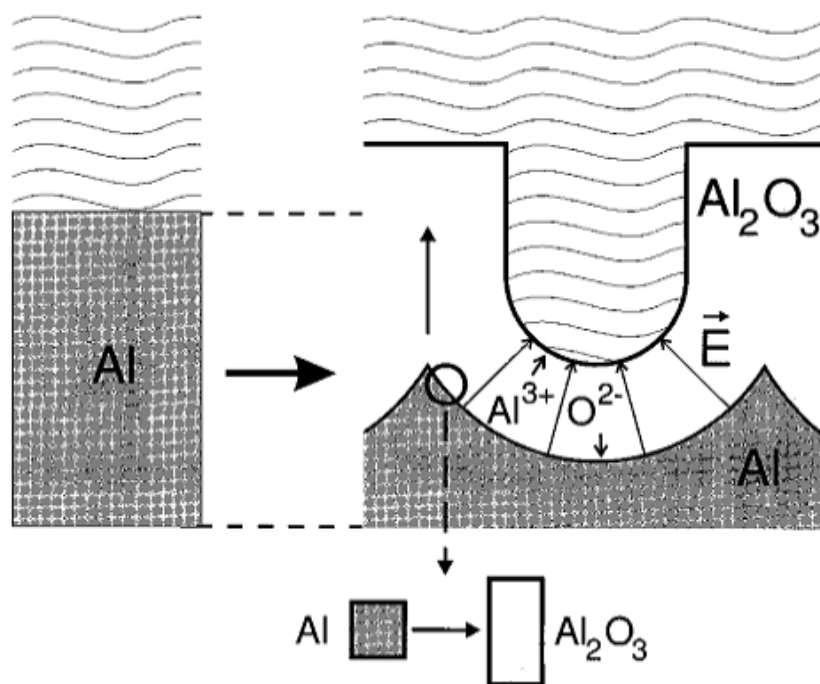**Figure 2-1 Schematic drawing of the idealized structure of AAO [26]**

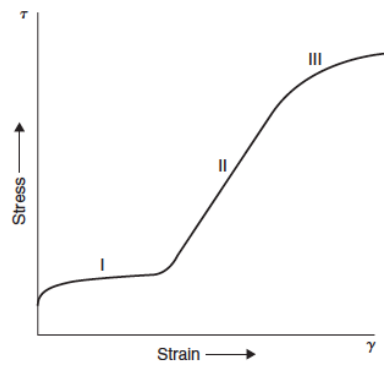**Figure 2-2 Ion transfer direction in AAO [35]**

Figure 2-3 Typical stress-strain curve showing the three stages of work hardening in a pure fcc metal crystal [49]
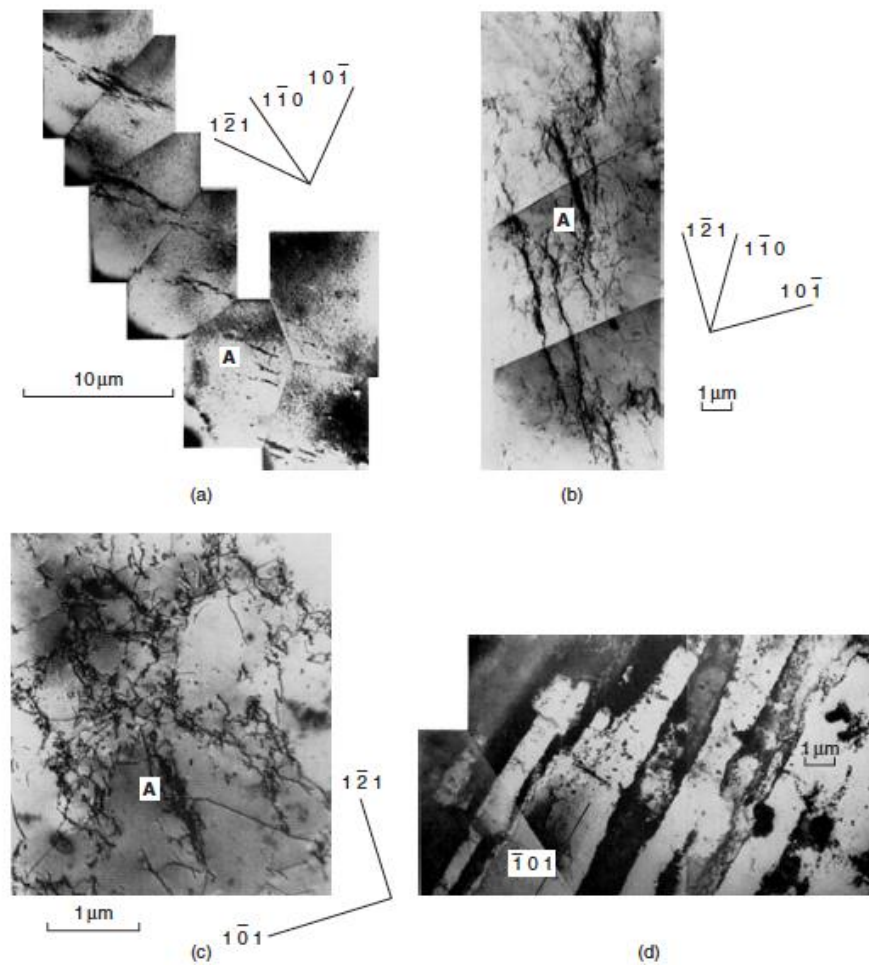

Figure 2-4 Dislocation structure observed in copper single crystals deformed in tension to: (a) Stage I, (b) end of easy glide and beginning of Stage II, (c) top of Stage II and (d) Stage III[49]
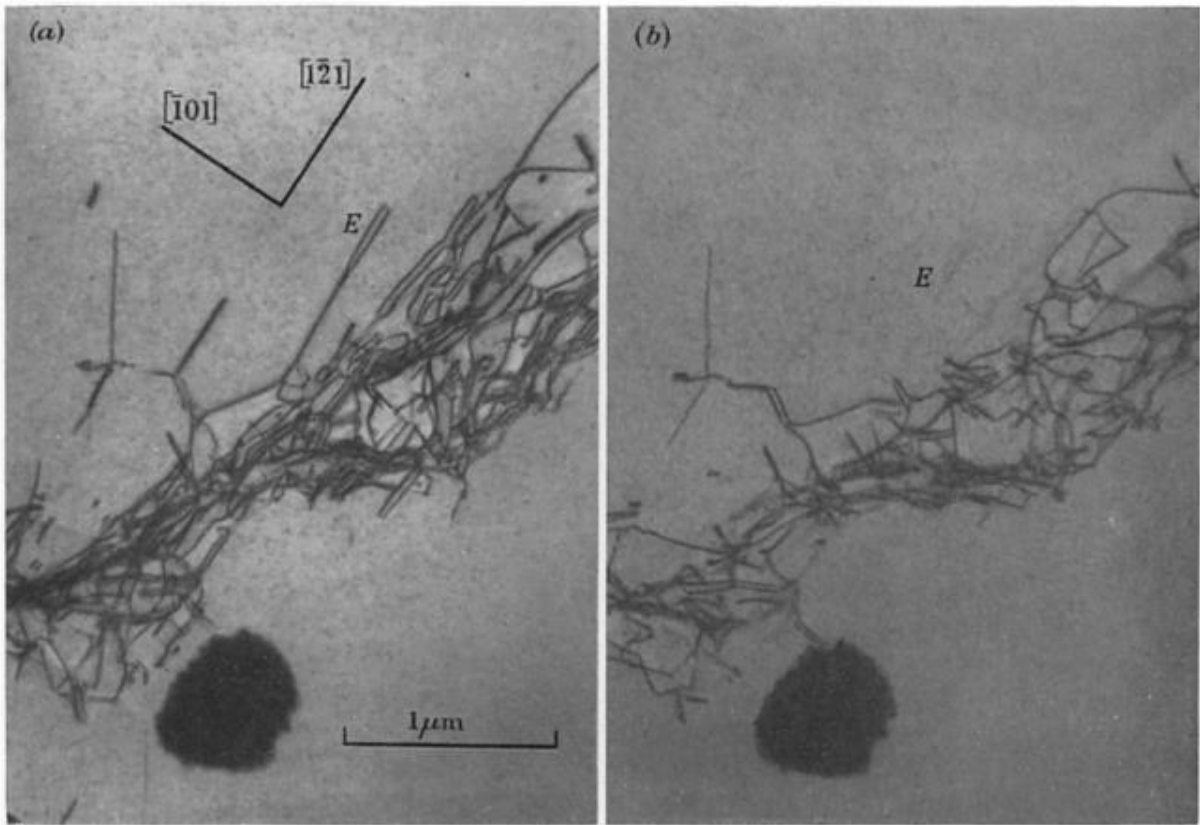
Figure 2-5 Copper crystals at the middle of stage II. (a) two beam condition when both primary and secondary dislocations are visible. (b) two beam condition when primary dislocations are invisible [46]
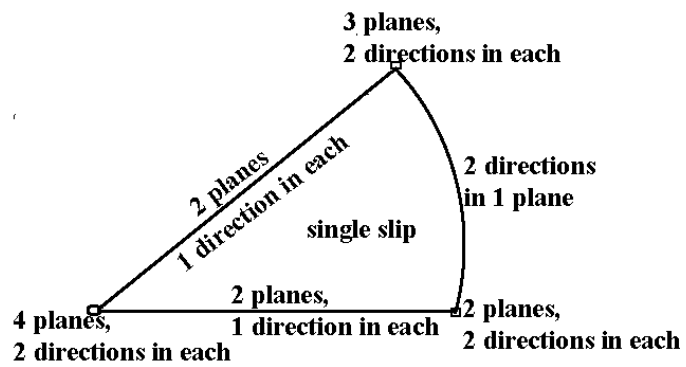

Figure 2-6 Unit triangle showing the number of slip systems for different crystal orientations in fcc metals [45]
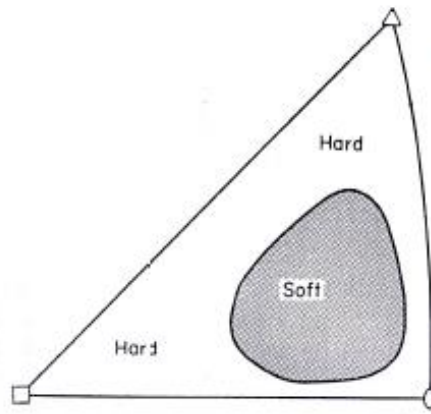
Figure 2-7 Unit triangle showing areas of soft and hard orientations [45]
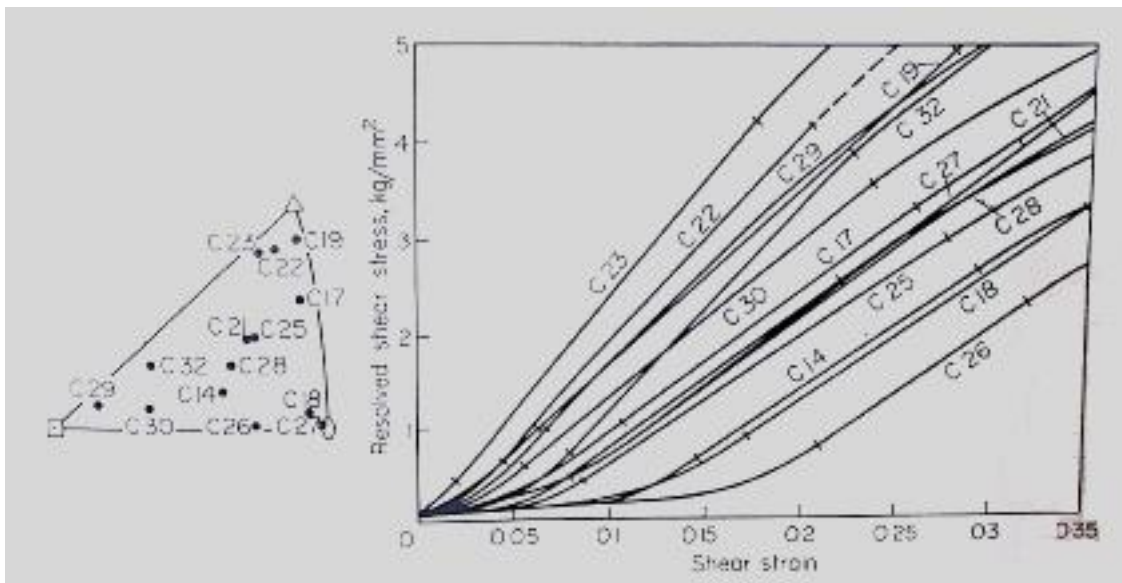

Figure 2-8 Resolved shear stress/strain curves of copper crystals as a function of orientation [45]
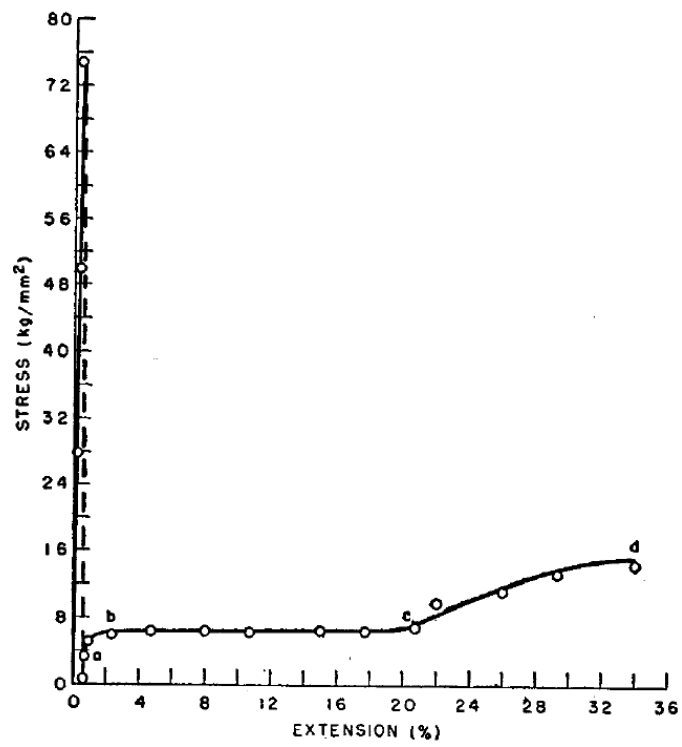
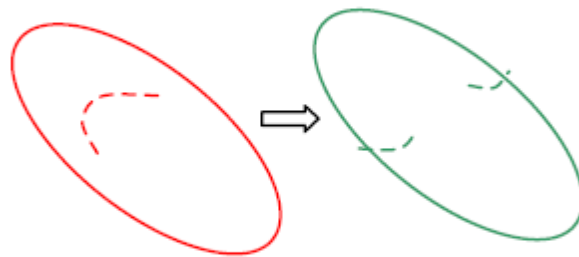Figure 2-9 Stress-extension curve of a [111] copper whisker [51]

Figure 2-10 A schematic sketch of how doubly-pinned Frank-Read Sources quickly become single-ended sources in samples of finite dimensions [18].
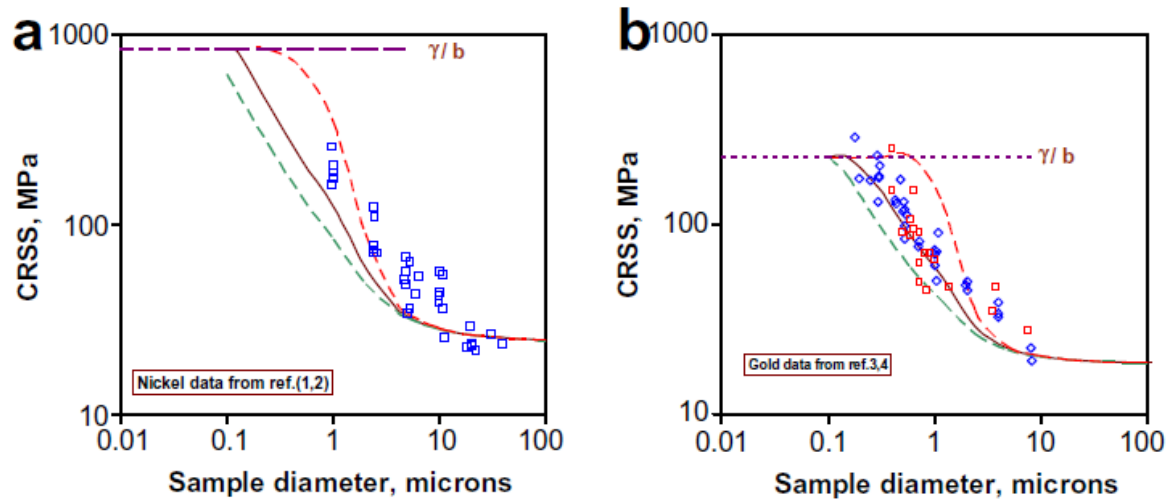
Figure 2-11 The model predictions of CRSS versus sample diameter for (a) nickel and (b) gold are shown in comparison with reported experimental data. The green and red dotted lines correspond to the low and upper standard deviations from the mean as predicted by the model [18]
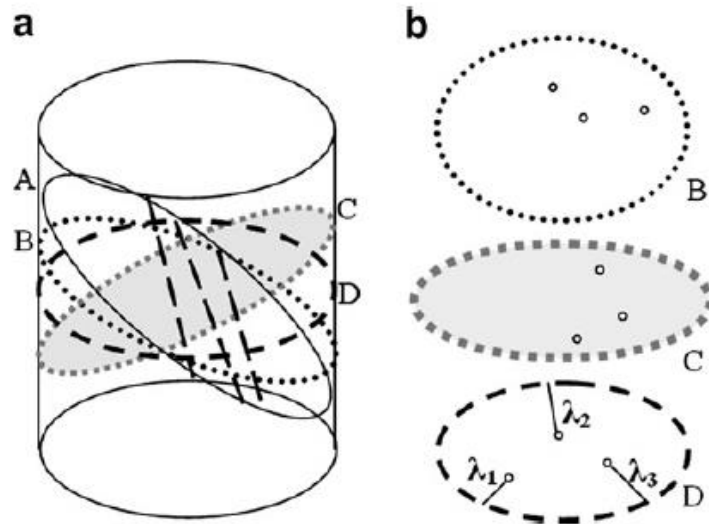

Figure 2-12 (a) Schematic showing that three mobile dislocations (dashed straight lines) on slip plane A become pinning points on non-parallel slip planes B, C and D. (b) The three non-parallel planes having pinning points due to the dislocations on A. The shortest distance λ from the source to the free surface is indicated for each of the three sources on plane D. [8]
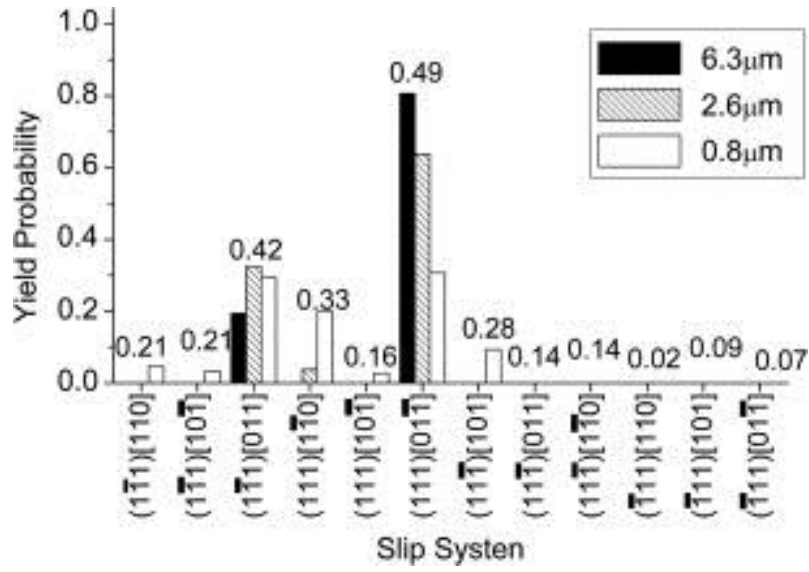
Figure 2-13 Yield probability against slip system for pillars with diameters 6.3, 2.6 and 0.8 μm. The numerical values above the bars represent the Schmid factors of the slip systems. [8]
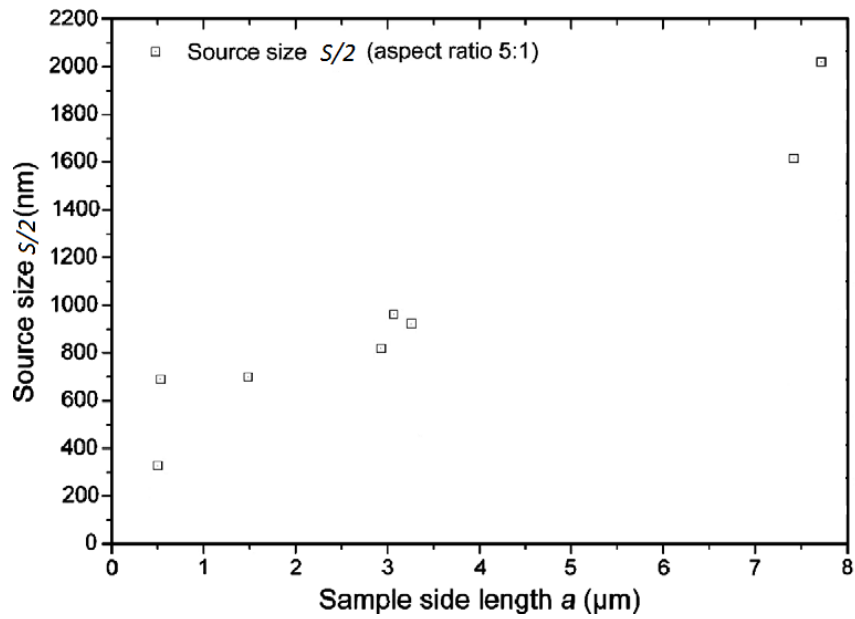
Figure 2-14 Calculated dependence of source sizes S/2 on the sample side length a for a single-armed source, adapted from Kiener's work [56]

41

Table 2-1 Surface concentration of Ga for different milling currents. The milling time was kept constant at 1000 s. [54]

Milling current [nA]	0.5	1	10
Surface concentration of Ga [at%]	5.5±0.6	8.7±0.9	18.6±1.9
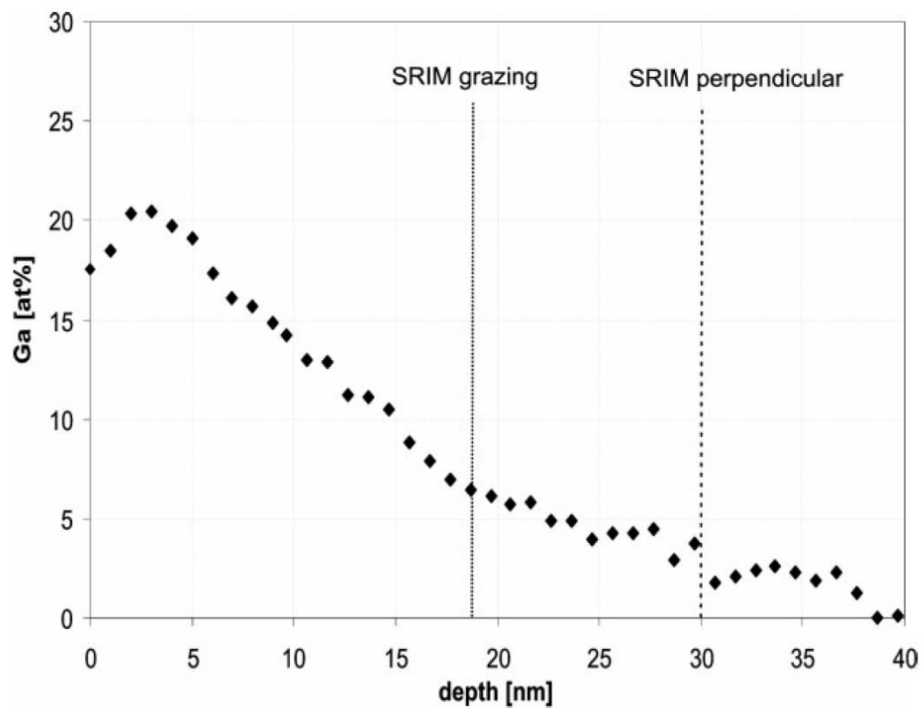
Figure 2-15 AES depth profile of the Ga concentration in a copper sample damaged by perpendicular Ga$^+$ ion bombardment at 30 keV and a current of 10 nA. [54]
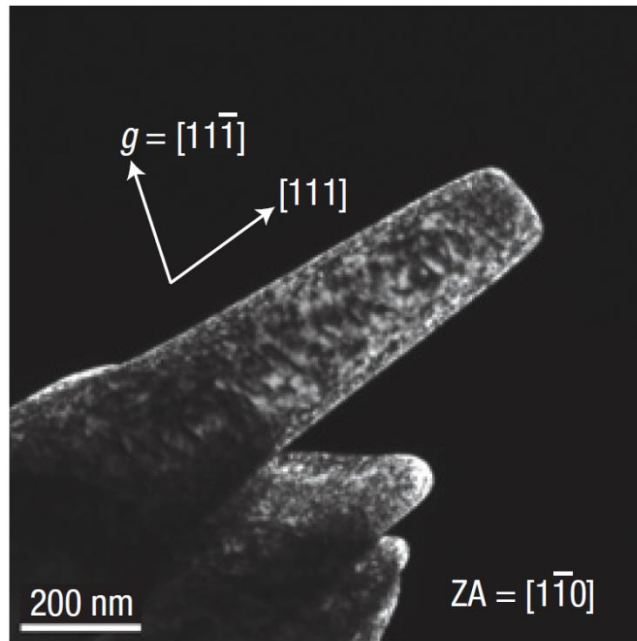
Figure 2-16 Dark-field TEM image of a FIB microfabricated 160-nm-diameter Ni pillar [16]
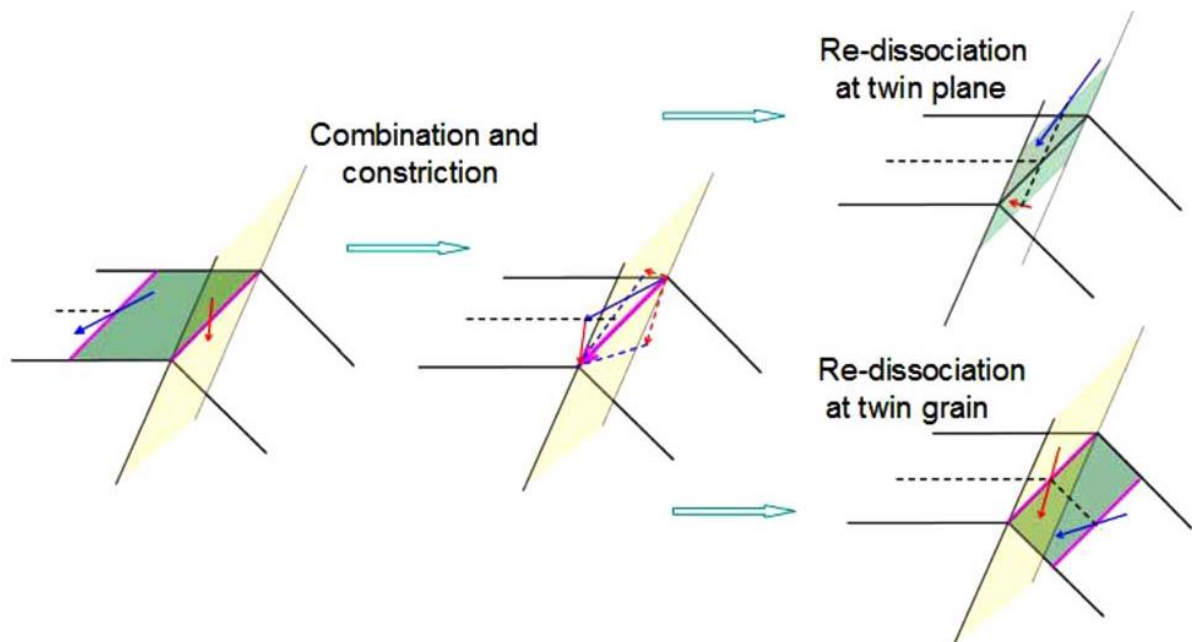
Figure 2-17 Schematic illustration of the two possible interaction modes between a screw dislocation and a coherent TB. [71]
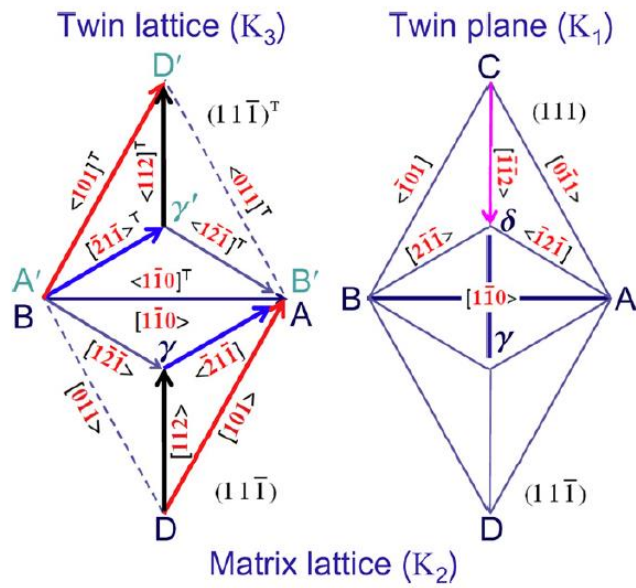
Figure 2-18 Dislocation notations in the Thompson tetrahedron. [72]
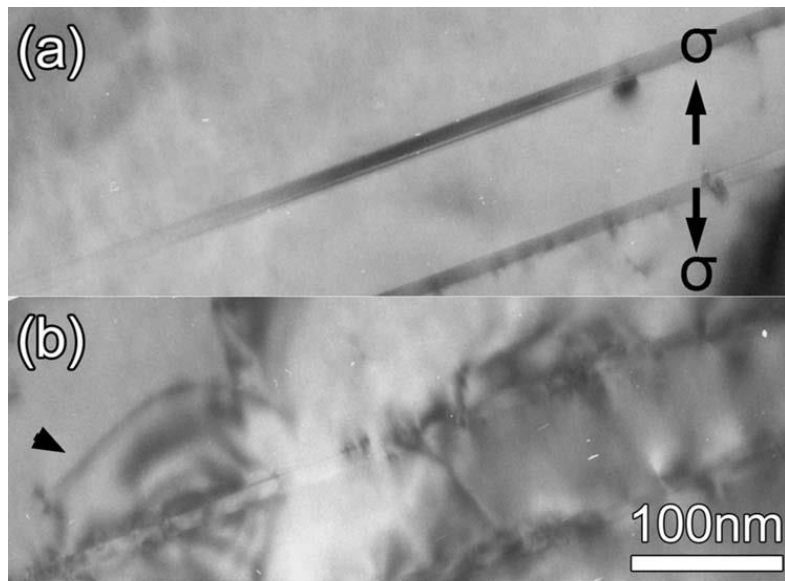
Figure 2-19 (a) and (b) are dynamic microstructure developments of TBs with increasing strain. The black arrowhead in (b) indicates the dislocation half-loops emitted from a TB. [68]

Chapter 3 Experimental Details

3.1 Experimental procedure of Cu nanowire fabrication

3.1.1 Preparation of AAO template

3.1.1.1 Pretreatment

A high purity aluminium sheet (99.99%, 0.3 mm in thickness) was ultrasonically degreased in acetone for 10 minutes and subsequently annealed under vacuum at 400°C for 3 hours to remove the residual stress due to cold rolling and to enlarge the grain size to optimize the conditions for uniform pore formation. The sheet was then electrochemically polished using a 1:4 v/v mixture solution of $HClO_4/C_2H_5OH$ at a constant current density of 0.8 A/cm^2 for 3 minutes to produce a relatively smooth surface.

3.1.1.2 Anodisation

The two-step anodisation process, which is a well-established technique [75], was adopted in this work to fabricate the AAO membrane. The aluminium sheet was first anodized at 0-10°C at a voltage of 40 V in 0.3 mol/L oxalic acid for 1 hour. A stainless steel plate was employed as the cathode and the aluminium sheet served as the anode. The alumina layer was then removed by a mixture of phosphoric acid (6 wt%) and chromic acid (1.8 wt%) at 60°C for 1 hour to leave a concave metal substrate on which the ordered porous aluminium oxide can be produced by repeating the anodisation process for a further 3 hours.

3.1.1.3 Post-treatment

This process involves two steps: first removing the remaining aluminium, and then removing the barrier layer as well. The aluminium substrate was etched in a mixture of 0.2 mol/L CuCl2 and 19 wt% HCl and the remaining barrier layer was removed using 5 wt% phosphoric acid.

The resulting free standing AAO template is an ultra-thin membrane, which is too fragile to handle. To address this key issue, the metal substrate was selectively etched instead of being completely removed; the remaining metal substrate secures necessary mechanical strength of the system in the subsequent experiment. Another advantage of this is that the template can be connected to the plating cell by clamping an alligator clip onto the metal edge directly in the following deposition procedure, which successfully avoids any possible damage resulting from the contact between the electric wire and the thin membrane.

3.1.2 Fabrication of Cu nanowires

A thin gold layer with a thickness of approximately 200 nm was sputtered on one side of the AAO before the electro-chemical deposition process to serve as the electrode. The deposition process was separately conducted under two different constant current densities, 1 mA/cm^2 and 10 mA/cm^2, in a solution of 0.1 mol/L Cu$_2$SO$_4$ in which the pH value was adjusted to 4 by adding sulphuric acid.

The whole fabrication process is illustrated in Figure 3-1.

3.1.3 Microstructure characterization

The morphology of the AAO and the nanowires was observed using scanning electron microscope (SEM) and transmission electron microscope (TEM). Small pieces of AAO were attached directly to a carbon tape for the examination of the template inside SEM. The observation of the copper nanowires needed partial removal of the AAO by etching the specimen in 1 mol/L NaOH for several minutes. Free-standing nanowires for TEM observations were prepared by completely dissolving the AAO template away and ultrasonically dispersing the nanowires in ethanol. A small droplet of the suspension was then placed onto a carbon coated TEM grid. The AAO template and the cross-sectional sample for TEM study was prepared by FIB milling.

3.2 Experimental procedure of Cu micropillar investigation

3.2.1 Compression sample preparation

A polycrystalline Cu (99.99% purity) sheet of approximately 2.5 mm × 1.5 mm × 0.5 mm was annealed at 850 °C for 24 hours in vacuum to encourage grain growth. It was then gradually ground and polished down to 1 μm finishing, followed by electropolishing using a 2:1 v/v mixture solution of H_3PO_4/H_2O at a constant voltage of 2 V for 5-10 minutes to produce a relatively smooth surface. EBSD characterization was performed on the polished sample afterwards to select grains from which the micropillars could be prepared. Before putting the sample into the SEM chamber for EBSD examination, five dots were marked on the sample surface, helping to locate the area of interest. An example of the EBSD mapping is shown in Figure 3-2.

The Cu sheet was then fixed onto a specimen stub with silver paint. The tweezers were in contact with the stub only in the handling procedure, as shown in

Figure 3-3. Thus the sample was well protected against damage during the transportation from FIB to nanoindenter.

A cross-sectional taper is quite common in samples under the FIB milling. This taper originates from the incident ion beam with its Gaussian profile. Ishitani et al. [76] sketched the accumulated beam profile, as represented by curve "c" in Figure 3-4. They then simulated time-dependent surface development of the sample, which clearly shows that the flat surface gradually becomes tapered after a certain milling time, as illustrated in Figure 3-4.

Because of this taper of the FIB, the micropillars were fabricated as two different cross-section prisms, cylindrical and square. The latter was taper-free, as explained by the different milling approach adopted later.

The milling condition was carefully chosen to minimize the taper on the cylindrical pillars, as listed in Table 3-1. The pattern applied was an annulus, as shown in Figure 3-5. D_o is the diameter of the outer circle, D_i is the diameter of the inner circle and Z is the milling depth (in this case the length of the pillar). The milling direction can be selected either from inner to outer (D_i to D_o) or outer to inner (D_o to D_i) in the user interface. Large (20-7 nA), medium (3-1 nA) and fine beams (0.5-0.05 nA) were used successively to perform rough, medium, and fine milling by repeating the circle patterning. The Cu sheet was tilted to 52° so that the ion beam was perpendicular to the sample surface. The material between the outer and inner circles was removed. The diameter of the outer circle in the first rough milling step defines the outer diameter of the round crater, while the diameter of the inner circle after the last fine

milling step defines the inner diameter of the crater, which is the pillar diameter as well. The relatively large size of these craters has several advantages. The most important is to avoid any contact between the indenter tip and the material surrounding the micropillar. It can also help in viewing the bottom of the pillar and thus the whole pillar before and after deformation. During compression, these large craters can facilitate the location of the micropillars on the nanoindenter, which is also equipped with an optical microscope.

The procedure to fabricate a square column is explained in Figure 3-6. A round pillar was initially milled at 52°, as with the previous cylinders. Tapering is not a problem at this stage, so the milling current adopted was relatively large in order to improve the milling efficiency. Four rectangular patterns were then applied to the top surface, forming a square shape with the desired length surrounded by a shallow groove, as shown in (a) and (b). After that, the sample was tilted to -2° so that the ion-beam was oriented approximately parallel to the side surface of the column. A rectangular pattern was then applied to the right side, with the left edge approaching the inner boundary of the groove, as shown in (c). The material coloured pink was milled away, as seen in (d). A beam current of 0.1 nA was employed here as this was the final milling step. This step was then carefully repeated three times after rotations of 90°. The small beam current together with the short milling depth, 2.2 μm in this case, makes the side surface sufficiently flat and thus a taper-free square column was finally obtained, as seen in (e).

3.2.1.1 Basic variants of the micropillars

The variants were designed taking four aspects into account: orientation (number of active slip systems), internal coherent interface, shape and size. Thus samples were oriented in the

[235] or [156] directions, with or without a twin boundary, with a cylindrical or square shape, and of different sizes.

The [235] and [156] orientations were chosen as they led to single or multiple slip during compression test. Cylindrical pillars are commonly adopted in the literature, as they are easy to fabricate. However, tapering of these pillars is common. Thus square pillars were also prepared here to avoid any variation in cross-section along the gauge length. The majority of the samples are either cylindrical with a diameter of 3 μm or square with a side length of 2.2 μm (in other words, the diagonal of the cross-section is approximately 3 μm).

These variants were organized into eight different data sets, as shown in Figure 3-7 and Table 3-2. Each set of compression tests was repeated 4 to 6 times to ascertain the reproducibility of the results.

3.2.1.2 Data analysis

The procedure used to analyze the true stress-strain curves is described below:

Instantaneous height of the pillar $L_i = L_0 - u$

where L_0 is the initial height of the pillar and u is the instantaneous displacement on the loading curve.

True strain $\varepsilon_{true} = \left| \int_{L_0}^{L_i} \frac{1}{L} dL \right| = -\ln \frac{L_i}{L_0}$

The initial height L_0 and the cross-sectional area A_0 of the pillar correlate with the instantaneous height L_i and the cross-sectional area A_i, according to conservation of pillar volume:

$A_0L_0 = A_iL_i$

The true stresses are calculated by dividing the instantaneous load P by the instantaneous area,

$$\sigma_{true} = \frac{P}{A_i} = \frac{PL_i}{A_0L_0}$$

3.2.2 TEM sample preparation

TEM sample preparation by twin-jet polishing was not suitable for this study as the sample sizes are too small. FIB was used again for this aspect to locate the samples precisely and extract TEM foils from them.

TEM specimens were produced from the deformed (both cylindrical and square ones) as well as the undeformed pillars. Foils of deformed single crystal pillars were extracted along planes perpendicular to the top surface. Foils of bicrystal pillars containing a twin boundary were fabricated along the plane perpendicular to both the twin boundary plane and the top surface, as shown in Figure 3-8.

Extra care was taken in the milling process to reduce redeposition and curtaining effects. Several steps were involved here, as illustrated below.

1) The sample was tilted to 52° (Figure 3-9 (a)). A layer of tungsten was applied to the top surface of the pillar (Figure 3-9 (b)), to protect the pillar head from being milled away in the

succeeding process. The sample was then tilted by 7° and rotated by 90°. Another coating was applied to this exposed side surface (Figure 3-9(c)).The opposite side surface was coated as well after rotating the pillar by 180° (Figure 3-9(d)). This not only helps protect the edge of the TEM foil but also provides additional space for welding the foil to the TEM grid in step 6. These coatings were 2 to 3 micrometres thick. The ion beam current employed here was 0.1 nA, as the sample was tiny; a larger current tended to induce milling rather than deposition.

2) The pillar was then tilted back to 52°, the normal milling position. A rectangular trench was dug in front of the crater, to enlarge the view of the pillar in step 4 below. The top and bottom sides were milled away, leaving a strip with a thickness of 1-1.5 μm. (Figure 3-9 (e) and (f))

3) The pillar was tilted to 0°, where upon an Omniprobe micromanipulator was inserted, approaching the strip top. The pillar was then welded to the Omniprobe by tungsten deposition. (Figure 3-9 (g) and (h))

4) The strip was separated from the pillar at the bottom by milling a narrow trench (Figure 3-9 (i)).

5) The strip was then lifted out by Omniprobe and welded to a TEM Cu grid by tungsten deposition. The Omniprobe was separated from the pillar strip by milling. (Figure 3-9 (j))

6) The stage was rotated by 180°. Certain amount of tungsten coating was applied to the joint part between the back of the pillar strip and the Cu grid to reinforce the attachment. (Figure 3-9 (k))

7) The sample was then tilted to 52° for the thinning process. A 0.1 nA beam current was used throughout these steps in order to minimize the beam damage. The foil was thinned to approximately 100 nm and then tilted by another $\pm 6°$ for the final polishing at 44 pA, 5 keV, to improve surface quality. (Figure 3-9 (l) to (o))

3.2.3 TEM observation

Dislocation analysis was conducted using TEM. Both conventional bright field TEM images and STEM images were taken. STEM can minimize the contrast due to bend contours, which can be a nuisance in conventional diffraction contrast imaging [23]. STEM also effectively removes the massive black dot contrast caused by ion beam damage, which is commonly seen in the literature [2, 6], altogether making the dislocation analysis easier.

3.3 Experimentation

3.3.1 Scanning Electron Microscopy (SEM)

SEM is a way of exploring the micro-and nano-world. Compared with TEM, for which the entire specimen must fit into a 3 mm diameter cup, SEM can be used to observe relatively large samples. Compared with the optical microscope, SEM not only is capable of examining rough specimens such as fracture surfaces due to its large depth of focus, but also can provide a much higher spatial resolution as well as chemical analysis.

SEM has three basic functions. Apart from imaging using secondary electrons or back-scattered electrons and chemical analysis by EDX (Energy-dispersive X-ray spectroscopy) and WDS (Wavelength Dispersive X-ray spectroscopy), SEM can be used to examine the

orientations of any crystalline grains via EBSD (Electron Back Scatter Diffraction). In this study we utilized EBSD to choose grains with an appropriate orientation.

For EBSD, samples are tilted approximately 70° relative to the electron beam direction. Some of the incident electrons are diffusely scattered by the atoms in the sample, forming a divergent source of electrons close to the sample surface. As can be seen from Figure 3-10, these electrons may be diffracted to form Kikuchi patterns when they strike atomic planes at angles satisfying the Bragg equation:

$$n\lambda = 2d \sin\theta,$$

where n is an integer, λ is the wavelength of the electrons, d is the spacing of the diffracting plane and θ is the angle of incidence of the electrons on the diffracting plane [77].

The crystal orientation is calculated from the Kikuchi pattern.

In this work, all the SEM images were taken using the secondary electrons.

3.3.2 Transmission Electron Microscopy (TEM)

Both JEOL 2100 and FEI TECNAI F20 transmission electron microscopes were used in this project. Transmission electron microscopy provides structural, phase and crystallographic data by imaging, diffraction and spectroscopy. So it has tremendous potential for understanding the links between structure and properties down to the atomic level.

A TEM has three basic components: the illumination system, the objective lens/stage and the imaging system. In the illumination system, the gun produces high-energy electrons, which are then transferred to the specimen by the condenser lenses. The beam-specimen interactions

take place in the objective lens/stage part, forming successively an image and diffraction pattern. The imaging system then magnifies this image or diffraction pattern and focuses it on the viewing screen. As may be seen from Figure 3-11, electrons passing through the thin specimen are brought into focus in the back focal plane (BFP) of the objective lens while an image is formed in the image plane [78]. If the BFP is selected by the intermediate lens as its object (a), then a diffraction pattern is projected onto the screen; if the image plane is selected then an image is obtained on the screen (b).

TEM not only is a central tool for the characterization of nanoscale materials and devices, but also plays an important role in defect analysis. In order to understand better the deformation mechanisms present, TEM analysis of dislocations was performed on the deformed and undeformed pillars.

3.3.3 Focused Ion Beam (FIB)

A Quanta 3D FEG focused ion beam microscope was used to fabricate the micropillars and prepare the transmission electron microscope (TEM) specimens. The dual beam system consists of an electron beam and an ion beam. The most common configuration is as shown in Figure 3-12 [79]. The electron beam and the ion beam are focused at the same position on the sample surface, allowing features to be observed using either of the beams. This newly developed state-of-the-art tool enables direct deposition of materials on, or removal from, the sample surface at predefined locations.

The focused ion beam is a precision machining tool at the micro- and nano-scale while having an imaging capability as well. It utilizes a liquid-metal source, usually Gallium (Ga), to

produce high energy ionized heavy atoms. The low melting temperature of Ga enables this massive element to remain conveniently in the liquid phase, thus to flow and wet a sharp tungsten needle. The extraction voltages applied to the aperture just below the tip efficiently pull the Ga atoms out from the needle tip and ionize them by field evaporation. These Ga+ ions then travel down the column after acceleration.

Similarly to the electrons in SEM, the ions are focused to a probe and raster across the sample surface. The interaction between the ions and surface atoms is either elastic or inelastic, corresponding to the machining and imaging capabilities respectively. Ion beam images display channeling contrast, arising from the sensitivity of the ion-atom interaction to the crystal orientation. Information about the grain size and grain morphology can be revealed by this intense grain orientation contrast.

Apart from milling and imaging, FIB has another basic function, deposition. A gas injection system (GIS) delivers a gas containing the deposition atoms above the sample surface. The primary ions impart some kinetic energy to these atoms after striking them in the beam path, causing them to impact the surface, to which they are fixed by intermolecular attractions. So, materials can be deposited at specific locations.

Although FIB imaging delivers high contrast, it inevitably results in sample erosion during operation. Thus combining an electron beam into the FIB system is necessary. This not only improves the nanoscale image resolution but also minimizes the sample damage. This dual beam system makes FIB a powerful tool in the realm of materials science, especially in nanotechnology.

3.3.4 Nanoindenter

Nanoindentation is a test in which the scale of penetration is measured in nanometres [80]. A typical nanoindenter has a depth resolution of less than a tenth of a nanometre and a force resolution of several nanonewtons. The basic principle involves pressing a sharp indenter into the material of interest. It is usually used to extract the elastic modulus and hardness of the sample from the load and depth of penetration. However, here, the nanoindenter was employed to perform uniaxial compression rather than indentation. A flat punch indenter tip was custom-machined out of a diamond Berkovich indenter using FIB, as seen in Figure 3-13. The diameter of the inner circle is 7 μm.

An Agilent Nano Indenter G200 in The University of Hong Kong was used for the compression tests. The essential components are displayed in Figure 3-14. The movement of a coil in a magnetic field applies the load. Displacement is measured by a capacitance gauge, as it is relatively easy to determine the distance between two parallel plates in an AC bridge circuit if the capacitance is measured. This G200 nanoindenter has a load resolution of the order of 50 nN and a displacement resolution of 0.01 nm, which make it perfect for probing very small volumes.
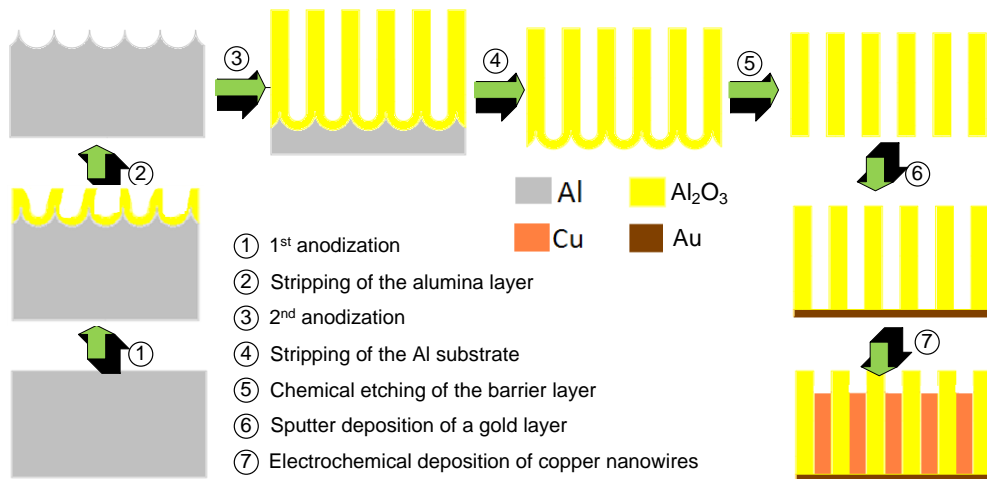
Figure 3-1 Illustration of the entire fabrication process of Cu nanowires
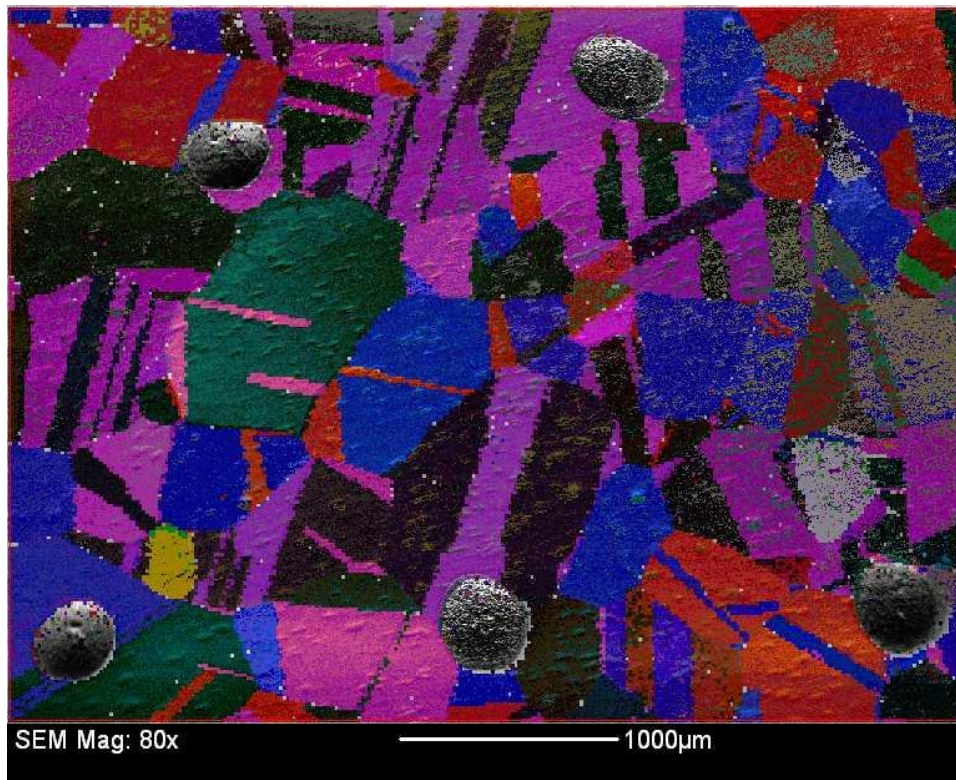
① 1st anodization
② Stripping of the alumina layer
③ 2nd anodization
④ Stripping of the Al substrate
⑤ Chemical etching of the barrier layer
⑥ Sputter deposition of a gold layer
⑦ Electrochemical deposition of copper nanowires

Al   Al₂O₃
Cu   Au

SEM Mag: 80x   1000µm

Figure 3-2 EBSD mapping of the copper sheet

58
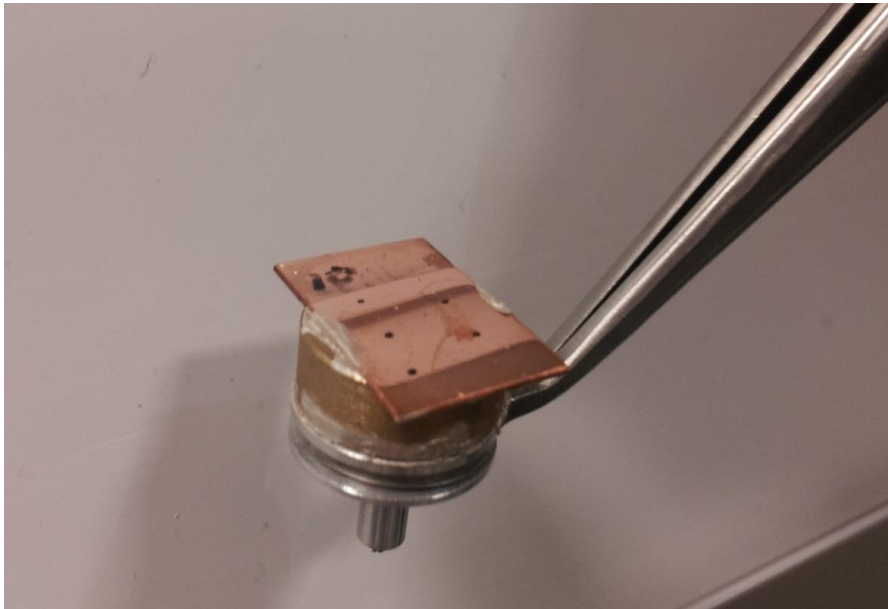
Figure 3-3 A copper sheet mounted on a specimen stub with silver paint
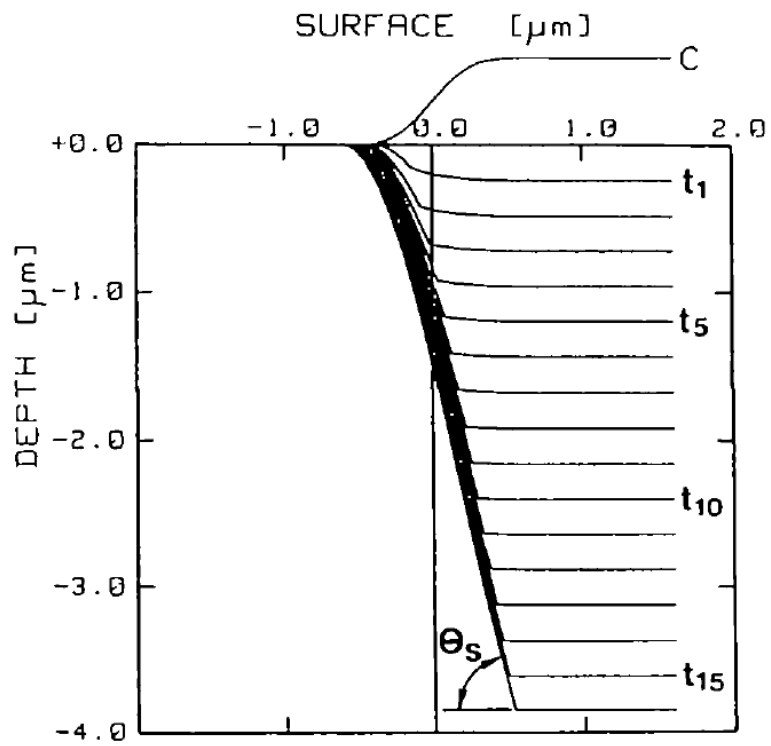
Figure 3-4 Time-dependent surface development in FIB trench milling, curve "C" represents an accumulated beam profile. [76]

Table 3-1 Typical milling conditions for the 5, 3 and 1 μm micropillars. D_0 and D_i are the outer and inner diameters at different stages, and Z is the input milling depth. I is the milling current

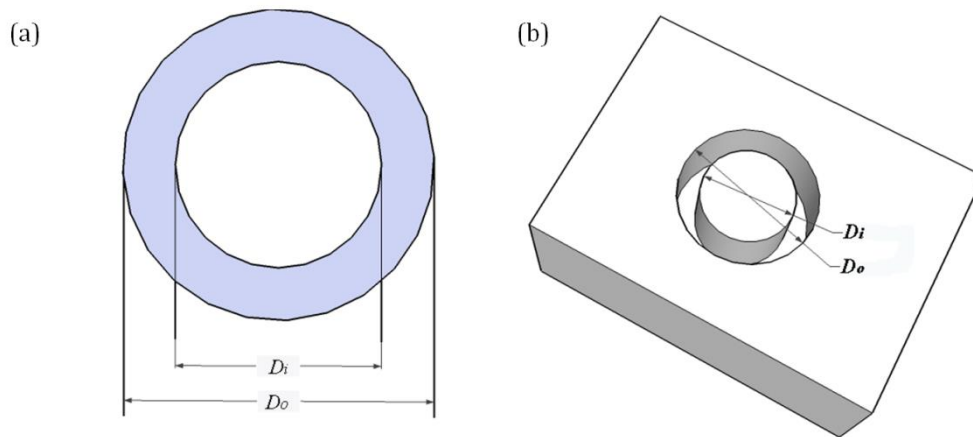| I (nA)	5 μm			3 μm			1 μm		
	D_o (μm)	D_i (μm)	Z (μm)	D_o (μm)	D_i (μm)	Z (μm)	D_o (μm)	D_i (μm)	Z (μm)
20	28	10	13	20	14	5	-	-	-
7	-	-	-	14	10	8	17	8	2
3	12	7	5	9.5	6	5.5	8	5	2
1	6.8	5.5	4.8	6.2	4	5	5	2.5	1.8
0.5	5.6	5	4.5	4	3.5	4.5	2.5	1.8	2
0.1	-	-	-	3.5	3	3.5	2	1.3	1.5
0.05	-	-	-	-	-	-	1.4	1	1

Figure 3-5 Fabricatioin method for cylindrical pillars. (a) Applied pattern of concentric circle and (b) schematic diagram of a pillar in a crater.
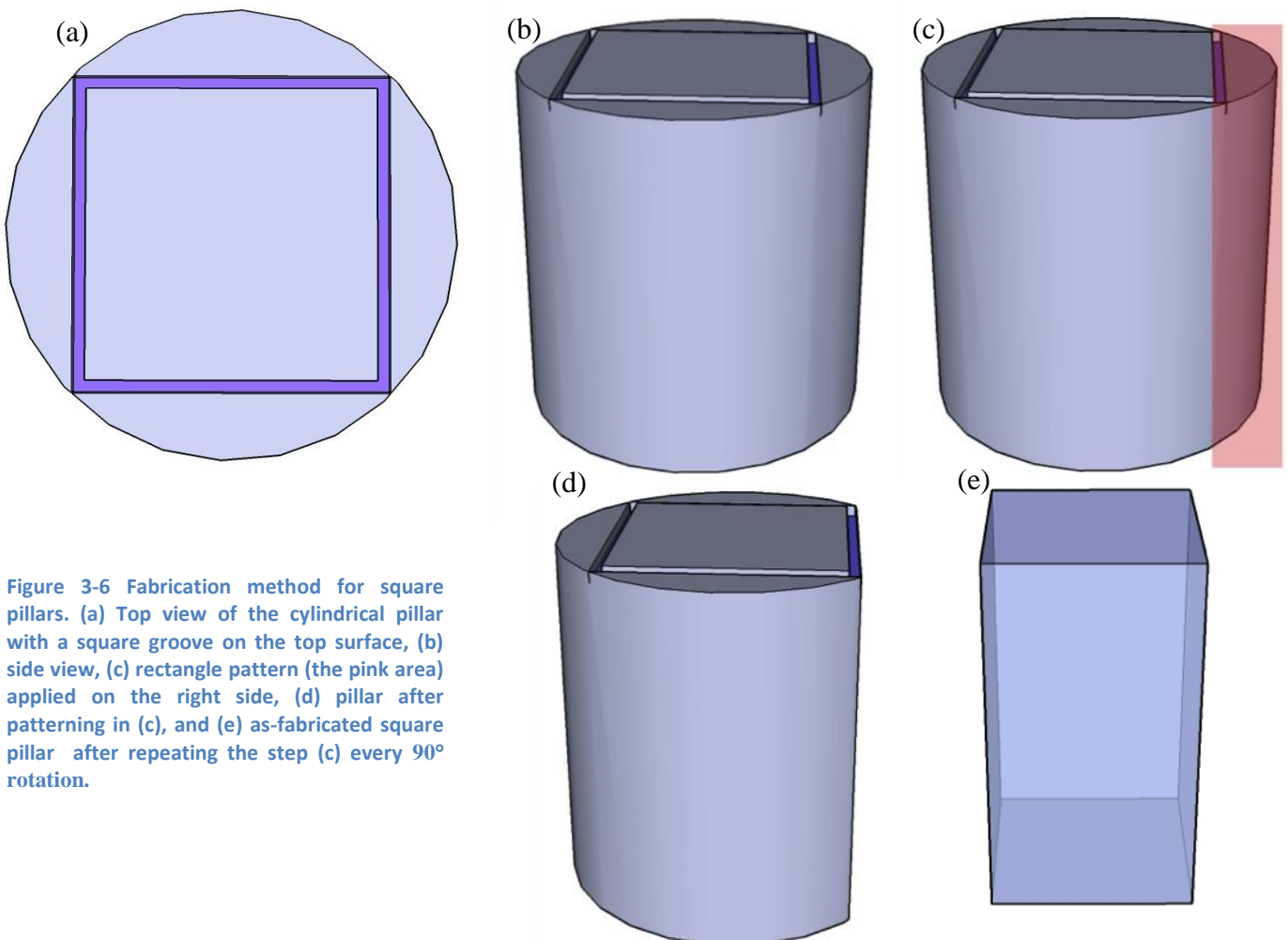

Figure 3-6 Fabrication method for square pillars. (a) Top view of the cylindrical pillar with a square groove on the top surface, (b) side view, (c) rectangle pattern (the pink area) applied on the right side, (d) pillar after patterning in (c), and (e) as-fabricated square pillar after repeating the step (c) every 90° rotation.
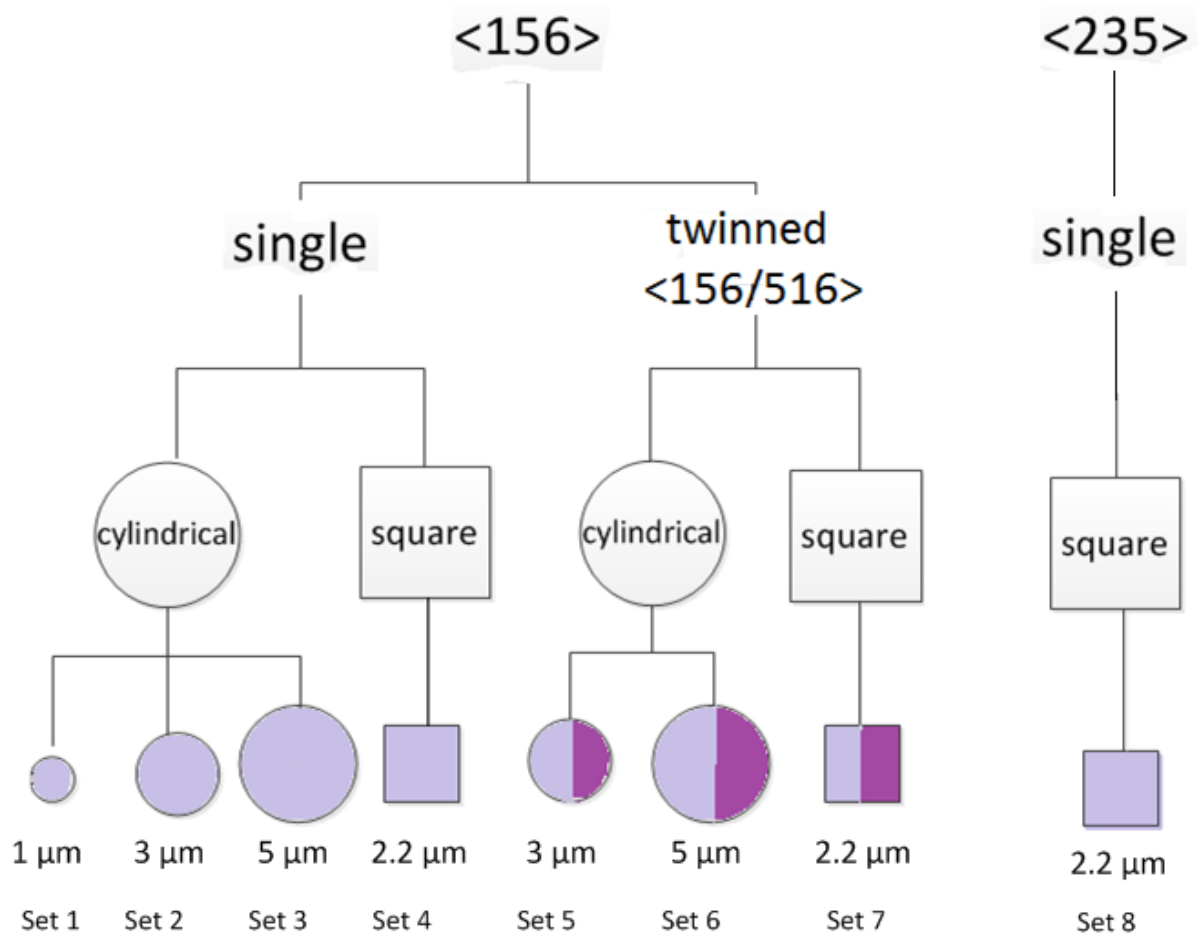
Figure 3-7 Overview of the configuration of the samples

Table 3-2 Summary of the 10 groups of micropillars

Data set	Orientation	Shape	Size/Diameter (µm)
1	156	Cylindrical	1
2	156	Cylindrical	3
3	156	Cylindrical	5
4	156	Square	2.2
5	156/516	Cylindrical	3
6	156/516	Cylindrical	5
7	156/516	Square	2.2
8	235	Square	2.2
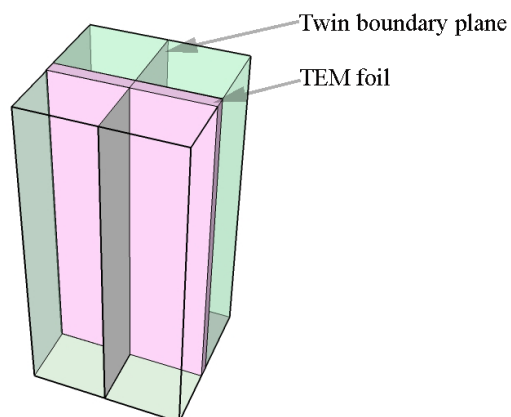
Figure 3-8 Schematic diagram of TEM foil extraction from a twinned pillar
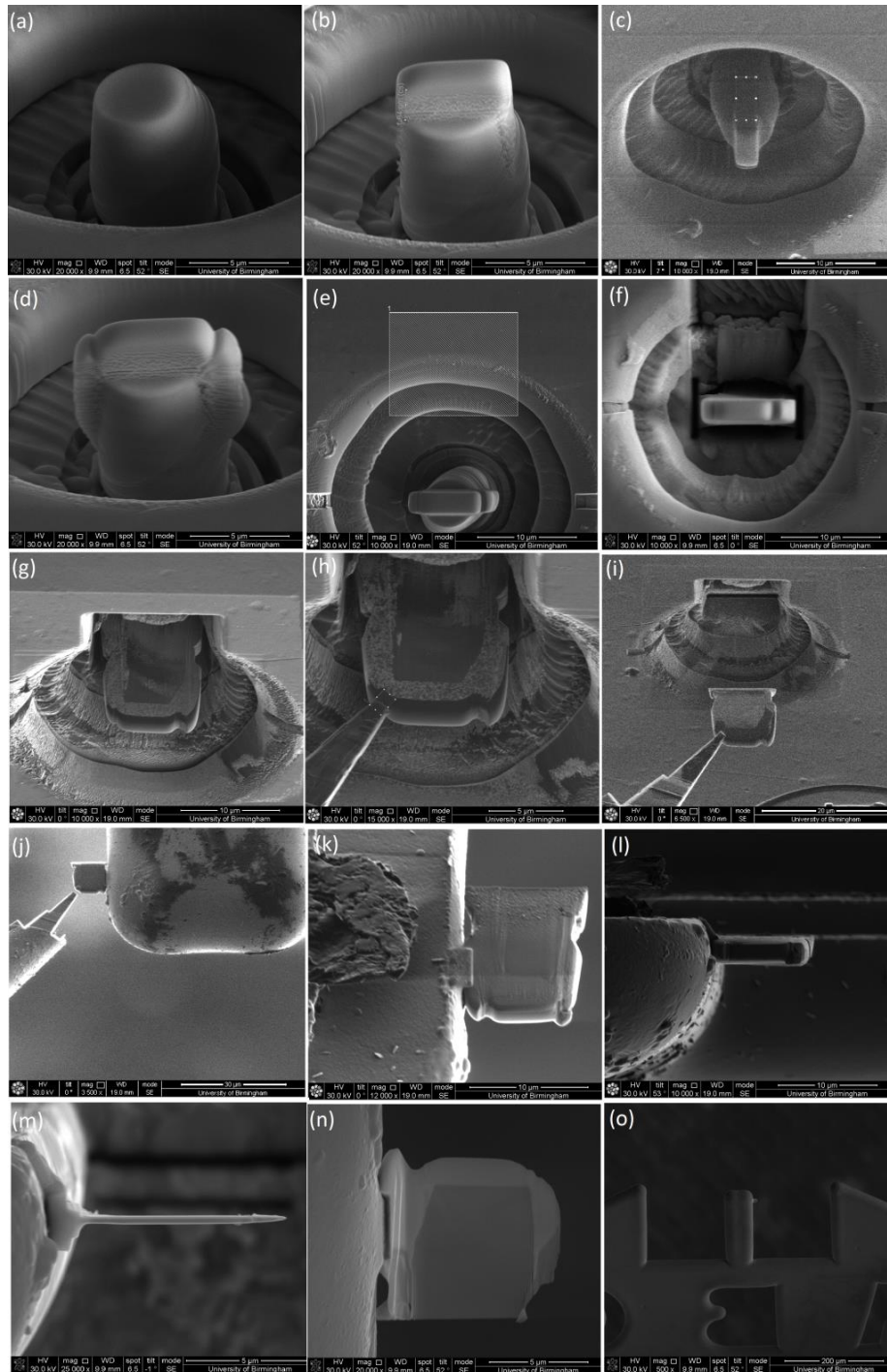
Figure 3-9 TEM sample extraction process: (a) SEM image of an as-compressed pillar. (b) SEM image of the pillar with W-coating on the top. (c) Ion-beam image of W-coating applied on the side surface. (d) SEM image of the pillar after coating. (e) Ion-beam image of the rectangle dug in front of the crater. (f) SEM image of the pillar strip. (g) Ion-beam image of the strip. (h) The strip was welded to the Omniprobe. (i) The strip was lifted out by the Omniprobe. (j) The strip was attached to the Cu grid. (k) The back of the strip was welded to the Cu grid to reinforce the attachment. (l) Ion-beam image of the Cu grid with the strip. (m) and (n) SEM image of the TEM specimen in different viewing directions. (o) low-mag SEM image of the Cu grid with the TEM specimen
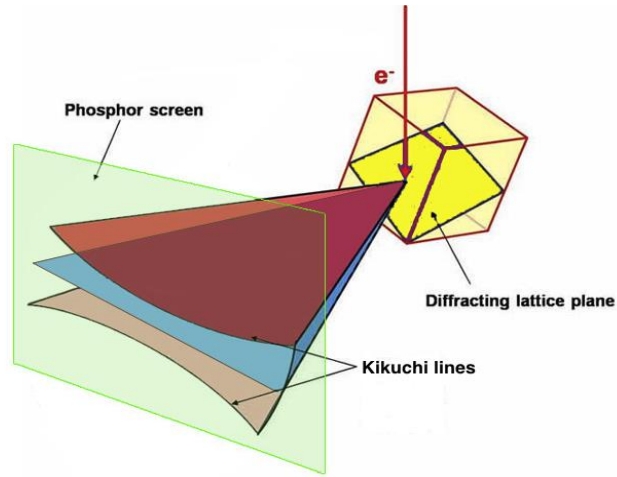
64

Figure 3-10 Formation of the electron backscattered diffraction pattern. Electrons from a divergent source incident on crystal planes at the Bragg angle are diffracted into a pair of cones to form Kikuchi bands in the diffraction pattern[77]
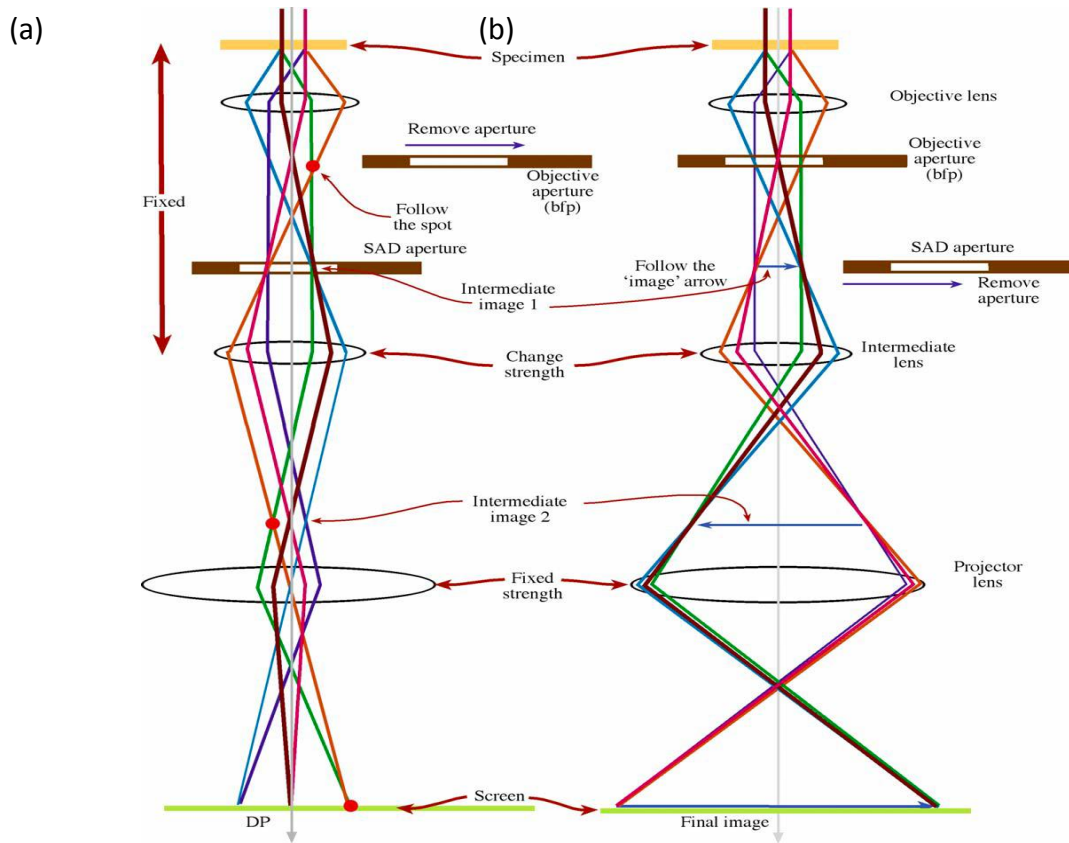

Figure 3-11 The two basic operations of the TEM imaging system (a) diffraction mode when the back focal plane of the objective lens is selected as the object of the intermediate lens and (b) image mode when the image plane is selected as the object [78]
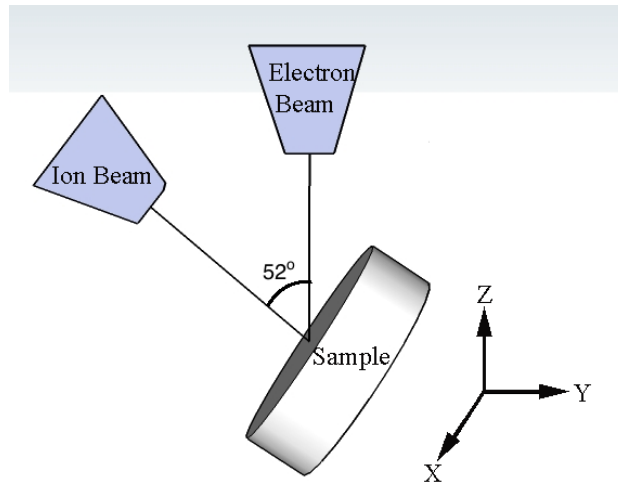
Figure 3-12 Schematic of the dual-beam system. The electron beam and ion beam are focused at the same position on the sample surface [79]
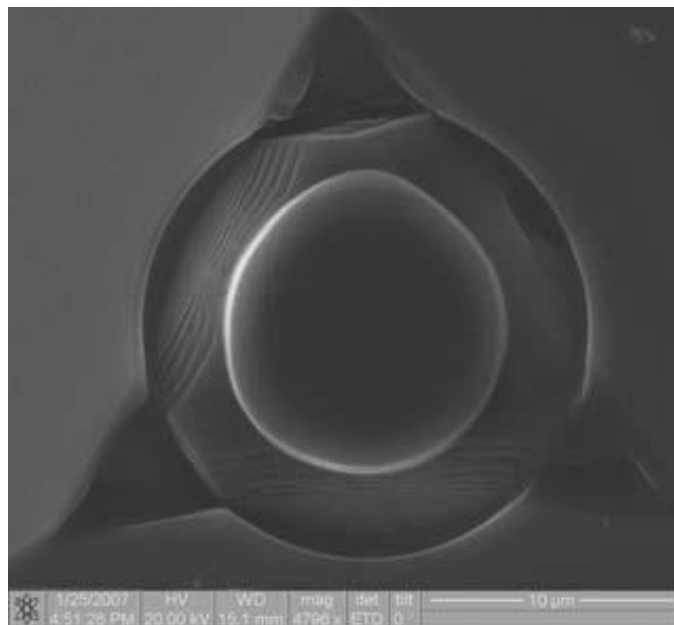

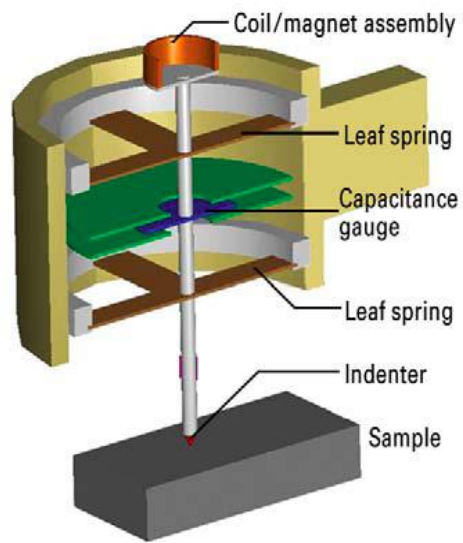**Figure 3-13 Berkovich diamond indenter with the FIB-flattened tip [81]**

Figure 3-14 Schematic diagram of the actuating and sensing mechanisms of the Nano Indenter G200 [82]

Chapter 4 Fabrication of Cu nanowires

4.1 Microstructure analysis of AAO template

4.1.1 Microstructure of AAO after first anodisation

A pure aluminium sheet was first anodized in 0.3 mol/L oxalic acid at 40 V for 1 hour. Figure 4-1 presents the resulting AAO surface observed using SEM. The image shows a disordered pore arrangement formed after a short period of anodisation. The result is consistent with that found by Masuda et al. [29], who claimed that the regularity of AAO was only achieved after a very long anodisation period, which was 160 hours in their case, under the same anodising condition. To gain a notably ordered pore arrangement but shorten the time-consuming process simultaneously, the oxide layer formed after first anodisation was removed by chemical etching, leaving a concave aluminium substrate as the starting material for the second anodisation. The concave pattern was utilized to improve the regularity of the AAO formed by the repeated anodising steps.

4.1.2 Microstructure of AAO after second anodisation

A highly ordered AAO template was obtained after a 3-hour second anodisation period, followed by an etching process in which the aluminium substrate was removed. The pore structure and the barrier layer of the as-prepared AAO can be seen in Figure 4-2.

Figure 4-2 (a) shows the ordered hexagonal close-packed pore structure of the resulting AAO template. The pore diameter and inter-pore distance measured from this SEM image were 60-

70 nm and 100 nm respectively, which were both in good accordance with the published literature [29]. Once the aluminium substrate has been removed from the bottom of AAO, the latter acts as a scallop shaped barrier layer (Figure 4-2 b), which has a high DC resistance and thus should also be removed before the electrochemical deposition process.

Figure 4-3 presents a cross section through the as-prepared AAO. The channels of the AAO are straight and parallel to each other, which makes the membrane an ideal host template to fabricate nanowires. The thickness of the sample, which determined the maximum length of the nanowires, was 16.2 μm in this case and approximately decreased to 12 μm after removal of the barrier layer. This observation indicates that the growth rate of AAO under such conditions is about 5.4 μm/h and thus the maximum length of the nanowires can be easily controlled by adopting various anodising durations. However, this duration should not be less than 3 hours although such a thick membrane is not a prerequisite for deposition. The resultant thickness ensures the mechanical strength needed for handling. A thinner membrane is too fragile and easy to break.

Figure 4-4 shows a STEM image of the AAO template. Although the whole AAO template is amorphous in terms of the microstructure, a duplex oxide layer is clearly presented by the different contrast in the image. The inner oxide layer in while, which is also called the cell boundary band, is known to be composed of relatively pure alumina; while the outer oxide layer, which was in contact with the electrolyte during the anodisation, is thought to have acid anion incorporation [83]. Thompson et al. [84] conducted STEM/EDX analysis on the AAO formed in phosphoric acid and found significant phosphorus yield in the EDX spectrum in the outer oxide layer. The different oxide layers suggest that two growth mechanisms exist

simultaneously for the AAO template: electrochemical reaction based on the direct ion transfer across the pure alumina region [35] and the deposition of the outer layer from the colloidal hydrous alumina [34].

4.1.3 Etching time of the barrier layer

5 wt% phosphoric acid was used as the etching solution to remove the barrier layer at room temperature. To determine the etching time for the as-prepared AAO, the bottom surface was observed after different etching times, as shown in Figure 4-5. Here, it can be seen clearly that after 70 mins, the pore bottoms were completely open. With a slightly longer etching time, the wall of the nanopores became obviously thinner due to the etching effect of the phosphoric acid through capillarity, which indicates a larger pore diameter. Thus the diameter of the nanowires can be controlled over a small range by using different etching times at this stage. Figure 4-6 presents the top surface of the AAO after etching for 80 minutes. The enlarged pore diameters ranged between 70-80 nm.

However, a longer etching time can result in the breakdown of the AAO template due to the dissolution of the pore walls, as shown in Figure 4-7.

4.2 Copper nanowires fabricated by electrochemical deposition

4.2.1 Cathode of the electrochemical reaction

Since alumina is nonconductive, a platinum or gold layer is normally sputtered on one side of the AAO to serve as the cathode in the following electrochemical deposition. Figure 4-8 shows the bottom surface of AAO after coating with gold over different times. The open ends

of the pores were only partially covered after 40 minutes and thus a longer coating time was adopted to ensure complete coverage.

The thickness of the gold layer after 50-minute coating was approximately 200 nm, measured from the cross-section image of the membrane, as shown in Figure 4-9.

NB When using the AAO membrane with its open ends partially covered (Figure 4-8 a) as the host template to conduct electrochemical deposition, hollow nanotubes instead of nanowires were obtained, as shown in Figure 4-10. The finding is in agreement with that found by Wang et al. [85].

4.2.2 Electrochemical deposition

As discussed before, current density is one of the parameters that can highly affect the microstructure of the resulting nanowires.

A current density of 10 mA/cm^2 was initially employed in the experiment, but no nanowires were found; instead, the surface of AAO was masked with a layer of bulk copper, as shown in Figure 4-11.

When the current density was reduced to 1 mA/cm^2, nanowires can be obtained. Figure 4-12 (a) displays the top view of densely packed nanowires embedded in the AAO template, indicating that a high pore-filling rate has been achieved. The nanowires are more recognizable after dissolving the template, as shown in Figure 4-12 (b). The nanowires are 70-80 nm in diameter, as seen in the cross-section view of the nanowires/AAO system using TEM in Figure 4-12 (c). The length of the nanowires can be controlled by using different deposition times.

TEM observation of individual nanowires has also been conducted. The diffraction pattern remains unchanged along the length of each nanowire in Figure 4-13, indicating that these nanowires are single crystal ones. However, various growth orientations were identified, as labelled in the images. It may be resulted from the polycrystalline nature of the sputtered gold layer, which serves as the deposition substrate. The bend contours inside the nanowires may be caused by the deformation resulted from ultra-sonication during sample preparation. In addition, twin boundaries which across the width (Figure 4-14 a) and along the growth orientation of the wires (Figure 4-14 b) exist in some of the nanowires. Their diffraction patterns are characteristic of an FCC material twinned on {111}.

These findings indicate that the current density during deposition should be maintained at a very low level. A higher current density causes severe hydrogen generation, which is the main side-reaction of the process, thereby hindering the deposition into the pores.

4.3 Summary

AAO template and Cu nanowires have been fabricated by electrochemical method and examined using electron microscopy. Single crystalline as well as twinned nanowires with diameters of 70-80 nm have been obtained.
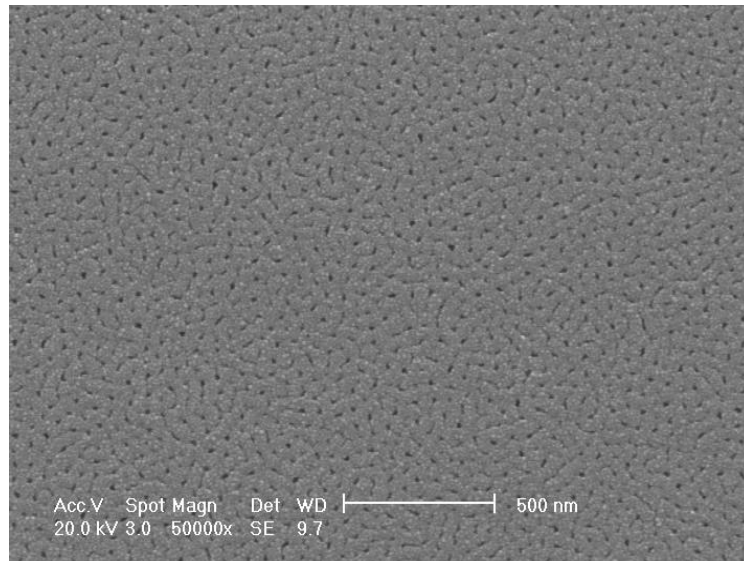
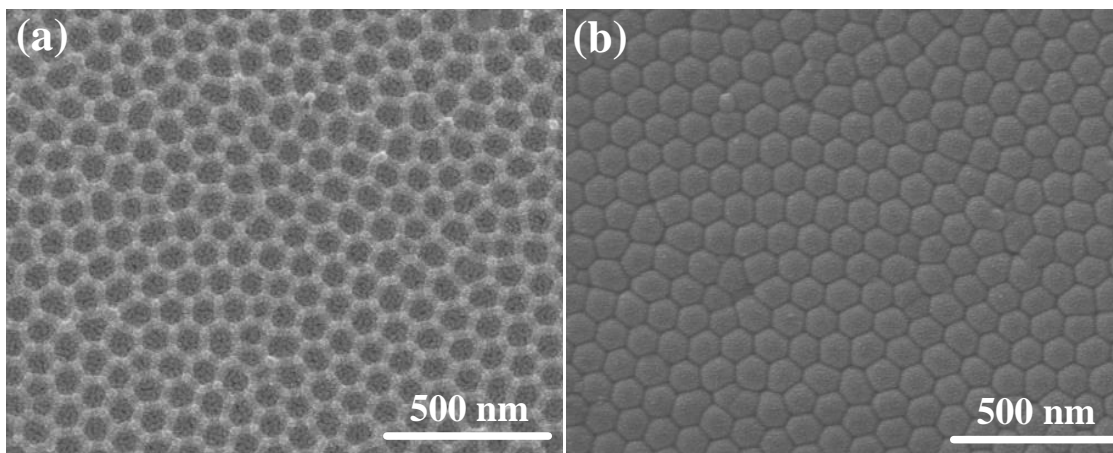**Figure 4-1 SEM image of AAO surface after 1st anodisation**

Figure 4-2 SEM images of AAO after 2nd anodisation: (a) view of the top surface, (b) view of the bottom surface (in contact with the aluminium substrate before etching) [anodisation conditions: 40 V, 0.3 mol/L $(COOH)_2$, 0°C]
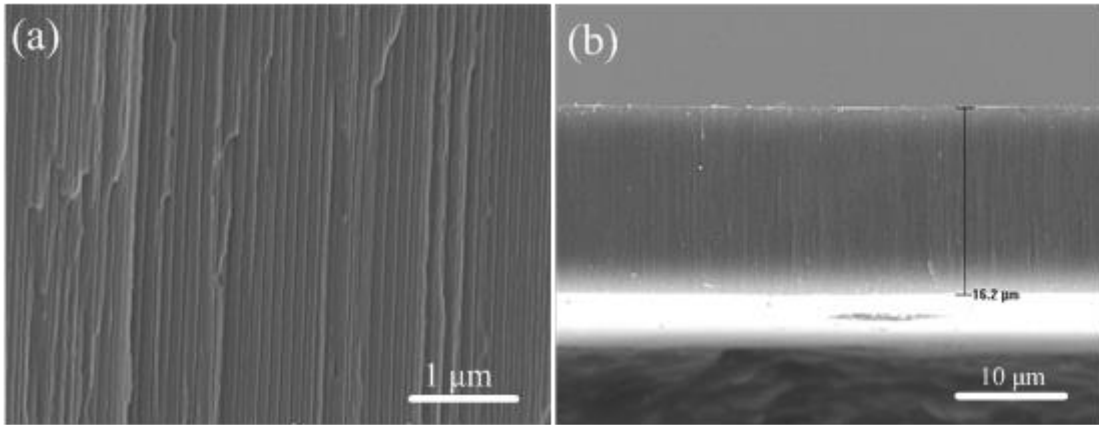
Figure 4-3 SEM images of the cross section of AAO (under the same condition as Figure 4-2):

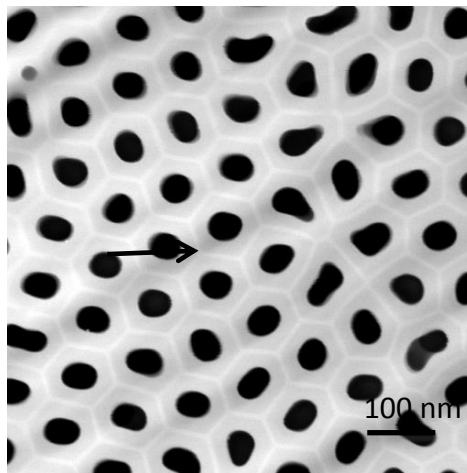(a) higher magnification, (b) lower magnification

Figure 4-4 STEM image of typical AAO, which clearly shows the cell
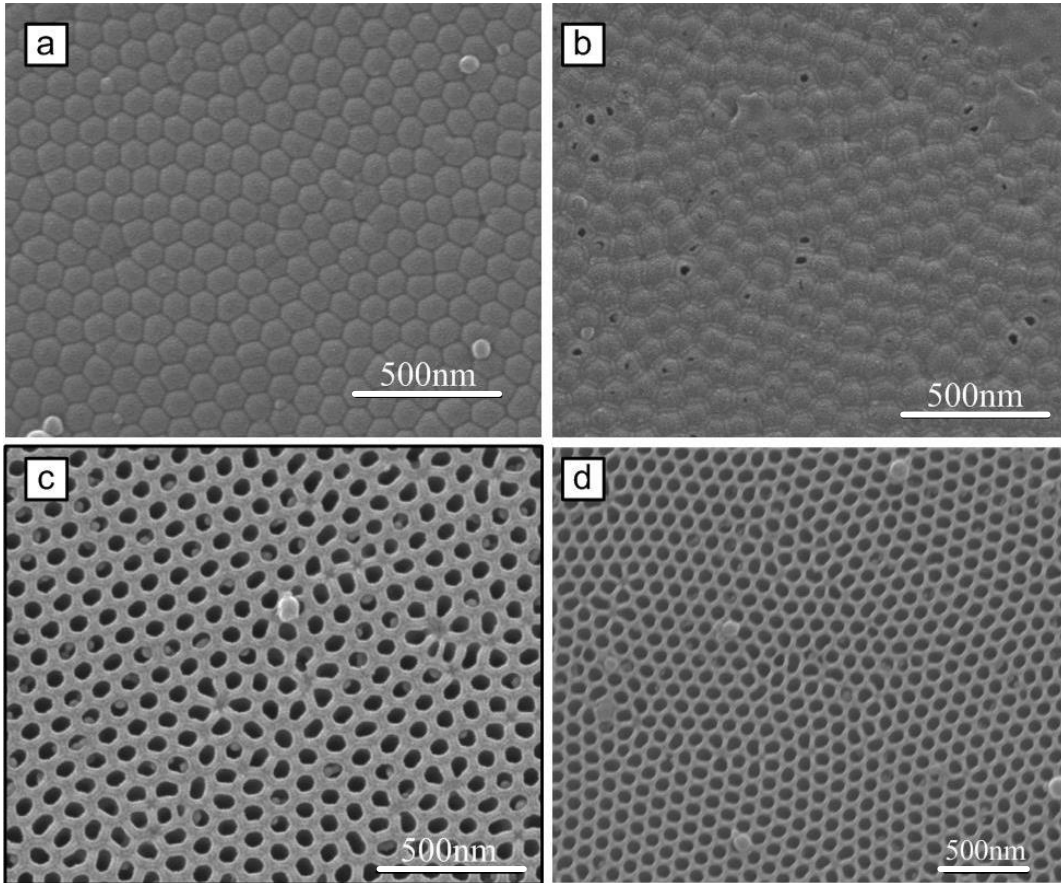boundaries, as indicated by the arrow.

Figure 4-5 SEM images of the bottom surface of AAO over different etching times:

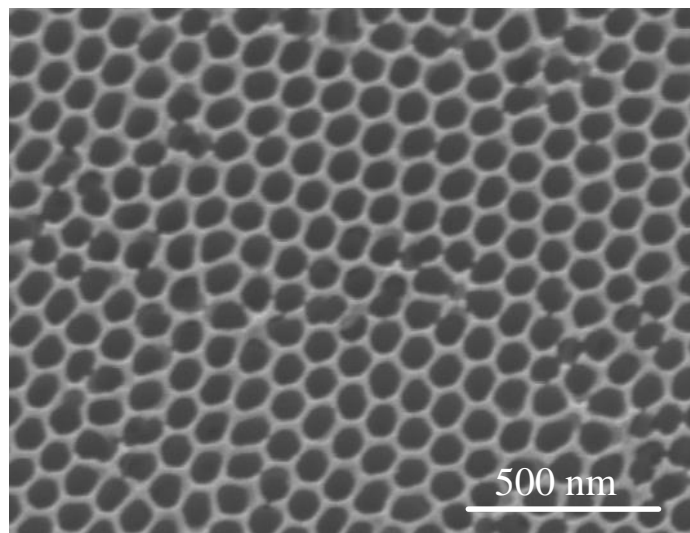**a: 50 mins, b: 60 mins, c: 70 mins, d: 80 mins**

Figure 4-6 SEM image of the top surface of AAO after etching in 5 wt% H3PO4 for 80 minutes
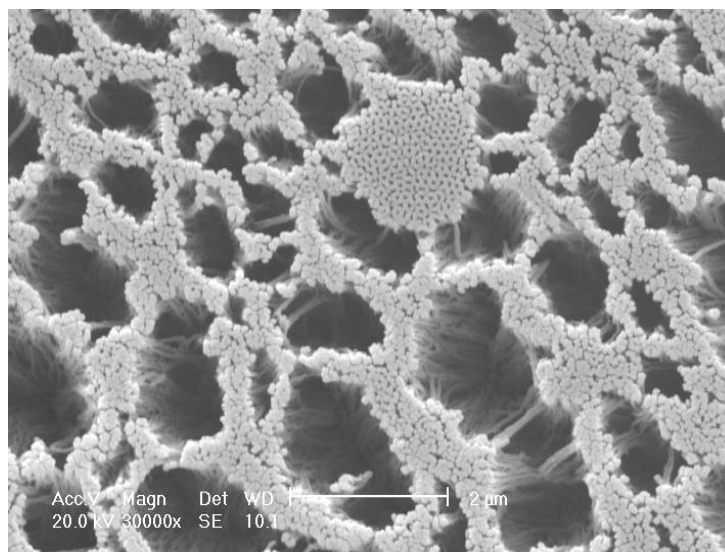
Figure 4-7 SEM image of the top surface of AAO after etching in 5 wt% H3PO4 for 90 minutes
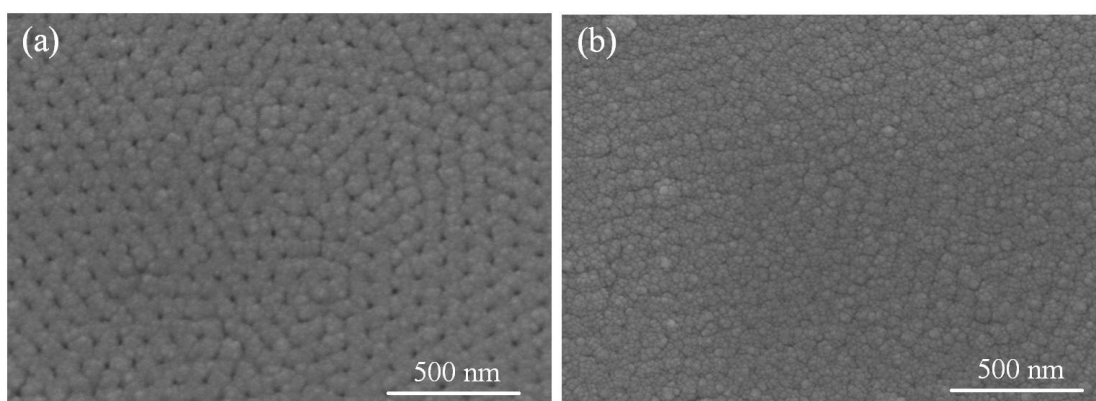
Figure 4-8 SEM images of AAO sputtered with gold over different coating times (a) 40 mins, (b) 50 min
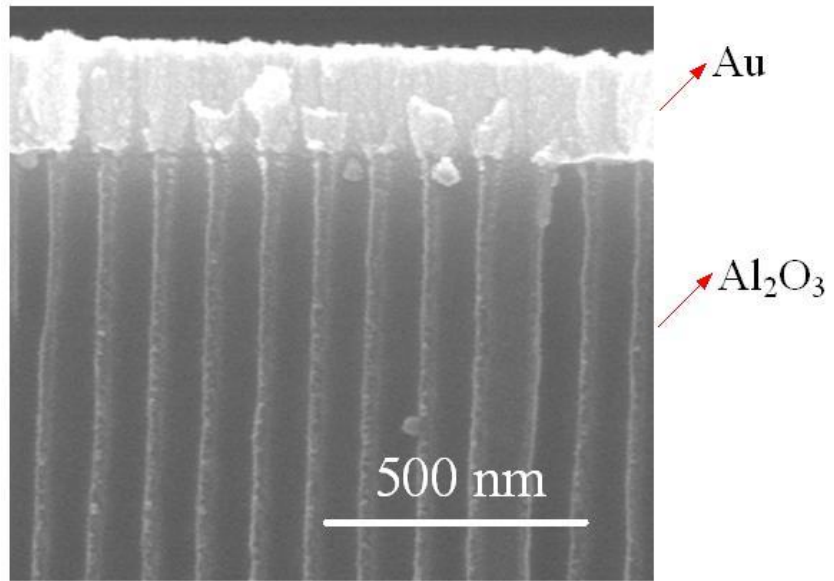
Figure 4-9 SEM cross-section view of AAO sputtered with gold for 50 mins
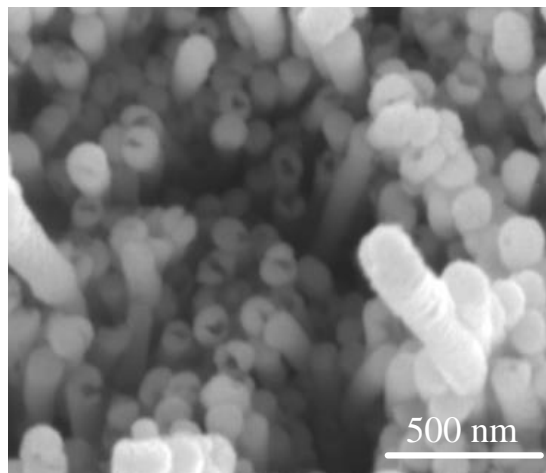
Figure 4-10 SEM image of copper nanotubes after dissolution of the AAO membrane
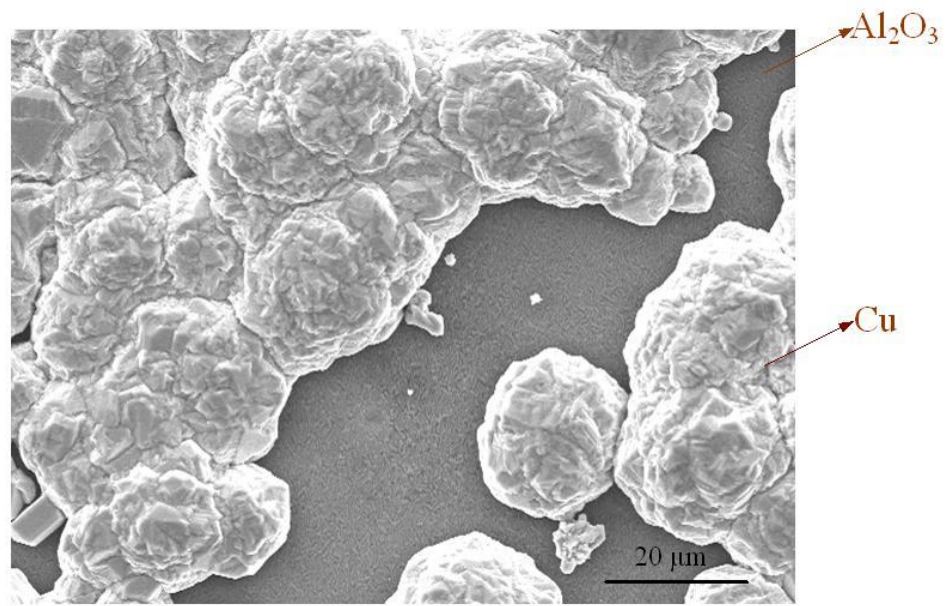
Figure 4-11 SEM image of bulk copper deposited on AAO [current density=10 mA/cm2]
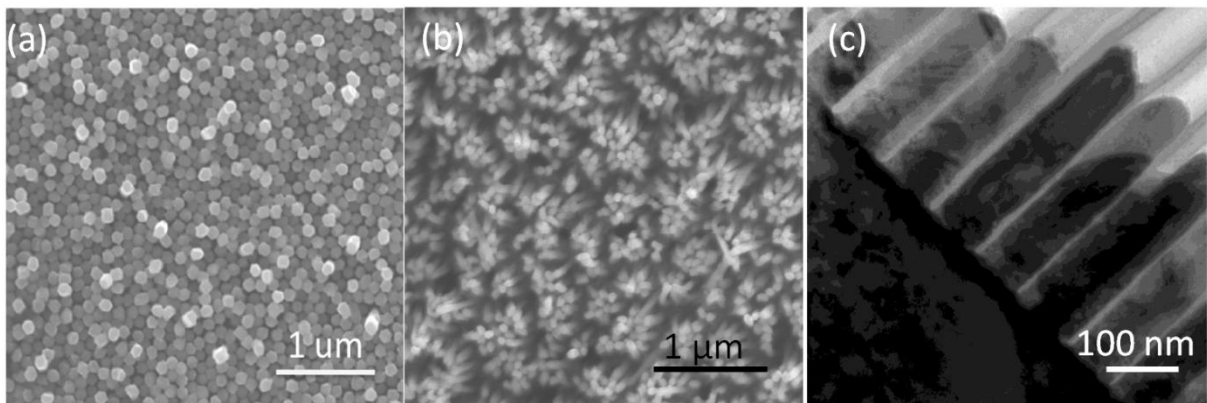
Figure 4-12 (a) SEM image of NWs grown in the AAO template in top view. (b) SEM image of free-standing NWs after dissolving the AAO template and (c) TEM image of NWs/AAO composite in cross-section view.
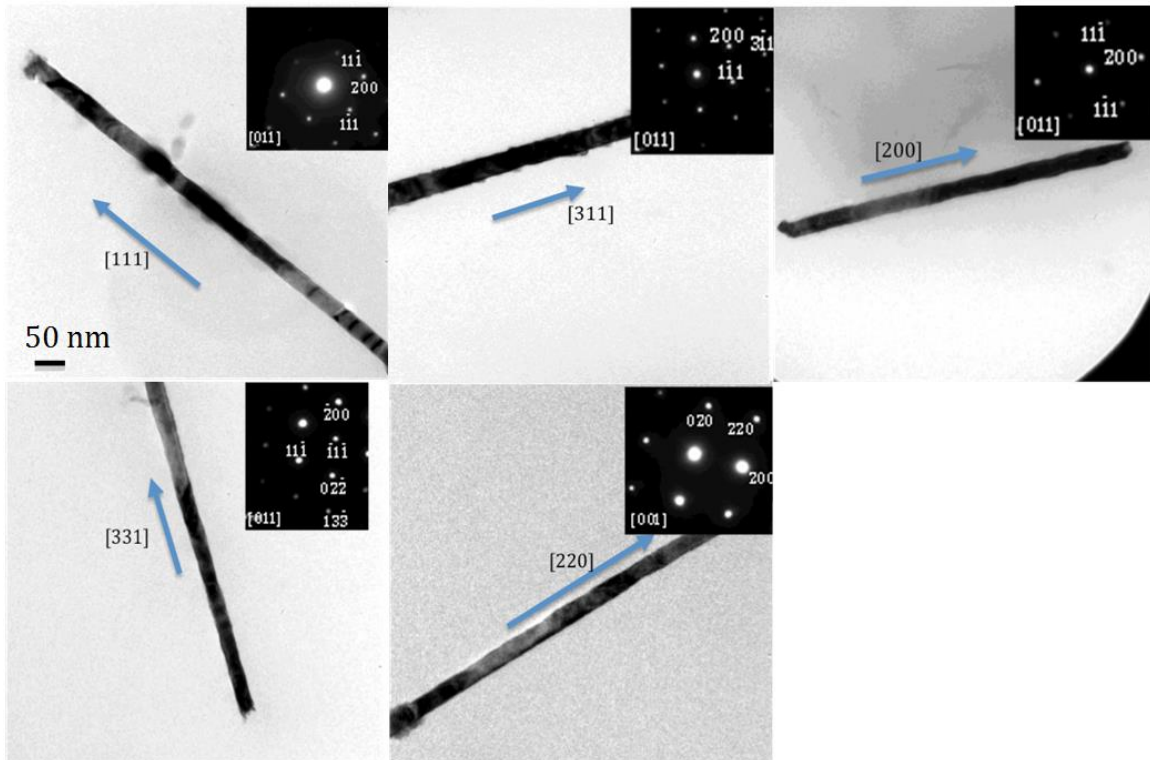
Figure 4-13 TEM images of copper nanowires with various growth orientations, the insets are the corresponding diffraction patterns.
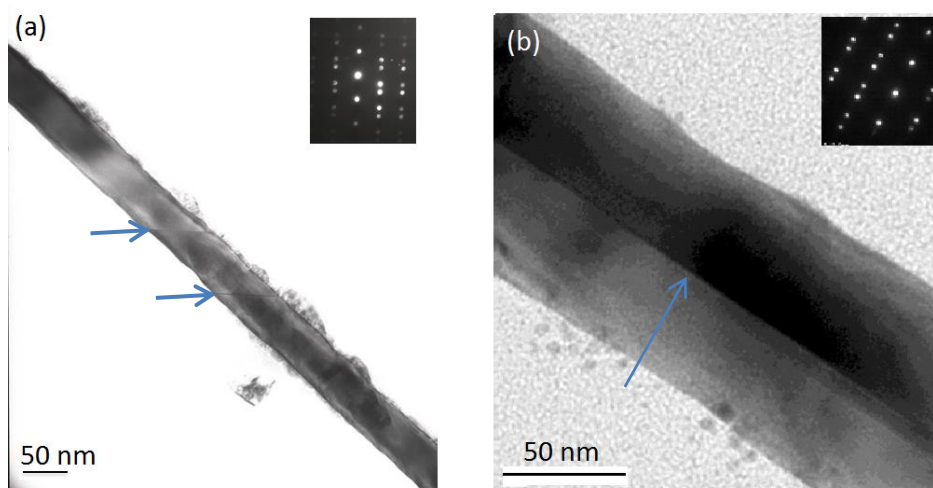
Figure 4-14 TEM images of (a) slanted twin boundaries and (b) vertical twin boundaries (indicated by the arrows) in single-crystal copper nanowires; the insets are the corresponding diffraction patterns.

Chapter 5 Compression Tests: mechanical data and surface morphology

5.1 Data analysis

In this section, load-displacement data measured via the nanoindenter during compression are converted into stress-strain curves. Flow stresses at a certain strain and the work-hardening rates are selected as representative data to characterize the mechanical response of the micro-pillars.

5.1.1 Stress and strain

5.1.1.1 [156] single crystal cylindrical pillars with different sizes

True stress-strain curves for [156] single crystal cylindrical pillars with three different sizes are shown in Figure 5-1. The diameters measured at half sample height position were approximately 1 μm, 3 μm and 5 μm. The exact measurements of each sample are listed in Table 5-1. Samples in each size range are assigned the same colour. Although the pillar diameters in each range are similar, the mechanical response is remarkably scattered, especially at higher stresses. The flow stresses diverge as the sample size shrinks. Overall, evident from the curves is a "smaller is stronger" trend, i.e., the flow stress increases with decreasing sample size, which has commonly been observed in fibbed small-scale samples [2, 9, 54, 56]. To illustrate the size-dependent hardening, the stresses for strain values of 0.05 were extracted and plotted in Figure 5-2, as flow stress versus pillar diameter on a log-log

scale. The results clearly demonstrate the size dependence of the strength by a power law relationship. The power exponent deduced from the data in Figure 5-2 is -0.33, which is in line with recent experiments on Cu microcrystals [10].

The flow stress-strain curves for the 1 μm diameter samples are obviously different from those for larger samples. Here, sporadic strain bursts of up to several percent frequently appear after the initiation of plastic flow. Elastic-like deformation segments separate these bursts, some of which are followed by a slight softening, as indicated by the arrows in Figure 5-1. On the contrary, in the 3 μm and 5 μm diameter samples, instead of the increments of nearly elastic loading, there is a gradual rise with increasing strain due to work hardening, as well as much smaller strain bursts.

5.1.1.2 Single crystal square pillars: [156] versus [235]

To compare the mechanical response of samples oriented for multiple slip and single slip, true stress-strain curves for 2.2 μm single crystal square pillars with [156] and [235] compression axes are plotted in Figure 5-3. These curves also manifest discrete deformation steps, like the other single crystal microsamples. However, there is a steeper increase in flow stress for Cu[156] after approximately 0.05 strain, indicating that this compression direction shows a greater amount of work hardening.

5.1.1.3 Cylindrical pillars: [156] single crystal versus [156]/[516] twinned

To examine the effect of internal structure on microcompression, single crystal and twinned pillars are compared here. 3 μm and 5 μm pillars containing twin boundaries were fabricated where the crystallographic directions of each side were identified as [156] and [516]. Only

these two sample sizes were feasible as it was found too difficult to FIB pillars of 1 μm diameter containing a twin boundary. The results are presented in Figure 5-4 and Figure 5-5, corresponding to the true stress-strain curves for 3 μm and 5 μm samples respectively. One can clearly see from both figures that the introduction of a twin boundary has a clear effect on the flow behaviour, leading to higher work hardening rates and thus larger flow stresses than for their single crystalline counterparts of similar sizes. However, at 3 μm, both single crystal and twinned samples are characterised by intermittent flow, while at 5 μm, twinned samples display fewer burst regions and the deformation is smoother as compared with the single crystal ones.

5.1.1.4 Square pillars: [156] single crystal versus [156]/[516] twinned

To avoid the tapering along the gauge length associated with cylindrical pillars, additional testing was performed on square shaped pillars with a side length of 2.2 μm for single crystal and twinned samples. They were extracted from the same region mentioned in section 5.1.1.3. The true stress-strain curves are presented in Figure 5-6. The red curves representing twinned samples all sit above the black ones, i.e., the single crystal pillars, which is in good agreement with the results obtained from the cylindrical samples. Again, all curves exhibit intermittent flow, like the 3 μm cylindrical ones.

5.1.1.5 Cylindrical vs square pillars

It is also worth comparing the hardening behaviour of the cylindrical pillars with that of the square ones. We aim to identify the shape effect on hardening at this length scale. Here cylindrical pillars with a diameter of 3.1 μm and square pillars with a side length of 2.2 μm are compared. The diameter of the cylindrical pillars is roughly the same as the diagonal of

the square cross section.

As indicated in Figure 5-7 and Figure 5-8, the square pillars have a much higher flow stress than the cylindrical ones in both single crystal and twinned samples. The curves for the cylindrical pillars reach a plateau at approximately 0.05 strain, maintaining a steady flow stress afterwards. However, the square pillars continue hardening until at least 0.15 strain in the single crystal tests and 0.1 strain in the twinned samples.

5.1.2 Work-hardening rate of single crystals

The hardening rate Θ is measured from linear fitting of the true stress-strain curves. Data between the yield point and approximately 10% strain were analyzed. In those tests where the maximum strain is below 0.1, hardening is determined up to the maximum level strain. This strain range was divided into two parts for more accurate linear fitting, similar to the approach used to determine different hardening stages in bulk materials. However, the characteristics of the two stages differ remarkably from the bulk counterpart. Here, hardening values are extremely high in stage I as compared with stage II, as stage I is the transition region from elastic deformation to stable plastic flow, as illustrated in Figure 5-9. On the contrary, the situation in bulk materials is quite the opposite: stage I is the easy glide region while stage II possesses a much higher hardening rate.

5.1.2.1 [156] single crystal cylindrical pillars with different sizes

According to the last section, we divided the plastic deformation regions of the stress-strain curves into two parts. Stage I hardening starts from the yield point to where the slope of the curve changes dramatically, the next part is considered as stage II. For a better understanding,

stages I and II are illustrated on stress-strain curves from three [156] single crystals with different sizes, as shown in Figure 5-10. One can clearly see from it and Figure 5-1, that 1 μm pillars not only yield at a higher strain level, but also start stage II hardening at a higher strain, compared to the other two sets of pillars. Figure 5-11 presents hardening rates for the two stages versus sample diameter for all the data shown in Figure 5-1. Stage I is quite similar in all the samples, regardless of the diameter. In stage II, the hardening rate is smaller for smaller samples; a few tests on the smallest pillars even show negative values. This does not contradict 'smaller is stronger' for the following two reasons. Firstly, the yield stress follows the rule that smaller samples yield at a higher stress. Secondly, referring back to the stress-strain curves again, the high stage I hardening behaviour occurs over a relatively wide range of strain for the smallest samples, about 0.04 on average compared with 0.01 strain for the other two sets, which contributes greatly to the high flow stress.

5.1.2.2 Single crystal square pillars: [156] versus [235]

Figure 5-12 plots the hardening rates of single crystal square pillars with two different orientations, which correspond to the tests described in 5.1.1.2. (a) shows the stage I hardening rates while (b) compares stage II hardening. Each orientation is composed of 5 tests to give an indication of scatter. To get a clear understanding of these data, the mean hardening rate and standard error for both orientations are plotted in Figure 5-13. Again, stage I hardening is pretty similar for both orientations, but stage II hardening is quite different. Hardening rates of 0.6-1.1 GPa were measured from [156] pillars while very low, even negative values were obtained from [235] pillars. Referring back to Figure 5-3, hardening starts from 0.03-0.05 strain for stage II in both orientations, leading to a definite separation of

84

flow curves after 0.05 strain, where [156] pillars begin to possess a higher flow stress.

5.2 Surface morphology of deformed pillars

Typical appearances of the deformed pillars are shown in this section. Activated slip systems are observed and analysed to shed light on the slip mechanism at this length scale.

5.2.1 [156] single crystal cylindrical pillars with different sizes

SEM images of deformed [156] single crystal cylindrical pillars with different diameters are shown in Figure 5-14 to Figure 5-16. In most cases slip bands are formed on two sets of slip planes, while in a few cases deformation occurs preferentially on only one set of planes (Figure 5-14b and Figure 5-16b). The number of activated slip systems does not depend on the strain level, as multiple slip develops in samples with the smallest strains as well. It is also worth noting that in those samples with two sets of slip planes, deformation patterns differ. In some cases deformation is distributed homogenously across the two sets of slip planes throughout the length of the pillar (Figure 5-14c, Figure 5-15b and Figure 5-16a) and barrelling occurs at a large strain (Figure 5-14c). In other cases one localized set of planes dominates the slip over a certain part of the gauge length, so that the pillars finally slide downwards at large strains and lose their shape integrity (Figure 5-14a, Figure 5-15c and Figure 5-16c). It should be noted that the position of the same set of slip planes is not fixed: they can occur at the top (Figure 5-14a) or at the base (Figure 5-15c) of the sample. Regarding the size effect, no obvious distinction in appearance can be found between the deformed pillars with different diameters. This is contrary to previous findings, where Ng and Ngan [6] reported fine slip bands in large pillars and coarse slip bands in smaller pillars.

The crystallographic orientation of the loading axis determines the active slip systems. To validate the consistency of the inclined slip planes in the SEM images with the resolved shear stress, Schmid factors of the easy slip systems when loaded along [156] direction were calculated and are presented in Table 5-2. The highest Schmid factor is 0.46 for the slip system $\frac{1}{2}[101](\bar{1}11)$. The second highest value is 0.40 for both the $\frac{1}{2}[10\bar{1}](111)$ and $\frac{1}{2}[110](\bar{1}11)$ slip systems. The slip system $\frac{1}{2}[\bar{1}10](111)$ possesses the lower Schmid factor of 0.32. A stereographic projection is presented in Figure 5-17 based on data extracted by EBSD. It shows how the {111} plane normals are arranged relative to the specimen axis. It is evident from the stereograph that both the $(1\bar{1}1)$ and $(\bar{1}\bar{1}1)$ plane normals are approximately 80-90 degrees away from the pillar axis. Only the (111) and $(\bar{1}11)$ slip planes are observed in the SEM pictures, which is consistent with the Schmid factors.

5.2.2 Single crystal square pillars: [235] versus [156]

Visual inspection of the deformed single crystal square pillars shows a remarkable difference between the [235] and [156] samples. Figure 5-18 presents [235] crystals after slight and severe deformations. Only one set of slip planes is activated in both cases, while for the deformed [156] crystals displayed in Figure 5-19, two sets of slip planes are observed. The crystal orientations along the edges of the square pillars were measured using EBSD and shown here together with the SEM images. Thus active slip planes can be verified by measuring the inclination angles of the slip traces and comparing them with the angles between possible slip traces and the loading axis, which are calculated using the following method:

1. Determine the index of the direction defined by the intersection of the pillar's front surface and the slip plane, i.e. the direction of the slip trace on the XZ plane. This is the cross product of the XZ plane normal (i.e. crystal orientation along Y axis) and the slip plane normal.

2. Calculate the actual inclination angle θ between the slip trace and the loading axis. The cosine of the angle between the two directions is given by

$$\cos \theta = \frac{h'h + k'k + ll'}{\sqrt{(h^2 + k^2 + l^2)}\sqrt{(h'^2 + k'^2 + l'^2)}}$$

3. Correct the apparent inclination angle θ' considering the tilt angle of 30° adopted for SEM imaging. $\theta' = \tan^{-1}(\frac{\tan\theta}{\sin 30°})$

The unit triangle containing the [235] orientation shown in Figure 5-20 implies single slip. The primary slip system for a [235] oriented crystal is $\frac{1}{2}[101](\bar{1}11)$. Hence we calculate the inclination between the $(\bar{1}11)$ slip trace and the [235] axis in this case. The index of the intersection line is $(\bar{1}11) \times (3\bar{6}2) = [853]$ and the angle between [853] and [235] is 41°. The apparent inclination θ' is calculated to be 60° after the tilt correction. This inclination matches sufficiently well the measured value of 63° from the SEM images in Figure 5-18.

The two slip planes which appeared in the [156] oriented crystals were determined as (111) and $(\bar{1}11)$ in the previous section. Here we can verify the results via the inclination angles as well. The indices of the (111) and $(\bar{1}11)$ slip traces on the pillar's front surface are $(111) \times (5\bar{3}2) = [53\bar{8}]$ and $(\bar{1}11) \times (5\bar{3}2) = [57\bar{2}]$ respectively. The actual inclination angles are 69° and 66° respectively, corresponding to 79° and 78° after tilt correction. The inclination angles measured from the SEM images in Figure 5-19 are 79° and 82°, matching adequately

the calculated ones.

5.2.3 [156]/[516] twinned cylindrical pillars

SEM images of the twinned cylindrical pillars with 5 μm and 3 μm diameters after deformation are shown in Figure 5-21 and Figure 5-22 respectively. The arrows indicate the slightly inclined twin boundary plane. The angle between the twin boundary plane and the loading axis is calculated as 8.4˚ from the EBSD results. SEM images were taken from two different directions. Figure 5-21 (a) and (b) reveal the morphology of the crystal on the left side only, while the remaining pictures were taken with the twin boundary plane almost in the centre of the front view, thus exposing both of the two component crystals. Two sets of slip planes are clearly present in both crystals. These localized coarse slip bands are symmetrical along the twin boundary. The number of visible slip traces is equal in the two crystals, indicating that the extent of deformation is the same on both sides of the twin boundary. Schmid factors for the [516] direction are presented in Table 5-3.

5.2.4 [156]/[516] Twinned square pillars

Twinned square pillars with different twin boundary positions are shown in Figure 5-23 and Figure 5-24. Figure 5-23(a) presents an undeformed pillar with the twin boundary sitting approximately in the centre. (b) and (c) show pillars with a similar twin boundary position after mild and severe deformation respectively. The morphologies of these deformed pillars are analogous to those of the cylindrical ones observed in the previous section, i.e., the slip bands are symmetrically distributed about the twin boundary. Two sets of slip planes are also observed in each component grain. An undeformed pillar with a twin boundary close to the

edge is shown in Figure 5-24(a); (b) and (c) present two similar pillars deformed to ~4.2% and ~22.5% strain, respectively. A symmetrical pattern of slip about the twin boundary was observed in (b) but is absent in (c). Two sets of slip planes are also quite visible in the large grain. Large shear deformation was evident in both Figure 5-23(c) and Figure 5-24(c); the pillars sheared in the same direction to the same extent despite the presence of the twin boundary.

5.3 Summary

1. The [156] single crystal cylindrical Cu pillars with diameters of 1 µm, 3 µm and 5 µm exhibit a 'smaller is stronger' trend, as has been found in other previous investigations of micropillars. Larger strain bursts frequently appear in the 1-µm pillars, while the 3-µm and 5-µm samples display a more continuous deformation. In our newly defined two stage hardening, all the samples show similarly high hardening rates in stage I and significantly lower hardening rates in stage II, where the hardening rates increase with increasing sample diameter. Furthermore, the 1-µm samples experience a longer stage I hardening than the larger samples. Additionally, the surface morphology observations reveal that most of the pillars possess two sets of slip planes; in a few cases only one set of slip planes appears. This is independent of the sample diameter and strain level.

2. The stress-strain curves for single crystal square pillars oriented in the [156] and [235] directions separate after approximate 0.05 strain due to different stage II hardening rates. Visual inspection of the sample surfaces indicates that the [235] pillars underwent single slip while the [156] pillars experienced multiple slip.

3. Both 3-µm and 5-µm [156] single crystal cylinders and [156]/[516] twinned cylinders were compared. Generally speaking, the twin boundary induces a higher work hardening rate; the corresponding stress-strain curves are still jumpy in the 3-µm pillars but become much smoother in the 5-µm samples. SEM examination of the twinned cylinders shows that localized coarse slip bands are developed symmetrically along the twin boundary. The two crystals are equally deformed, featuring the same number of slip traces distributed on two sets of planes.

4. The 2.2-µm square twinned [156]/[516] pillars also have higher hardening rates than the square single crystal ones. Surface observation again demonstrates that the slip bands are symmetrically distributed along the twin boundary. Moreover, under severe deformation, the two constituent grains of the twinned pillars shear in the same direction to the same extent, indicating coherent deformation.

5. The 2.2-µm square pillars and the 3-µm cylindrical pillars (the diagonal of the former equals the diameter of the latter) have been compared for both single crystals and twinned samples. The square ones have a much higher flow stress in both cases due to a significant increase in hardening rate.
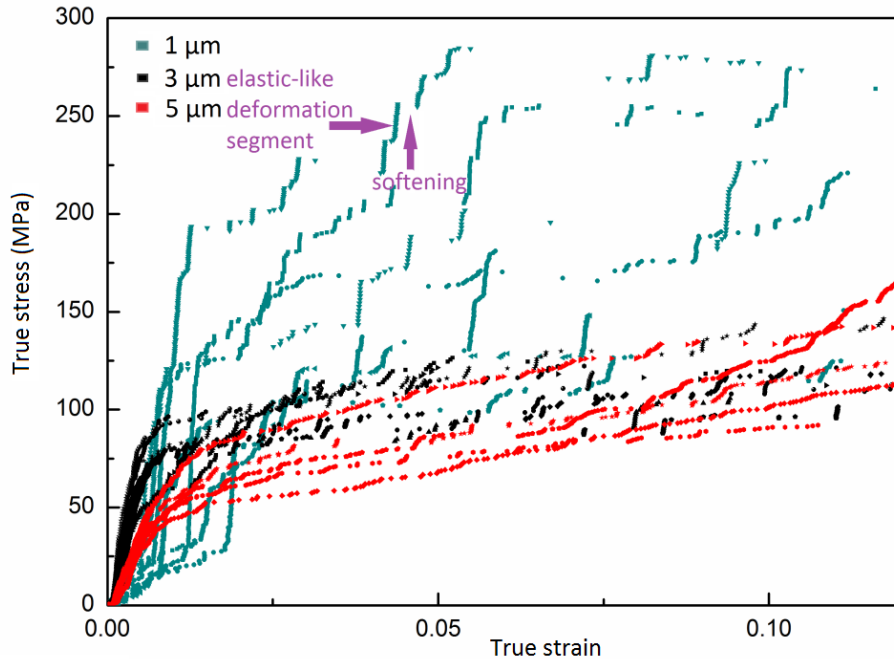
Figure 5-1 True stress versus true strain plots grouped by sample diameter

Table 5-1Exact measurements of the sample diameters of [156] single crystals

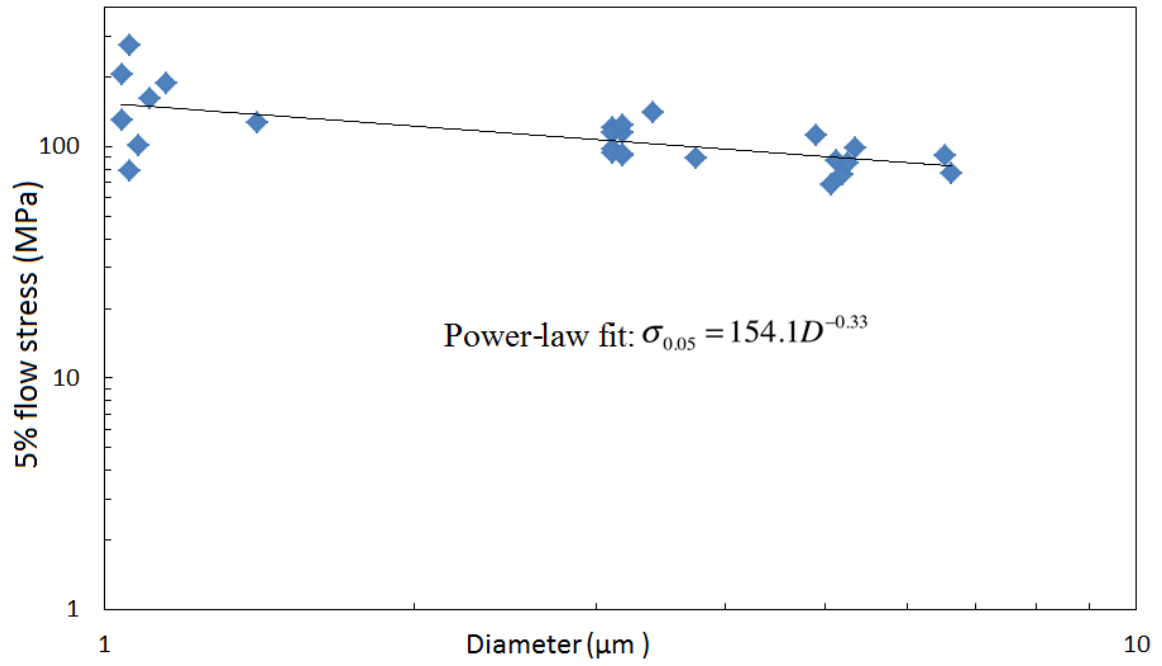| Group sizes	Exact measurements (μm)
1 μm	1.04, 1.04, 1.06, 1.08, 1.11, 1.15, 1.41
3 μm	3.1, 3.1, 3.1, 3.2, 3.2, 3.2, 3.2
5 μm	4.9, 5.1, 5.1, 5.2, 5.3

Figure 5-2 5% flow stress versus pillar diameter for cylindrical [156] single crystals plotted on a log-log scale.
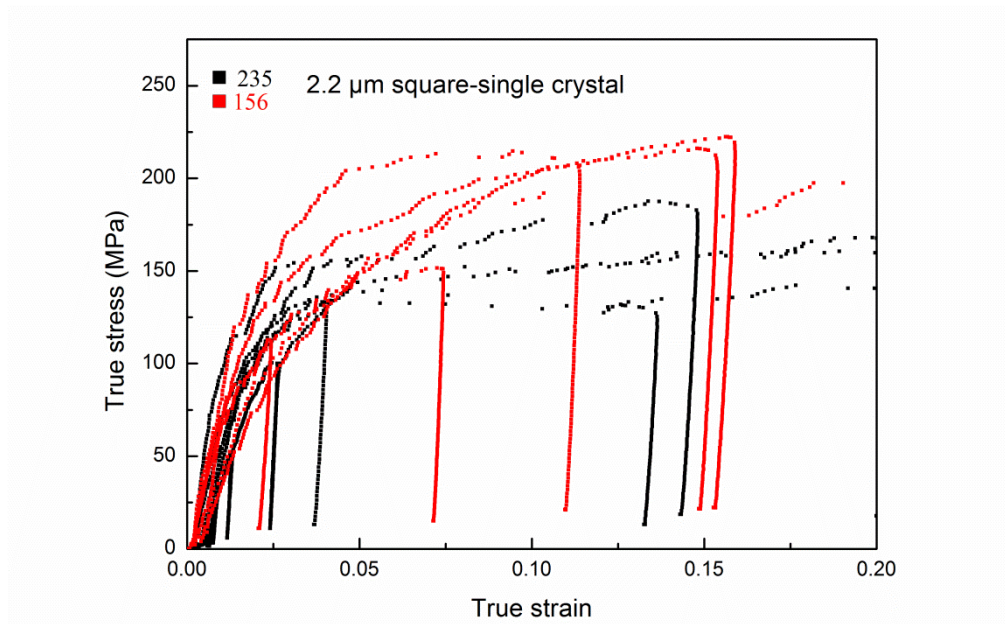

Figure 5-3 True stress-strain curves for 2.2 μm single crystal square pillars with [156] and [235] compression directions
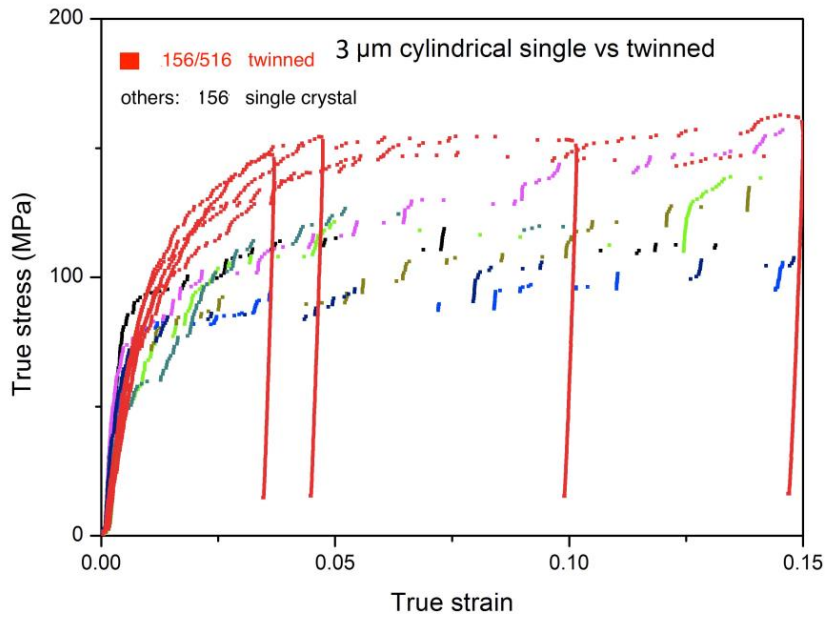
92

Figure 5-4 True stress-strain curves for 3 µm cylindrical pillars: [156] single crystals and [156]/[516] twinned crystals.
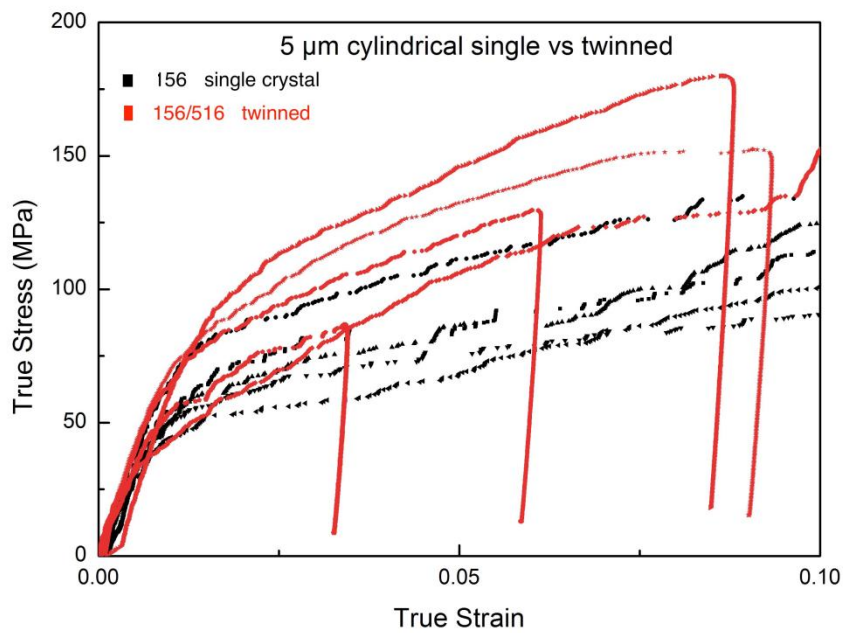

Figure 5-5 True stress-strain curves for 5 µm cylindrical pillars: [156] single crystals and [156]/[516] twinned crystals
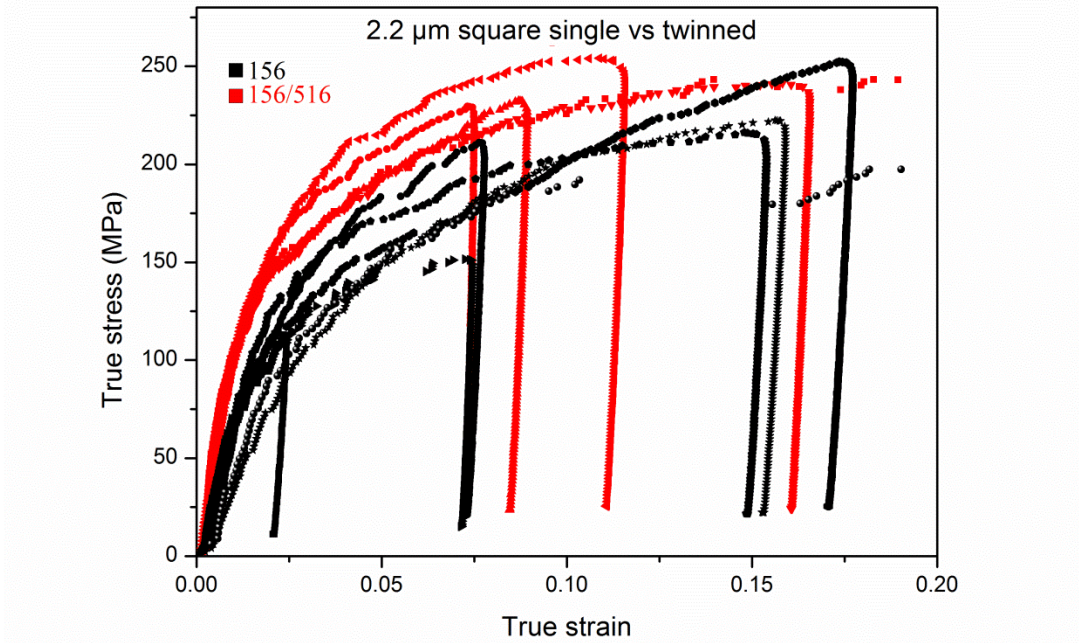
93

Figure 5-6 True stress-strain curves for 2.2 μm square pillars: [156] single crystals and [156]/[516] twinned crystals
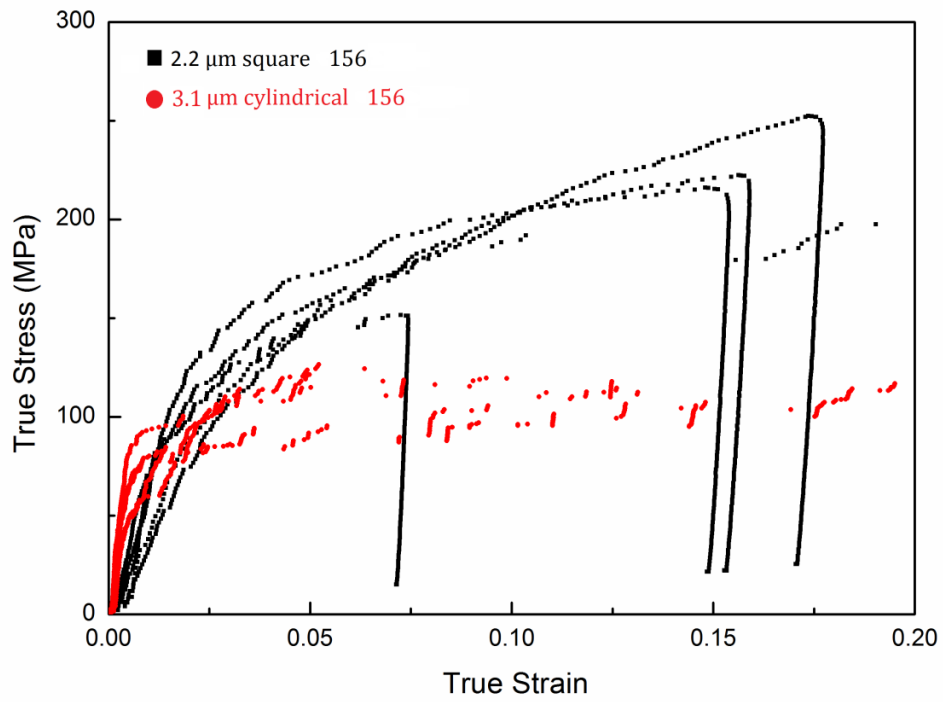

Figure 5-7 True stress-strain curves for 2.2 μm square and 3.1 μm cylindrical [156] single crystals
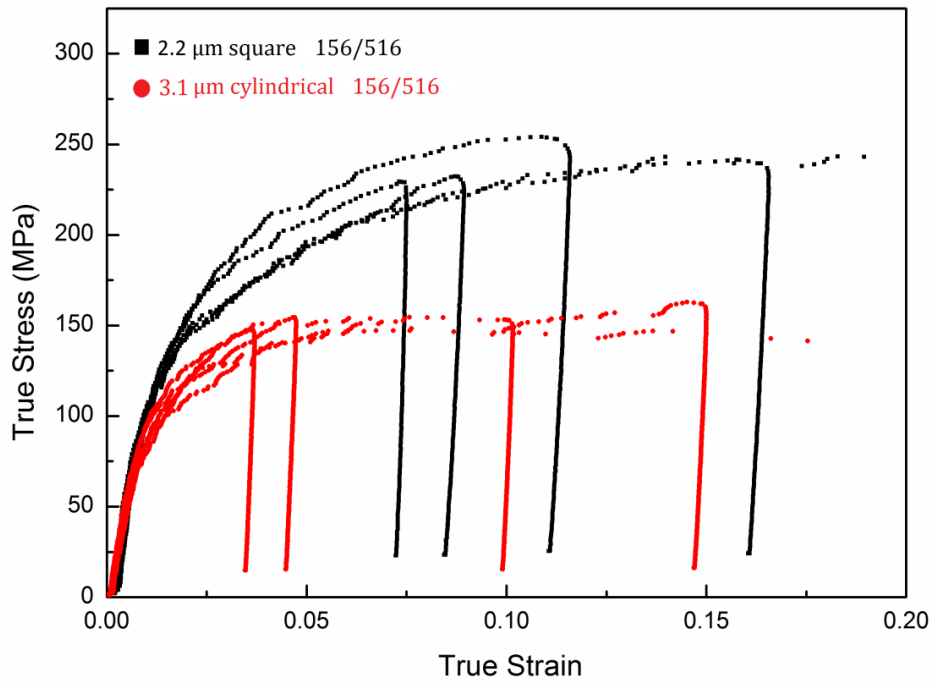
Figure 5-8 True stress-strain curves for 2.2 µm square and 3.1 µm cylindrical [156]/[516] twinned crystals
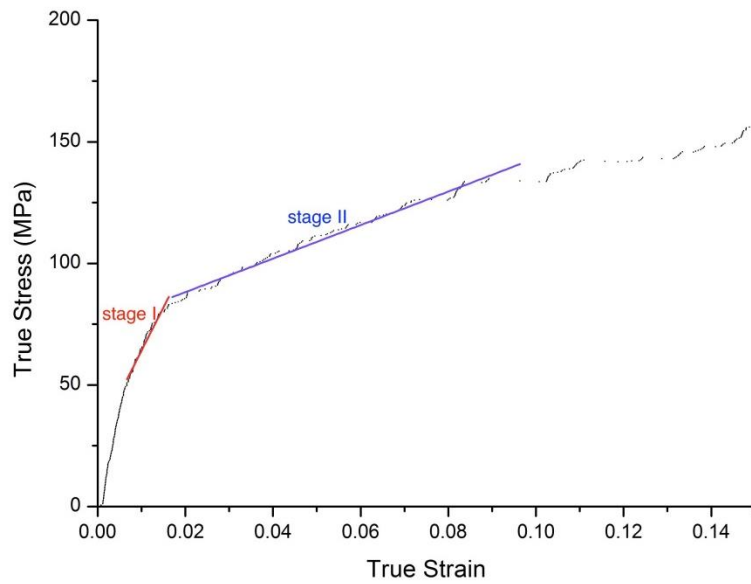
Figure 5-9 Typical linear fits for the calculation of work hardening rates of a stress-strain curve. Hardening is separated into Stage I and stage II via more accurate linear fitting
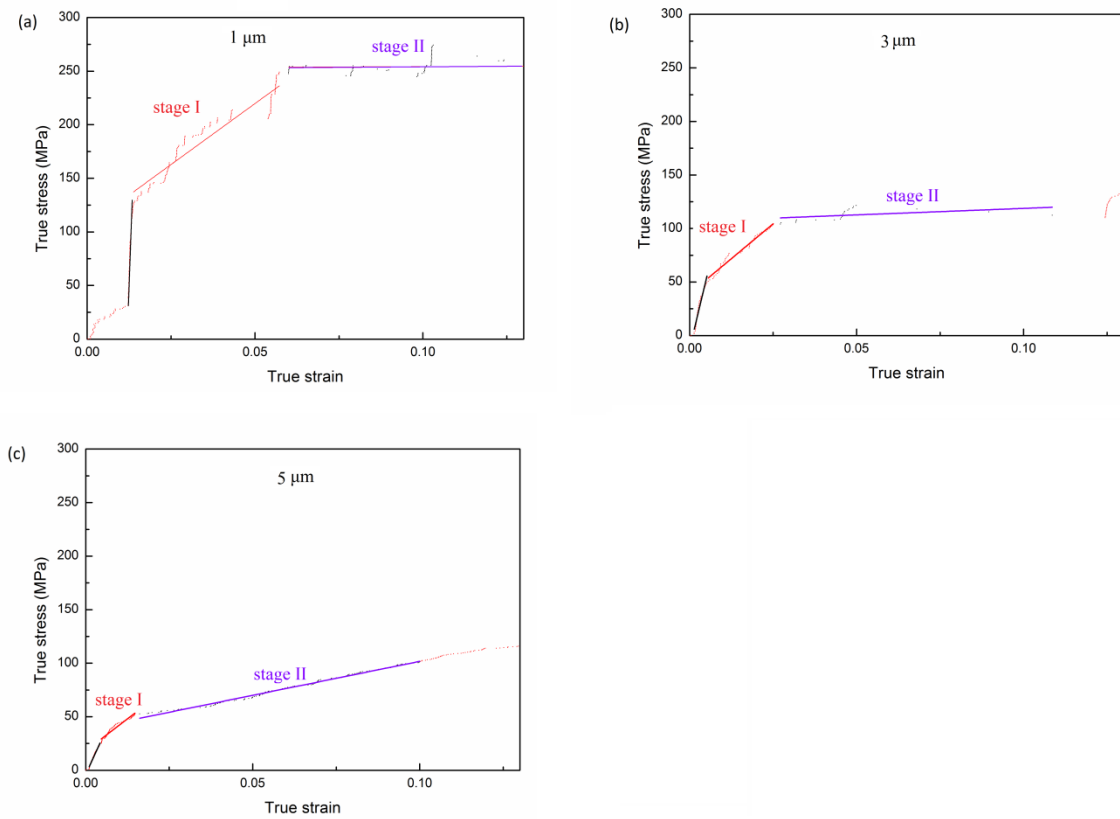
Figure 5-10 Illustration of Stages I and II in stress-strain curves of (a) 1 µm (b) 3 µm and (c) 5 µm [156] crystals

Figure 5-11 Hardening rate versus pillar diameter for [156] single crystal cylindrical pillars in (a) stage I and (b) stage II
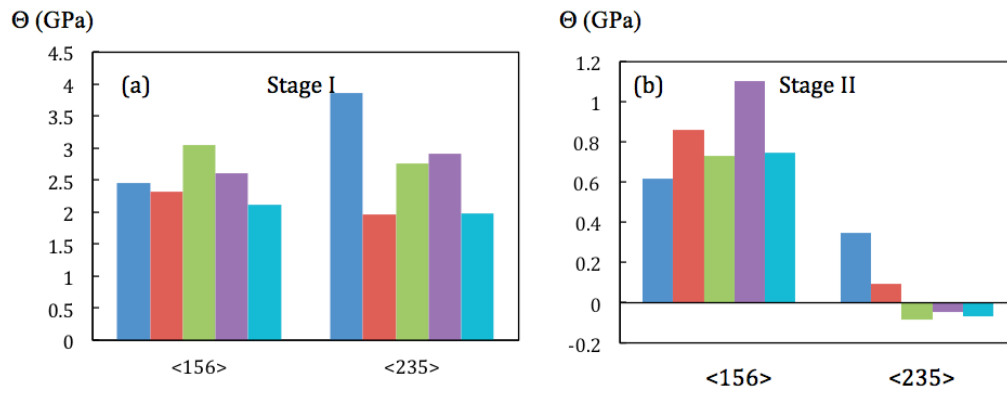
Figure 5-12 Comparison of hardening rates of 2.2 µm square [156] and [235] single crystals at a) stage I and b) stage II
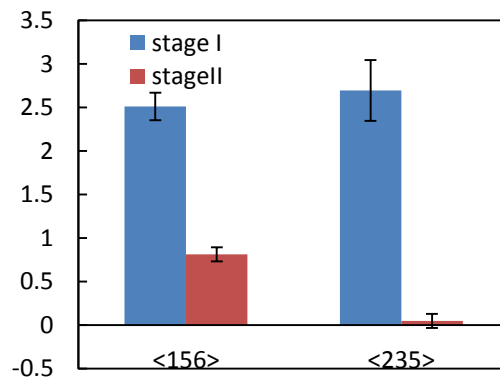
Figure 5-13 Mean hardening values of [156] and [235] single crystals in stage I and stage II. Error bars correspond to the standard error.
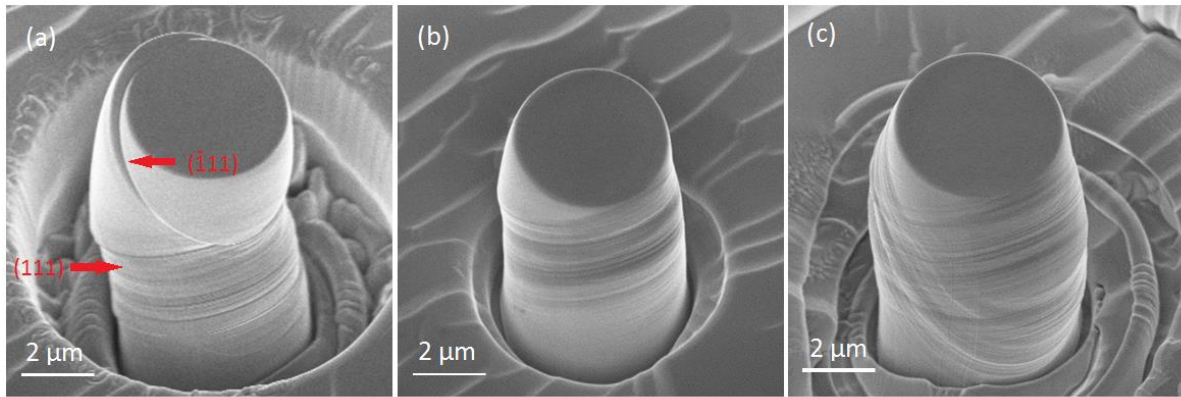
Figure 5-14 Representative SEM images of 5 μm diameter [156] cylindrical pillars deformed to (a) ~8.9% strain, (b) ~11.8% strain and (c) ~12.9% strain. Images were taken at a tilt angle of 30˚.

Figure 5-15 Representative SEM images of 3 μm diameter [156] cylindrical pillars deformed to (a) ~8.0% strain, (b) ~10.3% strain and (c) ~20.2% strain. Images were taken at a tilt angle of 30˚.
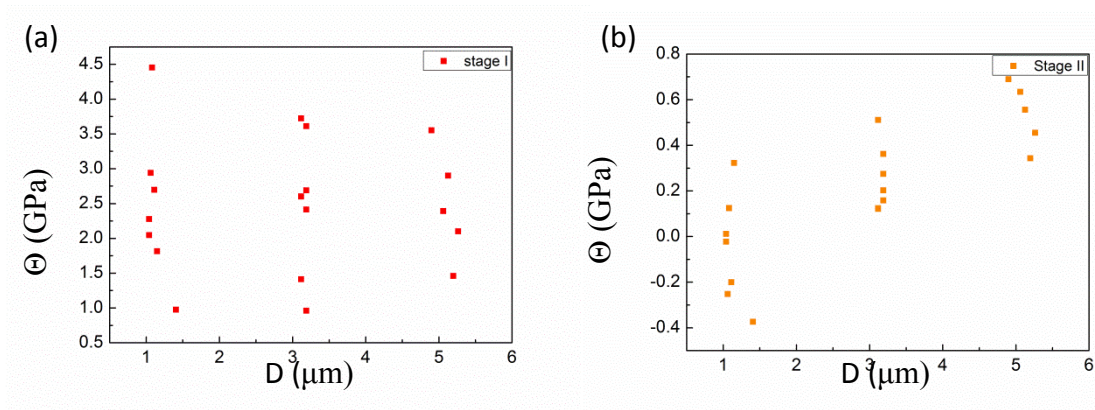

Figure 5-16 Representative SEM images of 1 μm diameter [156] cylindrical pillars deformed to (a) ~3.4% strain, (b) ~18.7% strain and (c) ~35.9% strain. Images were taken at a tilt angle of 30˚

Table 5-2 Schmid factor for [156] oriented crystals

Slip plane	Burgers vector $2b$	Schmid factor m
(111)	$[10\bar{1}]$	0.40
	$[0\bar{1}1]$	0.08
	$[\bar{1}10]$	0.32
$(\bar{1}11)$	$[101]$	0.46
	$[0\bar{1}1]$	0.07
	$[110]$	0.40
$(1\bar{1}1)$	$[011]$	0.14
	$[110]$	0.08
	$[10\bar{1}]$	0.07
$(11\bar{1})$	$[011]$	0
	$[\bar{1}10]$	0
	$[101]$	0

Figure 5-17 Stereographic projection showing {111} plane normals using sample section as the reference coordinate system
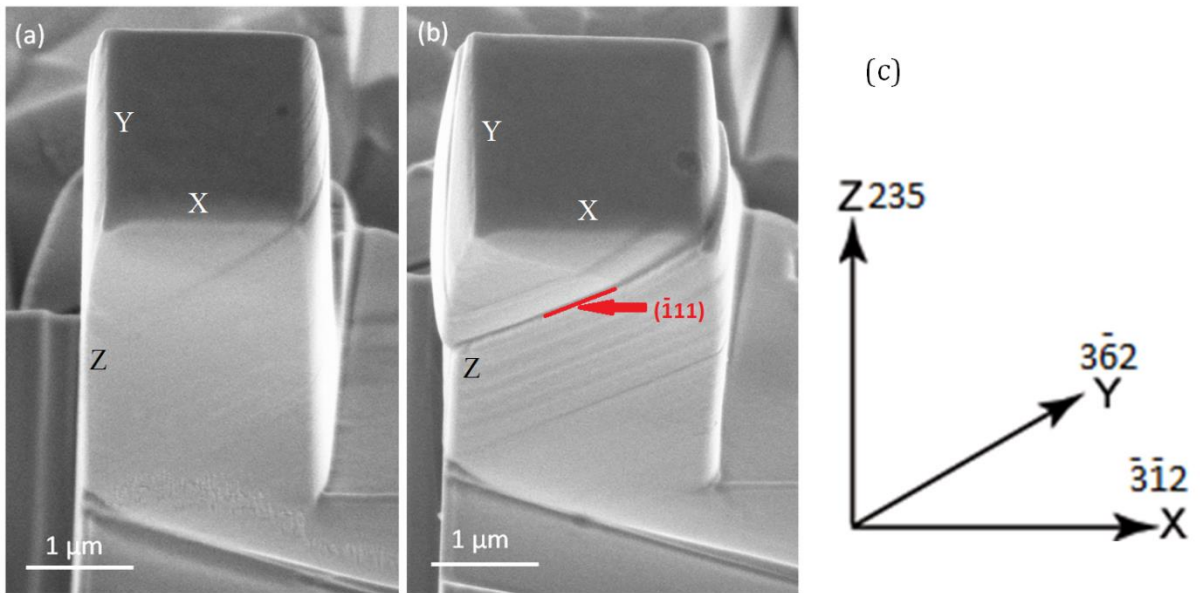
Figure 5-18 SEM image of [235] square pillars with a cross section of 2.2 μm × 2.2 μm with (a) 3.9% strain and (b) 14.0% strain. Images were taken at a tilt angle of 30˚. (c) Corresponding coordination system labelled with crystal orientation obtained from EBSD.
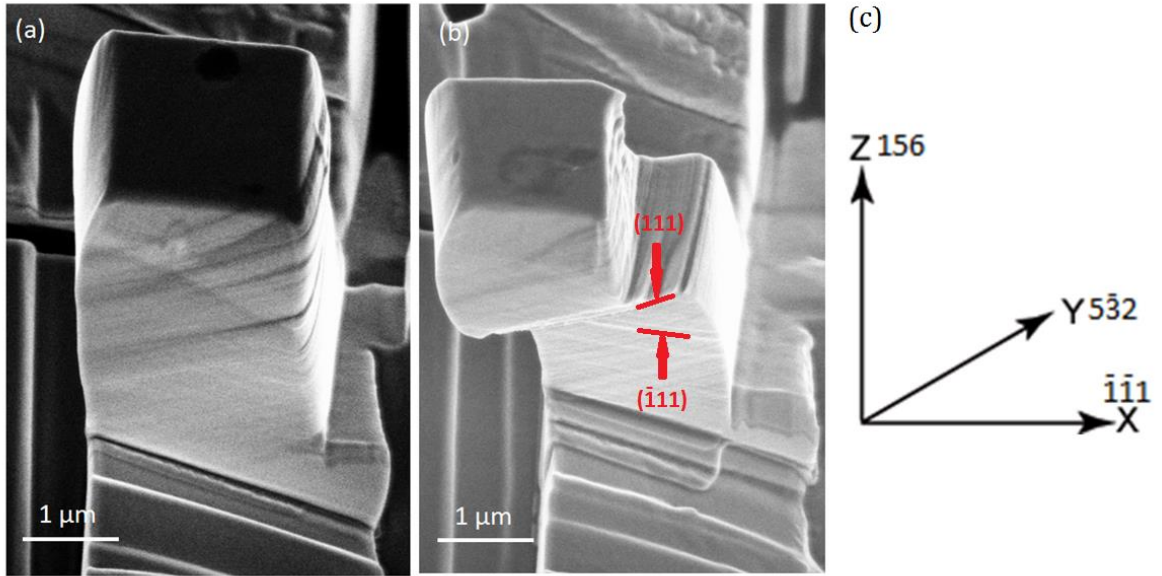
Figure 5-19 SEM image of [156] square pillars with a cross section of 2.2 μm × 2.2 μm after (a) 17.4% compression and (b) 30.6% compression. Images were taken at a tilt angle of 30˚. (c) Corresponding coordinate system labelled with crystal orientation obtained from EBSD.
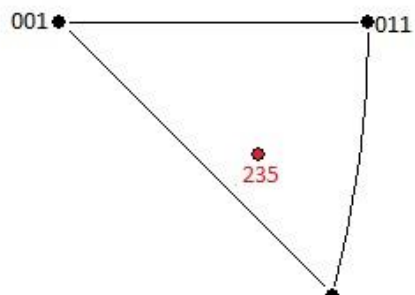
Figure 5-20 unit triangle containing [235] direction
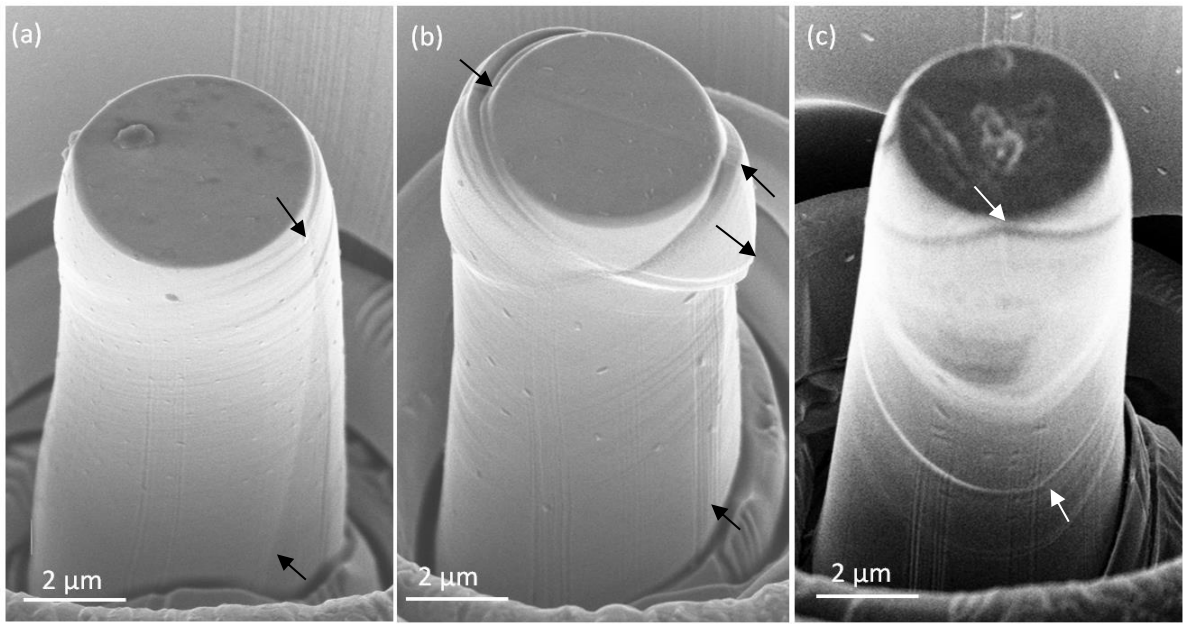
Figure 5-21 Representative SEM images of 5 μm diameter [156]/[516] cylindrical pillars deformed to (a) ~8.7% strain, (b) ~9.0% strain and (c) ~9.1% strain. Images were taken at a tilt angle of 30˚; the arrows indicate the twin boundary.
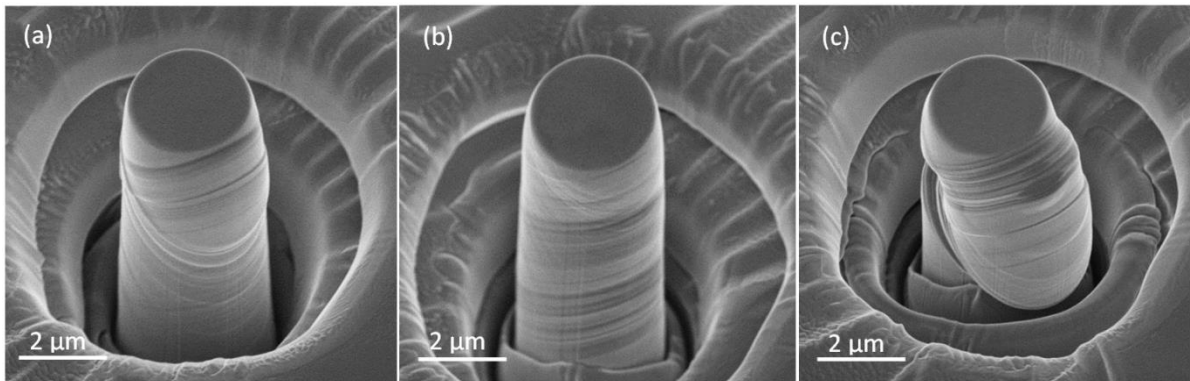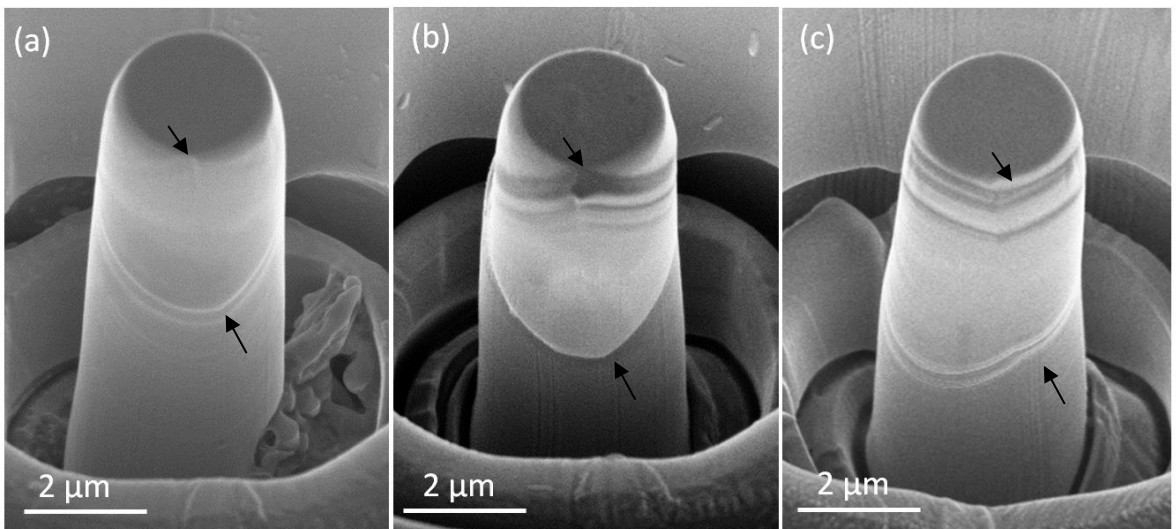

Figure 5-22 Representative SEM images of 3 μm diameter [156][/516] cylindrical pillars deformed to (a) ~8.9% strain, (b) ~11.8% strain and (c) ~12.9% strain. Images were taken at a tilt angle of 30˚; the arrows indicate the twin boundary position
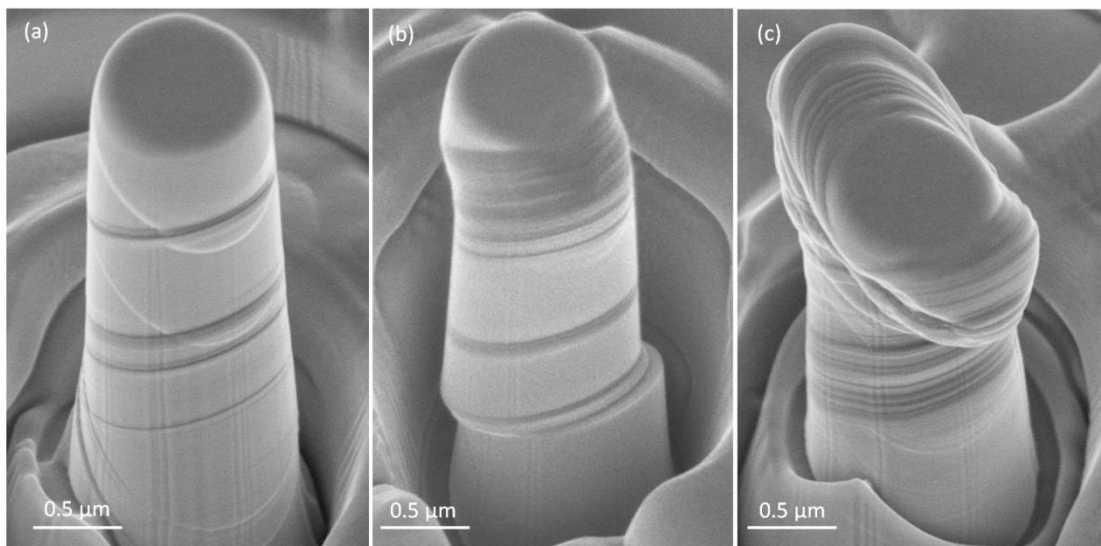
Table 5-3 Schmid factor for [516] oriented crystals

Slip plane	Burgers vector 2b	Schmid factor m
(111)	$[10\bar{1}]$	0.08
	$[0\bar{1}1]$	0.40
	$[\bar{1}10]$	0.32
($\bar{1}11$)	$[101]$	0.14
	$[0\bar{1}1]$	0.07
	$[110]$	0.08
($1\bar{1}1$)	$[011]$	0.46
	$[110]$	0.40
	$[10\bar{1}]$	0.07
($11\bar{1}$)	$[011]$	0
	$[\bar{1}10]$	0
	$[101]$	0
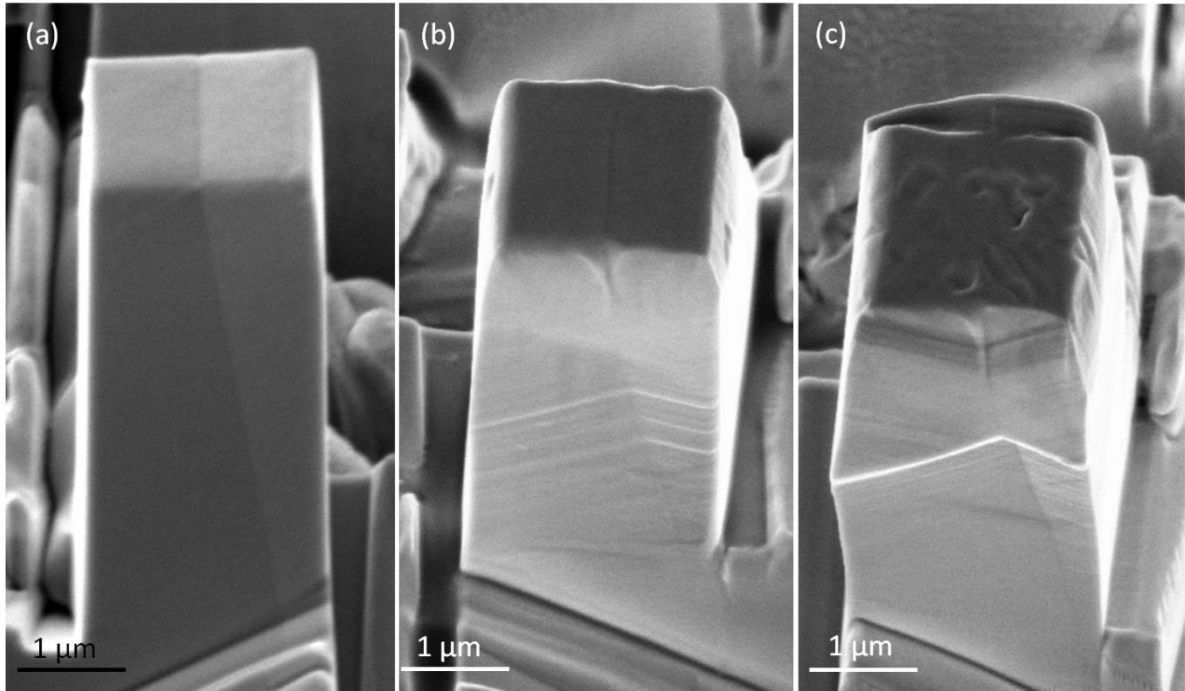
Figure 5-23 Representative SEM images of [156]/[516] square pillars with the twin boundary roughly in the centre. (a) Undeformed pillar taken at 52° tilt. (b) Mildly deformed pillar (~7.3% strain) taken at 30° tilt and (c) severely deformed pillar (~15.8% strain) taken at 30° tilt.
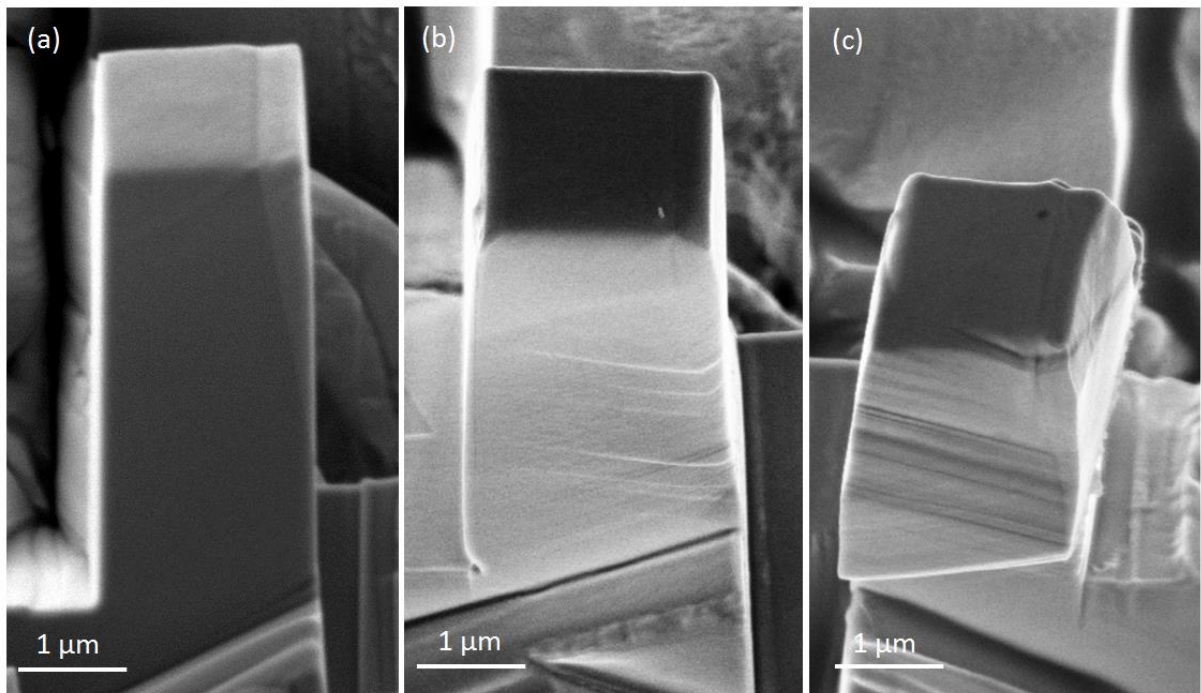
Figure 5-24 Representative SEM images of [156]/[516] square pillars with the twin boundary close to the edge. (a) Undeformed pillar taken at 52° tilt. (b) Mildly deformed pillar (~4.2% strain) taken at 30° tilt and (c) severely deformed pillar (~22.5% strain) taken at 30° tilt.

Chapter 6 Dislocation analysis

In this chapter the dislocation characters, densities and distributions in compressed as well as undeformed pillars are presented. These observations provide a firm experimental basis from which to deduce the deformation mechanisms of Cu pillars at the micron scale.

6.1 Undeformed Cu pillar

To assess the evolution of dislocation structures during deformation, knowledge of the initial dislocation arrangement in the undeformed sample is indispensable. To this end, a thin foil was extracted from an undeformed 2.6 μm micropillar and was then observed by STEM. Bright-field STEM images using one of the {111} reflections (which are the reflections frequently adopted in the subsequent examination of the deformed specimens) are shown in Figure 6-1 (a). From now on, all the montage STEM/TEM images are aligned such that the pillars stand on the substrate, i.e., the pillar top is the upper part of the image and the pillar base is the lower part. It is clear that the dislocations are non-uniformly distributed inside the pillar; some regions contain a relatively high density of dislocations while others are completely free of dislocations. Therefore, various initial dislocation distributions may exist in different micropillars, and this contribute to the scatter of their mechanical behaviour.

The dislocation density was calculated using the following equation [48]:

$$\rho = \frac{L}{V} = \frac{L}{At}$$

where L is the total length of the dislocation lines, V is the volume of the specimen, A is the

surface area and t is the foil thickness.

The dislocations were manually traced using Image J software, as shown in Figure 6-1(b). The length of each dislocation line was measured; hence the total length was obtained. Foil thickness was measured directly inside the FIB using SEM imaging. The initial dislocation density ρ_0 was determined to be $\sim 1.2 \times 10^{13} \mathrm{m}^{-2}$ from Figure 6-1(a). As the $\{111\}$ reflections only reveal half the dislocations, the starting dislocations are calculated to be $\sim 2.4 \times 10^{13} \mathrm{~m}^{-2}$ after corrected for the fraction of invisible ones under the used imaging condition. This value agrees with a similar study using the same sample preparation method [23], in which the density measurements ranged from $5.5 \times 10^{12} \mathrm{~m}^{-2}$ to $1.6 \times 10^{13} \mathrm{~m}^{-2}$.

6.2 Deformed [156] single crystal cylinder

6.2.1 1-μm [156] single crystal cylinder

A TEM foil obtained from a 1-μm single crystal pillar with 3.3% strain was extracted along the loading axis, in the way shown in Figure 6-2. The HKL channel 5 software gave the indices of the x, y, and z axes in the sample coordinate system after the EBSD acquisition was imported, see Figure 6-3. As illustrated in Figure 6-2, the foil normal corresponds to the y direction ($[\bar{5}\bar{3}3]$), and the pillar top corresponds to the z direction ([156]). The indices of the TEM sample must be consistent with this EBSD data. Zone axes close to the foil normal are identified in the stereographic projection in Figure 6-4. The nearest low index zone axis is $[\bar{2}\bar{1}1]$, whose diffraction pattern can be indexed unambiguously after identifying the 022 diffraction spot, as the pillar top orientation is close to the [011] direction. A Kikuchi pattern from this sample is sketched in Figure 6-5. By using this method, all the TEM samples were

indexed consistently, leading to consistency also of the Burgers vector analyses throughout the project.

The Schmid factors of the 12 slip systems for the [156] pillar are listed in Table 6-1, in which the four slip systems with the most high Schmid factors are highlighted in red. From now on, dislocations on slip systems having the highest Schmid factor are referred as primary dislocations and others as secondary. Table 6-2 lists the diffraction conditions adopted to image the dislocations in this deformed pillar cross section. The visibility of the dislocations in the four slip systems with the highest Schmid factors and the remaining two Burgers vectors are marked in the table, where ✓ means visible, ★ means edge-on when visible and ✗ means invisible.

STEM images using the above two-beam conditions are shown in Figure 6-6. Apart from the knot of dislocations in the top right corner, only a few are present in most of the sample. g·b analysis was carried out on these well separated dislocations, which were then classified into five different sets and labelled individually in the images. According to Table 6-2, set 1 dislocations have a Burgers vector $\frac{1}{2}[101]$ and may lie on $(\bar{1}\bar{1}1)$ or $(\bar{1}11)$. As the dislocations are not in the edge-on condition in Figure 6-6(a), they must be on $(\bar{1}\bar{1}1)$ (unless they are grown-in dislocations), on which there is no resolved shear stress because the plane is parallel to the loading axis [156]. Set 2 dislocations have a Burgers vector $\frac{1}{2}[0\bar{1}1]$, almost perpendicular to the pillar's loading axis and again with a negligible resolved shear stress. Set 3 dislocations have a Burgers vector $\frac{1}{2}[10\bar{1}]$ and lie either on (111) or on $(1\bar{1}1)$. If lying on $(1\bar{1}1)$, they should have been edge-on in Figure 6-6(b). Hence set 3 dislocations are

107

$\frac{1}{2}(111)[10\bar{1}]$ type, having a high Schmid factor of 0.4. Set 4 dislocations have a Burgers vector $\frac{1}{2}[\bar{1}10]$, which may glide on (111) or ($\bar{1}\bar{1}1$). Again, this dislocation line does not appear to be edge-on in Figure 6-6(d), so it must lie on ($\bar{1}\bar{1}1$), the same as set 1. The last set of dislocations have a Burgers vector $\frac{1}{2}[011]$, which is nearly parallel to the loading axis. It possesses either none or very small resolved shear stress, depending on the slip plane. In conclusion, apart from set 3 dislocations, all the others should be immobile as they cannot be driven by the applied stress. Set 3 dislocations belong to one of the active slip systems: $\frac{1}{2}(111)[10\bar{1}]$. The dislocation density of this slip system was measured to be $\sim 8.8 \times 10^{12}\mathrm{m}^{-2}$, which is comparable with the initial dislocation density.

The SEM image of this deformed pillar is shown in Figure 6-7, which clearly shows two operative slip planes. Slip is more active on (111) than on ($\bar{1}11$). In terms of conventional plasticity, a well-developed dislocation network is expected inside this sample, as slip on different systems is activated. However, this is not the case from our STEM observations. Only a few dislocations remain inside the crystal, together with the immobile pre-existing ones. This result therefore suggests that the majority of the mobile glide dislocations have left this small pillar. This observation supports the dislocation starvation theory proposed by Greer et al. [15], in which the increased strength of microcrystals is attributed to escape of the dislocations.

6.2.2 3-μm [156] single crystal cylinder

A TEM foil extracted from a 3-μm [156] oriented pillar with 7.8% compressive strain was examined under various diffraction conditions, as summarized in Table 6-3. When choosing

the reflection g vectors, we usually select three different {111} beams, which are sufficient to determine the Burgers vectors. Here two extra g vectors are used to display the edge-on image of some dislocations. Note that Table 6-3 is different from Table 6-2, because the TEM foils of the two samples were not extracted from the same position. BF-STEM images are shown in Figure 6-8. Some of the dislocations are edge-on, for example the $\frac{1}{2}(\bar{1}11)[101]$ type dislocations are edge-on in (a), they align along the $(\bar{1}11)$ trace; the $\frac{1}{2}(\bar{1}11)[110]$ type dislocations are edge-on in (d), and they lie along the (111) trace; while in (e), both the $\frac{1}{2}(111)[10\bar{1}]$ and the $\frac{1}{2}(\bar{1}11)[110]$ type dislocations are edge-on and parallel to the (111) trace.

The dislocation structure was significantly different from that in the 1-μm sample. Owing to the taper, the pillar top was more heavily stressed and consequently the dislocations are too dense to be differentiated from each other. However, incipient dislocation cells are quite evident in most of the sample, especially in Figure 6-8 (e). The cell walls are composed of massively tangled dislocations while the cell interiors are relatively dislocation-free. The average cell diameter in this sample is about 1 μm. The cell size is defined by its mean diameter, i.e., the square root of the interior area of each cell. To our knowledge, this is the first study showing the presence of dislocation cells inside deformed microcrystals. Dislocations at the bottom of the specimen are less tangled as there are fewer dislocations. The dislocation arrangement is also in line with the SEM observation of this deformed pillar, presented in Figure 6-9, which shows that the deformation took place mainly in the upper part of the pillar. This dislocation substructure is consistent with that in Stage II glide of bulk samples. Hence the result indicates that for copper microcrystals over 3-μm in diameter, the

dislocation arrangement is similar to that in conventional (bulk) plasticity.

To analyse the dislocation distribution between individual slip systems, the dislocations were colour-coded using Photoshop. Table 6-4 lists the colour chosen for each system. To begin with, we focus on the bottom right region of the specimen, as most dislocations in this area are separated from each other. BF-STEM images under three different two-beam conditions are shown in Figure 6-10. With the help of Table 6-3, $\frac{1}{2}(111)[10\bar{1}]$ type dislocations are labelled in (a), $\frac{1}{2}(111)[\bar{1}10]$ and $\frac{1}{2}(\bar{1}11)[101]$ type dislocations in (b) and $\frac{1}{2}(\bar{1}11)[110]$ type dislocations in (c).

To assess the edge or screw character of the dislocations, the Burgers vector orientations are projected next to the STEM images in Figure 6-10. The beam direction in (a) is [110] and the angle between the (111) slip plane and the (110) projection plane is 35°. The projections of the three Burgers vectors on this (111) plane have been drawn by the side of the STEM image. If the direction of dislocation lines is parallel with the projection of the corresponding Burgers vector, the dislocations are screw type; if perpendicular, they are edge type; all the other ones are mixed type. The red dislocations labelled in (b) are also visible in (a). Their line vectors are close to the $[1\bar{1}0]$ direction (Burgers vector direction), so the red dislocations are screw type. The blue dislocations seem to have a screw character in this figure, but they are actually quite mixed when we look at the whole sample area later. Similarly, we draw the projections of the three Burgers vectors on $(1\bar{1}\bar{1})$ in (b) and (c), as this slip plane is also 35° away from the $(10\bar{1})$ projection plane. From these two figures we conclude that most of the yellow dislocations are screw while the purple ones are mixed.

110

The dislocations in the montage images in Figure 6-8 (b), (c) and (d) are then traced to reveal their distribution across the sample (except for the pillar top). The results are merged into one picture, shown in Figure 6-11 (note, only the distinguishable ones were marked, as those in the cell walls and tangles are too dense to analyse). The cell walls are also superimposed on this image and are sketched in solid black lines.

The primary dislocations, which are long yellow lines in the figure, are screw type. For secondary dislocations, most of the red ones are also screw, while the purple and blue ones are quite mixed. The existence of many screw dislocations is unexpected and is in contradiction with the report of Prinze and his co-workers [86], who observed very few screw dislocations in their cell structure.

The long thick wall of the dislocation cells, as indicated by the arrow in Figure 6-11, is aligned parallel to the primary edge orientation.

6.2.3 5-μm [156] single crystal cylinder

An SEM micrograph of a heavily deformed 5-μm [156] oriented pillar is displayed in Figure 6-12 and TEM micrograph in Figure 6-13. The dislocation density has increased significantly due to the more severe deformation (18% strain). The specimen is rather deformed and so imaging the whole of it at once is impossible, as shown in Figure 6-13: the bottom part is out of contrast owing to the change of diffraction condition. Therefore, we focused on the black oval area marked on the picture to perform the dislocation analysis. In addition, dense primary dislocation arrays are observed in the region marked with a red rectangle. Their interaction with secondary dislocations is found in the purple rectangle, where the dislocation tangles are

presented.

Again, all the diffraction conditions are summarized in Table 6-5. The corresponding images are displayed in Figure 6-14, in which some dislocations are edge-on in each of (a), (b), (d) and (f). Similar to the approach we adopted in the previous section, the projection lines of Burgers vectors are drawn to the right of (c)~(f). Figure 6-15 illustrates the distribution of dislocations on different slip systems within the tangled area. (The blue ones were traced from (c), the yellow and purple ones from (e) and the red ones from (f)). Similarly to the earlier described 3-μm sample, most of the yellow and red dislocations are screw type, while the blue and purple ones are mixed.

6.3 [156] oriented single crystal square pillar

The TEM assessment of a [156] square pillar was carried out on a sample deformed to 2.3% strain. Table 6-6 lists the diffraction conditions. Figure 6-16 contains the TEM images taken under the above conditions. Slightly tangled dislocations are formed within the sample. Discernible dislocations belonging to different slip systems within the square are colour-coded and displayed in Figure 6-17. It is clear that all the four slip systems predicted on the basis of Schmid factors (Table 6-1) are activated and no others.

Excepting the pre-existing dislocations, all the ones developed via deformation are revealed in Figure 6-16 (b) and (c) with perfect complementary according to Table 6-6, i.e, the images present all the dislocations without repetition. Thus to calculate the dislocation density, the dislocation lines in these two figures were traced and measured using Image J, as shown in Figure 6-18. The densities are measured to be $5.6 \times 10^{13}\ \mathrm{m}^{-2}$ and $5.4 \times 10^{13}\ \mathrm{m}^{-2}$

respectively. Hence the total density within the sample is about 1.1×10^{14} m^{-2}, which is an order of magnitude higher than the 10^{13}m^{-2} initial dislocation density in the undeformed sample.

6.4 [235] oriented single crystal square pillar

Dislocation analysis of a [235] oriented single crystal square pillar was carried out on a specimen deformed to 3.9% strain. Schmid factors for the 12 slip systems are calculated and listed in Table 6-7; the systems with the four largest Schmid factors are in red. $\frac{1}{2}(\bar{1}11)[101]$ has the largest Schmid factor and thus is regarded as the primary slip system. Table 6-8 summarizes the visibility of the dislocations under the diffraction conditions adopted.

The dislocations were well separated and more uniformly distributed than the arrangements in the other types of pillar, as shown in Figure 6-19. Note that the bottom half of the foil was amorphized during FIB thinning and so was ignored when analysing the dislocations. The relatively long dislocation lines are found in all three images and hence they belong to the primary slip system, according to Table 6-8. The three Burgers vectors on the $(\bar{1}11)$ primary slip plane are projected to the image plane of Figure 6-19 (a). The line vectors of these long dislocations are close to the [101] direction, indicating that they are screw type. Some of them have steps, as labelled in the picture. This may result from cross-slip between adjacent planes. The short and almost vertically oriented dislocations near the pillar top might be caused by the complex stress status in that area, where friction forces between the top surface and the indenter play a certain role. A few other dislocations, unexpected from the Schmid factor calculation, are found in Figure 6-19 (b) and (c), as indicated by the arrows. These dislocations are perhaps pre-existing ones, introduced before deformation. Dislocation pile-

ups are not observed across the sample, proving that these dislocations belong to one slip system only. The result is in accord with the SEM observation of the deformed pillar surface, where only parallel slip planes are found, as seen in Figure 6-20.

The dislocation density was measured to be 5.2×10^{13} m^{-2} in Figure 6-19(a) using Image J. This value is ~4 times higher than that for the undeformed sample measured in 5.1. It is only about half the density measured from its counterpart oriented in [156] direction which was analysed in 5.3, despite the fact that the latter was deformed to a lower strain of 2.3%.

6.5 Deformed [156]/[516] twinned cylinder

The EBSD derived crystal orientations across the twin boundary from which the twinned pillars were milled are presented in Figure 6-21. The indices of the x, y, and z axes in the sample coordinate system for the composed crystals are $x \sim [3\bar{2}\bar{2}], y \sim [25\bar{2}], z \sim [516]$ for the left 516 grain and $x \sim [\bar{5}5\bar{3}], y \sim [\bar{5}\bar{3}3], z \sim [156]$ for the right 156 grain. Note that the coordinate system is automatically indexed by the EBSD software and may not be exactly orthogonal.

The <111> pole figures for these two crystals are plotted in Figure 6-22. The position of the $[\bar{1}11]$ pole in the 516 grain coincides with the $[1\bar{1}1]$ pole in the [156] grain, indicating that the $(\bar{1}11)$ plane on the left and the $(1\bar{1}1)$ plane on the right are the common twinning plane of the pillars.

6.5.1 3-μm [156]/[516] twinned cylinder

A TEM foil was extracted from a 3-μm [156]/[516] twinned cylindrical pillar with 4.6%

strain.

Table 6-9 lists the visibility of the dislocations under the chosen diffraction conditions in the [516] oriented crystal on the left. Figure 6-23 presents the BF-STEM images in the same sequence of diffraction conditions in the above table. Note, the dislocations in the right hand [156] crystal are also in contrast in (b) and (d) because the g vector here is perpendicular to the common twinning plane. The projections of the Burgers vectors onto $(1\bar{1}1)$ and (111) have been sketched in (a) (b) and (c) (d) respectively. It can be seen from the images that besides the isolated dislocations, most of the dislocations are tangled into continuous dislocation walls, which run throughout the pillar in various directions. Both dislocation-free regions (F) and carpets (C) of interactions with secondary dislocations appear along the dislocation walls (see Figure 6-23 (a)). Also, it has been noted that more dislocation-free regions are found between the dislocation walls and the twin boundary in all the STEM images.

Similarly to the strategy adopted in 6.2, those distinguishable dislocations belonging to different slip systems were traced and colour-coded, and then merged into one picture in Figure 6-24. It is clear that the dislocations belong to the four slip systems with the highest Schmid factors. Referring back to the Burgers vector projections in Figure 6-23(a), (c) and (d), it is found that most of the yellow and red dislocations are screw dislocations while the purple and blue ones are mixed.

Table 6-10 summarizes the diffraction conditions for the [156] oriented crystal. The corresponding STEM images are presented in Figure 6-25. Dislocation bundles developed in the top half of the pillar, where there is more space between the inclined twin boundary and

115

the free surface as compared to the bottom. Individual dislocation lines are abundant as well, especially the long ones near the pillar top (Figure 6-25 (a), (c) and (d)). Some of them were terminated by a dislocation tangle, which hindered the dislocation movement. The colour-coding for this [156] oriented grain in Figure 6-26 shows the distribution of the dislocations from the four slip systems listed in Table 6-10. The long dislocations prevailing in the top part belong to the primary slip system coloured in yellow and are screw dislocations according to its Burgers vector projection in Figure 6-25 (c). The remaining dislocations from the secondary slip systems are somewhat mixed.

In each constituent grain, two of the four sets of activated dislocations are parallel to the twin boundary plane and thus are shared by both grains. As seen in Figure 6-27, ACD and B′C′D′ corresponds to the twin boundary plane in the [516] grain and the [156] grain. Therefore Burgers vectors CD (C′D′) and CA (C′B′) in the [516] grain can easily glide into the [156] grain by cross-slip.

Reviewing the pictures for both crystals, we find that there is a certain accumulation of dislocations at the twin boundary, especially for those in the right hand crystal. (Figure 6-23(b), (d) and Figure 6-25). Both dislocation walls/tangles and individual dislocations terminate at the twin boundary, no penetration was observed.

6.5.2 5-μm [156]/[516] twinned cylinder

The dislocations within a 5-μm cylindrical twinned pillar deformed to 5.8% strain were analysed. Table 6-11 summarizes the diffraction conditions for the left hand [156] oriented grain, and the corresponding STEM images are displayed in Figure 6-28. Although the left

hand grain also occupies a larger portion of the whole pillar like in the previously analysed 3-µm sample, the well-defined continuous dislocation walls found in the smaller sample were not observed here. Instead, there are separate dislocation clusters, more individual dislocations and fewer dislocation-free areas. Due to the dense dislocation arrangement in the pillar top and amorphized area at the bottom, only dislocations within the rectangle marked in Figure 6-28 (a) were traced and colour-coded for different slip systems. Figure 6-29 shows the colour-coded dislocations. Again, dislocations from the four slip systems with the highest Schmid factors were all encountered. The yellow primary dislocations seem to be predominant, some of which are screw while others are mixed (see the projection of the 101 direction in Figure 6-28 (a)).

Table 6-12 and Figure 6-30 present the result for the right hand [516] oriented grain. Generally speaking, a dislocation cell structure is evident in this grain, as can be seen from Figure 6-30 (b) and (c). In the upper half of the foil, where the pillar was severely stressed, dislocations piled up against the twin boundary (Figure 6-30 (b)), while in the lower region where there are fewer dislocations, the twin boundary and the tangled dislocation clusters form enclosed cells, within which no dislocations can be found (Figure 6-30 (c)). The colour-coded dislocations for the area marked in Figure 6-30 (a) are displayed in Figure 6-31. Dislocations belonging to $\frac{1}{2}(1\bar{1}1)[110]$ system were not traced as they are only visible in Figure 6-30 (c), in which individual dislocations are too difficult to recognize. Again the primary yellow dislocations are found to be abundant; furthermore, blue ones are frequently seen near the dislocation walls.

6.6 Deformed [156]/[516] twinned square pillar

A 2.2 μm twinned square pillar deformed to 8.4% strain was fib-thinned and observed.

Table 6-13 outlines the diffraction conditions for the left hand [516] oriented grain and Figure 6-32 presents the corresponding STEM image. These images clearly show that several cells developed at the top while individual dislocations were revealed in the lower part. Again, colour-coding for the dislocations has been carried out and is shown in Figure 6-33. Only a few yellow primary dislocations were found while secondary dislocations from all the other three slip systems were frequently seen. The red dislocations which were traced from Figure 6-32 (d) are screw according to the projection of $[\bar{1}10]$ direction in that figure, while both the purple and the blue ones traced from Figure 6-32 (a) and (c) are mixed. The blue ones seem to be most commonly seen, and similarly to the last sample, they contributed to the formation of dislocation walls, indicated by the arrow in Figure 6-32(c).

Table 6-14 summarizes the imaging conditions for the right hand [156] oriented grain and the STEM images are presented in Figure 6-34. A dislocation cell structure prevails throughout most of the imaging area, with no dislocations within the cells. Again very few primary dislocations were seen according to the colour-coding in Figure 6-35, while secondary dislocations were often observed. The $\frac{1}{2}(111)[\bar{1}10]$ dislocations especially (which are the straight lines in Figure 6-34(d)), are widely distributed across the sample.

6.7 Summary

1. The dislocation distribution in the undeformed pillar is non-uniform; the initial

dislocation density was determined to be approximately $2.4 \times 10^{13} \mathrm{m}^{-2}$.

2. Although various slip traces belonging to different slip systems were observed in the **1-µm [156] single crystal cylinder**, only a few dislocation lines belonging to one of the active slip systems were identified. Most of the dislocations have left the sample before interaction and multiplication and thus no dislocation network developed.

3. The dislocation arrangement in a **3-µm [156] single crystal cylinder** with 7.8% strain is similar to that in stage II of a bulk sample, a dislocation cell structure with an average cell size of 1 µm. Dislocations from four different slip systems were identified: screw dislocations as well as mixed ones. A severely deformed 5-µm [156] single crystal shows a remarkable increase in dislocation density. The dislocation distribution for different slip systems in the analysed area is similar to that in the 3-µm [156] sample.

4. A **2.2-µm [156] square pillar** deformed to 2.3% strain displays slightly tangled dislocations stemming from the same four slip systems as in the [156] cylinders. The dislocation density was measured to be around $1.1 \times 10^{14} \mathrm{m}^{-2}$. A **[235] oriented square pillar** with the same size but deformed to 3.9% strain shows that well-separated long screw dislocations from the primary slip system are uniformly present across the sample. The corresponding dislocation density was determined to be $5.2 \times 10^{13} \mathrm{m}^{-2}$, only half that in the previous less deformed [156] square pillar with 2.3% strain.

5. Continuous dislocation walls run throughout the left hand [156] grain of a **3-µm [156]/[516] twinned cylinder** with 4.6% strain. Both dislocation-free regions and carpets were observed along the dislocation walls. Dislocations bundles developed in

the smaller right hand [156] grain and many individual dislocations were randomly distributed. Both dislocation walls/bundles and individual dislocation lines terminate at the twin boundary, suggesting the barrier effect of the interface. A similar phenomenon was found in a **5-µm [156]/[516] twinned cylinder** with 5.8% strain. Dislocations pile up against the twin boundary; some of the tangled clusters and the twin boundary even form an enclosed cell structure with absolutely no dislocations inside the cell.

6. A **2.2-µm [156]/[516] square pillar** deformed to 8.4% strain also shows clear dislocation cells in both of the grains. But, differently from the twinned cylinders, only a few primary dislocations belonging to the slip system with the highest Schmid factor were recognized: most of the dislocations arise from the secondary slip systems.
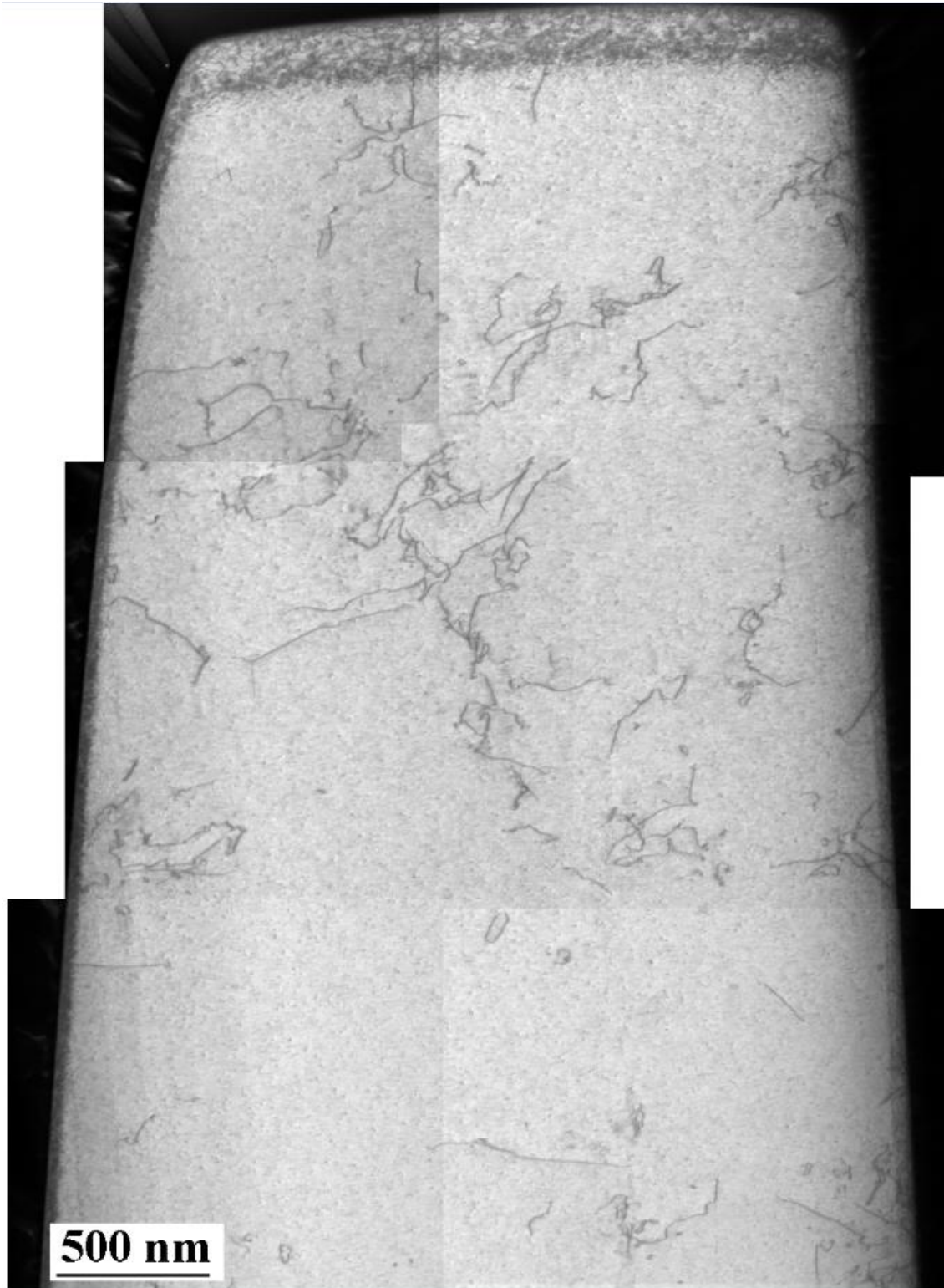
Figure 6-1(a) A bright field STEM image showing the dislocations in an undeformed crystal using one of the {111} reflections
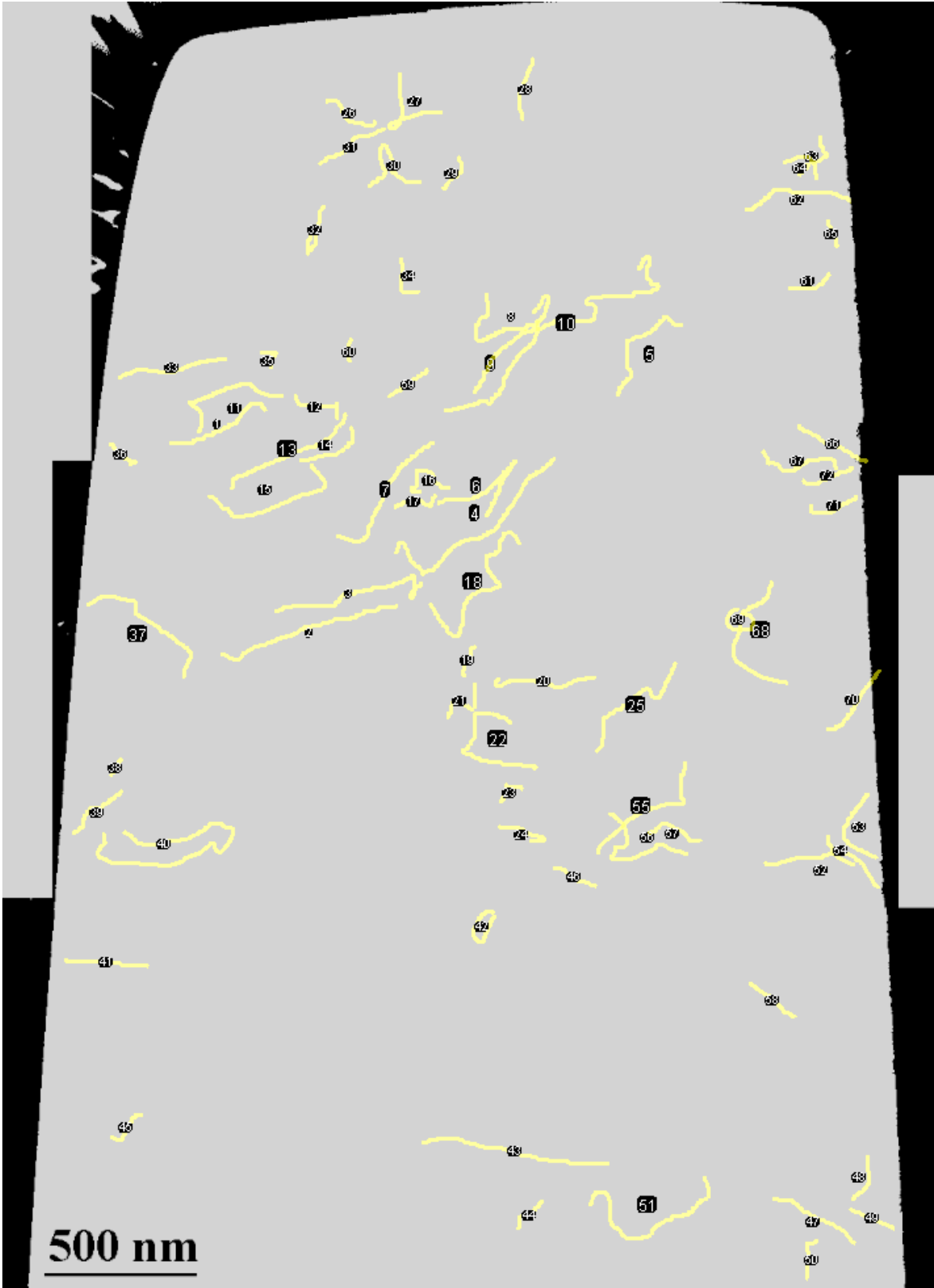
Figure 6-1 (b) All dislocation lines in (a) were traced using Image J software.
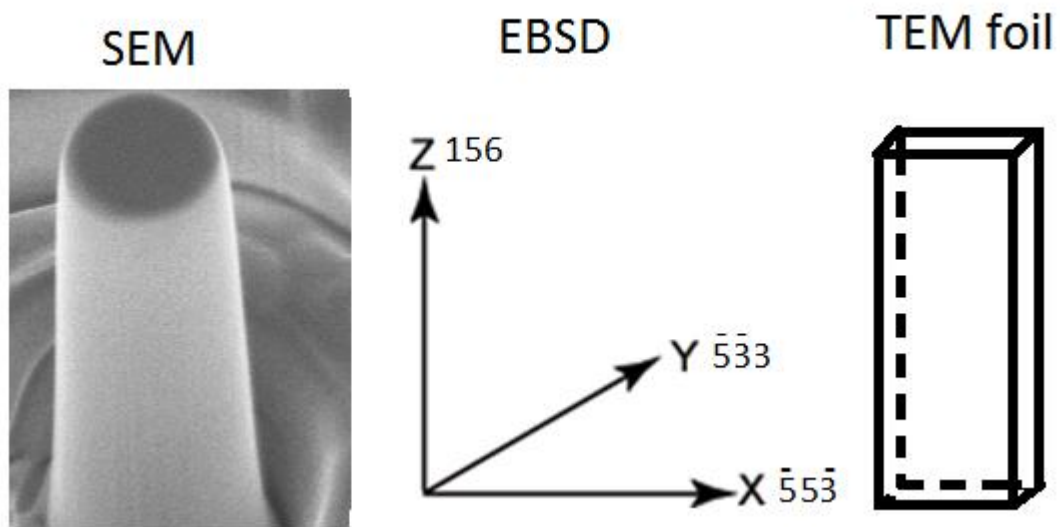
122

Figure 6-2 Schematic diagram showing the orientation determination of TEM foil according to EBSD data. Foil normal orientation corresponds to Y direction while pillar top orientation corresponds to Z direction.
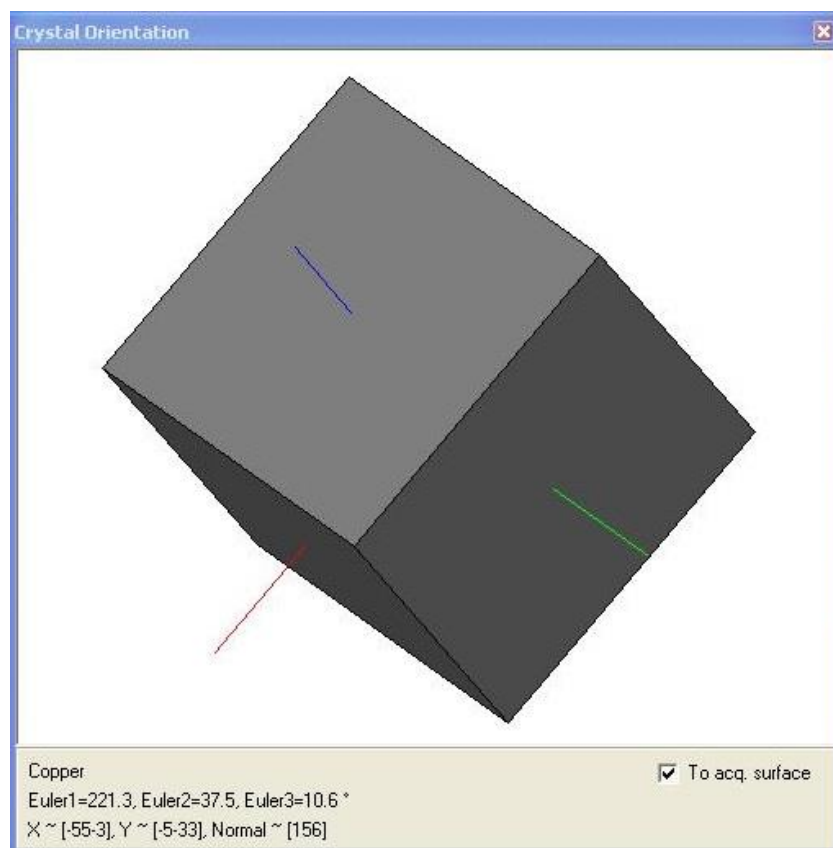

Figure 6-3 The indices of the x, y, and z axes at the foil-extraction location given by the HKL channel 5 software
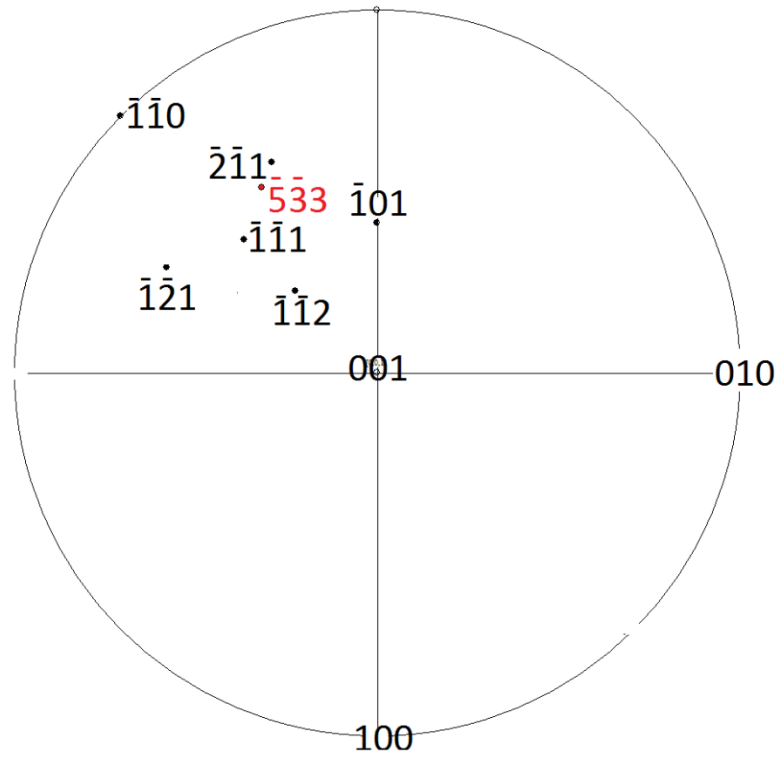
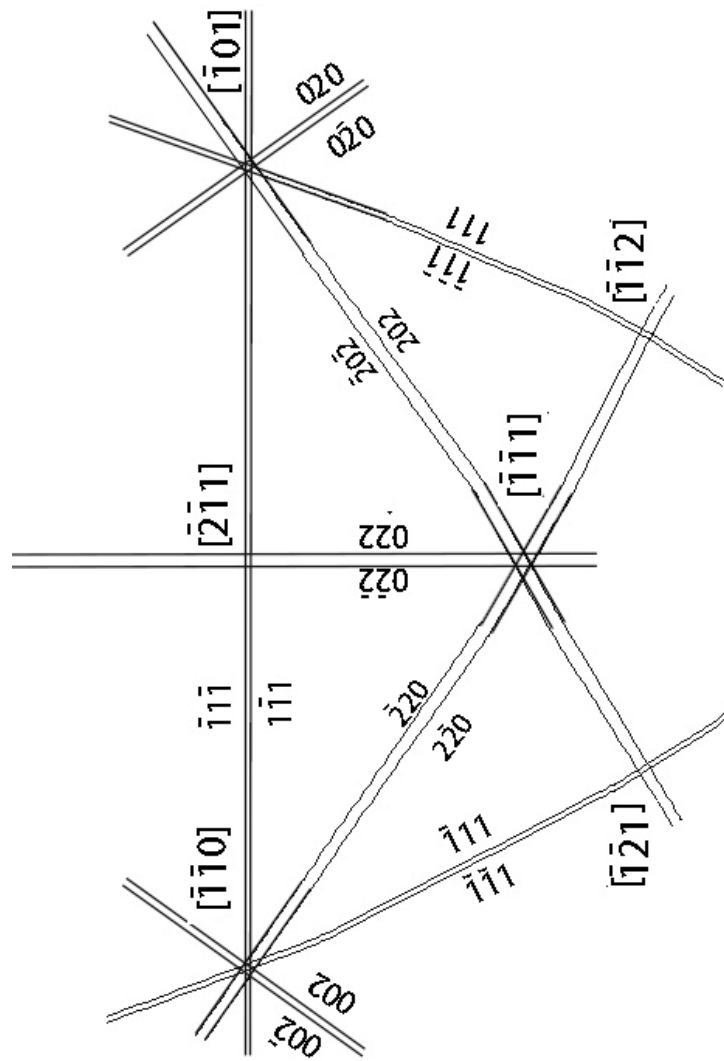**Figure 6-4 Stereographic projection showing the low-index zone axes close to the foil normal**

Figure 6-5 Kikuchi pattern of 1-μm [156] cylindrical crystal viewed along $[\bar{5}\bar{3}3]$

Table 6-1 Schmid factor of [156] oriented crystals

Slip plane	Burgers vector b	Schmid factor m
(111)	[10$\bar{1}$]	0.40
	[0$\bar{1}$1]	0.08
	[$\bar{1}$10]	0.32
($\bar{1}$11)	[101]	0.46
	[0$\bar{1}$1]	0.07
	[110]	0.40
(1$\bar{1}$1)	[011]	0.14
	[110]	0.08
	[10$\bar{1}$]	0.07
(11$\bar{1}$)	[011]	0
	[$\bar{1}$10]	0
	[101]	0

Table 6-2 Summary of the analysis of 1-μm [156] cylindrical crystal from different diffraction conditions

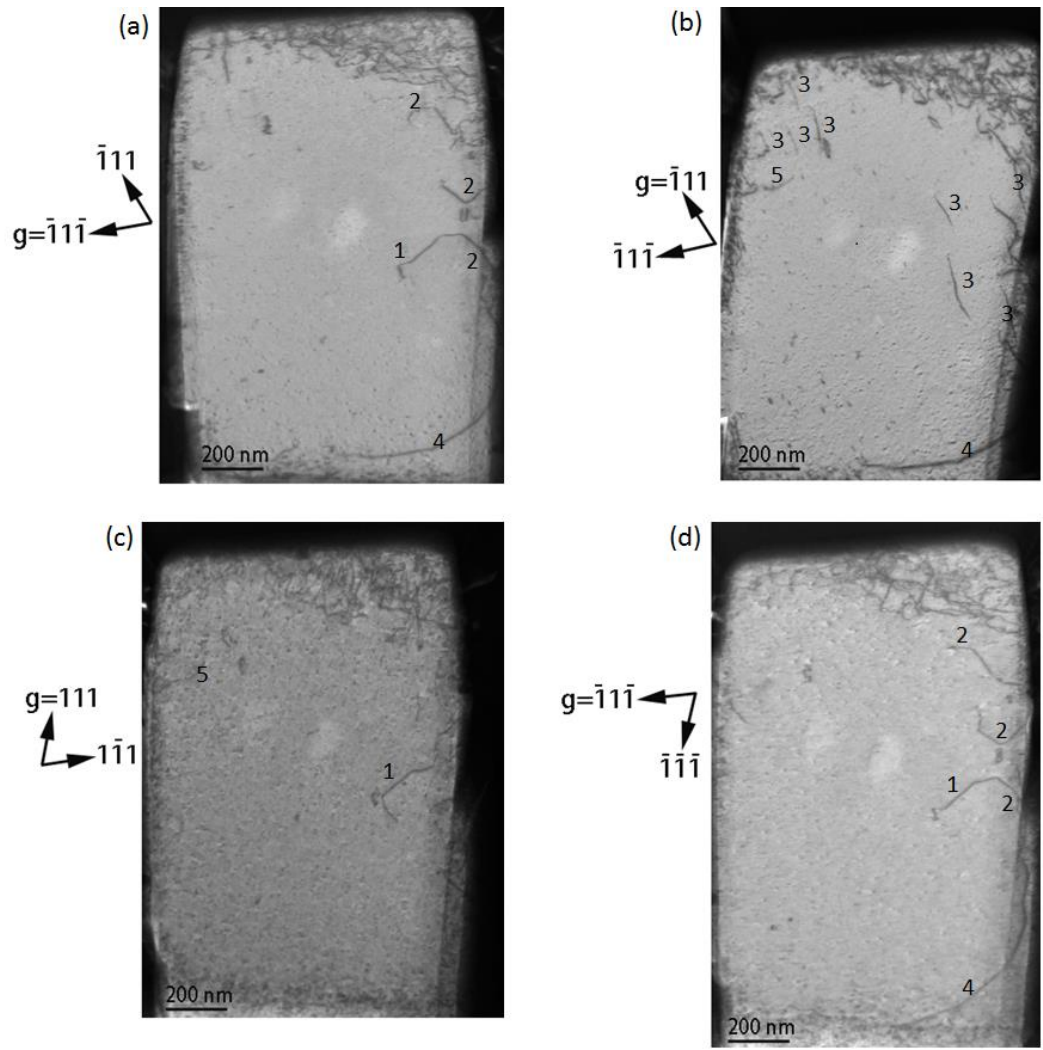| Beam direction	g	Slip system $\frac{1}{2}(\bar{1}11)[101]$	Slip system $\frac{1}{2}(\bar{1}11)[110]$	Slip system $\frac{1}{2}(111)[10\bar{1}]$	Slip system $\frac{1}{2}(111)[\bar{1}10]$	Burgers vector $\frac{1}{2}[0\bar{1}1]$	Burgers vector $\frac{1}{2}[011]$
$[\bar{1}\bar{1}0]$	$g_1=\bar{1}1\bar{1}$	✓ ★	✗	✗	✓	✓	✗
	$g_2=\bar{1}11$	✗	✗	✓	✓	✗	✓
$[\bar{1}01]$	$g_3=\bar{1}\bar{1}\bar{1}$	✓	✓	✗	✗	✗	✓
	$g_4=\bar{1}1\bar{1}$	✓	✗	✗	✓ ★	✓	✗

✓ : Visible   ★ : Edge-on   ✗ : Invisible

127

Figure 6-6 Bright field STEM images showing the dislocations in a 1-μm [156] cylindrical crystal after 3.3% strain. (a) g=$\bar{1}1\bar{1}$, BD~[$\bar{1}\bar{1}0$], (b) g=$\bar{1}11$, BD~[$\bar{1}\bar{1}0$], (c) g=111, BD~[$\bar{1}01$], and (d) g=$\bar{1}1\bar{1}$, BD~[$\bar{1}01$]
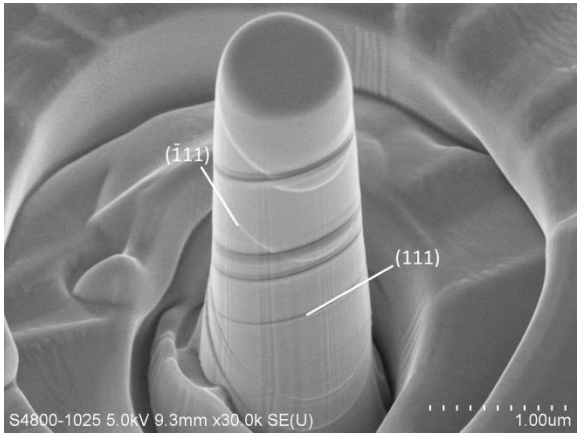

Figure 6-7 SEM image of the deformed pillar from which the TEM foil was extracted

128

Table 6-3 Summary of the analysis of 3-μm [156] cylindrical crystal from different diffraction conditions

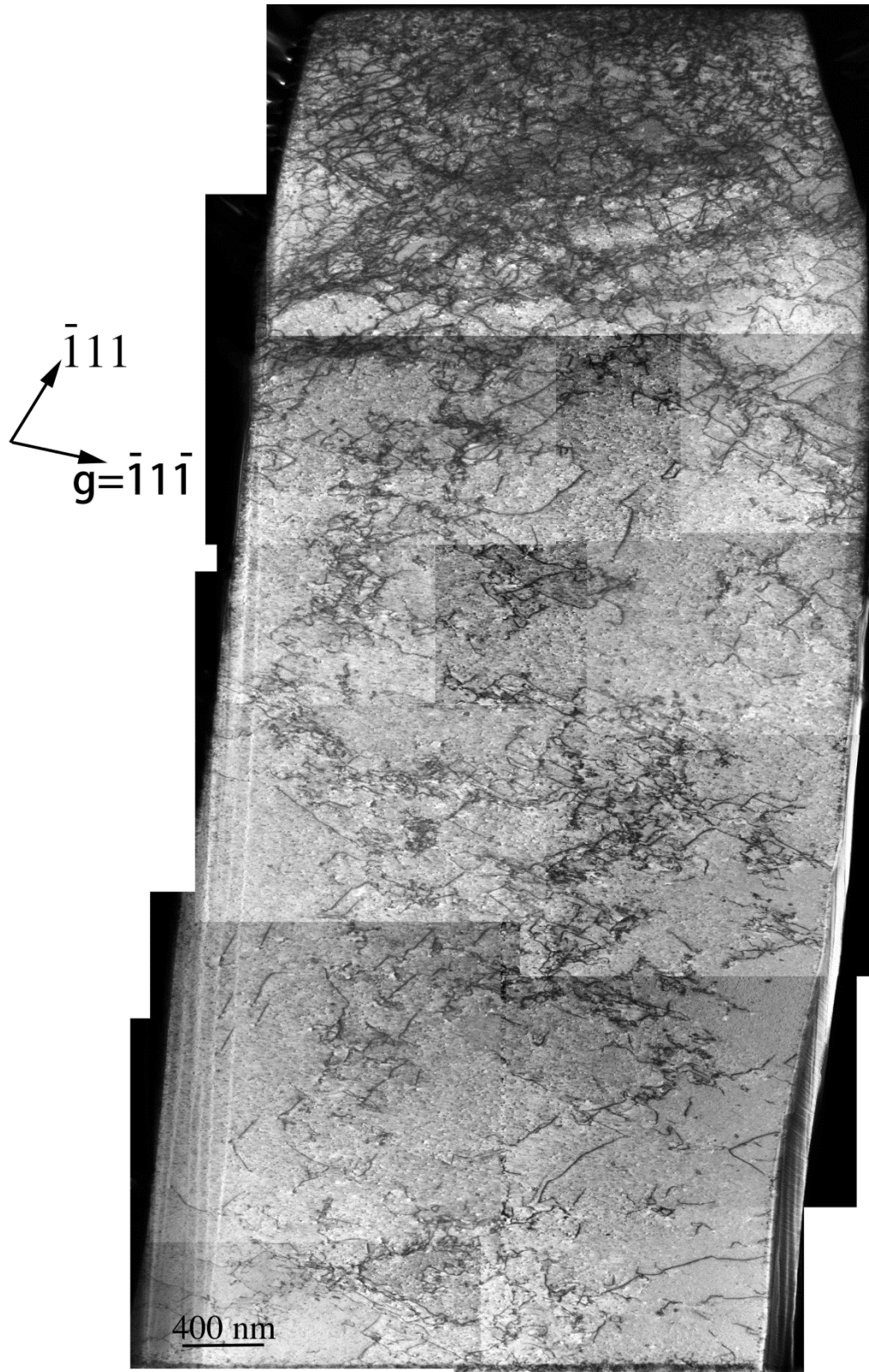| Beam direction	g	Slip system $\frac{1}{2}(\bar{1}11)[101]$	Slip system $\frac{1}{2}(\bar{1}11)[110]$	Slip system $\frac{1}{2}(111)[10\bar{1}]$	Slip system $\frac{1}{2}(111)[\bar{1}10]$	Burgers vector $\frac{1}{2}[0\bar{1}1]$	Burgers vector $\frac{1}{2}[011]$
[110]	$\bar{1}1\bar{1}$	✓ ★	✗	✗	✓	✓	✗
	$1\bar{1}\bar{1}$	✗	✗	✓	✓	✗	✓
[10$\bar{1}$]	$\bar{1}\bar{1}\bar{1}$	✓	✓	✗	✗	✗	✓
	$\bar{1}1\bar{1}$	✓	✗	✗	✓ ★	✓	✗
[11$\bar{2}$]	$2\bar{2}0$	✓	✗	✓ ★	✓ ★	✓	✓

Figure 6-8 (a) A bright field STEM image showing the dislocations inside the [156] specimen, g=$\bar{1}1\bar{1}$, BD~[110]
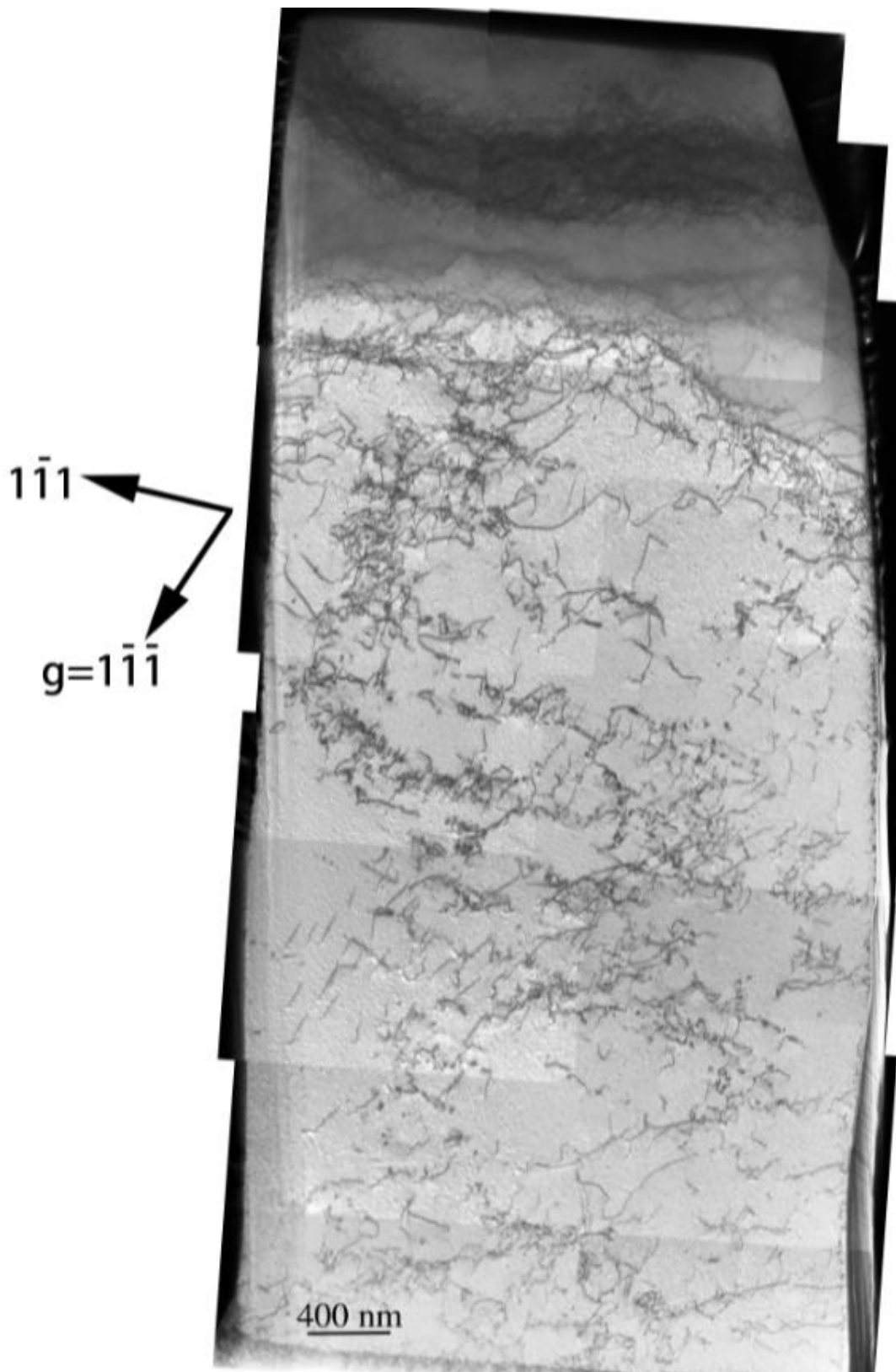
Figure 6-8 (b) A bright field STEM image showing the dislocations inside the [156] specimen, g=1$\bar{1}\bar{1}$, BD~[110]
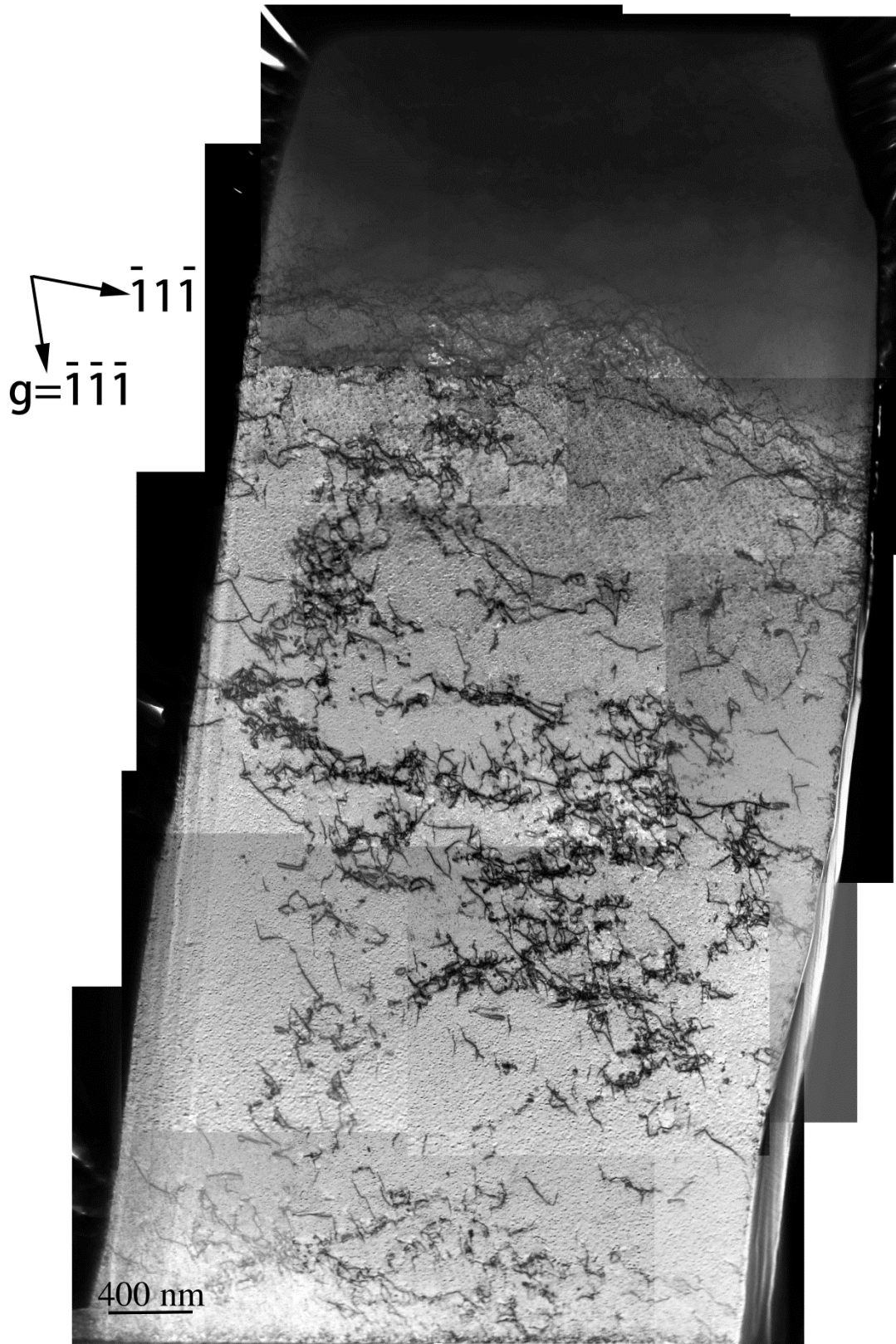
Figure 6-8 (c) A bright field STEM image showing the dislocations inside the [156] specimen, g=$\overline{1}\overline{1}\overline{1}$, BD~[10$\overline{1}$]
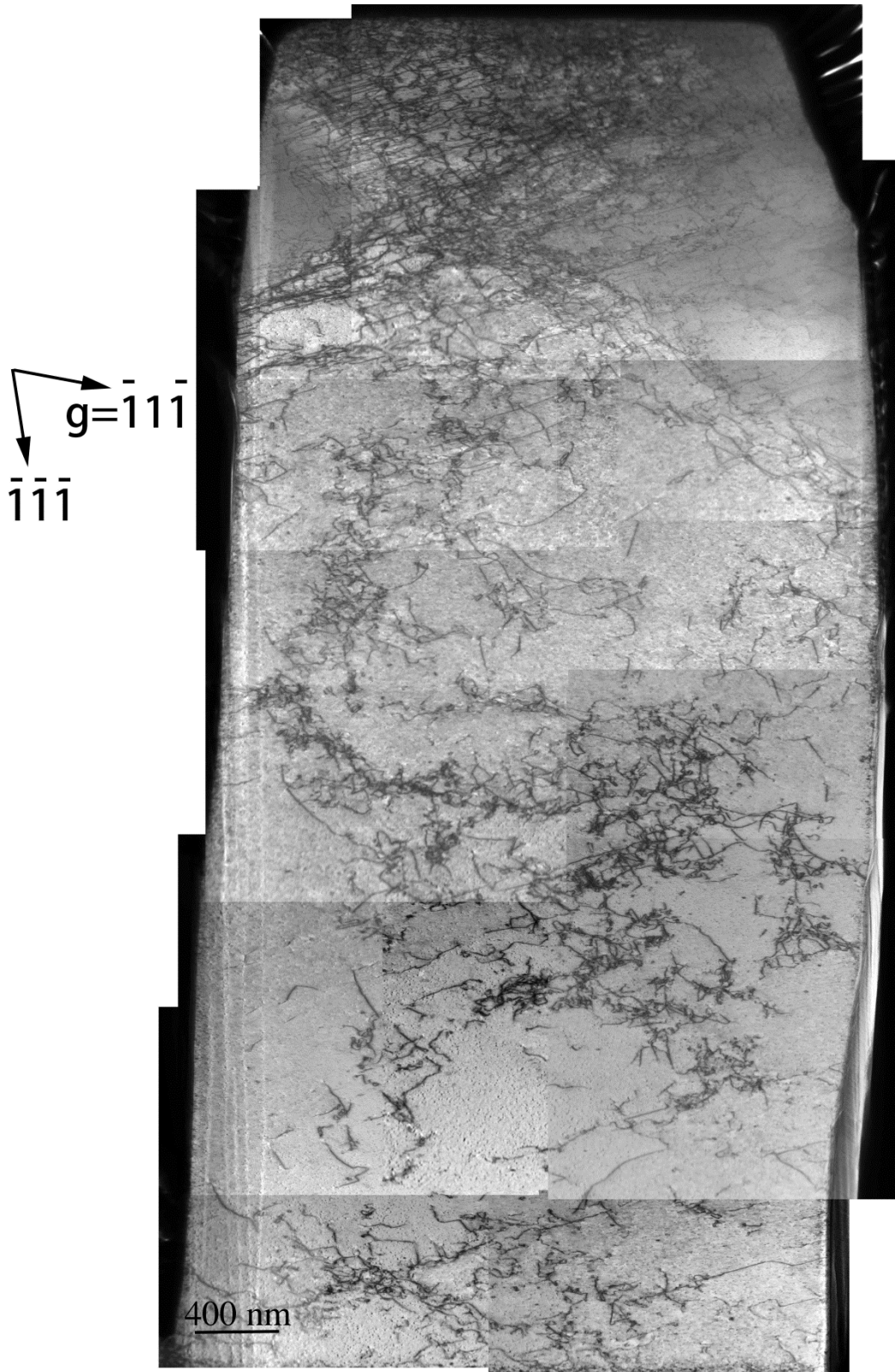
Figure 6-8 (d) A bright field STEM image showing the dislocations inside the [156] specimen, g=$\overline{1}1\overline{1}$, BD~[$10\overline{1}$]
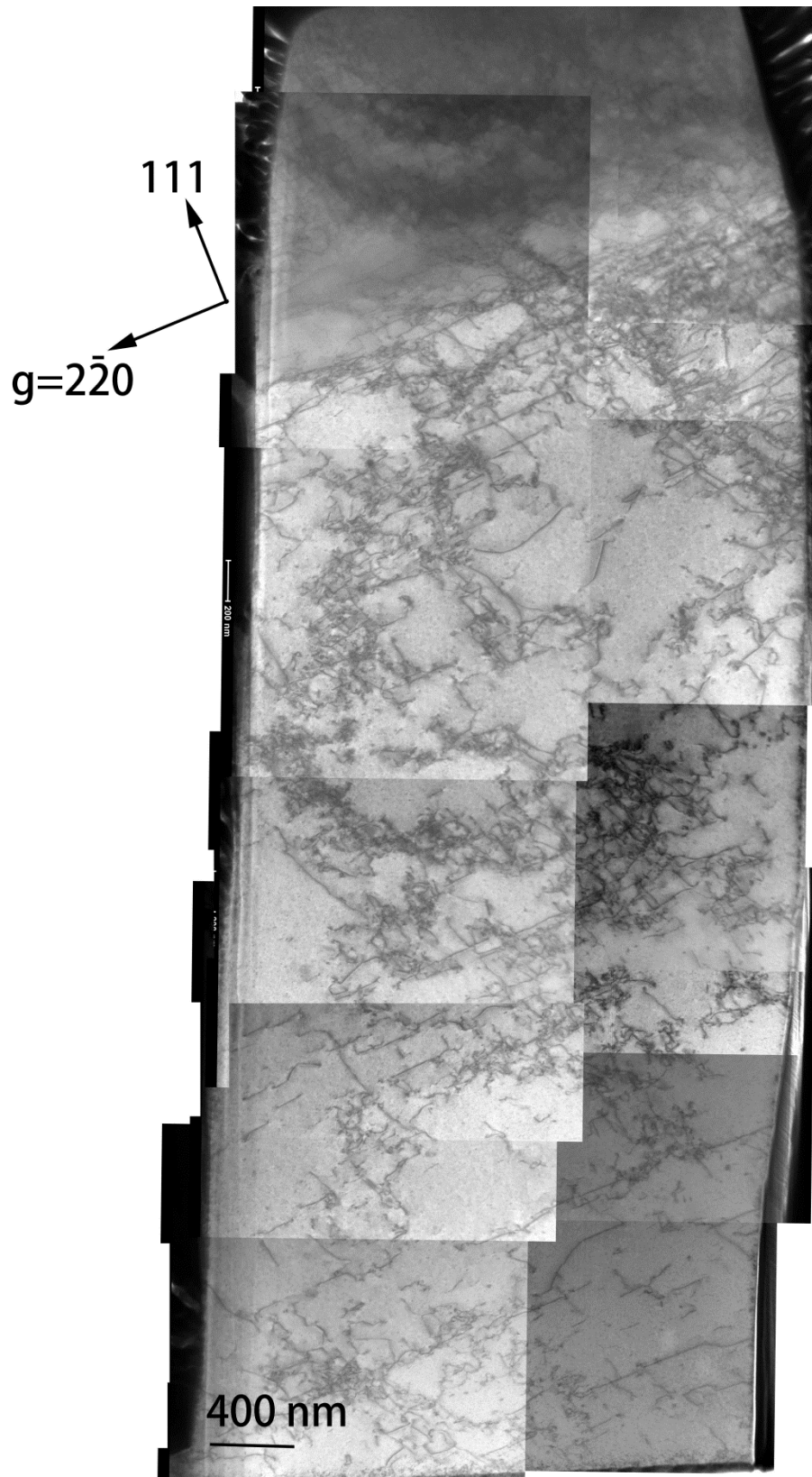
Figure 6-8 (e) A bright field STEM image showing the dislocations inside the [156] specimen, g=2$\bar{2}$0, BD~[11$\bar{2}$]
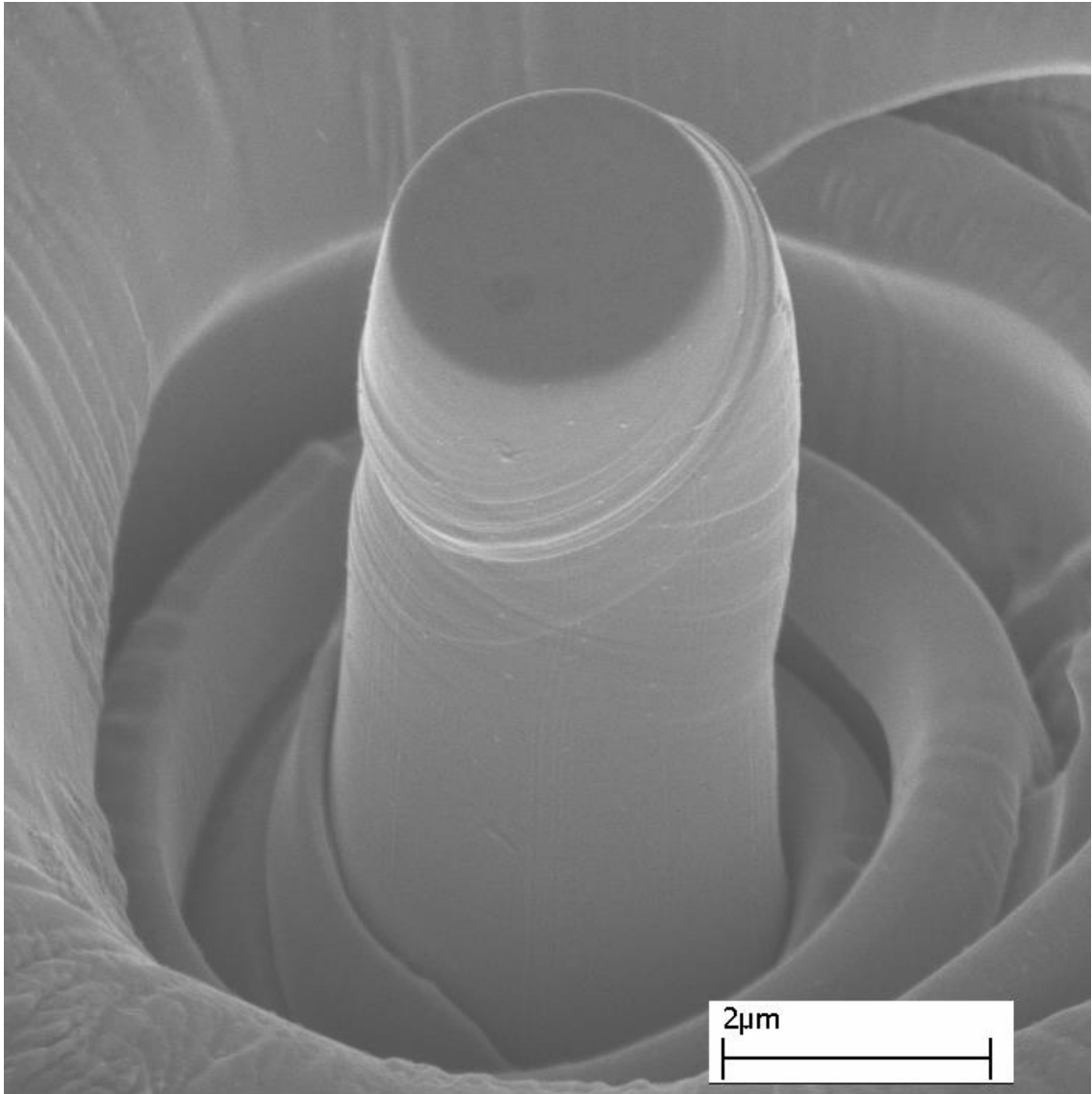
Figure 6-9 SEM image of the deformed pillar from which the TEM foil was extracted

Table 6-4 The four most highly stressed slip systems with a loading direction of [156]

No	Slip system	Schmid Factor	Colour coding
1	$\frac{1}{2}(\bar{1}11)[101]$	0.46	Yellow
2	$\frac{1}{2}(\bar{1}11)[110]$	0.40	Purple
3	$\frac{1}{2}(111)[10\bar{1}]$	0.40	Blue
4	$\frac{1}{2}(111)[\bar{1}10]$	0.32	Red
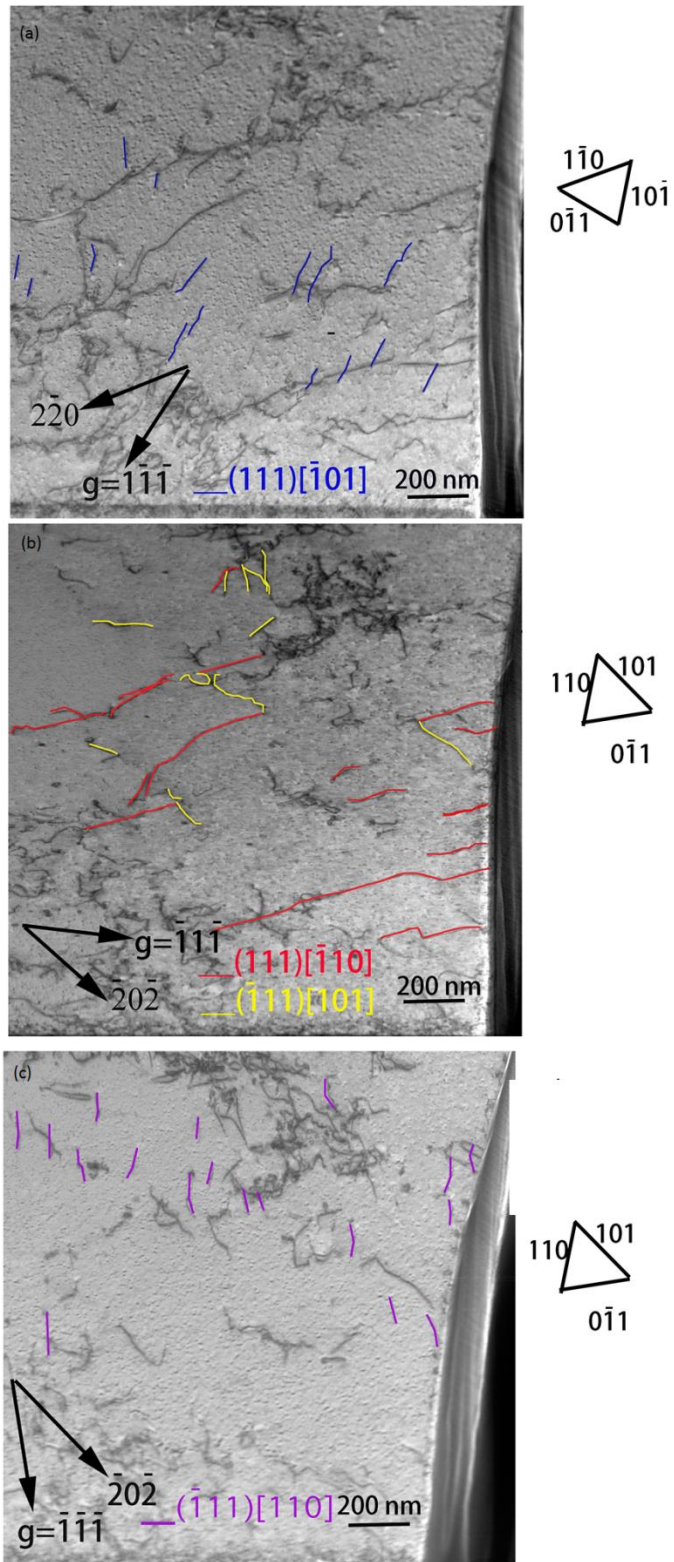
Figure 6-10 BF-STEM images of the bottom right region. (a) g=1$\overline{1}\overline{1}$, BD~[110], (b) g=$\overline{1}$1$\overline{1}$, BD~[10$\overline{1}$] and (c) g=$\overline{1}\overline{1}\overline{1}$, BD~[10$\overline{1}$]
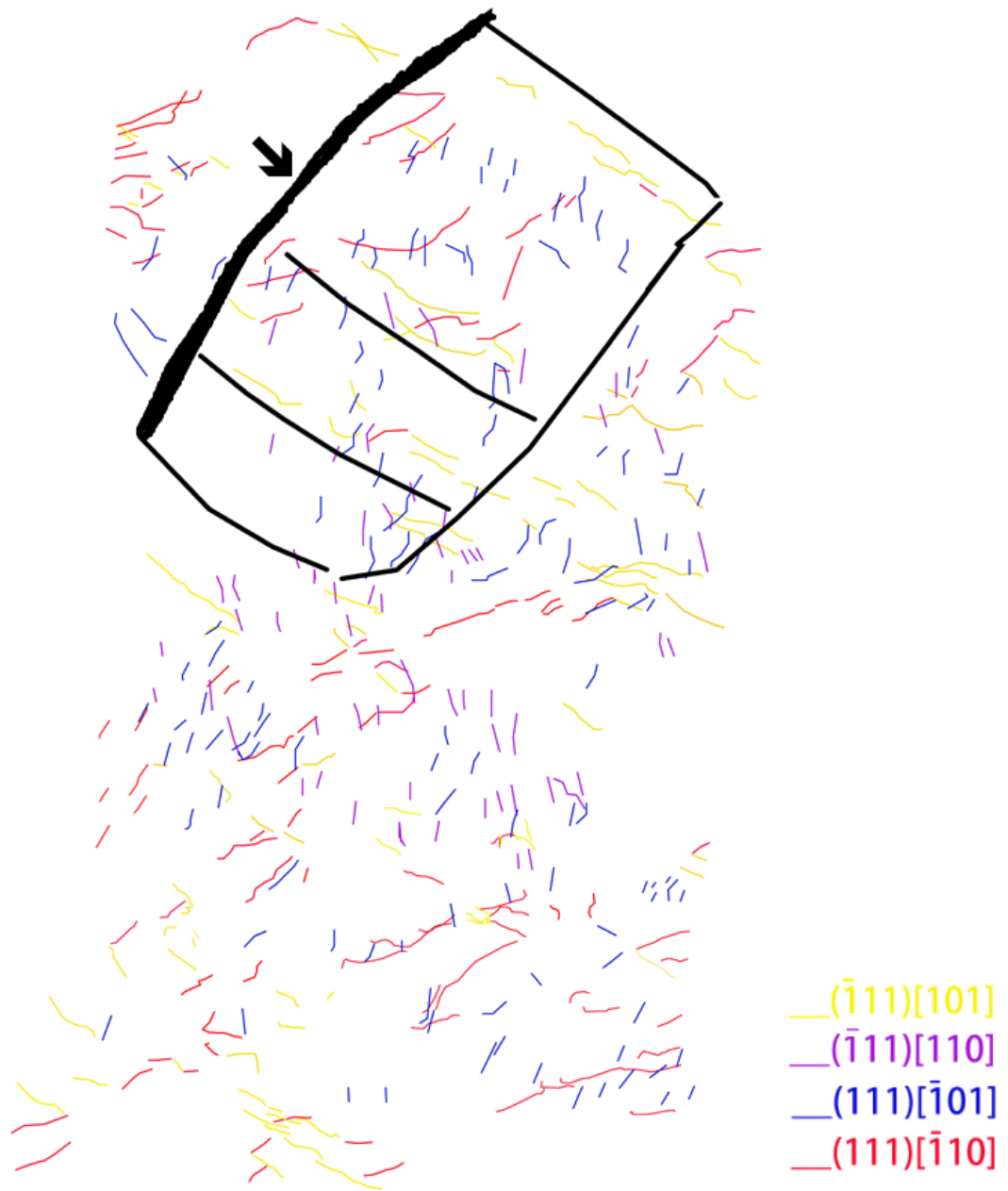
Figure 6-11 Dislocation distribution on different slip systems across the sample.
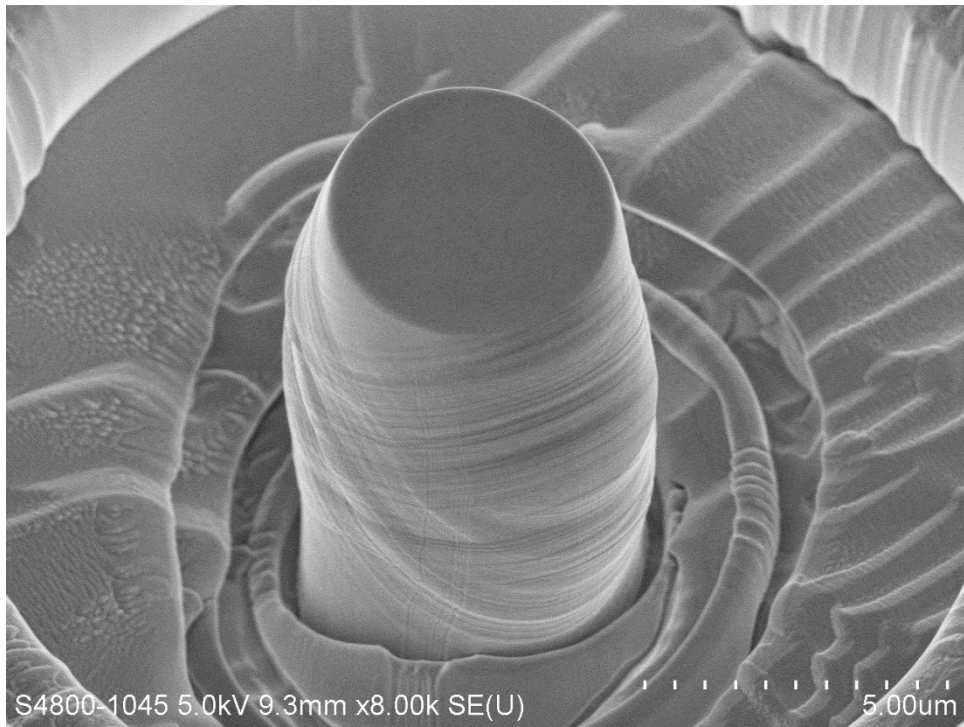
Figure 6-12 SEM image of the 5-µm 156 pillar with 18.5% strain
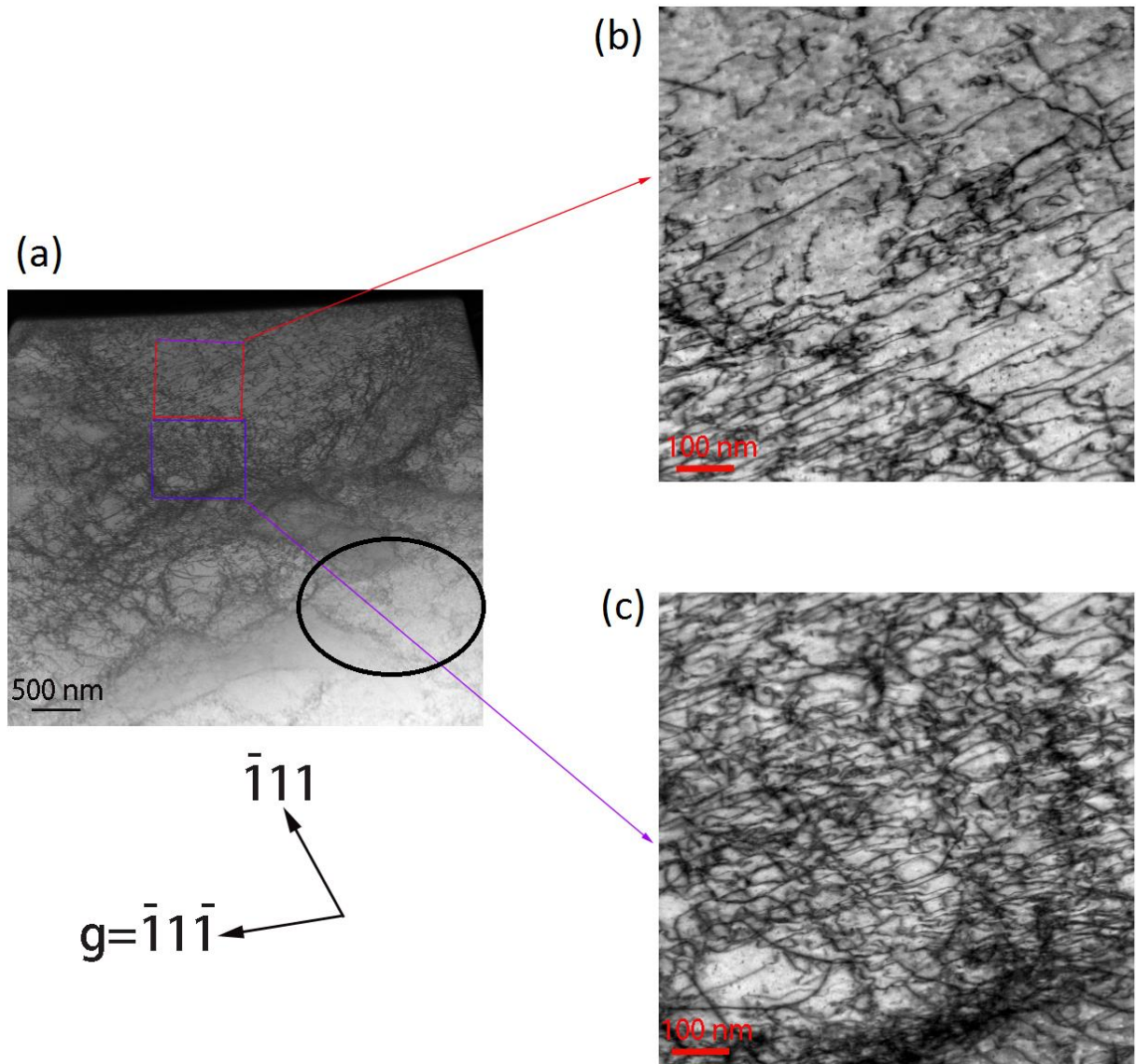
Figure 6-13 (a) A low magnification STEM image showing the formation of subgrains inside the pillar after severe (18% strain) deformation. Magnified images of the interaction regions between different slip systems marked by the rectangles are presented in (b) and (c). g=$\bar{1}1\bar{1}$, BD~$[\bar{1}\bar{1}0]$

Table 6-5 Summary of the analysis of 5-µm 156 grain from different diffraction conditions

Beam direction	g	Slip system $\frac{1}{2}(\bar{1}11)[101]$	Slip system $\frac{1}{2}(\bar{1}11)[110]$	Slip system $\frac{1}{2}(111)[10\bar{1}]$	Slip system $\frac{1}{2}(111)[\bar{1}10]$	Burgers vector $\frac{1}{2}[0\bar{1}1]$	Burgers vector $\frac{1}{2}[011]$
$[\bar{1}\bar{2}1]$	$\bar{2}0\bar{2}$	✓ ★	✓ ★	✘	✓	✓	✓
$[\bar{1}\bar{1}2]$	$\bar{2}20$	✓	✘	✓ ★	✓ ★	✓	✓
$[\bar{1}\bar{1}0]$	$\bar{1}11$	✘	✘	✓	✓	✘	✓
	$\bar{1}1\bar{1}$	✓ ★	✘	✘	✓	✓	✘
$[\bar{1}01]$	$\bar{1}\bar{1}\bar{1}$	✓	✓	✘	✘	✘	✓
	$\bar{1}1\bar{1}$	✓	✘	✘	✓ ★	✓	✘

Figure 6-14 Bright field TEM image showing the dislocations in the same region of a 5-μm [156] cylindrical crystal after 18.5% strain. (a) g=$\bar{2}0\bar{2}$, BD~[$\bar{1}\bar{2}1$], (b) g=$\bar{2}20$, BD=[$\bar{1}\bar{1}2$] (c) g=$\bar{1}11$, BD~[$\bar{1}\bar{1}0$], (d) g=$\bar{1}1\bar{1}$, BD~[$\bar{1}\bar{1}0$], (e) g=$\bar{1}1\bar{1}$, BD~[$\bar{1}01$], and (f) g=$\bar{1}1\bar{1}$, BD~[$\bar{1}01$]
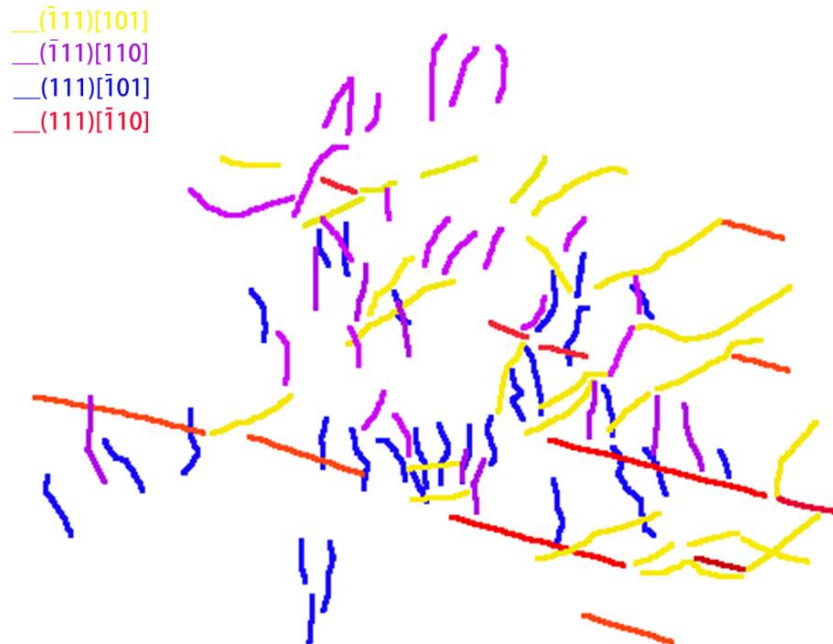
Figure 6-15 Dislocation distribution in the imaged area. The yellow and purple ones were traced from Figure 5-14 (e), the red ones from (f) and the blue ones from (c)

142

Beam direction	g	Slip system $\frac{1}{2}(\bar{1}11)[101]$	Slip system $\frac{1}{2}(\bar{1}11)[110]$	Slip system $\frac{1}{2}(111)[10\bar{1}]$	Slip system $\frac{1}{2}(111)[\bar{1}10]$	Burgers vector $\frac{1}{2}[0\bar{1}1]$	Burgers vector $\frac{1}{2}[011]$
$[\bar{2}\bar{1}1]$	$\bar{1}1\bar{1}$	✓	✗	✗	✓	✓	✗
$[\bar{1}\bar{1}2]$	$\bar{1}1\bar{1}$	✓	✓	✗	✗	✗	✓
$[\bar{1}\bar{2}1]$	$\bar{1}11$	✗	✗	✓	✓	✗	✓

Figure 6-16 (a) Bright field TEM image showing the dislocations in a 2.2-µm [156] square crystal-7 with 2% strain, g=$1\bar{1}\bar{1}$, BD~$[\bar{2}\bar{1}1]$
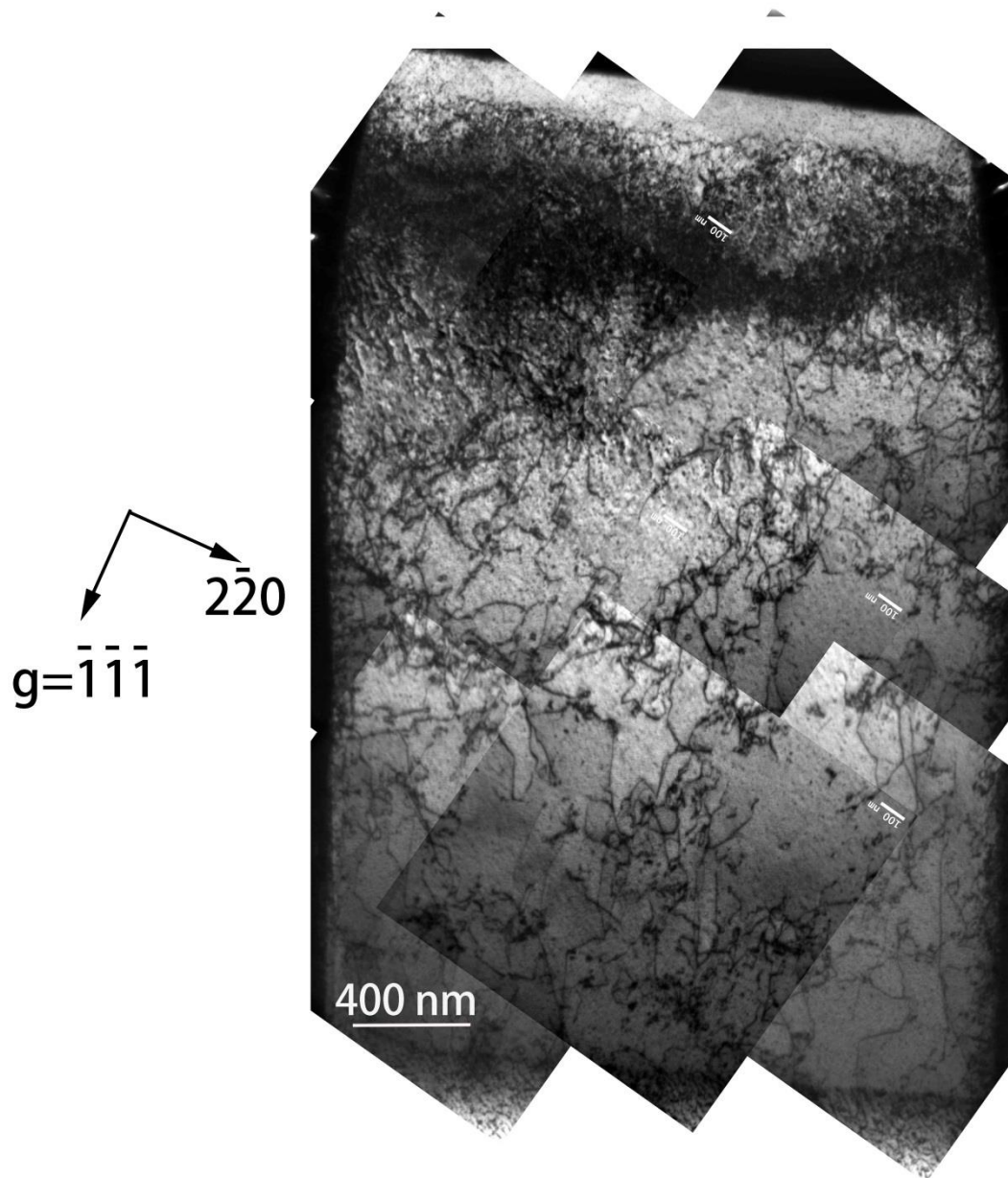
Figure 6-16 (b) Bright field TEM image showing the dislocations in a 2.2-µm [156] square crystal-7 after 2% strain, g=$\overline{1}1\overline{1}$, BD~$[\overline{1}12]$
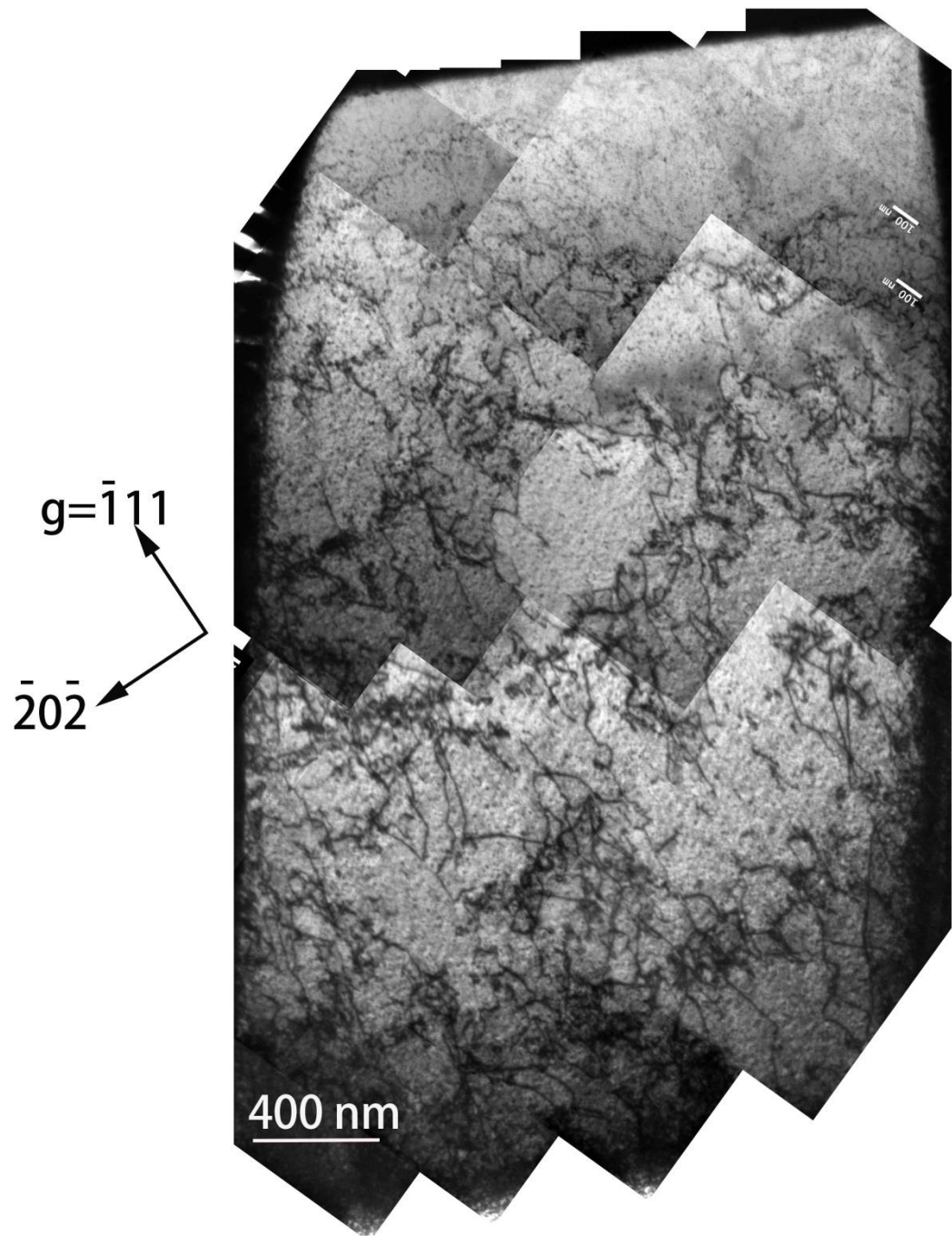
Figure 6-16 (c) Bright field TEM image showing the dislocations in a 2.2-µm [156] square crystal-7 after 2% strain g=$\bar{1}$11, BD~[$\bar{1}\bar{2}$1]

Figure 6-17 Colour-coding for the dislocations in the marked area in Figure 5-16 (a).
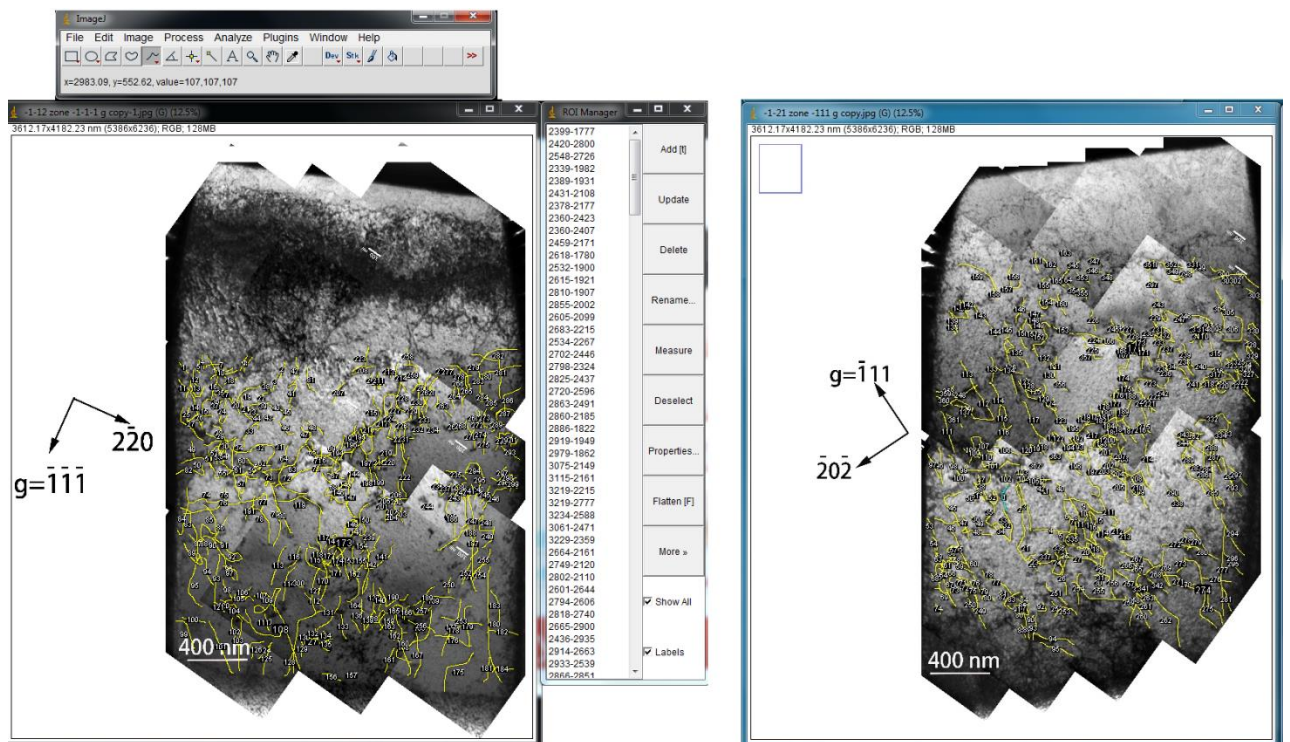
Figure 6-18 Dislocation lines traced in Image J, the figures corresponds to Figure 6-16 (b) and (c).

147

Table 6-7 Schmid factors of [235] oriented crystals

Slip plane	Burger's vector b	Schmid factor m
(111)	$[10\bar{1}]$	0.32
	$[0\bar{1}1]$	0.21
	$[\bar{1}10]$	0.11
$(\bar{1}11)$	$[101]$	0.45
	$[0\bar{1}1]$	0.13
	$[110]$	0.32
$(1\bar{1}1)$	$[011]$	0.34
	$[110]$	0.21
	$[10\bar{1}]$	0.13
$(11\bar{1})$	$[011]$	0
	$[\bar{1}10]$	0
	$[101]$	0

Table 6-8 Summary of the analysis of the 2.2-μm [235] square single crystal from different diffraction conditions

Beam direction	g	Slip system $\frac{1}{2}(\bar{1}11)[101]$	Slip system $\frac{1}{2}(1\bar{1}1)[011]$	Slip system $\frac{1}{2}(\bar{1}11)[110]$	Slip system $\frac{1}{2}(111)[10\bar{1}]$	Burgers vector $\frac{1}{2}[0\bar{1}1]$	Burgers vector $\frac{1}{2}[1\bar{1}0]$
$[\bar{1}01]$	111	✓	✓ ★	✓	✘	✘	✘
	$1\bar{1}1$	✓	✘	✘	✘	✓	✓
$[\bar{1}\bar{1}0]$	$1\bar{1}1$	✓ ★	✘	✘	✘	✓	✓

✓ : Visible   ★ : Edge-on   ✘ : Invisible
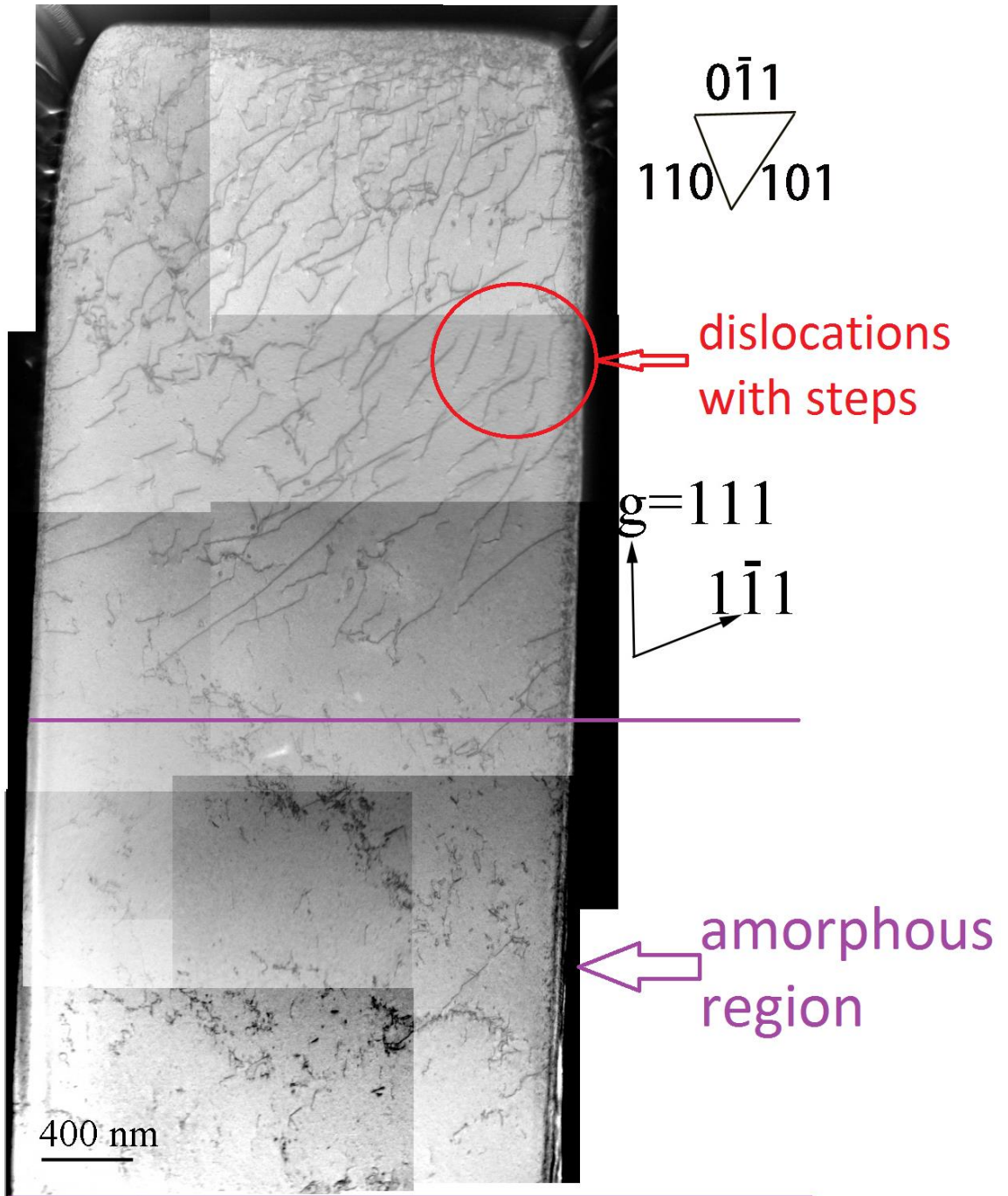
Figure 6-19(a) A bright field STEM image showing the dislocations inside the [235] specimen, g=111, BD~[$\bar{1}$01]. The bottom part was amorphized during FIB-milling.
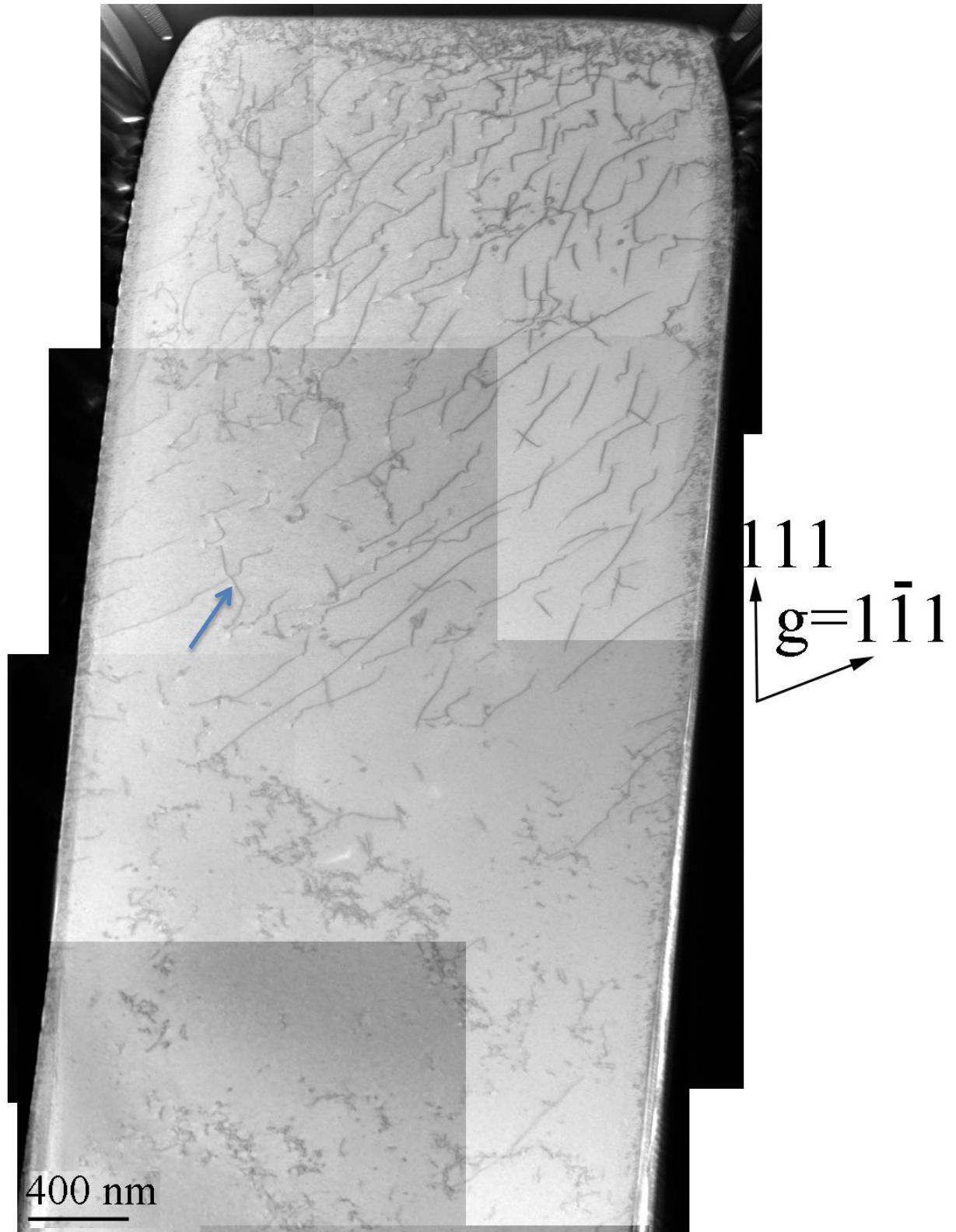
Figure 6-19 (b) A bright field STEM image showing the dislocations inside the [235] specimen, g=1$\bar{1}$1, BD~[$\bar{1}$01]. The arrow indicates a possibly pre-existing dislocation.
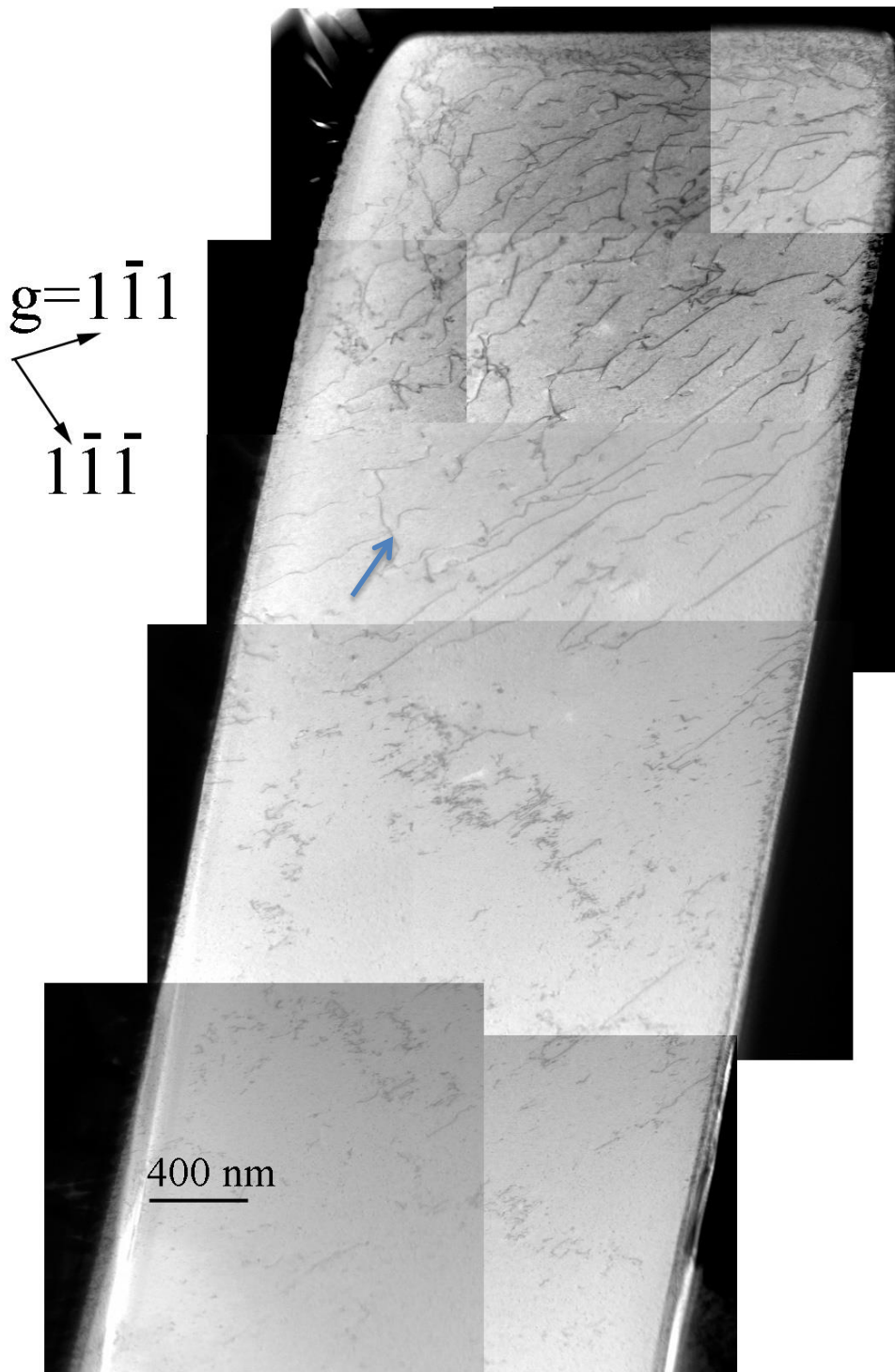
Figure 6-19 (c) A bright field STEM image showing the dislocations inside the [235] specimen, g=1$\bar{1}$1, BD~[$\bar{1}\bar{1}$0]
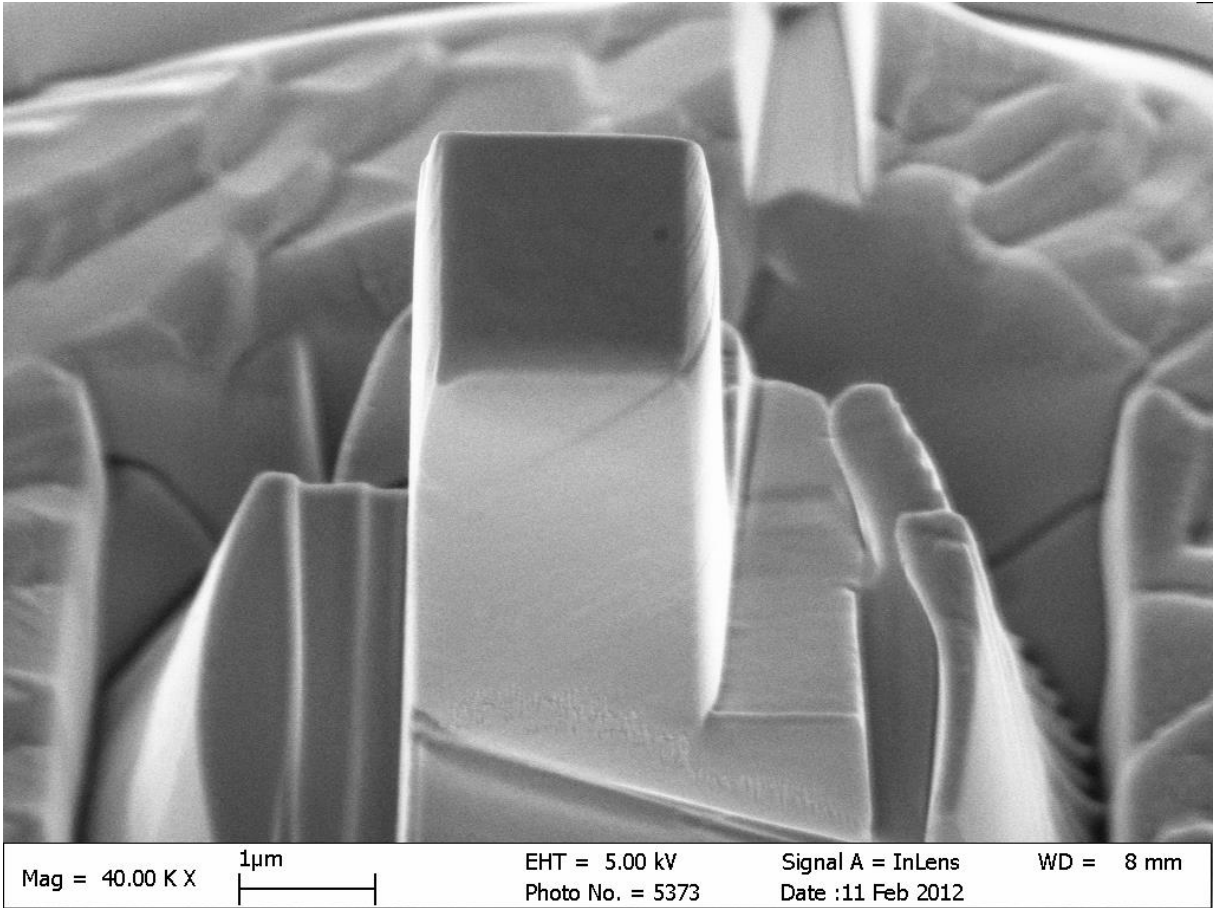
Figure 6-20 Surface morphology examination of the [235] square single crystal deformed to 3.9% strain. (SEM picture)
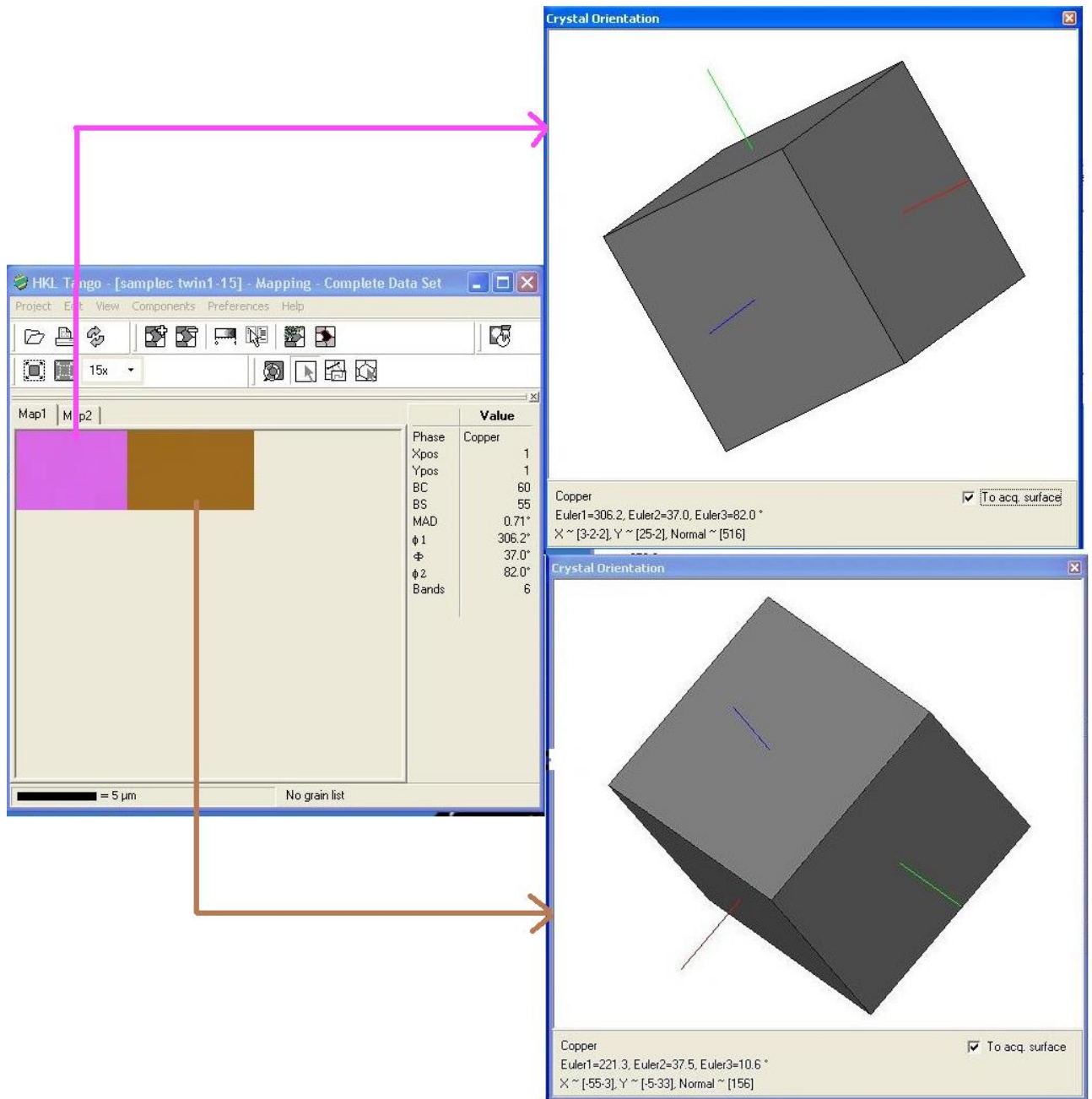
Figure 6-21 EBSD Crystal orientations on both sides of the twin boundary
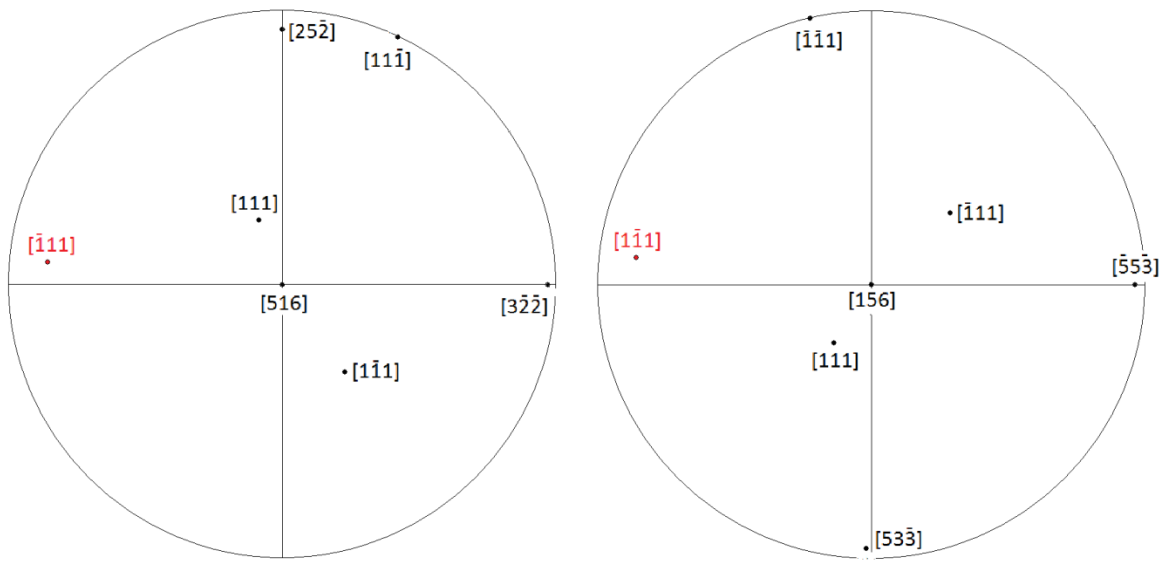
Figure 6-22 The <111> pole figures of the two composed grains in the twinned pillar

155

Table 6-9 Summary of the diffraction conditions for the 516 grain in a 3-μm [156/516] twinned cylinder

Beam direction	g	Slip system $\frac{1}{2}(1\bar{1}1)[011]$	Slip system $\frac{1}{2}(1\bar{1}1)[110]$	Slip system $\frac{1}{2}(111)[0\bar{1}1]$	Slip system $\frac{1}{2}(111)[\bar{1}10]$	Burgers vector $\frac{1}{2}[10\bar{1}]$	Burgers vector $\frac{1}{2}[101]$
$[01\bar{1}]$	111	✓	✓	✗	✗	✗	✓
	$1\bar{1}\bar{1}$	✓	✗	✗	✓ ★	✓	✗
$[110]$	$\bar{1}1\bar{1}$	✗	✗	✓	✓	✗	✓
	$1\bar{1}\bar{1}$	✓ ★	✗	✗	✓	✓	✗
$[11\bar{2}]$	$\bar{2}20$	✓	✗	✓ ★	✓ ★	✓	✓

Figure 6-23 (a) A bright field STEM image showing the dislocations inside the 516 grain, g=111, BD~[01$\bar{1}$]
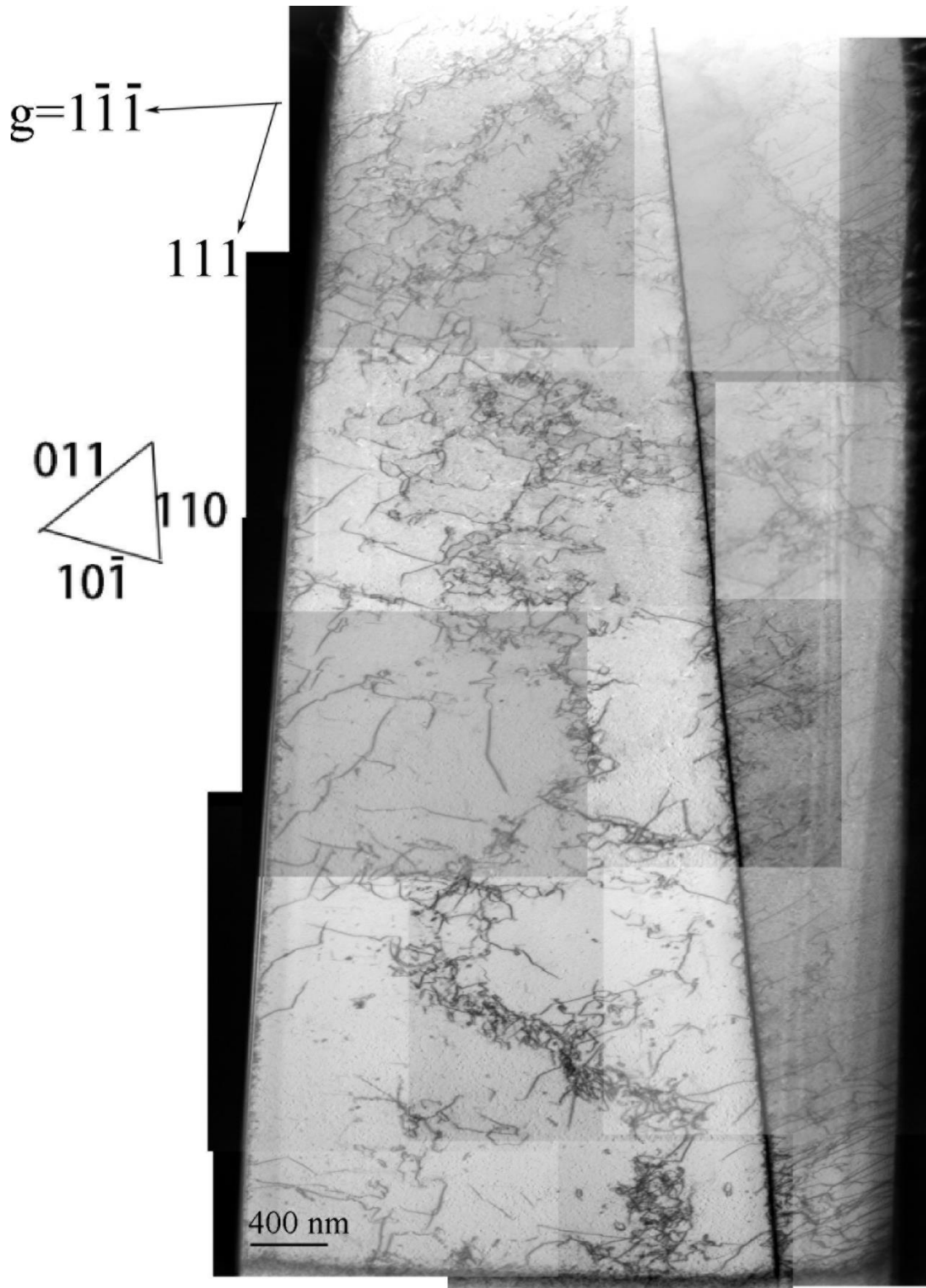
Figure 6-23 (b) A bright field STEM image showing the dislocations inside the 516 grain, g=1$\overline{1}\overline{1}$, BD~[01$\overline{1}$]
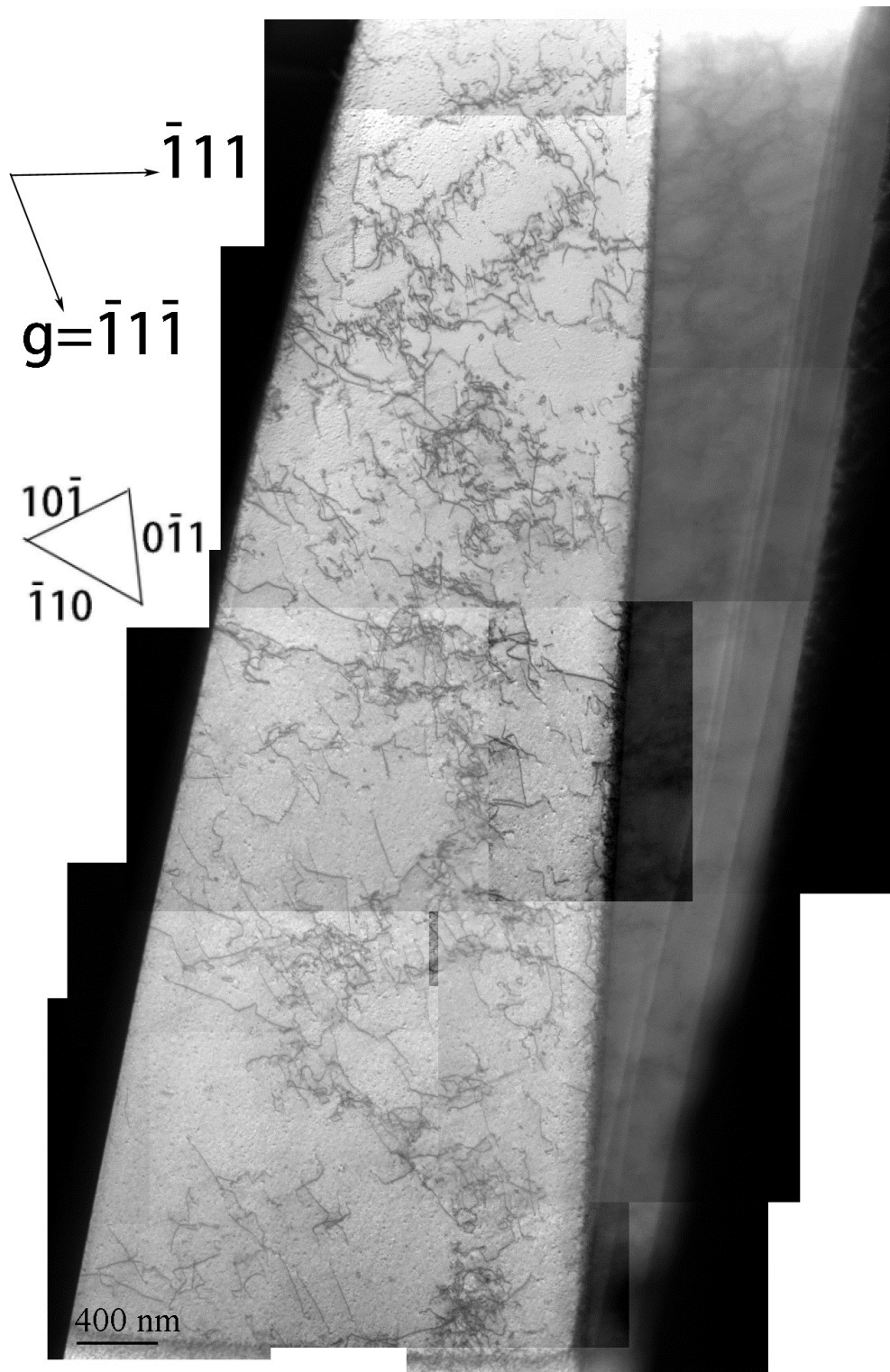
Figure 6-23 (c) A bright field STEM image showing the dislocations inside the 516 grain, g=$\bar{1}1\bar{1}$, BD~[110]
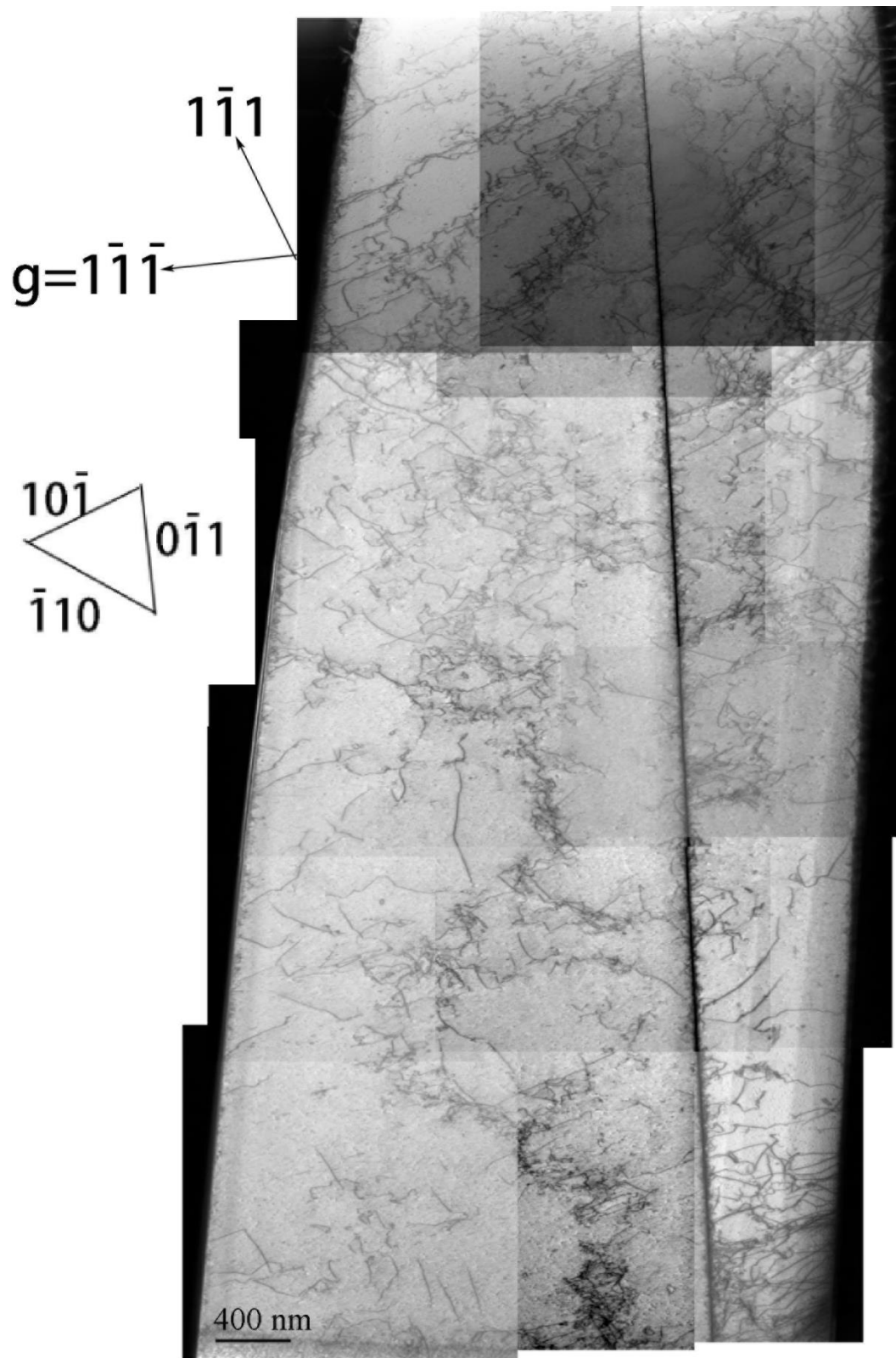
Figure 6-23 (d) A bright field STEM image showing the dislocations inside the 516 grain, g=1$\overline{1}\overline{1}$, BD~[110]
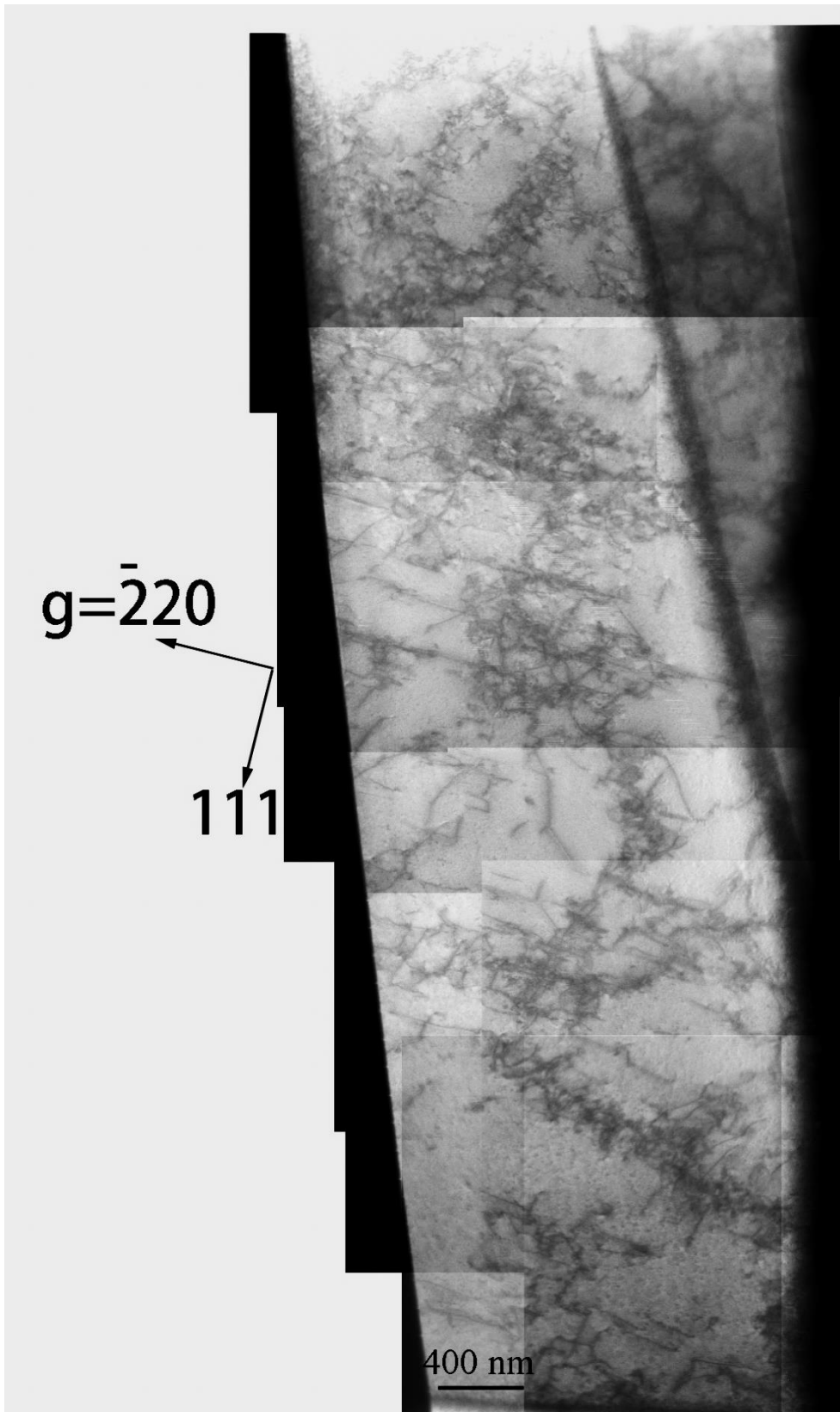
Figure 6-23 (e) A bright field STEM image showing the dislocations inside the 516 grain, g=$\bar{2}$20, BD~[11$\bar{2}$]
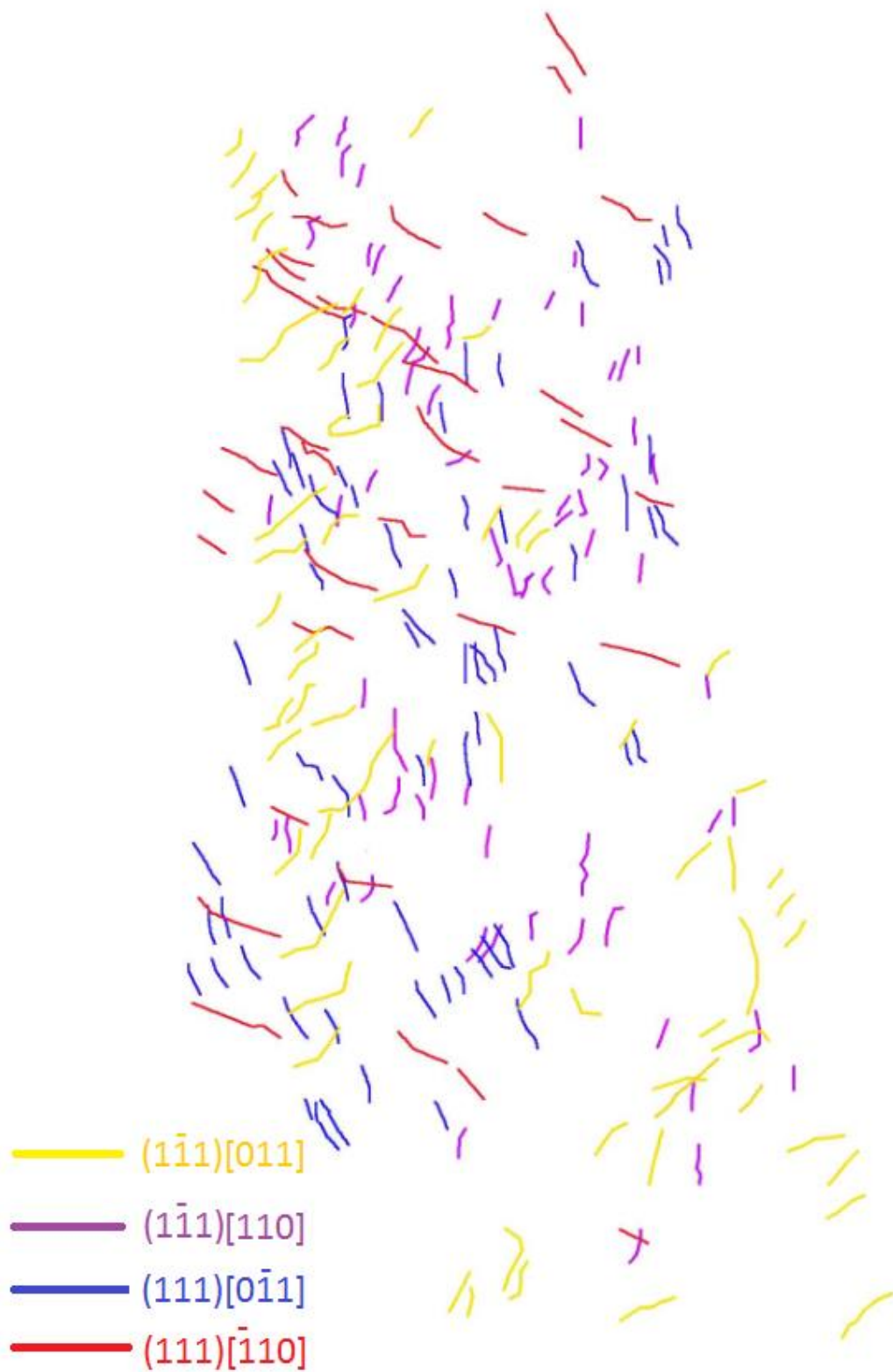
Figure 6-24 Colour-coding for the dislocations in the left hand 516 grain. The yellow and purple dislocations are traced from Figure 6-23 (a), the blue ones from (c) and the red ones from (d)

162

Table 6-10 Summary of the diffraction conditions for the 156 grain in a 3-μm [156]/[516] twinned cylinder

Beam direction	g	Slip system $\frac{1}{2}(\bar{1}11)[101]$	Slip system $\frac{1}{2}(\bar{1}11)[110]$	Slip system $\frac{1}{2}(111)[10\bar{1}]$	Slip system $\frac{1}{2}(111)[\bar{1}10]$	Burgers vector $\frac{1}{2}[0\bar{1}1]$	Burgers vector $\frac{1}{2}[011]$
$[\bar{1}\bar{1}0]$	$\bar{1}1\bar{1}$	✓ ★	✗	✗	✓	✓	✗
	$\bar{1}11$	✗	✗	✓	✓	✗	✓
$[\bar{1}01]$	$\bar{1}1\bar{1}$	✓	✓	✗	✗	✗	✓
	$\bar{1}1\bar{1}$	✓	✗	✗	✓ ★	✓	✗

Figure 6-25 (a) A bright field STEM image showing the dislocations inside the 156 grain, g=$\bar{1}1\bar{1}$ BD~[$\bar{1}\bar{1}0$]

Figure 6-25 (b) A bright field STEM image showing the dislocations inside the 156 grain, g=$\bar{1}$11 BD~[$\bar{1}\bar{1}$0]
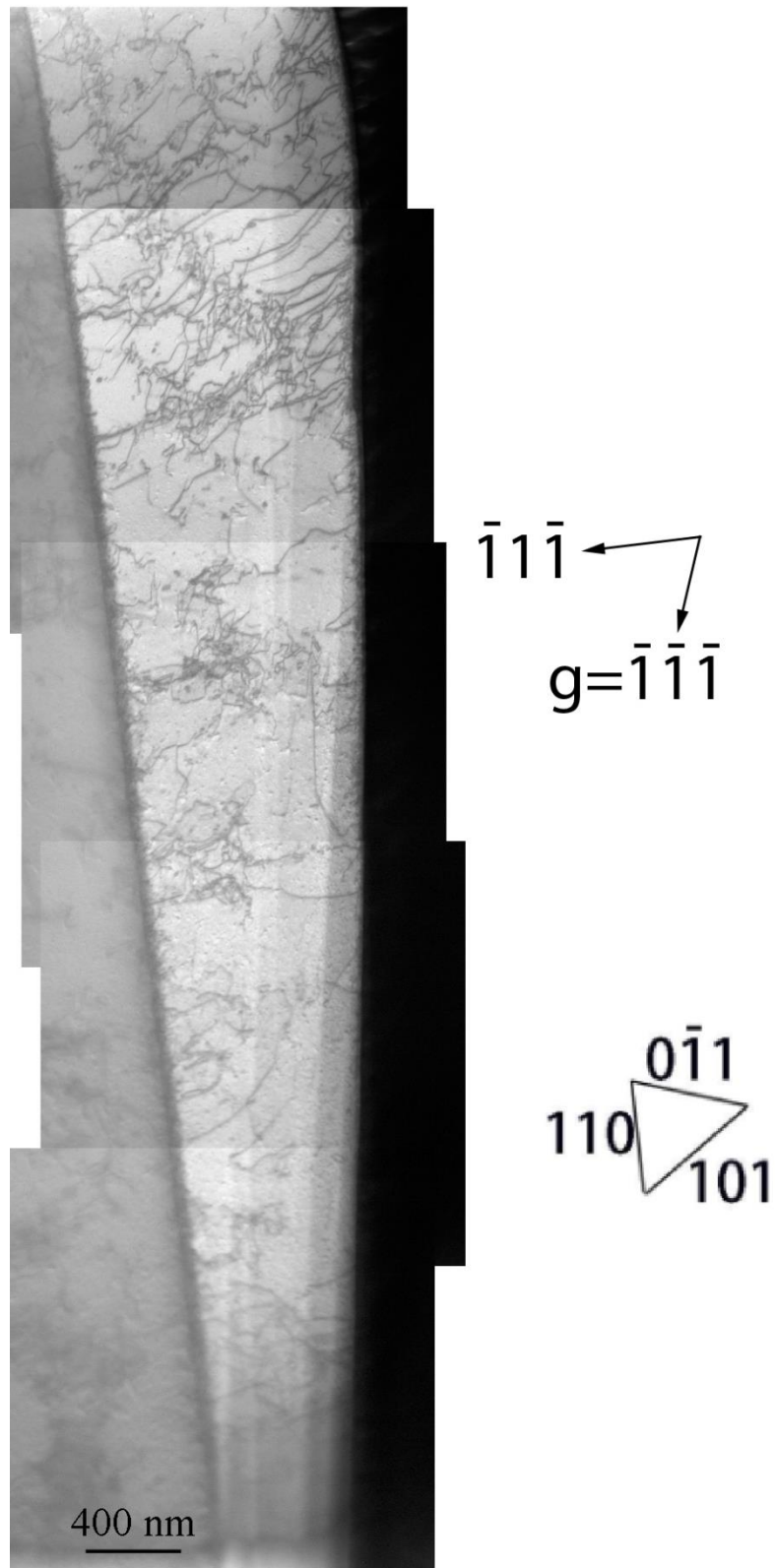
Figure 6-25 (c) A bright field STEM image showing the dislocations inside the 156 grain, g=$\overline{1}\overline{1}\overline{1}$ BD~[$\overline{1}$01]

Figure 6-25 (d) A bright field STEM image showing the dislocations inside the 156 grain, g=$\bar{1}1\bar{1}$ BD~[$\bar{1}01$]

Colour-coding legend:

$(\bar{1}11)[101]$
$(\bar{1}11)[110]$
$(111)[\bar{1}01]$
$(111)[\bar{1}10]$

Figure 6-26 Colour-coding for the dislocations in the right hand 156 grain. The yellow and purple dislocations are traced from Figure 6-25 (c), the blue ones from (b) and the red ones from (a)

168
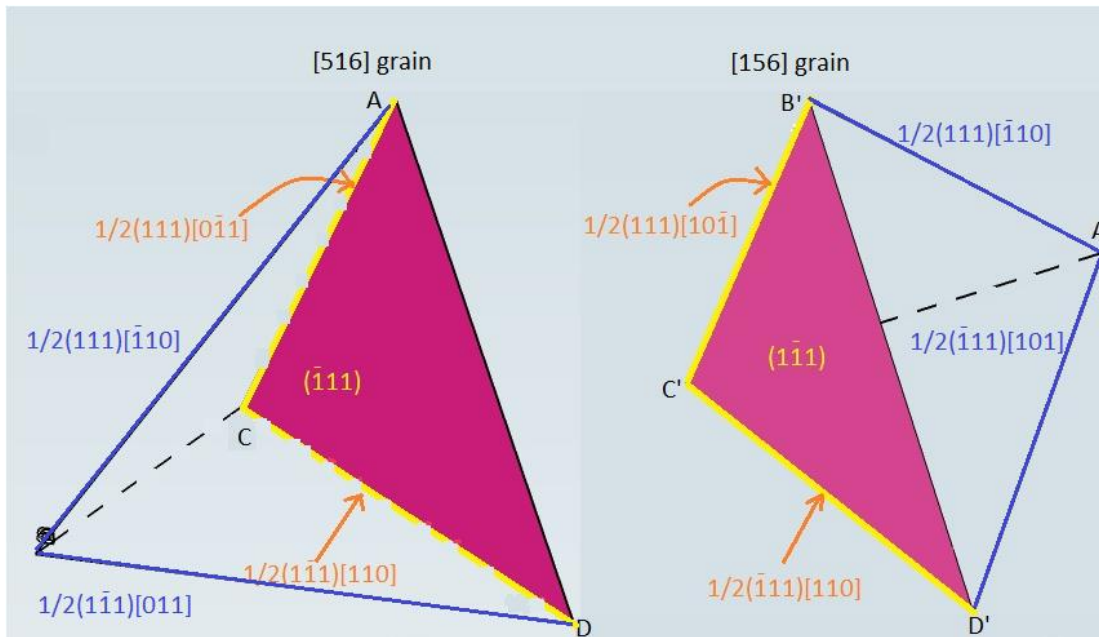
Figure 6-27 Thompson tetrahedron ABCD and A'B'C'D' for the [516] and [156] grain. ACD and B'C'D' corresponds to the twin boundary plane. Burgers vector DC and CA in the [516] grain and D'C' and C'B' in the [156] grain are parallel to the twin boundary plane thus are shared by both grains. Dislocation DC (D'C') can cross-slip from the glide plane BCD in the [516] grain into A'C'D' in the [156] grain; dislocation CA (C'B') can cross-slip from the glide plane ABC in the [516] grain into A'B'C' in the [156] grain.

Table 6-11 Summary of the diffraction conditions for the 156 grain in a 5-μm [156/516] twinned cylinder

| Beam direction	g	Slip system $\frac{1}{2}(\bar{1}11)[101]$	Slip system $\frac{1}{2}(\bar{1}11)[110]$	Slip system $\frac{1}{2}(111)[10\bar{1}]$	Slip system $\frac{1}{2}(111)[\bar{1}10]$		Burgers vector $\frac{1}{2}[0\bar{1}1]$	Burgers vector $\frac{1}{2}[011]$
$[\bar{1}01]$	$1\bar{1}1$	✓	✗	✗	✓	★	✓	✗
	$\bar{1}\bar{1}\bar{1}$	✓	✓	✗	✗		✗	✓
$[\bar{1}00]$	$0\bar{2}\bar{2}$	✓	✓	✓	✓		✗	✓

169

Figure 6-28(a) A bright field STEM image showing the dislocations inside the [156] grain, g=1$\bar{1}$1 , BD~[$\bar{1}$01]

Figure 6-28(b) A bright field STEM image showing the dislocations inside the [156] grain, g=$\overline{1}\overline{1}\overline{1}$, BD~[10$\overline{1}$]

Figure 6-28(c) A bright field STEM image showing the dislocations inside the [156] grain, g=0$2\bar{2}$, BD~[$\bar{1}$00]

$\_\_(\bar{1}11)[101]$
$\_\_(\bar{1}11)[110]$
$\_\_(111)[\bar{1}01]$
$\_\_(111)[\bar{1}10]$
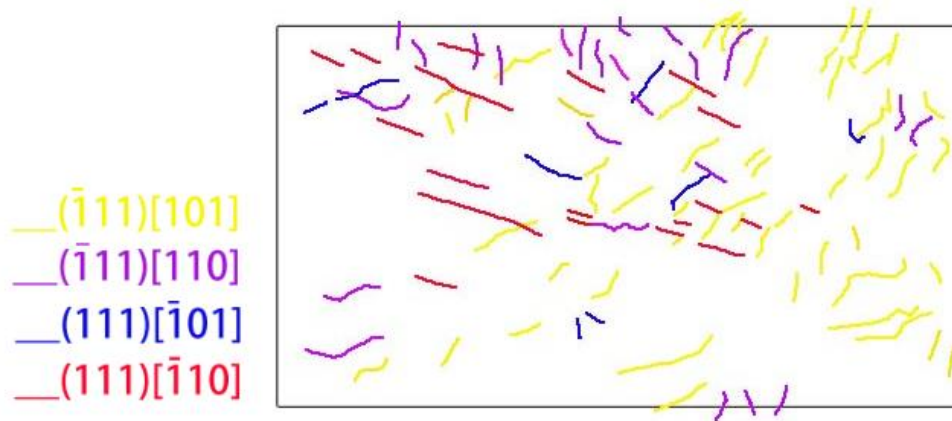
Figure 6-29 colour-coding for the dislocations from different slip systems in the area marked in Figure 6-28(a). The yellow and red ones are traced from (a), the purple ones from (b) and the blue ones from (c).

Table 6-12 Summary of the diffraction conditions for the [516] grain in a 5-µm [156/516] twinned cylinder

Beam direction	g	Slip system $\frac{1}{2}(1\bar{1}1)[011]$	Slip system $\frac{1}{2}(1\bar{1}1)[110]$	Slip system $\frac{1}{2}(111)[0\bar{1}1]$	Slip system $\frac{1}{2}(111)[\bar{1}10]$	Burgers vector $\frac{1}{2}[10\bar{1}]$	Burgers vector $\frac{1}{2}[101]$
[110]	$\bar{1}1\bar{1}$	✗	✗	✓	✓	✗	✓
	$1\bar{1}\bar{1}$	✓ ★	✗	✗	✓	✓	✗
[211]	$02\bar{2}$	✗	✓	✓	✓	✓	✓

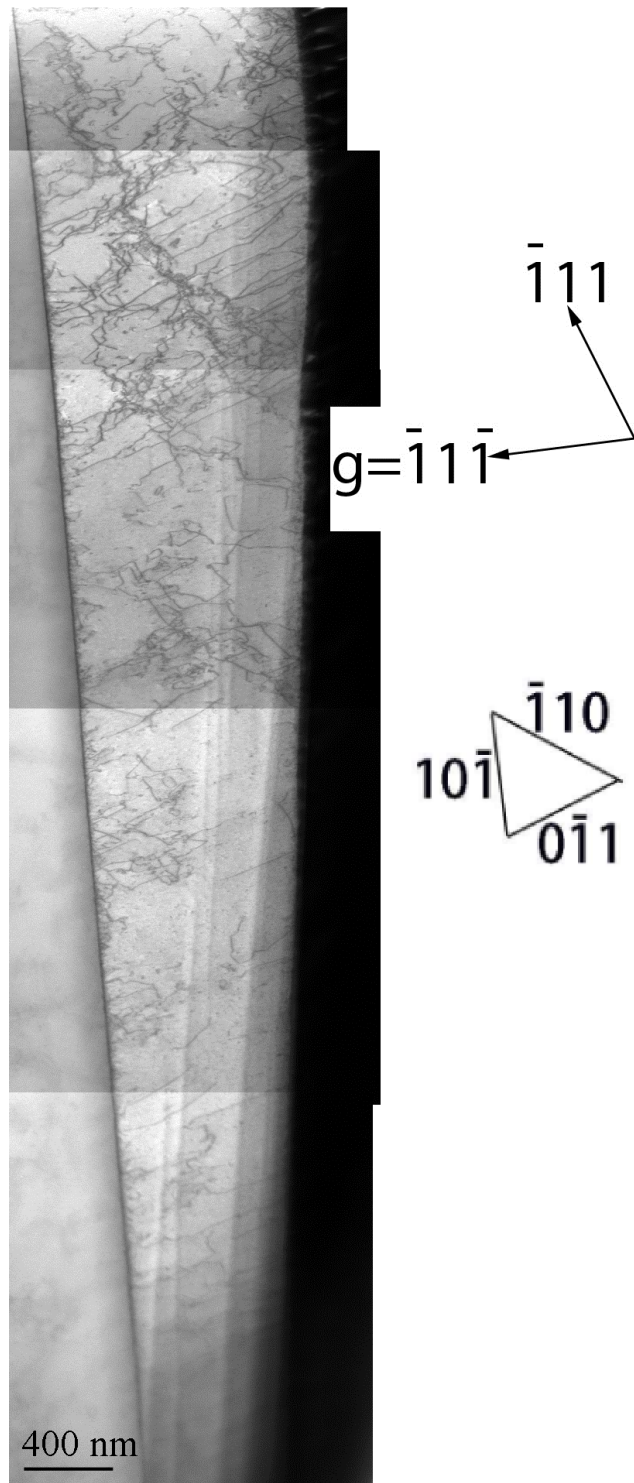**Figure 6-30(a) A bright field STEM image showing the dislocations inside the [516] grain, g=$\bar{1}1\bar{1}$, BD~[110]**
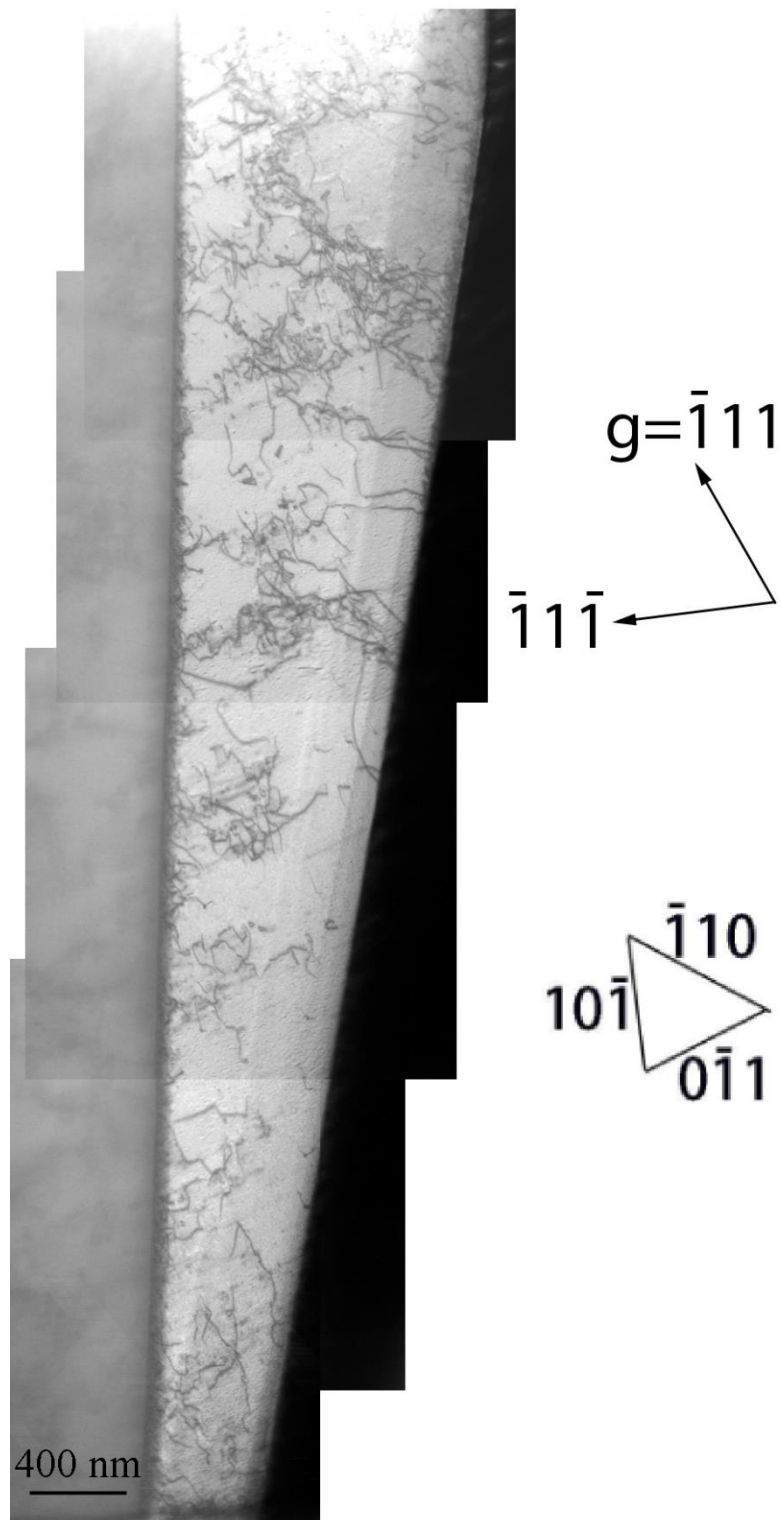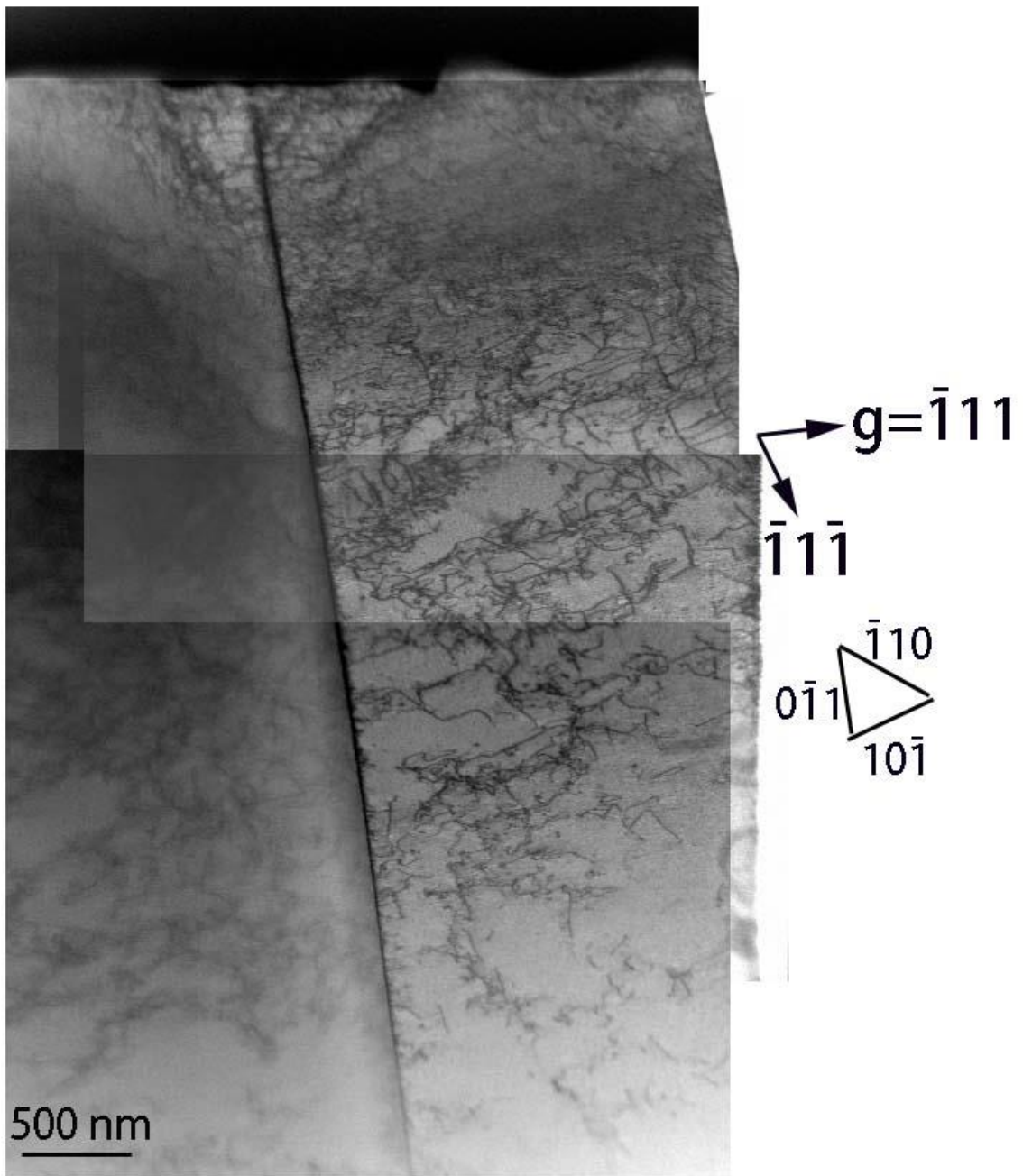
Figure 6-30 (b) A bright field STEM image showing the dislocations inside the [516] grain, g=$\bar{1}$11, BD~[110]
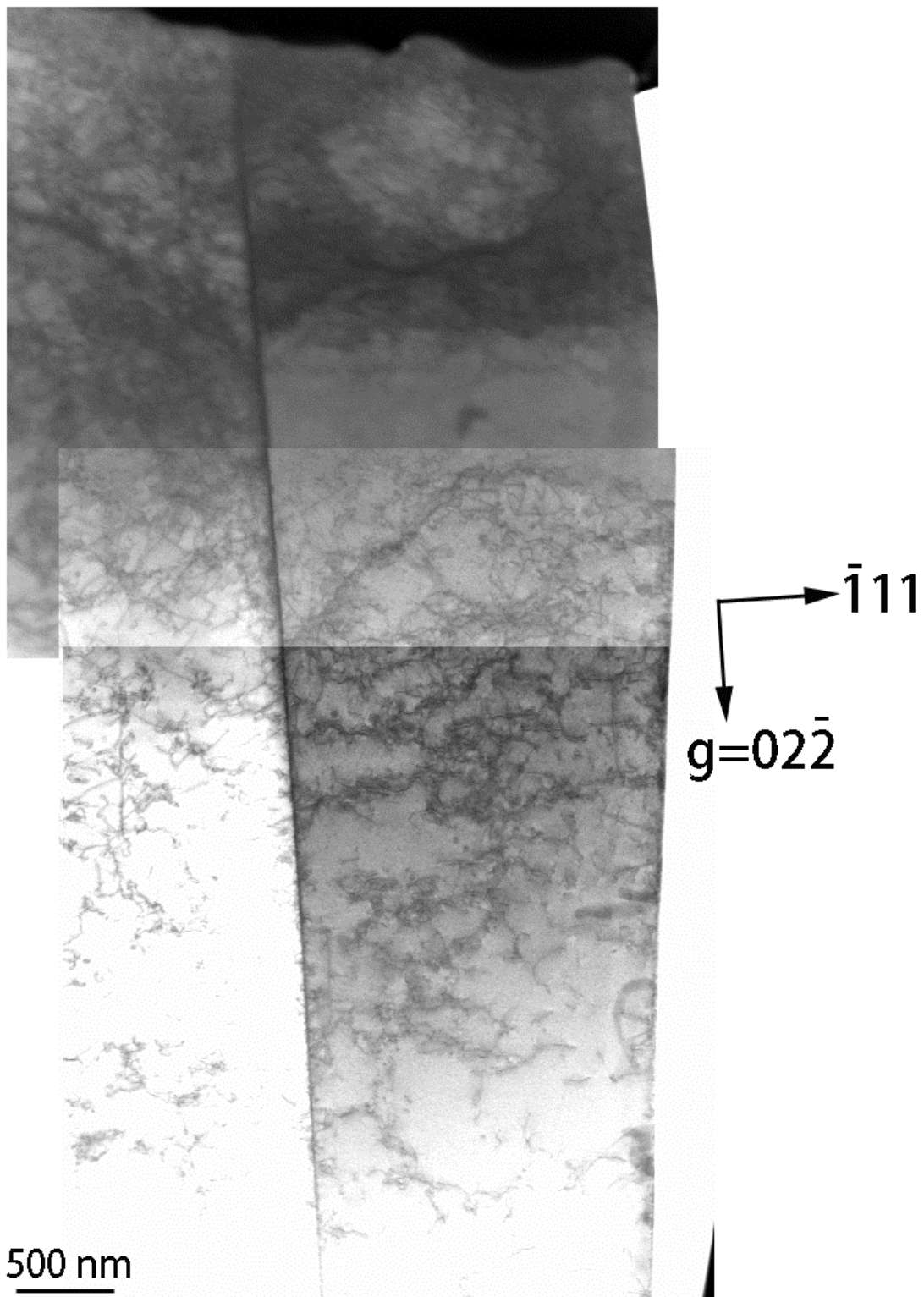
Figure 6-30 (c) A bright field STEM image showing the dislocations inside the [516] grain, g=02$\bar{2}$ BD~[211]
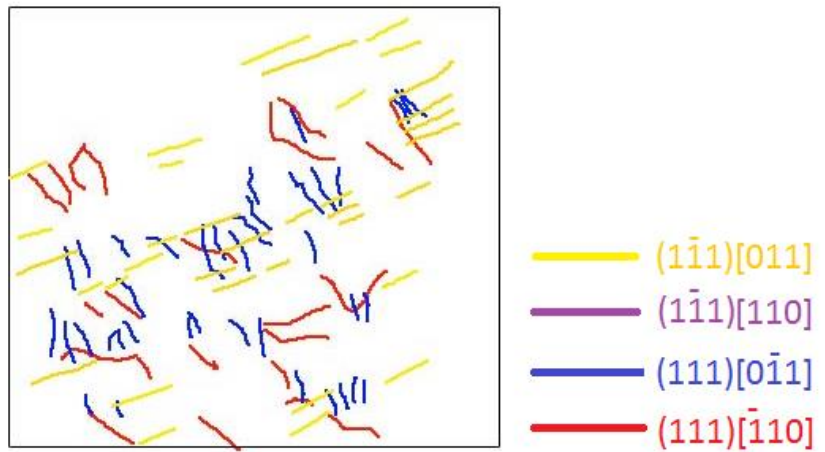
Figure 6-31 colour-coding for the dislocations from different slip systems in the area marked in Figure 6-28(a)

Table 6-13 Diffraction conditions for the [516] grain from the twinned square pillar

Beam direction	g	Slip system $\frac{1}{2}(1\bar{1}1)[011]$	Slip system $\frac{1}{2}(1\bar{1}1)[110]$	Slip system $\frac{1}{2}(111)[0\bar{1}1]$	Slip system $\frac{1}{2}(111)[\bar{1}10]$	Burgers vector $\frac{1}{2}[10\bar{1}]$	Burgers vector $\frac{1}{2}[101]$
[01$\bar{1}$]	111	✓	✓	✗	✗	✗	✓
	$\bar{1}$11	✓	✗	✗	✓ ★	✓	✗
[110]	$\bar{1}1\bar{1}$	✗	✗	✓	✓	✗	✓
	$\bar{1}$11	✓ ★	✗	✗	✓	✓	✗

177

Figure 6-32 (a) A bright field STEM image showing the dislocations inside the [516] grain, g=111, BD~[01$\bar{1}$]
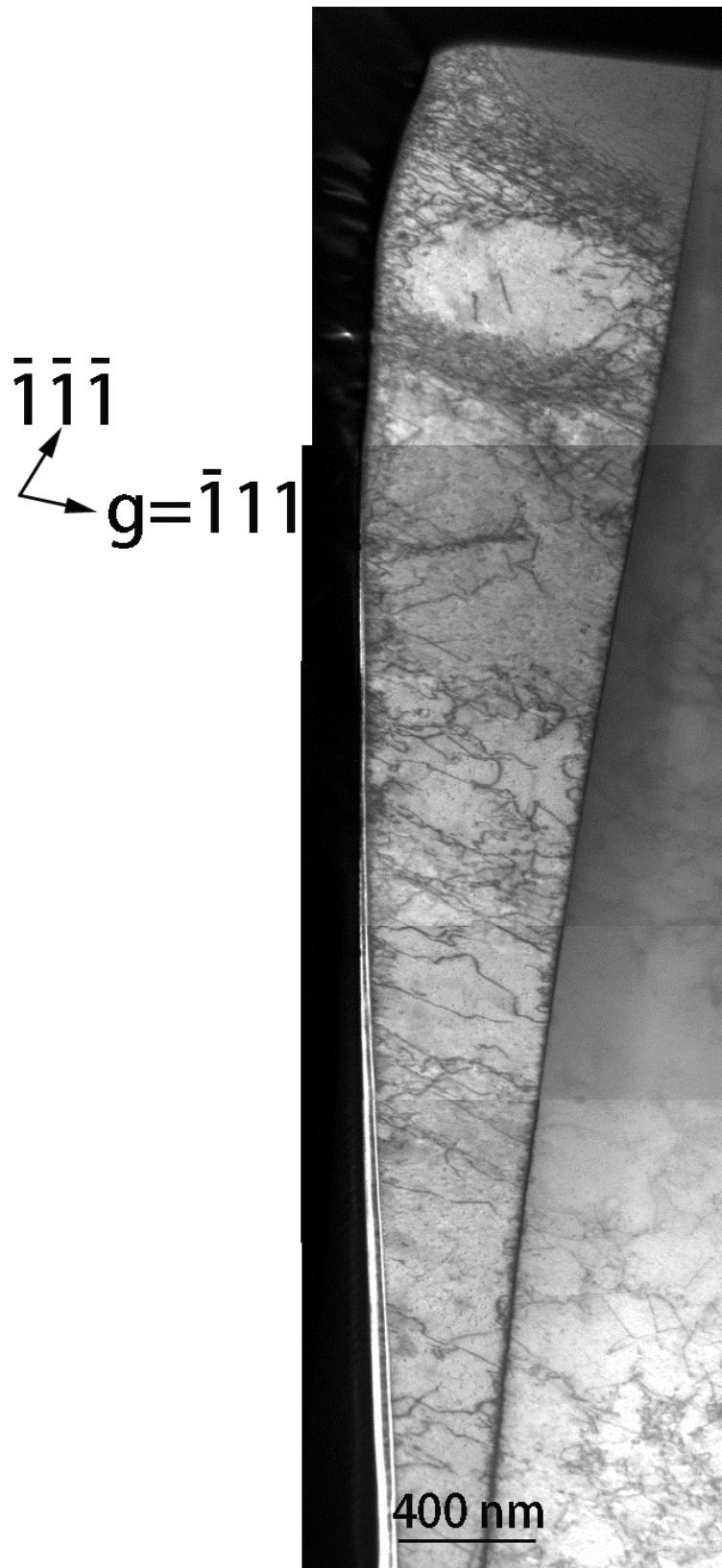
Figure 6-32 (b) A bright field STEM image showing the dislocations inside the [516] grain, g=$\bar{1}$11, BD~[01$\bar{1}$]
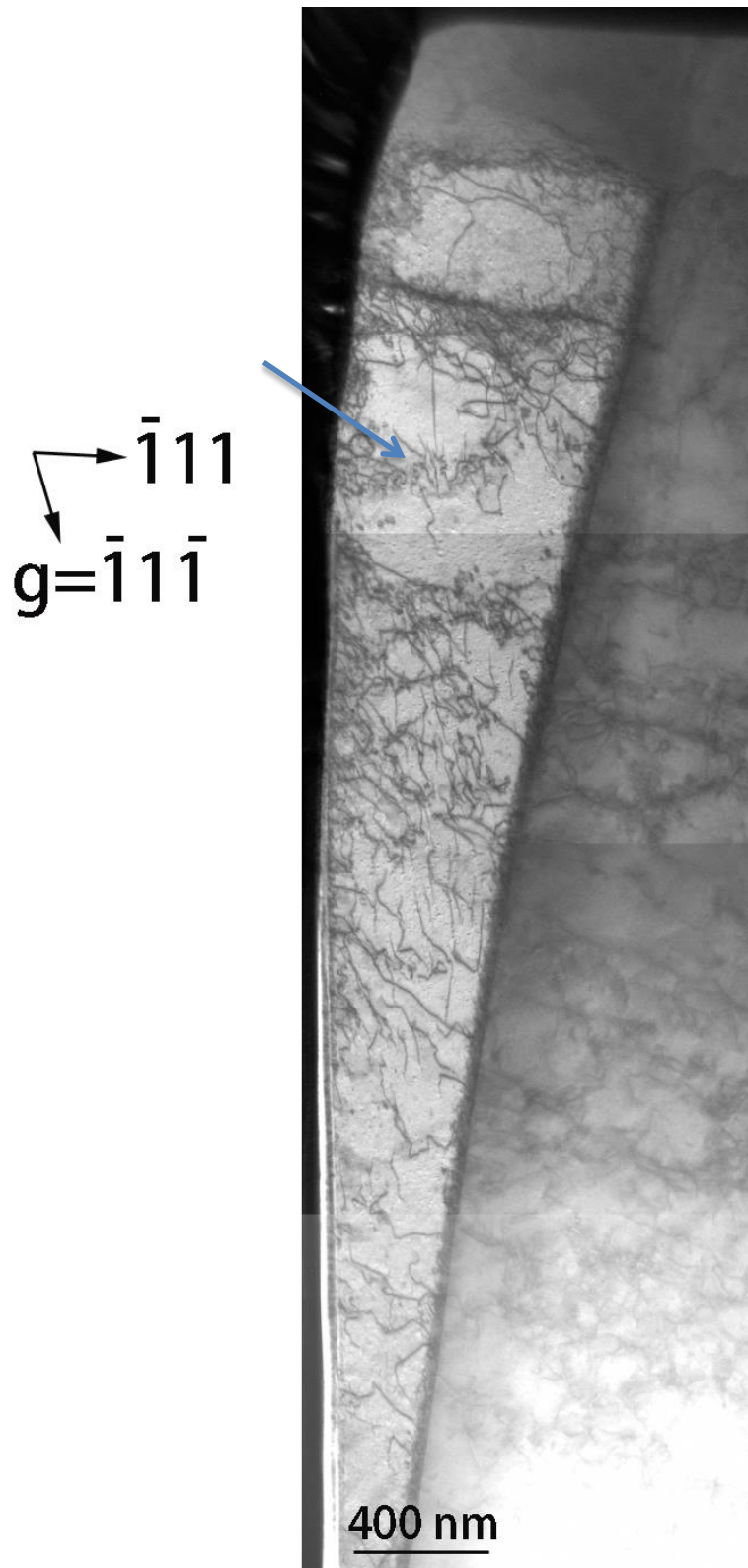
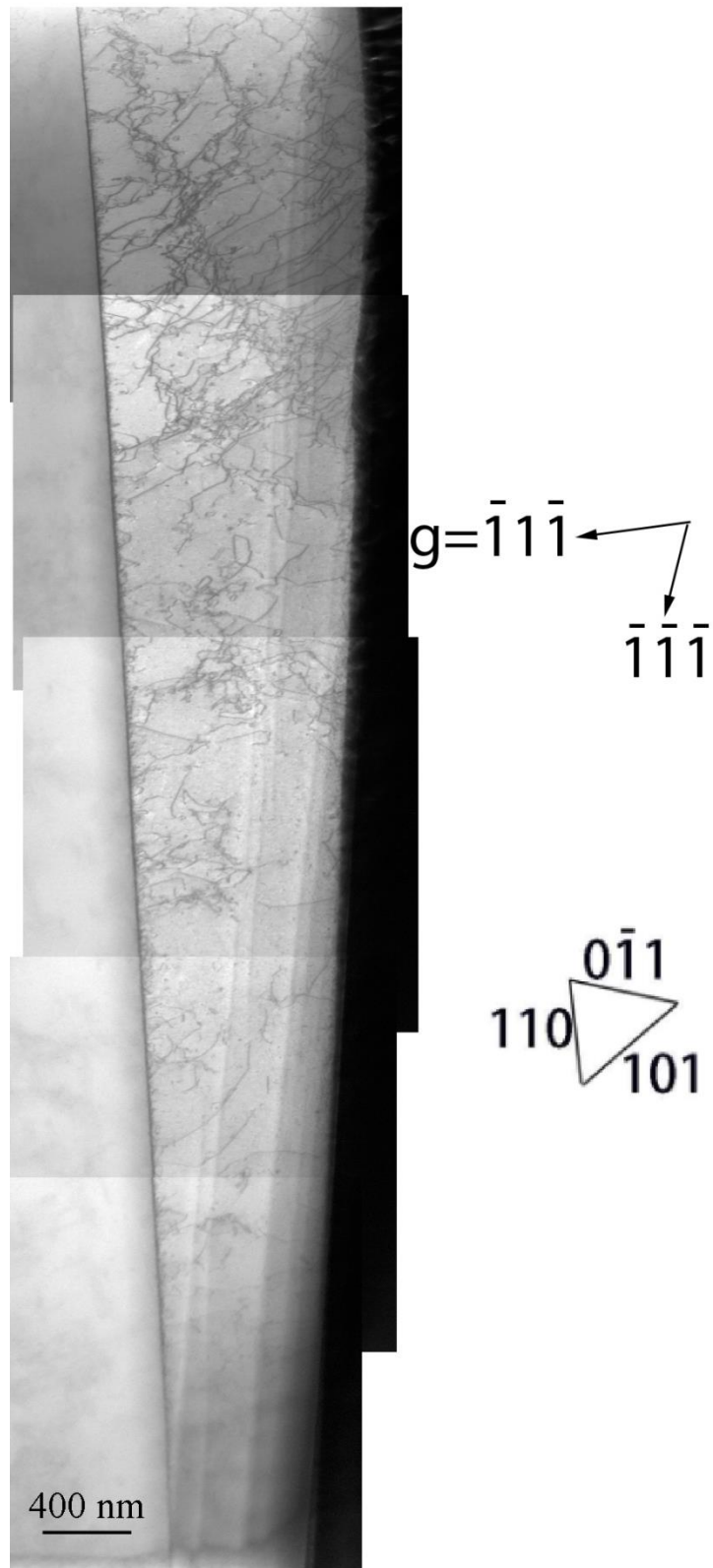**Figure 6-32 (c) A bright field STEM image showing the dislocations inside the [516] grain, g=$\bar{1}1\bar{1}$, BD~[110]. The arrow indicates the abundant$\frac{1}{2}$(111)[0$\bar{1}$1] dislocations in the dislocation walls.**
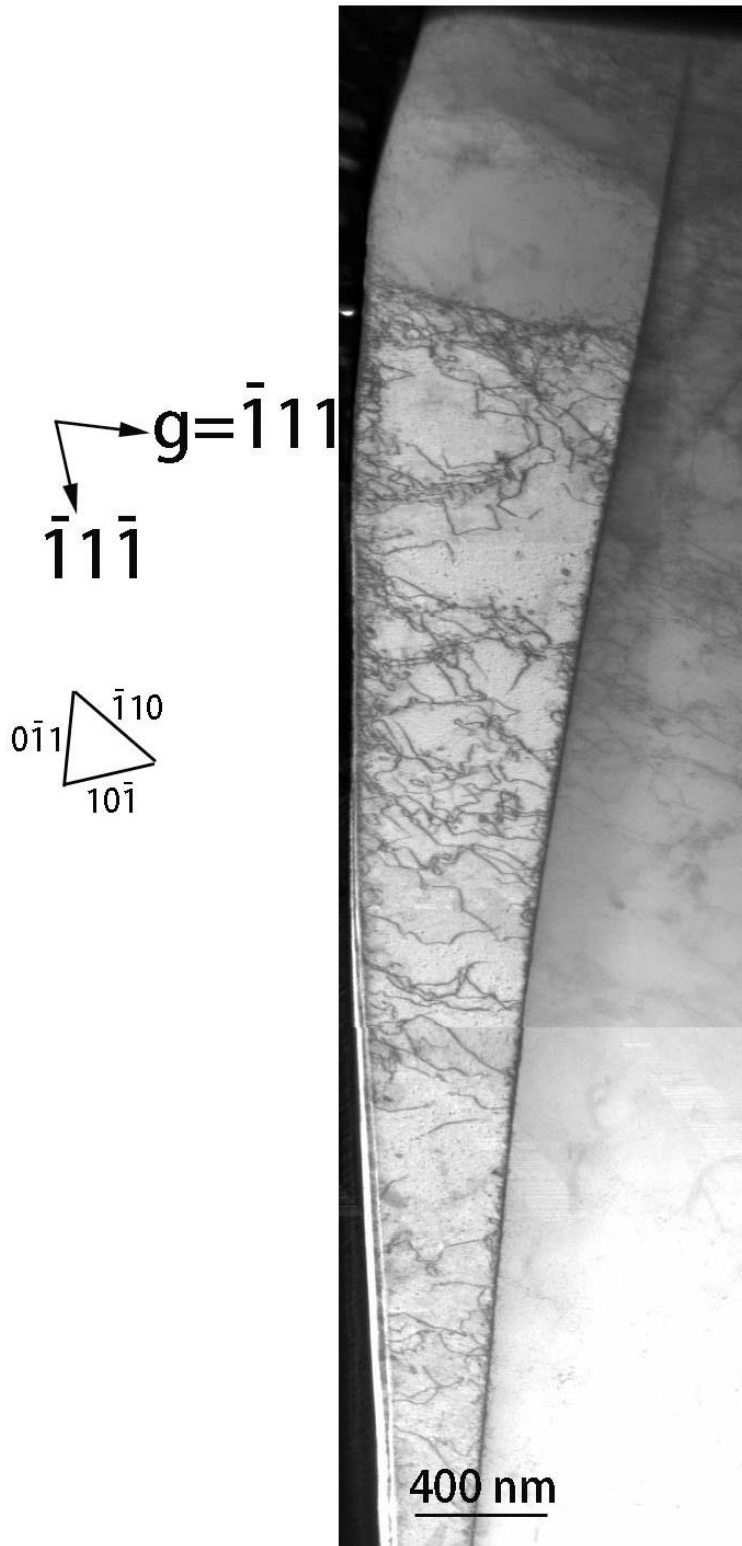
Figure 6-32 (d) A bright field STEM image showing the dislocations inside the [516] grain, g=$\bar{1}$11, BD~[110]

Legend:
- (1Ī1)[011] (yellow)
- (1Ī1)[110] (purple)
- (111)[0Ī1] (blue)
- (111)[Ī10] (red)
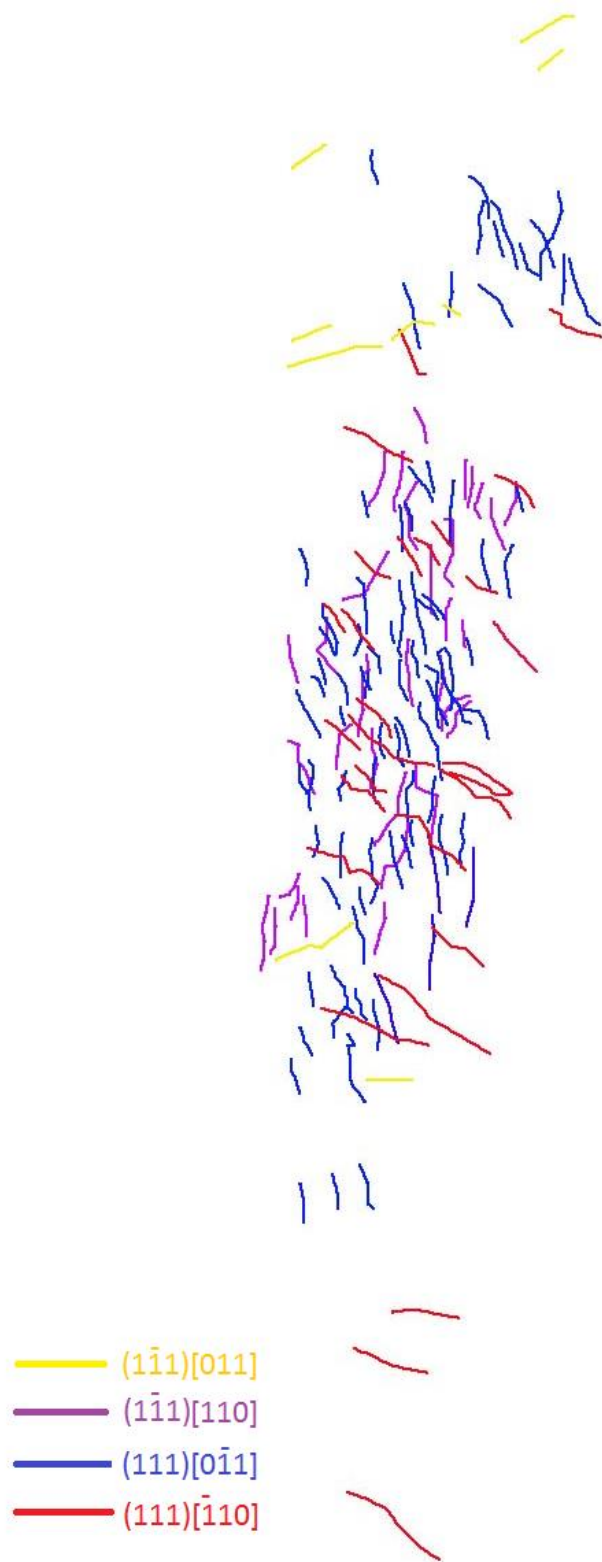
Figure 6-33 colour-coding for the dislocations from different slip systems in the [516] grain.

Table 6-14 Diffraction conditions for the [156] grain from the twinned square pillar

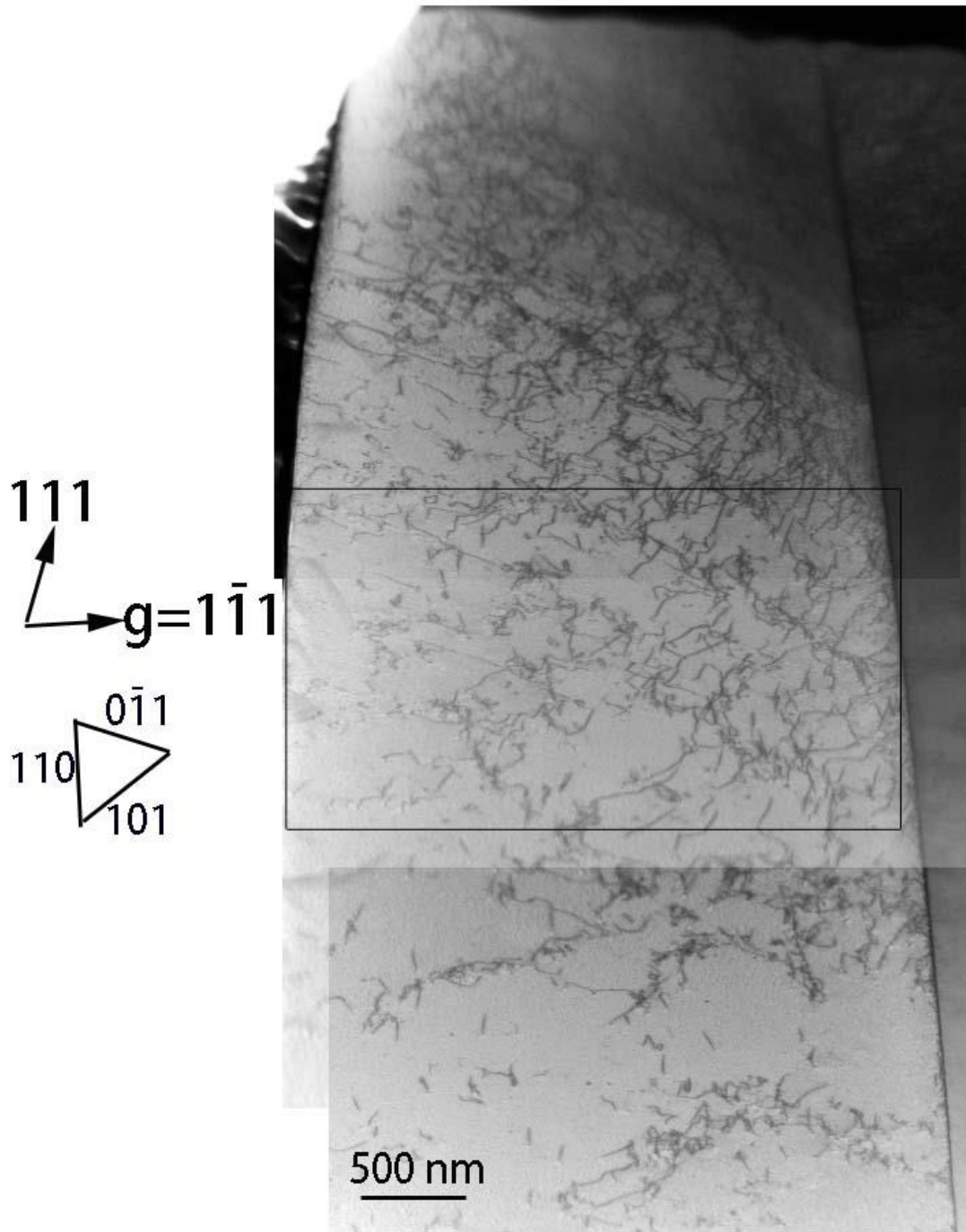| Beam direction	g	Slip system $\frac{1}{2}(\bar{1}11)[101]$	Slip system $\frac{1}{2}(\bar{1}11)[110]$	Slip system $\frac{1}{2}(111)[10\bar{1}]$	Slip system $\frac{1}{2}(111)[\bar{1}10]$	Burgers vector $\frac{1}{2}[0\bar{1}1]$	Burgers vector $\frac{1}{2}[011]$
$[\bar{1}\bar{1}0]$	$1\bar{1}1$	✓ ★	✗	✗	✓	✓	✗
	$1\bar{1}\bar{1}$	✗	✗	✓	✓	✗	✓
$[\bar{1}01]$	$\bar{1}\bar{1}\bar{1}$	✓	✓	✗	✗	✗	✓
	$1\bar{1}1$	✓	✗	✗	✓ ★	✓	✗

Figure 6-34 (a) A bright field STEM image showing the dislocations inside the [156] grain, g=1$\bar{1}$1 BD~[$\bar{1}\bar{1}$0]
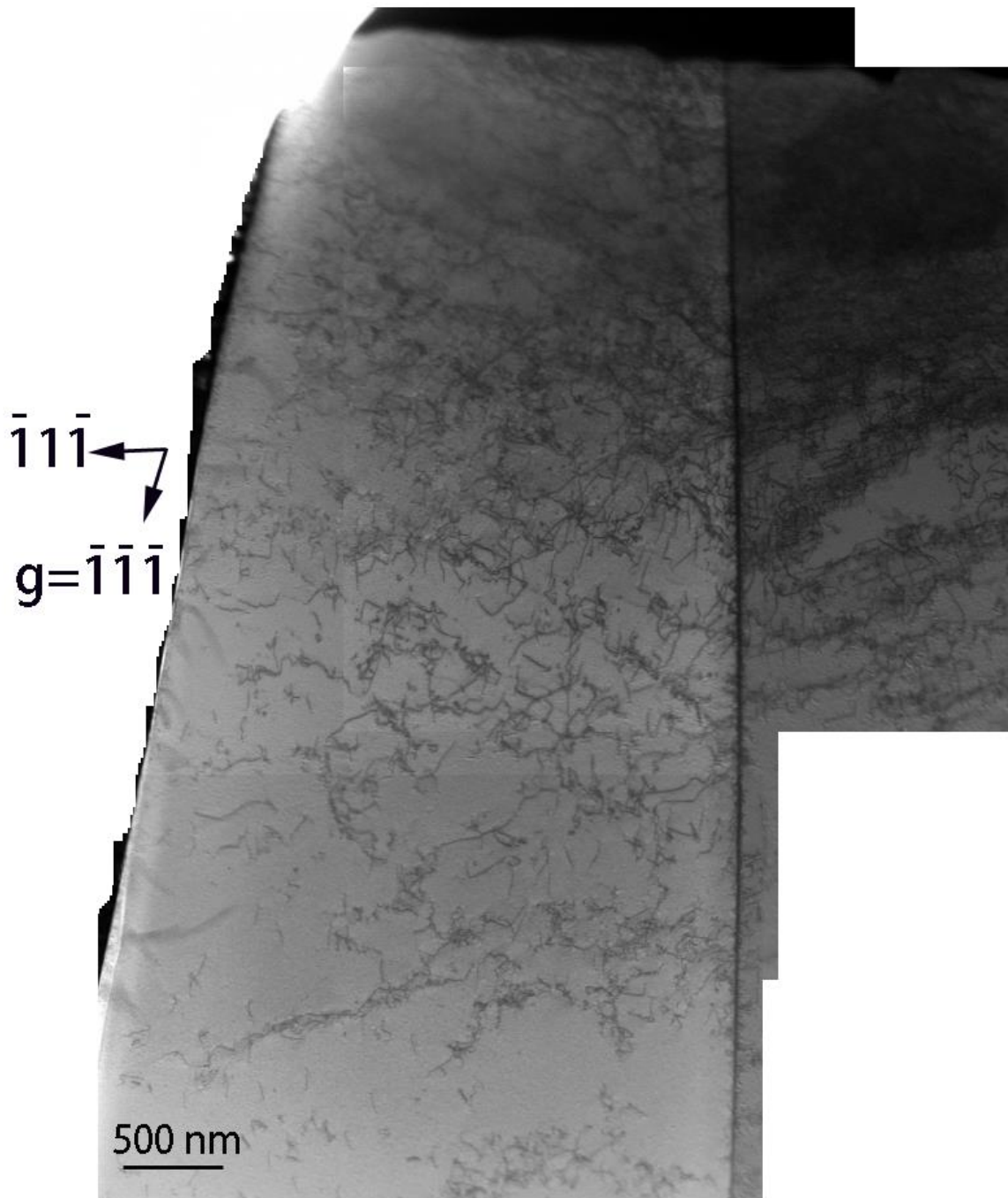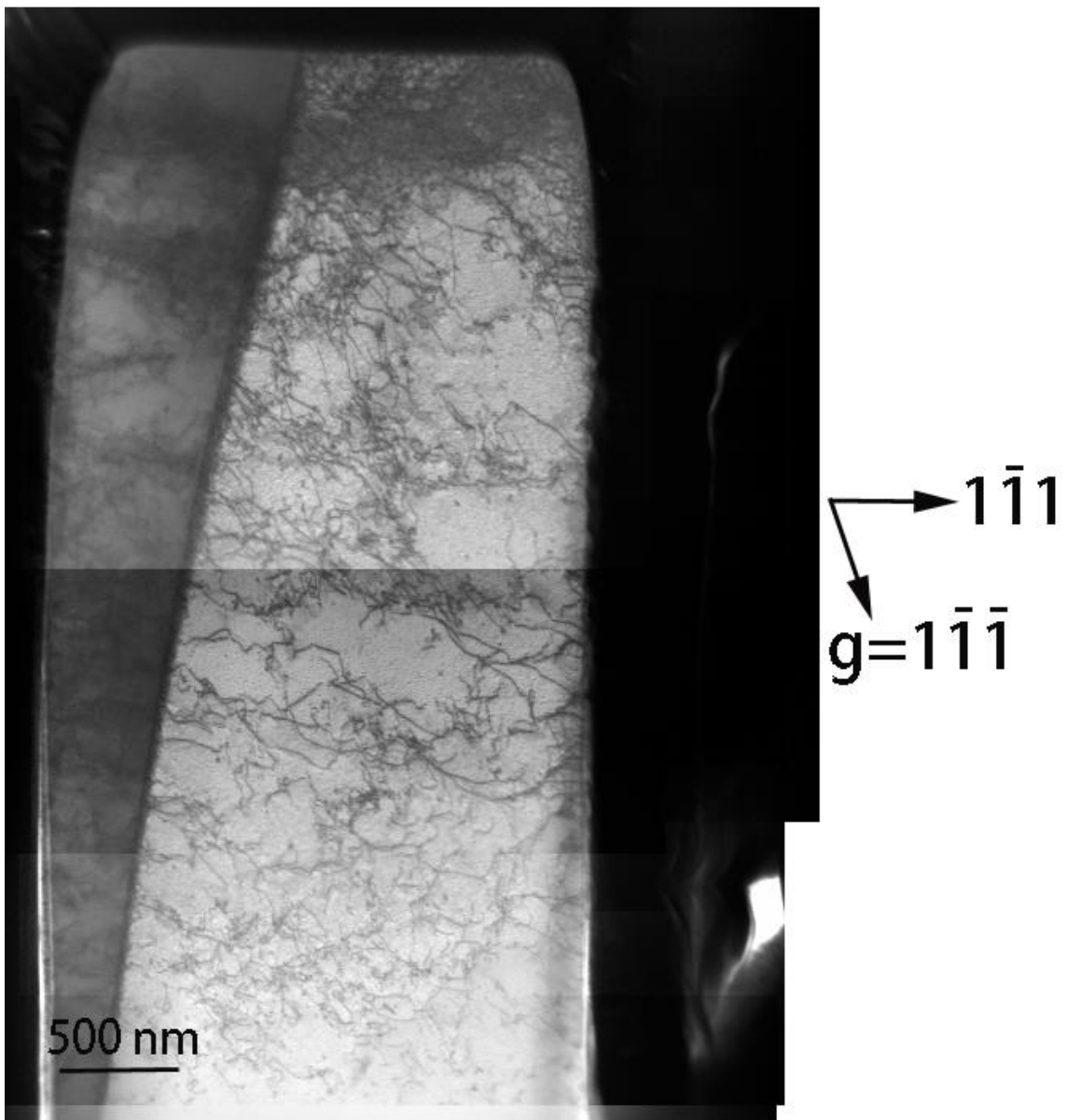
Figure 6-34 (b) A bright field STEM image showing the dislocations inside the [156] grain, g=1$\bar{1}\bar{1}$ BD~[$\bar{1}\bar{1}$0]
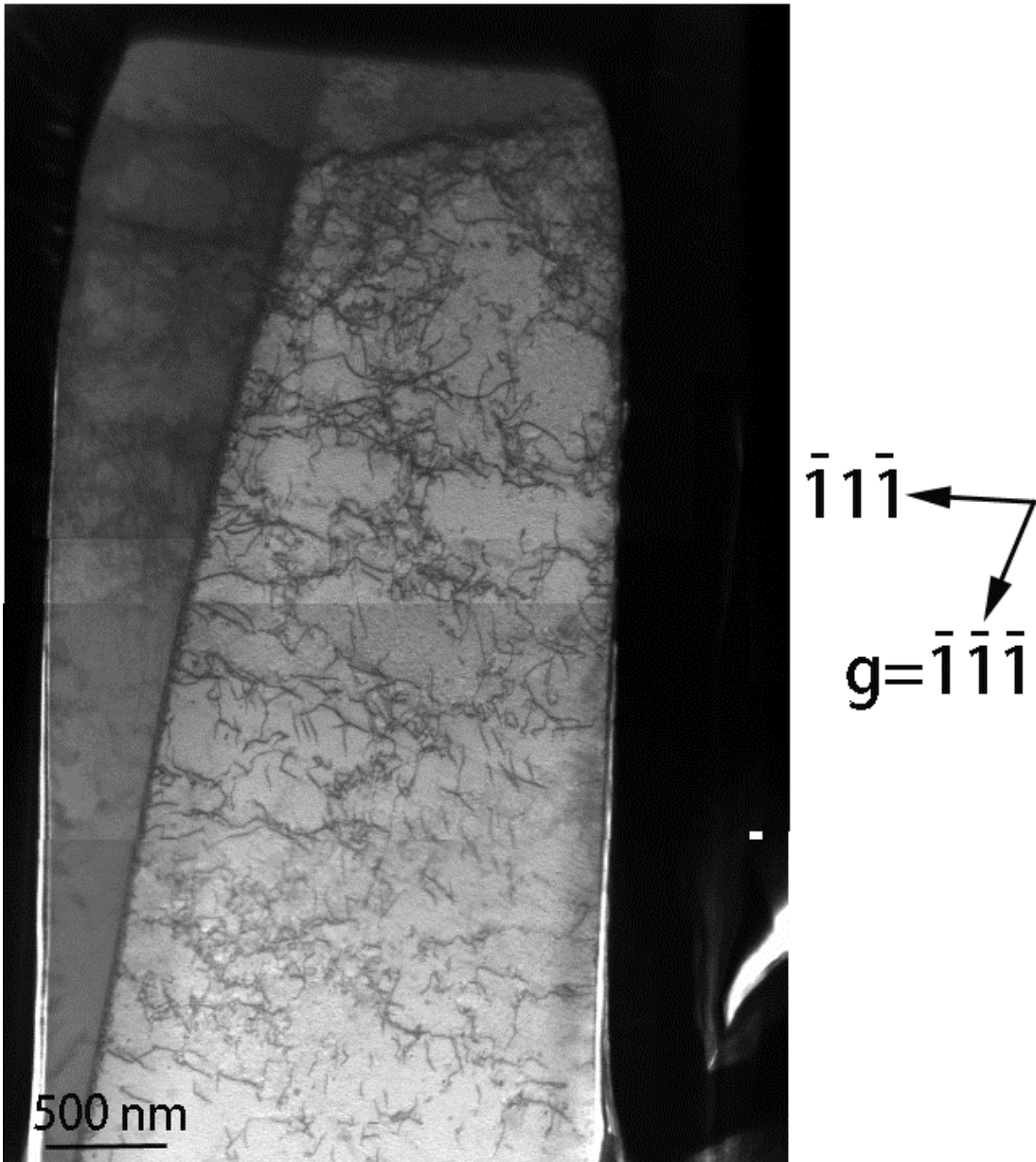
Figure 6-34 (c) A bright field STEM image showing the dislocations inside the [156] grain, g=$\overline{1}\overline{1}\overline{1}$ BD~$[\overline{1}01]$
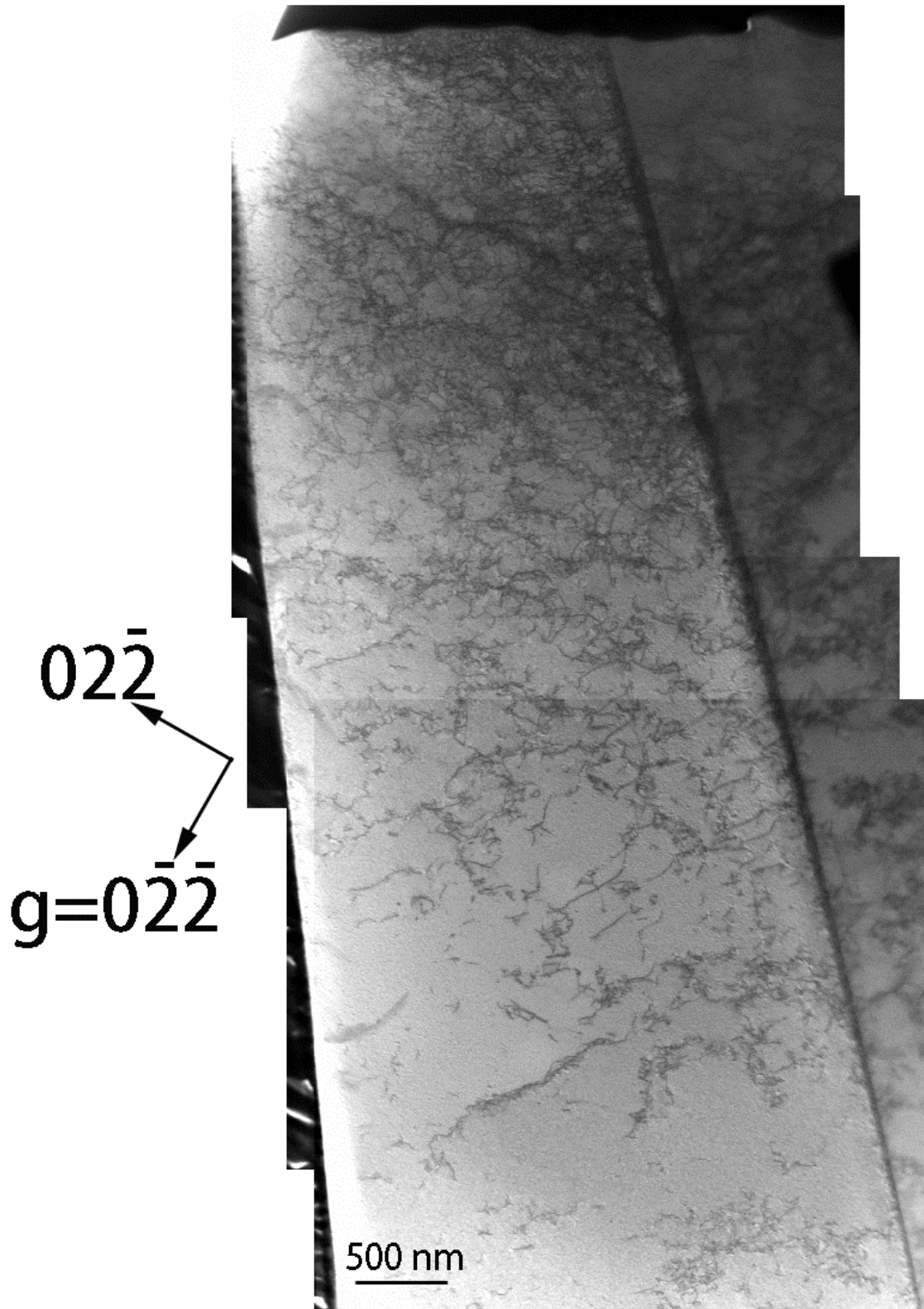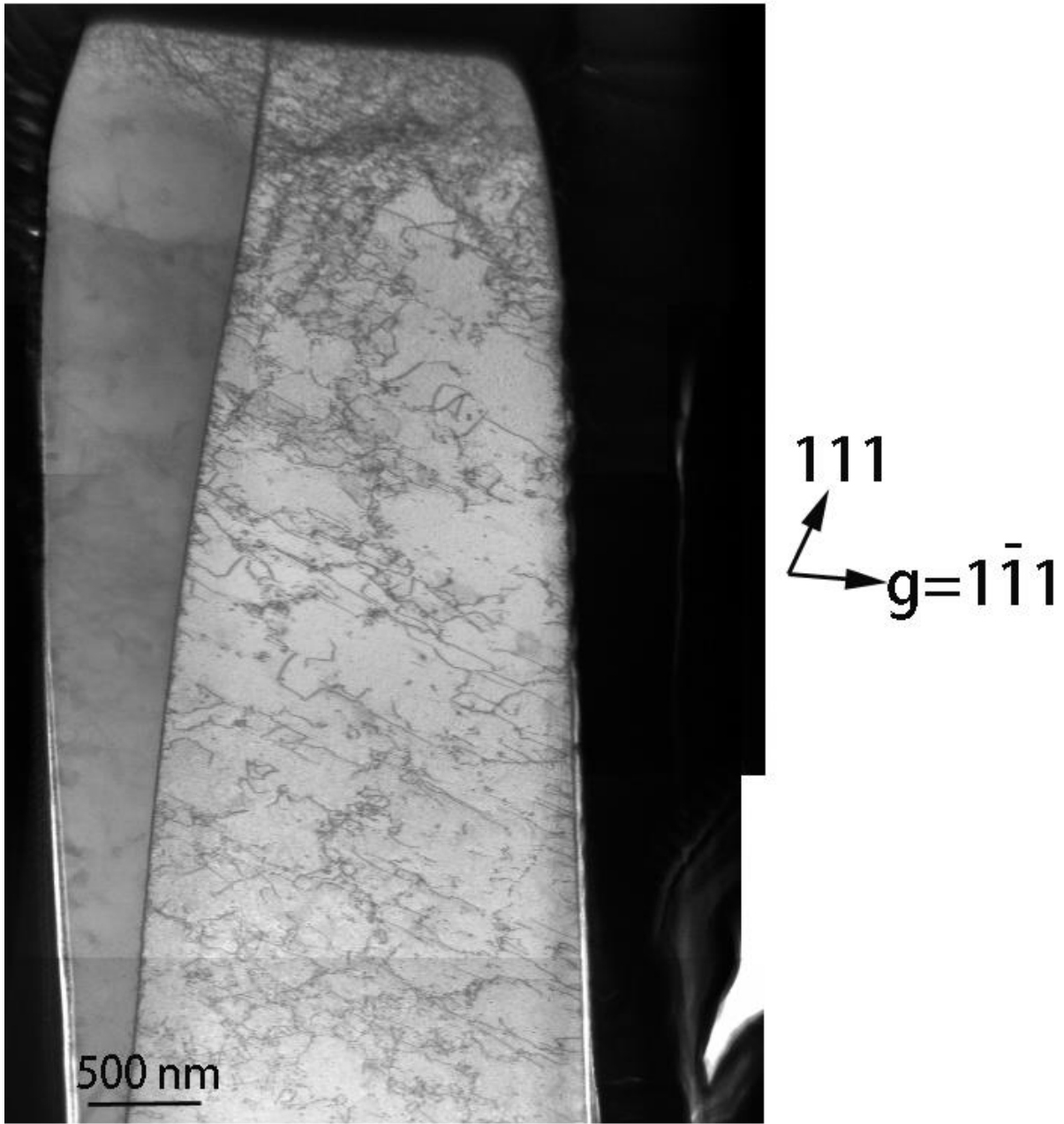
Figure 6-34 (d) A bright field STEM image showing the dislocations inside the [156] grain, g=1$\bar{1}$1 BD~[$\bar{1}$01]
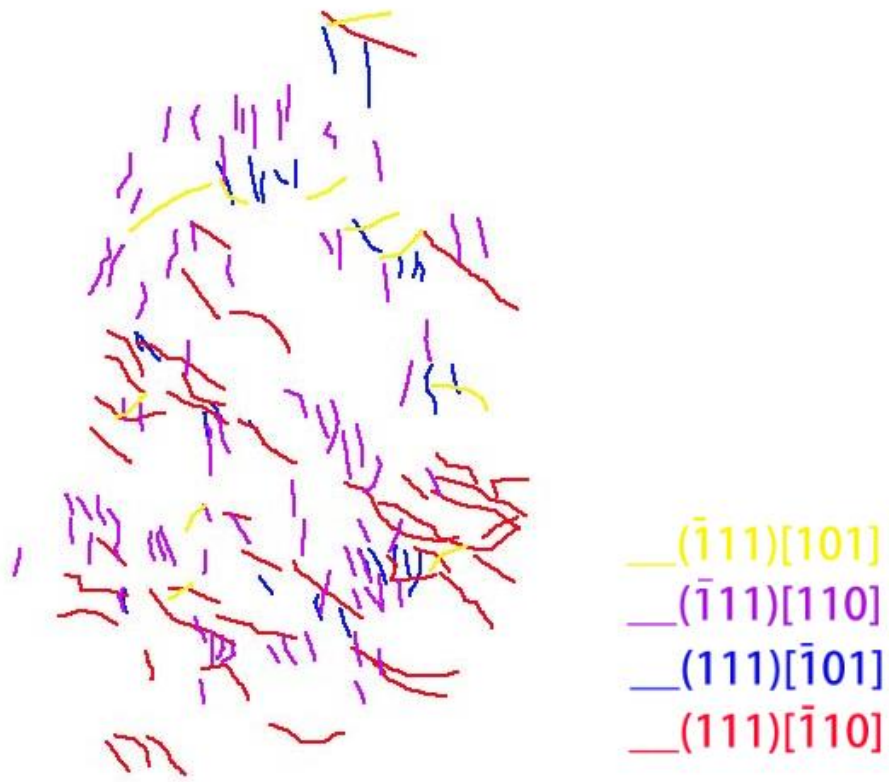
Figure 6-35 colour-coding for the dislocations belonging to different slip systems in the [156] grain.

$$(\bar{1}11)[101]$$
$$(\bar{1}11)[110]$$
$$(111)[\bar{1}01]$$
$$(111)[\bar{1}10]$$

Chapter 7 Discussion on Micropillars

There is a voluminous literature on the deformation of micropillars. Most of the work however has been concerned with the stress-strain curve; very little work has been done on correlating the observed dislocation structure with mechanical behaviour. Here we have attempted to show how the evolution of the dislocation structure is responsible for the micromechanical properties.

7.1 [156] single crystal cylindrical pillars with different sizes

The stress-strain curves obtained from the compression of the [156] oriented single crystal cylinders again confirm that 'smaller is stronger'. Several more novel findings are as follows:

7.1.1 Critical dimension for different deformation mechanisms

The 1-μm pillars exhibit distinctly different deformation behaviour from that of the larger samples. The stress-strain curves for the smallest, 1-μm, samples display larger strain bursts separated by nearly elastic segments. Note that the elastic slope in the micropillars is commonly measured to be lower than the bulk Young's modulus, due to the uncorrected stiffness of the load frame, dislocation removal from the free surfaces and any slight misalignment between the sample and the nanoindenter [16, 17, 87]. The larger samples show a much more gradual hardening with smaller strain bursts. The dislocation observations reveal the origin of the above differences. Only a few dislocations are seen in the STEM images of the deformed 1-μm pillar in Figure 6-6, indicating that most of the dislocations corresponding to the slip traces observed on the sample surface have left the sample. However, a large

number of dislocations were discovered in the deformed 3-µm (Figure 6-8) and 5-µm (Figure 6-13) samples. Even a dislocation cell structure was discernible.

These observations suggest that there is a significant change between 1 µm and 3 µm. Dislocation source activation controls the deformation below 1 µm and dislocation interactions are significant above it.

7.1.2 Dislocation networks in the 3-µm pillar

While the stress-strain curves of micropillars have been extensively investigated, only a few attempts have been made at post-mortem dislocation observations [5, 6, 23, 88]. Also, most of the images contain salt-and-pepper contrast due to Ga^+ implantation during FIB as well as severe bend contouring, making the dislocations difficult to image. Our (higher quality!) STEM/TEM images display the dislocations explicitly and are the first to show a clear cell structure in deformed micropillars.

The dislocation arrangement and density in the 1-µm pillar are comparable with or even less dense than that in the undeformed sample. Due to the severe deformation of the 5-µm pillar, only a small fraction of the dislocations was analysed. Nevertheless, a clear dislocation cell structure was observed in the 3-µm pillar after deformation. A long thick dislocation wall runs parallel to the primary edge orientation in Figure 6-11. A similar phenomenon was reported by Prinze et al. [86], who found an open cell structure with long walls along the primary edge dislocation orientation in deformed bulk Cu single crystals. As described in the literature review, dislocation dipole bundles are elongated along the primary edge dislocation direction during conventional stage I. At the beginning of Stage II, secondary dislocations are activated

near these bundles. Their interaction with the primary dislocations produces Lomer-Cottrell locks, which are obstacles to the gliding dislocations, resulting in continuous dense bundles upon further deformation. The bundles then grow with increasing strain and eventually develop into cell boundaries. Livingston [89] suggested that short walls containing thinner bundles are established after the thick walls. Argon et al. [90] further pointed out that the growth of new dislocation bundles is triggered by the bowing out of free segments from the existing walls. Elastic interaction inside the cell traps segments with opposite Burgers vectors, thus dividing the cell into smaller ones.

The average cell size measured from this sample is about 1 μm, which is consistent with dislocations being unlikely to be trapped in samples with a dimension of, or smaller than, 1 μm.

7.1.3 Atypical two-stage hardening in micromechanics

In this study we defined an atypical two-stage hardening according to the slope of the stress-strain curves, as shown in Figure 5-9. The hardening rates are quite similar in all the samples in stage I and are characterised by high values ranging from 1 to 4.5 GPa; they decrease with decreasing sample diameter in stage II, much lower values around several hundred MPa, even with negative values in the smallest samples, as can be seen in Figure 5-11. It is also worth noting that the stage I hardening in the 1-μm pillars occurs over a wider range of strain than for the larger pillars. There is a greater scatter in work hardening rate as well, which may be caused by the stochastic strain bursts more frequently seen in the 1-μm pillars. The strengthening in stage I is perhaps due to alternating processes of activation and exhaustion of single-armed dislocation sources: with increasing strain, smaller and smaller sources must be

activated. The strengthening in stage II might be forest hardening, as discussed below.

It is generally agreed that the operative dislocation sources in the micron-sized samples are single-armed spirals and that the number of the sources is limited due to the small sample volumes. These spiral dislocation sources have been observed in a number of in-situ TEM deformation investigations [17, 22]. The source truncation theory suggests that the source length decreases with decreasing sample dimension, which explains the size dependency of the yield strength sufficiently [18].

Stage I hardening begins right after yielding, which marks the activation of the weakest, i.e., easiest source in the sample. The source normally stops operating after several cycles, either because of interaction with the grown-in dislocations [14] or because of back stresses generated by the emitted dislocations [17], which are pinned by pre-existing dislocations. This is called source exhaustion. After the source shuts down, a harder spiral source would be activated at a higher stress and then the exhaustion and activation process is repeated. Therefore, it is believed that the stage I hardening arises from the gradual exhaustion of the dislocation sources.

As the newly generated dislocations can readily annihilate at the free surfaces of the 1-μm pillars, they are unlikely to be pinned and serve as dislocation sources, therefore it takes longer time for these newly generated dislocations to affect the deformation response than in larger pillars. Hence stage I hardening which is based on the activation of the pre-existing single armed dislocation sources tends to last over a longer period. After a stable flow stress is reached, very low or even negative stage II strain hardening was exhibited. This is probably due to the appearance of new dislocation sources at higher strain. As a few emitted

dislocations still remain in the pillars after the burst, for instance the set 3 dislocations shown in Figure 6-6, they act as new sources and consequently the next burst happens at a lower stress. However, for 3-μm and 5-μm pillars, the emitted dislocations are more likely to remain in the samples and a number of dislocation junctions form and provide new sources for dislocation multiplication [91]. Hence the plasticity moves to stage II more quickly. As seen in Figure 6-8 and Figure 6-13, considerable dislocation storage was observed in the larger samples. Also, more dislocation interaction happens as the sample size increases; in other words, the free surfaces have less influence on the plastic flow of the larger samples, so the stage II hardening rate increases with increasing sample size. Moreover, the hardening rates Θ for the larger pillars range from 0.12 to 0.69 GPa during stage II (Figure 5-11), and the corresponding normalized hardening rates:

$$\frac{\theta}{G} = \frac{\frac{d\tau}{d\gamma}}{G} = (\Theta * m^2)/G,$$

are calculated to be 0.0005 to 0.003 with the shear modulus of G=48 GPa and Schmid factor m of 0.46. The upper bound of these normalized hardening rates reaches the value in the conventional stage II hardening for bulk materials ($\frac{\theta_{II}}{G} = \frac{1}{300} \to \frac{1}{150}$,) [92]. Hence the interpretation of stage II hardening in micropillar deformation as being based on dislocation interactions, similar to that in bulk material, is reasonable. On the other hand, the existence of the free surfaces does contribute to the relief of the internal network to some extent, leading to a somewhat lower hardening value in the micropillars compared that in the bulk material. Thus we conclude that stage II hardening is controlled by a dislocation-escape-mediated forest hardening process.

Hardening rates at the micron and submicron scale have been studied by several groups [4, 5, 16, 92], the hardening behaviour was ascribed to either dislocation starvation or dislocation interaction, exclusively, rather than simultaneously.

Volkert and Lilleodden[4] reported that strain hardening rates for Au single crystals with diameters ranging from 180 nm to 8 μm increase significantly with decreasing sample diameter, following a power law trend. They argued that the dislocation density in smaller samples decreases due to dislocation starvation and thus an increased applied stress is needed to nucleate or activate new sources. However, our dislocation observations have proved that this simple assumption about dislocation density is not reasonable for large samples.

In in situ Laue microcompression of a square Cu pillar with a side length of 6 μm, Maaβ et al. [92] observed work hardening behaviour comparable to stage II hardening in bulk copper. They also found the formation of a low angle boundary where GNDs are organized to accomplish lattice curvature. Hence they suggested that deformation on this length scale agrees with classical plasticity instead of with dislocation starvation.

Frick et al. [5] also found a size dependence of hardening rate on pillar diameter over the range 165 nm to 1.97 μm for Ni single crystals, with a similar power law exponent to that obtained by Volkert and Lilleodden[4]. They observed an increased dislocation density in the deformed pillars compared with the undeformed ones as well as dislocation pile-ups at the pillar base. They therefore inferred that the hardening behaviour is caused by the dislocation interactions. However, they noted that dislocation starvation was found in smaller samples with high hardening rates in a previous study [16]. Therefore, they concluded that there is a transition in hardening mechanism from source exhaustion to dislocation interaction as the

sample size is increased. This conclusion agrees with our opinion in principle. As shown in Figure 5-10, in our study, the length of stage I hardening (the exhaustion hardening) decreases and stage II hardening (the forest hardening) increases as the sample diameter expands from 1 µm to 5 µm. Nevertheless, the two stage hardening mechanism proposed here provides a more straightforward understanding of the deformation.

7.1.4 Strain bursts

The 1-µm samples exhibit larger strain bursts than the larger samples. Strain bursts appear as jumps in the stress-strain curve, indicating plastic instability in the sample at the micrometre and submicrometre scale. The bursts result from dislocation avalanches and correspond to the formation of slip traces. Csikor et al. [12] carried out three-dimensional simulations of the dynamics of dislocation interactions. They pointed out that the dislocation avalanches arise from the unravelling of jammed dislocations and each avalanche happens on one slip system only, even in multiple slip conditions. In addition, their simulations suggest that the characteristic avalanche strain decreases with increasing sample size, which is supported by the observations reported here.

Further analysis of the strain bursts was reported later by Wang et al. [11]. They performed in-situ TEM compression of Al pillars and found that the dislocations on one set of slip planes moved collectively out of the sample during an avalanche, while some jammed dislocations were still left afterwards on other slip planes, which agrees with the simulations of Csikor's group. However, this experimental investigation demonstrates the existence of two different formation mechanisms for the dislocation bursts, determined by sample size. In pillars with diameters ranging from 80 to 300 nm, the bursts come from explosively generated and

195

instantly escaping dislocations. No dislocations were left after the bursts. In larger samples with a diameter between 300 to 1000 nm, the bursts originate from the destruction of jammed dislocations stored during deformation and the pillars are not necessarily dislocation-free after each burst. The softening after some bursts observed in the stress-strain curves of our 1-μm samples suggests that they were formed via a jamming destruction mechanism.

7.1.5 How many slip systems?

The surface morphology for the [156] cylinders shown in Figure 5-14 to Figure 5-16 indicates that although most of the deformation takes place on two inclined sets of slip planes, single slip does occur, despite the pillar diameters and the strain level. This uncertainty concerning single or multiple slip can be ascribed to the limited number of dislocation sources in these small samples.

A related but slightly different result was reported by Kiener and Minor [14], who investigated Cu single crystals with a [100] strain axis. They found that the deformation morphology was controlled by the sample diameter, i.e., by the number of available sources in the samples. In their in-situ TEM compression study, single slip was observed in samples with diameters less than ~180 nm, while multiple slip was discovered in samples with diameters larger than ~ 400 nm and double slip was found in samples in the intermediate range. They concluded that the scarcity of the dislocation sources in those smaller samples led to the single slip behaviour although the samples were oriented for multiple slip. As the sample volume becomes bigger, the pillars deform in a way more akin to that of bulk [100] Cu crystals. Our results show that single and multiple slip can occur both in 1-μm and in 5-μm pillars. Ng and Ngan [8] investigated the yield probability on different slip systems for Al

pillars with different diameters. They performed Monte Carlo simulations and found that as sample size reduces, secondary and sometimes tertiary slip planes have an increasing probability of yielding. This is because, due to the deficient dislocation sources, the most easily operating ones may not happen to lie on the planes with the highest Schmid factor. These two studies together enable us to explain the occasional presence of single slip in our [156] oriented samples: the limited number of dislocation sources and their stochastic distribution mean that on a certain set of slip planes either no dislocation sources exist or the source sizes are unfavourable for activation. Hence the easiest-yielding sources are available on only one of the two slip planes calculated from the Schmid factor and single slip only was observed in some cases.

7.2 Effect of crystal orientation

Evident differences exist between the mechanical response of the square single crystals oriented in a [156] direction and those in a [235] direction. A comparison of the mechanical data (Figure 5-3 and Figure 5-12) suggests that the two sets of pillars have similar stage I hardening behaviour but the [156] pillars have a higher stage II hardening rate, leading to a separation of the flow curves at higher strain. Their corresponding surface morphology, displayed in Figure 5-18 and Figure 5-19, reveals that single slip occurs in the [235] pillars but multiple slip in the [156] pillars. Finally, the dislocation morphologies shown in Figure 6-16 and Figure 6-19 demonstrate that dislocation tangles are built up from dislocations on different slip systems in the [156] pillar, while well separated primary screw dislocations remain in the [235] pillar. Furthermore, the dislocation density of the [156] pillar deformed to 2.3% strain is two times higher than that of the [235] pillar deformed to 3.9% strain. The

activation of the secondary dislocations in [156] samples increases the forest density and thus boosts the effective storage of the system, leading to a higher total dislocation density.

This result can be satisfactorily interpreted through the two stage hardening model discussed in the previous section. As the two sets of pillars have the same dimensions, then according to the source truncation theory, the dislocation activation processes should be analogous. Therefore, their stress-strain curves overlap in stage I. As the deformation proceeds, dislocation interactions between the four activated slip systems dominate the stage II hardening in the [156] pillars, while only one active slip system prevails in the [235] pillars. Hence the former exhibits stronger forest hardening. This phenomenon again supports our argument that different hardening mechanisms contribute to the flow stress at different levels of plastic strain.

As Uchic et al. suggested in an overview article [93], it is normally presumed that the significance of crystal orientation diminishes as the sample size decreases. Therefore, only a few studies have attempted to investigate the effect of crystal orientation on the deformation of micropillars.

Volkert and Lilleodden [4] were the first to extend the compression experiments on Au micropillars to different orientations. They also found that the crystallographic orientation determines the number of active slip systems. However, they claimed that the orientation has no obvious influence on the yield stress and the hardening rate, which contradicts our findings. Although the sample diameter in their study ranges from 180 nm to 8 μm, we found that most of their data are confined to the submicron scale and thus in fact their result is not representative for micropillars. They also explained that this insensitivity of the stress-strain

behaviour to orientation was a result of insignificant storage of dislocations. They assumed that egress of dislocations happened in the micropillars, leading to no forest hardening from secondary slip. While more work, especially dislocation analysis, needs to be done to verify the effect of orientation on submicron samples, our result suggests that forest hardening still works, at least for 3-µm Cu pillars.

More recently, Kiener et al.[94] investigated the compression of Cu micropillars oriented in the <100> and <111> directions. Their study would have been easier to interpret if they had used the same sample geometry for the two orientations. Unfortunately, their comparison was made between tapered circular shaped <100> Cu and straight square shaped <111> Cu. Nevertheless, they found that the <111> direction is more hardenable, as expected from the deformation of bulk crystals. They also performed simulations and found that the self-organization of dislocations at some level resulted in the evolution of dislocation substructures, leading to work hardening. This conclusion agrees with our observation of larger pillars. However, both the <100> and <111> directions adopted in their study are multiple slip orientations and thus the influence of the number of activated slip systems on micromechanics cannot be identified.

7.3 Effect of twin boundary

7.3.1 Twin boundary in cylinders

Higher work hardening rates are found in both 3-µm and 5-µm twinned cylinders as compared to the single crystal ones. As can be seen in Figure 5-4 and Figure 5-5, the curves of the twinned pillars are all above those of the single crystal ones.

Previous studies suggest that boundaries, especially twin boundaries, can serve as dislocation sinks as well as sources during the deformation [19, 67]. In a recent investigation of 400-nm to 2-µm bicrystalline aluminium pillars containing a high angle grain boundary [19], a decreased degree of work hardening together with larger strain burst extents was found in the stress-strain curves, compared with their single crystalline counterparts. In addition, no dislocation pile-ups were observed in the vicinity of the boundary region. Therefore, the authors concluded that the grain boundary in their study might act as a dislocation sink at such small length scales. In another study, Ni et al. [67] identified the significant influence of dislocation densities on the mechanical response of twinned samples. They reported that dislocations can react with a twin boundary by penetrating the boundary or being absorbed by it, provided that the dislocation density is low (less than $4 \times 10^{15} \ m^{-2}$ in their definition). However, in the case of a high dislocation density (larger than $2 \times 10^{16} \ m^{-2}$) in a twinned grain, the dislocations tangle with each other in front of the boundary instead of penetrating across it.

In our study, a visual inspection of the twinned samples shows that the slip traces in the two constituent grains distribute along the twin boundary in a mirror symmetry relation. It indicates that the initial deformation develops by dislocations cutting through the twin boundary instead of being simply blocked by it. It is worth noting that at this stage we cannot rule out another possibility that dislocation sources pinned in the grain boundary may cause symmetrical deformation in the two grains as well. This may be further studied using in situ SEM compression, where the formation of slip traces can be observed directly. Considering dislocations cutting through the boundary only, as seen in Figure 6-27, Burgers vectors DC and CA in the [516] grain and Burgers vectors D′C′ and C′B′ in the [156] grain are coplanar

Burgers vectors, thus these dislocations can easily glide into the other grain by cross-slip. As discussed in the literature in 2.4.1, the other two activated 60º Burgers vectors (BD and AB in the [516] grain and B′A′ and A′D′ in the [156] grain) may be transferred directly into the neighboring twin grain and leave an additional partial dislocations along the boundary or partly penetrate the boundary and form sessile twin boundary dislocations pinned at the boundary [72], which strengthen the pillar. As the deformation continues, the dislocation density begins to increase remarkably due to the interactions of the dislocations from different slip systems. At this point, the twin boundary starts to block the dislocations. As can be seen in Figure 6-23, Figure 6-25, Figure 6-28 and Figure 6-30, dislocation pile-ups against the twin boundary are evident; some are in the form of tangles. There is no match up of the dislocation arrangements across the twin boundary, indicating no slip transfer in the final deformation. This idea explains the higher work hardening rates observed in the twinned pillars. As the dislocations from different slip systems interact with each other and boost their density, they are more likely to be pinned at the boundary. Consequently, the twin boundary now serves as a dislocation barrier, similar to the dislocation cell walls, impeding further dislocation propagation and thus strengthening the pillar.

A similar study was conducted by Ng and Ngan[20] on Al bicrystal micropillars containing a high angle grain boundary. Similar to our observation, smaller and less frequent strain bursts together with higher work hardening rates were found in their study. However, the incoherent nature of the interface in those pillars leads to incompatible deformations in the two constituent grains, revealed by the large shear deformation along the grain boundary.

7.3.2 Twin boundary in square pillars

A strengthening effect of the twin boundary was also detected in the square pillars. This is in contradiction of a recent study of Cu square pillars with a coaxial twin boundary [95]. In that study, the twin boundary is parallel to the loading axis of the pillars, the primary Burgers vectors are the same in the constituent grains and parallel to the twin boundary as well. These screw type dislocations can cut through the boundary easily by cross-slip with negligible resistance. Although sharing a common feature with their study in that the pillars deform symmetrically along the twin boundary, the samples in our investigation deform via multiple slip while only one slip system was operative in their study. Therefore, forest dislocations are not expected in that single slip system, and the corresponding dislocation density may not be high enough to trigger the blocking function of the twin boundary as it does in our study. On the contrary, dislocation tangles, even a cell structure, are evident in our twinned square pillars and the substructure terminates at the twin boundary without penetration, as shown in Figure 6-32 and Figure 6-34. Also, the activated dislocations in our study contain not only those with Burgers vectors parallel to the twin boundary plane but also the non-parallel ones, the latter cannot glide over the twin boundaries without impediment as discussed in the previous section.

7.4 Effect of the sample geometry

Other studies involving the geometry comparison normally adopt samples with the same cross-sectional area. As the key issues in the micro-compression deformation are dislocation source truncation and dislocation starvation, square prisms with a diagonal length equal to the cylinder's diameter were selected in our study, i.e., the longest escape distance was the same

in these two geometries.

The tapered cylinders resulting from the perpendicular ion beam milling resulted in a strain gradient. The stress is more concentrated at the top parts of the pillars with their smaller cross-sectional area. The morphology observation of the deformed cylinders shows that the deformation tends to be more confined to the top of the 1-µm samples in the [156] single crystals (Figure 5-16). This is because the specimen taper is more severe in smaller samples. Additionally, the 3-µm and 5-µm twinned crystals (Figure 5-21 and Figure 5-22) also display a more localized deformation towards the pillar top as compared with that in the single crystals (Figure 5-14 and Figure 5-15). This may due to the assistance of the twin boundary in dislocation accumulation, which amplifies the strain gradient effect. However, due to the simplicity of the sample preparation, this tapered geometry is widely adopted in micropillar investigations, despite the fact that a larger deformation in the pillar top is frequently observed [4, 7, 96].

Although the square pillars are free of taper, the presence of side edges may raise other issues. Using three-dimensional finite element simulations, Kiener et al. [97] showed that slight stress inhomogeneities between the sides and the body of the square geometry exist. Nevertheless, they compared cylindrical and square pillars for (100) Cu and suggested that due to the experimental scatter, the difference between the two geometries caused by the side edges is trivial. It is however worth noting that the aspect ratio for those pillars was confined to 1.3:1 and therefore the dislocations are more likely to glide into the base of the pillars [56], as there is less (free) side wall therefore less chance of dislocation escape. The dislocation pile-ups at the pillar base may contribute effectively to the strain hardening [5] and mask the

difference caused by the geometries in this case.

In our study the square pillars exhibit a significant increase in hardening rate (thus a higher flow stress) in the later stage of deformation as compared to the cylindrical ones (Figure 5-7 and Figure 5-8). It is noticed that the primary dislocations which have the highest Schmid factor of 0.46 (coloured in yellow in all the STEM or TEM images) are no longer frequently seen in these square pillars, for both single crystal and twinned samples (Figure 6-17, Figure 6-33 and Figure 6-35). Instead, secondary dislocations with lower Schmid factors of 0.40 and 0.32 are generally present. This is different from the observations of the cylindrical pillars with the same orientation, where the number of primary dislocations is comparable with that of the secondary ones, if not more, as shown in Figure 6-11, Figure 6-15, Figure 6-24, Figure 6-26, Figure 6-29 and Figure 6-31. Hence the higher flow stress in the square pillars may be attributed to the deformation carried by slip systems with lower Schmid factors. This may be ascribed to the inhomogeneous state of stress caused by the sides.

It is highly possible that the remarkably higher strengths found in the square pillars are caused by the size effect. The cross-sectional area of the square pillars is 4.84 μm^2 while that of the cylinders is 7.54 μm^2, hence the former exhibit higher strengths.

7.5 Summary

1. A critical dimension exists between 1 μm and 3 μm, governing different deformation mechanisms for Cu micropillars. The dislocation cell structure found in the 3-μm [156] sample has a cell size of about 1 μm, indicating that the dislocations are unlikely to be retained in samples smaller than this.

2. The high hardening rates in stage I deformation of the micropillars arise from the alternate activation and exhaustion of single-armed dislocation sources while a dislocation-escape mediated forest hardening controls the deformation in stage II.

3. Strain bursts are caused by the collective escape of dislocations on one set of slip planes, resulting in the unravelling of the jammed dislocations stored during deformation.

4. The limited number of dislocation sources in the micropillars leads to uncertainty whether single or multiple slip exists in the [156] single crystals.

5. The number of activated slip systems controls the dislocation arrangement and density in the 2.2-µm [235] and [156] square prisms, resulting in higher hardening rates and flow stresses in the latter.

6. In twinned pillars, dislocations can cut through the twin boundary when the deformation begins, as the dislocation density increases with further deformation, the twin boundary starts to block their movement and the dislocation walls/clusters are pinned at the boundary.

7. Different from the dislocations in the cylindrical pillars, the majority of dislocations identified in the square pillars belong to secondary slip systems which have lower Schmid factors. Also, the cross-sectional area in the square pillars is smaller than that in the cylindrical ones. Both of them may contribute to the higher strengths found in the square pillars.

Chapter 8 Conclusions and future work

8.1 Conclusions

The present study focuses on small-scale Cu samples: the fabrication of Cu nanowires and the investigation on the deformation behaviour of Cu micropillars.

The following conclusions can be drawn:

1. Single crystal Cu nanowires with different growth orientations as well as twin boundaries have been obtained using simple direct-current electrochemical deposition at a low current density.

2. The plastic deformation of single crystal micropillars can be divided into two distinct stages. Stage I deformation characterised by a high hardening rate is controlled by the gradual exhaustion and activation of single-armed dislocation sources. Stage II deformation featuring a relatively low hardening value is dominated by dislocation-escape mediated forest hardening.

3. Dislocations are not retained in pillars smaller than 1 μm; on the contrary, dislocation networks and even cell structures have been observed in the larger samples.

4. Due to the limited number of dislocation sources in the micropillars, single slip occurs in some of the multiple-slip oriented [156] cylinders, despite the pillar diameters and levels of strain.

5. The [235] square pillars exhibit lower hardening rates than the [156] ones. Dislocation examination shows that separate long primary screw dislocation arrays prevail in the

former while intensive dislocation interactions are found in the latter.

6. In general, the [156]/[516] twinned pillars exhibit higher hardening rates than the [156] single crystals, for both cylinders and square prisms. Dislocations can cut through the twin boundary in the early stage of deformation, but, as the dislocation density increases with, the twin boundary starts to block the dislocation movement and to strengthen the pillar.

7. Both single crystalline and twinned square pillars display higher hardening rates than their cylindrical counterparts. In the square pillars, stress inhomogeneities are caused by the side edges. The dislocation distribution on the various slip systems is different from that in the cylindrical ones. The fact that the cross-sectional area of the square pillars is smaller than that of the cylinders maybe more likely to contribute to the higher strengths of the former.

8.2 Suggestions for future work

Following the fabrication of the Cu nanowires, mechanical testing of the nanowires such as in-situ TEM tensile tests would be of interest. The influence of the crystal orientation and the twin boundary orientations (i.e., slanted versus vertical) are worth exploring.

A detailed dislocation microstructure evolution in the deformed micropillars has not been studied. Further work would involve the TEM analysis of the micropillars deformed to different strain levels. Dislocation inspection in the base material beneath the pillars would also, be beneficial to reveal the constraints of the base material on the deformation response.

Twinned pillars with a single slip system in each of the constituent grain are worth exploring

(for example, the [235]/[325] pillars), so that the effect of the twin boundary in the single slip and multiple slip systems can be compared.

Towards a better understanding of the effect of sample geometry, comparison of the pillars would be made between cylinders and square prisms with the same cross-sectional area and aspect ratio. In addition, taper-free cylindrical pillars using a more complicated FIB milling process, lathe milling (the ion beam strikes the bulk sample at an oblique angle and produces pillars with a uniform cross section), need to be fabricated to reflect a more accurate interpretation of the microcompression tests.

List of References:

1.   Uchic MD, Dimiduk DM, Florando JN and Nix WD, *Sample dimensions influence strength and crystal plasticity.* Science, 2004. **305**(5686): p. 986-989.

2.   Greer JR and Nix WD, *Nanoscale gold pillars strengthened through dislocation starvation.* Physical Review B, 2006. **73**(24): p. 245410-1-245410-6.

3.   Uchic MD and Dimiduk DA, *A methodology to investigate size scale effects in crystalline plasticity using uniaxial compression testing.* Materials Science and Engineering a-Structural Materials Properties Microstructure and Processing, 2005. **400**: p. 268-278.

4.   Volkert CA and Lilleodden ET, *Size effects in the deformation of sub-micron Au columns.* Philosophical Magazine, 2006. **86**(33-35): p. 5567-5579.

5.   Frick CP, Clark BG, Orso S, Schneider AS and Arzt E, *Size effect on strength and strain hardening of small-scale [111] nickel compression pillars.* Materials Science and Engineering a-Structural Materials Properties Microstructure and Processing, 2008. **489**(1-2): p. 319-329.

6.   Ng KS and Ngan AHW, *Stochastic nature of plasticity of aluminum micro-pillars.* Acta Materialia, 2008. **56**(8): p. 1712-1720.

7.   Lai YH, Chen HM, Lee CJ, Huang JC and Jang JSC, *Strain burst speeds in metallic glass micropillars.* Intermetallics, 2010. **18**(10): p. 1893-1897.

8.   Ng KS and Ngan AHW, *Breakdown of Schmid's law in micropillars.* Scripta Materialia, 2008. **59**(7): p. 796-799.

9.   Dimiduk DM, Uchic MD and Parthasarathy TA, *Size-affected single-slip behavior of pure nickel microcrystals.* Acta Materialia, 2005. **53**(15): p. 4065-4077.

10.   Kiener D, Rester M, Scheriau S, Yang B, Pippan R and Dehm G, *Influence of external and internal length scale on the flow stress of copper.* International Journal of Materials Research, 2007. **98**(11): p. 1047-1053.

11.   Wang ZJ, Li QJ, Shan ZW, Li J, Sun J and Ma E, *Sample size effects on the large strain bursts in submicron aluminum pillars.* Applied Physics Letters, 2012. **100**(7): p. 071906-1-071906-3.

12. Csikor FF, Motz C, Weygand D, Zaiser M and Zapperi S, *Dislocation avalanches, strain bursts, and the problem of plastic forming at the micrometer scale.* Science, 2007. **318**(5848): p. 251-254.

13. Zhang X and Aifantis KE, *Interpreting strain bursts and size effects in micropillars using gradient plasticity.* Materials Science and Engineering a-Structural Materials Properties Microstructure and Processing, 2011. **528**(15): p. 5036-5043.

14. Kiener D and Minor AM, *Source-controlled yield and hardening of Cu(100) studied by in situ transmission electron microscopy.* Acta Materialia, 2011. **59**(4): p. 1328-1337.

15. Greer JR, Oliver WC and Nix WD, *Size dependence of mechanical properties of gold at the micron scale in the absence of strain gradients.* Acta Materialia, 2005. **53**(6): p. 1821-1830.

16. Shan ZW, Mishra RK, Asif SaS, Warren OL and Minor AM, *Mechanical annealing and source-limited deformation in submicrometre-diameter Ni crystals.* Nature Materials, 2008. **7**(2): p. 115-119.

17. Kiener D and Minor AM, *Source Truncation and Exhaustion: Insights from Quantitative in situ TEM Tensile Testing.* Nano Letters, 2011. **11**(9): p. 3816-3820.

18. Parthasarathy TA, Rao SI, Dimiduk DM, Uchic MD and Trinkle DR, *Contribution to size effect of yield strength from the stochastics of dislocation source lengths in finite samples.* Scripta Materialia, 2007. **56**(4): p. 313-316.

19. Kunz A, Pathak S and Greer JR, *Size effects in Al nanopillars: Single crystalline vs. bicrystalline.* Acta Materialia, 2011. **59**(11): p. 4416-4424.

20. Ng KS and Ngan AHW, *Deformation of micron-sized aluminium bi-crystal pillars.* Philosophical Magazine, 2009. **89**(33): p. 3013-3026.

21. Han SM, Phillips MA and Nix WD, *Study of strain softening behavior of Al-Al3Sc multilayers using microcompression testing.* Acta Materialia, 2009. **57**(15): p. 4473-4490.

22. Oh SH, Legros M, Kiener D and Dehm G, *In situ observation of dislocation nucleation and escape in a submicrometre aluminium single crystal.* Nature Materials, 2009. **8**(2): p. 95-100.

23. Norfleet DM, Dimiduk DM, Polasik SJ, Uchic MD and Mills MJ, *Dislocation structures and their relationship to strength in deformed nickel microcrystals.* Acta Materialia, 2008. **56**(13): p. 2988-3001.

24. Jin CG, Jiang GW, Liu WF, Cai WL, Yao LZ, Yao Z, et al., *Fabrication of large-area single crystal bismuth nanowire arrays.* Journal of Materials Chemistry, 2003. **13**(7): p. 1743-1746.

25. Li FY, Zhang L and Metzger RM, *On the growth of highly ordered pores in anodized aluminum oxide.* Chemistry of Materials, 1998. **10**(9): p. 2470-2480.

26. Gerein NJ and Haber JA, *Effect of ac electrodeposition conditions on the growth of high aspect ratio copper nanowires in porous aluminum oxide templates.* Journal of Physical Chemistry B, 2005. **109**(37): p. 17372-17385.

27. Keller F, Hunter MS and Robinson DL, *Structural Features of Oxide Coatings on Aluminium.* Journal of the Electrochemical Society, 1953. **100**(9): p. 411-419.

28. Faust CL, Keller F, Hunter MS and Robinson DL, *Structural Features of Oxide Coatings on Aluminum - Discussion.* Journal of the Electrochemical Society, 1954. **101**(6): p. 335-336.

29. Masuda H and Fukuda K, *Ordered metal nanohole arrays made by a 2-step replication of honeycomb structures of anodic alumina.* Science, 1995. **268**(5216): p. 1466-1468.

30. Asoh H, Nishio K, Nakao M, Tamamura T and Masuda H, *Conditions for fabrication of ideally ordered anodic porous alumina using pretextured Al.* Journal of the Electrochemical Society, 2001. **148**(4): p. B152-B156.

31. Li AP, Muller F and Gosele U, *Polycrystalline and monocrystalline pore arrays with large interpore distance in anodic alumina.* Electrochemical and Solid State Letters, 2000. **3**(3): p. 131-134.

32. Nielsch K, Choi J, Schwirn K, Wehrspohn RB and Gosele U, *Self-ordering regimes of porous alumina: The 10% porosity rule.* Nano Letters, 2002. **2**(7): p. 677-680.

33. Osulliva.Jp and Wood GC, *Morphology and Mechanism of Formation of Porous Anodic Films on Aluminium.* Proceedings of the Royal Society of London Series a-Mathematical and Physical Sciences, 1970. **317**(1531): p. 511-543.

34. Thompson GE, Furneaux RC, Wood GC, Richardson JA and Goode JS, *Nucleation and Growth of Porous Anodic Films on Aluminum.* Nature, 1978. **272**(5652): p. 433-435.

35. Jessensky O, Muller F and Gosele U, *Self-organized formation of hexagonal pore arrays in anodic alumina.* Applied Physics Letters, 1998. **72**(10): p. 1173-1175.

36. Li AP, Muller F, Birner A, Nielsch K and Gosele U, *Hexagonal pore arrays with a 50-420 nm interpore distance formed by self-organization in anodic alumina.* Journal of Applied Physics, 1998. **84**(11): p. 6023-6026.

37. Su ZX and Zhou WZ, *Formation Mechanism of Porous Anodic Aluminium and Titanium Oxides.* Advanced Materials, 2008. **20**(19): p. 3663-3667.

38. Li XM, Wang DS, Tang LB, Dong K, Wu YJ, Yang PZ, et al., *Controllable synthesis of Ag nanorods using a porous anodic aluminum oxide template.* Applied Surface Science, 2009. **255**(17): p. 7529-7531.

39. Huang XH, Li L, Luo X, Zhu XG and Li GH, *Orientation-controlled synthesis and ferromagnetism of single crystalline Co nanowire arrays.* Journal of Physical Chemistry C, 2008. **112**(5): p. 1468-1472.

40. Wang XW, Fei GT, Xu XJ, Jin Z and Zhang LD, *Size-dependent orientation growth of large-area ordered Ni nanowire arrays.* Journal of Physical Chemistry B, 2005. **109**(51): p. 24326-24330.

41. Gao T, Meng GW, Zhang J, Wang YW, Liang CH, Fan JC, et al., *Template synthesis of single-crystal Cu nanowire arrays by electrodeposition.* Applied Physics a-Materials Science & Processing, 2001. **73**(2): p. 251-254.

42. Tian ML, Wang JU, Kurtz J, Mallouk TE and Chan MHW, *Electrochemical growth of single-crystal metal nanowires via a two-dimensional nucleation and growth mechanism.* Nano Letters, 2003. **3**(7): p. 919-923.

43. Paunovic M and Schlesinger M, *Fundamentals of electrochemical deposition [electronic resource]*. 2nd ed. Electrochemical Society series. Hoboken, N.J.: Wiley; 2006

44. Toimil-Molares ME, Buschmann V, Dobrev D, Neumann R, Scholz R, Schuchert IU, et al., *Single-crystalline copper nanowires produced by electrochemical deposition in polymeric ion track membranes.* Advanced Materials, 2001. **13**(1): p. 62-65.

45.   Honeycombe RWK, *The plastic deformation of metals*. London: Edward Arnold; 1968

46.   Steeds JW, *Dislocation Arrangement in Copper Single Crystals as a Function of Strain.* Proceedings of the Royal Society of London Series a-Mathematical and Physical Sciences, 1966. **292**(1430): p. 343-373.

47.   Smallman RE and Bishop RJ, *Modern physical metallurgy and materials engineering : science, process, applications.* Norwich, NY: Knovel; 2003

48.   Hull D and Bacon DJ, *Introduction to dislocations [electronic resource]*. 5th ed. Materials science and technology (New York, N.Y.). Oxford: Butterworth-Heinemann; 2011

49.   Smallman RE, Ngan AHW and Sciencedirect, *Physical metallurgy and advanced materials engineering [electronic resource]*. [S.l.]: Butterworth-Heinemann; 2007

50.   Brenner SS, *Tensile Strength of Whiskers.* Journal of Applied Physics, 1956. **27**(12): p. 1484-1491.

51.   Brenner SS, *Plastic Deformation of Copper and Silver Whiskers.* Journal of Applied Physics, 1957. **28**(9): p. 1023-1026.

52.   Bei H, Shim S, George EP, Miller MK, Herbert EG and Pharr GM, *Compressive strengths of molybdenum alloy micro-pillars prepared using a new technique.* Scripta Materialia, 2007. **57**(5): p. 397-400.

53.   Dou R and Derby B, *A universal scaling law for the strength of metal micropillars and nanowires.* Scripta Materialia, 2009. **61**(5): p. 524-527.

54.   Kiener D, Motz C, Schoberl T, Jenko M and Dehm G, *Determination of mechanical properties of copper at the micron scale.* Advanced Engineering Materials, 2006. **8**(11): p. 1119-1125.

55.   Gilman JJ, *Deformation in crystalline materials.* Appl Micromech Flow Solid, 1953: p. 185-190.

56.   Kiener D, Grosinger W, Dehm G and Pippan R, *A further step towards an understanding of size-dependent crystal plasticity: In situ tension experiments of miniaturized single-crystal copper samples.* Acta Materialia, 2008. **56**(3): p. 580-592.

57. Schuster BE, Wei Q, Ervin MH, Hruszkewycz SO, Miller MK, Hufnagel TC, et al., *Bulk and microscale compressive properties of a Pd-based metallic glass.* Scripta Materialia, 2007. **57**(6): p. 517-520.

58. Maass R, Van Petegem S, Grolimund D, Van Swygenhoven H and Uchic MD, *A strong micropillar containing a low angle grain boundary.* Applied Physics Letters, 2007. **91**(13).

59. Rinaldi A, Peralta P, Friesen C and Sieradzki K, *Sample-size effects in the yield behavior of nanocrystalline nickel.* Acta Materialia, 2008. **56**(3): p. 511-517.

60. Aitken ZH, Jang D, Weinberger CR and Greer JR, *Grain Boundary Sliding in Aluminum Nano-Bi-Crystals Deformed at Room Temperature.* Small, 2013: p. 100-108.

61. Schuster BE, Wei Q, Zhang H and Ramesh KT, *Microcompression of nanocrystalline nickel.* Applied Physics Letters, 2006. **88**(10): p. 103112-1-103112-3.

62. Kheradmand N and Vehoff H, *Orientation Gradients at Boundaries in Micron-Sized Bicrystals.* Advanced Engineering Materials, 2012. **14**(3): p. 153-161.

63. Shim S, Bei H, Miller MK, Pharr GM and George EP, *Effects of focused ion beam milling on the compressive behavior of directionally solidified micropillars and the nanoindentation response of an electropolished surface.* Acta Materialia, 2009. **57**(2): p. 503-510.

64. Bei H, Shim S, Pharr GM and George EP, *Effects of pre-strain on the compressive stress-strain response of Mo-alloy single-crystal micropillars.* Acta Materialia, 2008. **56**(17): p. 4762-4770.

65. Kelly A and Groves GW, *Crystallography and crystal defects.* London: Longman; 1970

66. Hirth JP and Lothe J, *Theory of dislocations.* McGraw-Hill series in materials science and engineering. New York: McGraw-Hill; 1968

67. Ni S, Wang YB, Liao XZ, Figueiredo RB, Li HQ, Ringer SP, et al., *The effect of dislocation density on the interactions between dislocations and twin boundaries in nanocrystalline materials.* Acta Materialia, 2012. **60**(6-7): p. 3181-3189.

68. Wang YB, Wu B and Sui ML, *Dynamical dislocation emission processes from twin boundaries.* Applied Physics Letters, 2008. **93**(4).

69. Remy L, *Twin-Slip Interaction in Fcc Crystals.* Acta Metallurgica, 1977. **25**(6): p. 711-714.

70. Cahn RW, *Plastic Deformation of Alpha-Uranium - Twinning and Slip.* Acta Metallurgica, 1953. **1**(1): p. 49-70.

71. Jin ZH, Gumbsch P, Ma E, Albe K, Lu K, Hahn H, et al., *The interaction mechanism of screw dislocations with coherent twin boundaries in different face-centred cubic metals.* Scripta Materialia, 2006. **54**(6): p. 1163-1168.

72. Jin ZH, Gumbsch P, Albe K, Ma E, Lu K, Gleiter H, et al., *Interactions between non-screw lattice dislocations and coherent twin boundaries in face-centered cubic metals.* Acta Materialia, 2008. **56**(5): p. 1126-1135.

73. Lu K, Lu L and Suresh S, *Strengthening Materials by Engineering Coherent Internal Boundaries at the Nanoscale.* Science, 2009. **324**(5925): p. 349-352.

74. Jang DC, Li XY, Gao HJ and Greer JR, *Deformation mechanisms in nanotwinned metal nanopillars.* Nature Nanotechnology, 2012. **7**(9): p. 594-601.

75. Wang Z and Brust M, *Fabrication of nanostructure via self-assembly of nanowires within the AAO template.* Nanoscale Research Letters, 2007. **2**(1): p. 34-39.

76. Ishitani T, Tsuboi H, Yaguchi T and Koike H, *Transmission Electron-Microscope Sample Preparation Using a Focused Ion-Beam.* Journal of Electron Microscopy, 1994. **43**(5): p. 322-326.

77. Schwartz AJ, *Electron backscatter diffraction in materials science*. 2nd ed. New York: Springer; 2009

78. Williams DB and Carter CB, *Transmission electron microscopy : a textbook for materials science*. 2nd ed. New York, N.Y.: Springer; 2009

79. Yao N and Cambridge Books O, *Focused Ion Beam Systems [electronic resource] : Basics and Applications.* 1st ed. Cambridge books online. Cambridge: Cambridge University Press; 2007

80. Fischer-Cripps AC, *Nanoindentation [electronic resource]*. Mechanical Engineering Series, 10941-5122. New York, NY: Springer New York; 2011

81.   Gemperle A, Zarubova N and Gemperlova J, *Reactions of slip dislocations with twin boundary in Fe-Si bicrystals.* Journal of Materials Science, 2005. **40**(12): p. 3247-3254.

82.   Paidar V, Palval PP and Kadeckova S, *Plastic-Deformation of Symmetrical Bicrystals Having Sigma-3 Coincidence Twin Boundary.* Acta Metallurgica, 1986. **34**(11): p. 2277-2289.

83.   Thompson GE and Wood GC, *Porous Anodic Film Formation on Aluminum.* Nature, 1981. **290**(5803): p. 230-232.

84.   Thompson GE, Furneaux RC, Wood GC and Hutchings R, *Stem-Edax Analysis of Cell-Walls in Porous Anodic Films Formed on Aluminum.* Journal of the Electrochemical Society, 1978. **125**(9): p. 1480-1482.

85.   Wang YH, Ye CH, Fang XS and Zhang L, *A simple method for synthesizing copper nanotube arrays.* Chemistry Letters, 2004. **33**(2): p. 166-167.

86.   Prinz F and Argon AS, *Dislocation Cell-Formation during Plastic-Deformation of Copper Single-Crystals.* Physica Status Solidi a-Applied Research, 1980. **57**(2): p. 741-753.

87.   Zhang H, Schuster BE, Wei Q and Ramesh KT, *The design of accurate micro-compression experiments.* Scripta Materialia, 2006. **54**(2): p. 181-186.

88.   Gu R and Ngan AHW, *Effects of pre-straining and coating on plastic deformation of aluminum micropillars.* Acta Materialia, 2012. **60**(17): p. 6102-6111.

89.   Livingston JD, *The density and distribution of dislocations in deformed copper crystals.* Acta Metallurgica, 1962. **10**(3): p. 229-239.

90.   Argon AS, Orowan E and Massachusetts Institute Of T, *Physics of strength and plasticity.* Cambridge: M.I.T. Press; 1969

91.   Liu ZL, Liu XM, Zhuang Z and You XC, *Atypical three-stage-hardening mechanical behavior of CU single-crystal micropillars.* Scripta Materialia, 2009. **60**(7): p. 594-597.

92.   Maass R, Van Petegem S, Grolimund D, Van Swygenhoven H, Kiener D and Dehm G, *Crystal rotation in Cu single crystal micropillars: In situ Laue and electron backscatter diffraction.* Applied Physics Letters, 2008. **92**(7): p. 071905-1-071905-3.

93.   Uchic MD, Shade PA and Dimiduk DM, *Micro-compression testing of fcc metals: A selected overview of experiments and simulations.* Jom, 2009. **61**(3): p. 36-41.

94.   Kiener D, Guruprasad PJ, Keralavarma SM, Dehm G and Benzerga AA, *Work hardening in micropillar compression: In situ experiments and modeling.* Acta Materialia, 2011. **59**(10): p. 3825-3840.

95.   Li LL, An XH, Imrich PJ, Zhang P, Zhang ZJ, Dehm G, et al., *Microcompression and cyclic deformation behaviors of coaxial copper bicrystals with a single twin boundary.* Scripta Materialia, 2013. **69**(2): p. 199-202.

96.   Frick CP, Orso S and Arzt E, *Loss of pseudoelasticity in nickel–titanium sub-micron compression pillars.* Acta Materialia, 2007. **55**(11): p. 3845-3855.

97.   Kiener D, Motz C and Dehm G, *Micro-compression testing: A critical discussion of experimental constraints.* Materials Science and Engineering a-Structural Materials Properties Microstructure and Processing, 2009. **505**(1-2): p. 79-87.